Deposition of advanced phosphor coatings by flame spray pyrolysis

Vom Promotionsausschuss der
Technischen Universität Hamburg-Harburg
zur Erlangung des akademischen Grades
Doktor-Ingenieur
genehmigte Dissertation

von
Roman Kubrin
aus Stavropol

2011

Gutachter:

Prof. Dr. Wolfgang Bauhofer (TU Hamburg-Harburg)
Prof. Dr. Stefan Heinrich (TU Hamburg-Harburg)

Tag der mündlichen Prüfung:

01. November 2011

Diese Dissertation wurde vom Cuvillier Verlag Göttingen als Buch unter ISBN 978-3-95404-019-3 veröffentlicht (www.cuvillier.de).

Contents

1. Introduction

In the last several decades, we have witnessed unprecedented changes to people's way of life which were possible through rapid advances in science and technology. Undoubtedly, miniaturization of solid-state electronic devices provided the biggest contribution to the onset of a new era both in scientific research and in development of novel consumer goods.

The beginning of the nano-age can be dated back to 1959, the year when the first integrated electronic circuits were patented and Richard Feynman gave his talk "There's plenty of room at the bottom" introducing the field of nanotechnology. It was, however, not until 1990s, that actual nanotechnologies were developed and today, 50 years after the invention of ICs and Feynman's lecture at Caltech, there is still a lot of unexplored space not only "at the bottom" of electronics but also in other scientific areas, for example, in solid-state luminescence.

Research on inorganic light-emitting materials was initially focused on properties of phosphor powders consisting of particles significantly larger than the wavelengths of visible light. Most of the phosphors in use nowadays consist of particles with the sizes ranging from several micrometers to several tens of micrometers. However, down-scaling of phosphor particle size into the sub-micrometer and nano-range could be advantageous for numerous applications, e.g., digital imaging in the ultraviolet spectral range.

The first semiconductor imaging integrated circuits called charge-coupled devices (CCDs) were invented in October 1969, just ten years after the invention of electronic ICs. (It must be mentioned that the authors of CCDs were awarded with the Nobel Prize in physics in 2009 because of the high impact of their invention on modern society.) Since then, the performance of image sensors has been constantly pushed to its physical limits. As of 2011, pixel size of the state-of-the-art CCDs and their successors based on CMOS-technology is below 2 μm. Main global vendors already have a 0.9 μm technology node on the roadmap for the nearest future (for back-side illuminated CMOS chips). Following the progress in fabrication of integrated circuits, resolution of image sensors could relatively soon reach the diffraction limits for visible light (0.2-0.3 μm).

Advances in digital imaging do not merely rely on the ongoing development in the field of manufacturing of semiconductor ICs but also support it. CCDs are widely utilized in photolithography (the predominant method of material structuring in IC-industry), e.g., in systems for mask inspection or adjustment of laser beams. At the current stage of development of IC-manufacturing technology, the market of lithography tools is dominated by 248 nm and 193 nm wavelength optical systems. There are several next-generation lithography candidates: extreme ultraviolet lithography, nano-

imprint, and multi-beam e-beam maskless patterning. However, they are still far away from being commercialized. UV lithography will continue to be the mainstream technology for at least next 10 years or more and the requirements imposed on mask inspection tools and excimer laser adjustment systems will become considerably more stringent, because there will be a demand for the highest achievable resolution and high sensitivity to radiation in a range of deep UV (DUV: $\lambda < 300$ nm) at the same time.

Sufficient sensitivity of solid-state detectors to UV-light may be acquired via special device architecture of the image sensor, choice of material, etc. However, it is also possible to enhance the UV-performance of standard front-illuminated silicon CCDs by introducing a phosphor plate in front of it, which would convert the UV radiation into the visible light. This approach could substantially lower the prices of lithography mask inspection systems and laser beam profilers for the cases where sub-optical resolution is not necessary. However, it may appear critical to be able to produce phosphor screens with extremely high resolution (as close to diffraction limits as can be).

Inorganic crystalline phosphors are known for their photostability and high efficiency. Usually, phosphor coatings are applied in the form of a porous particulate layer, which has higher brightness of luminescence (as compared to single crystals). The resolution of powder screens is limited by the size of the phosphor particles. Performance of the screens can be improved by reduction of the phosphor particle size. Along with high-resolution digital imaging in the UV range, applications of inorganic phosphors which could benefit from a decreased particle size of phosphors include CCD-based X-Ray imaging, plasma display panels, field emission displays, phosphor-converted white light-emitting diodes, and electroluminescent displays.

Synthesis and further processing of phosphor powders with reduced particle size are quite challenging and although the nano-age for inorganic phosphors was entered in the late 1990s, high-throughput low-cost techniques for fabrication of screens from sub-micrometer-sized phosphors are still in great demand. Performance of such screens should be thoroughly investigated because it can be strongly affected by various effects of decreased particle size.

This thesis is dedicated to a study and further development of flame spray pyrolysis – a method which combines the synthesis of fine or ultrafine phosphor powders (with particle size ranging from approximately 1 µm down to 10 nm) and their deposition onto phosphor screens in a single processing step. The scope of the present investigation is further limited to photoluminescence (PL) of non-patterned phosphor screens made of rare earth-doped oxide phosphors, although many conclusions are also valid for luminescence excited by X-rays and cathode rays as well as for other types of phosphors.

2. Potential of phosphor coatings with decreased particle size

2.1. Phenomenon of luminescence: theory and related terminology

The word *phosphor* was coined in the 17th century and means “light bearer” in Greek.[1] This term is commonly used for any solid material exhibiting light emission due to *luminescence*. It should be added that contrary to popular belief, most of the phosphors do not contain the chemical element *phosphorus*.

Luminescence is defined as a phenomenon in which the electronic state of a substance (i.e., of a phosphor) is excited by some kind of external energy and the excitation energy is given off as light.[1] Depending on the type of the involved external energy, luminescence is further subdivided into *photoluminescence* (excited by photons), *cathodoluminescence* (excited by incident electron beam), and *electroluminescence* (excited by applied electrical field), to name a few. Heat can also participate in excitation of luminescence (e.g., thermoluminescence); however, the latter should not be confused with the thermal radiation from heated objects (incandescence, i.e., a part of blackbody radiation emitted in the visible range).[2] Light emission taking place simultaneously with excitation is usually referred to as *fluorescence*, whereas an *after-glow* observed after the excitation has been interrupted is called *phosphorescence*.[1]

There is a substantial difference between mechanisms of luminescence in inorganic and organic compounds.[1] For inorganic materials, one further distinguishes luminescence due to band-to-band electronic transitions in semiconductors *(band-gap luminescence)* and emission from localized centers (e.g., impurity atoms) in insulating hosts *(characteristic luminescence)*.[1,3,4] Most of the currently applied phosphors are polycrystalline inorganic materials consisting of a transparent host (*matrix*) intentionally doped with small amounts of impurities (*activators,* which emit light, and *sensitizers*, which improve the efficiency of excitation).[1,5] The present study is devoted to phosphors of this type.

2.1.1. Efficiency of phosphors and luminescent devices

In practically any application of phosphors, the objective is to obtain a sufficient brightness of emission at the lowest possible energy consumption. Obviously, the efficiency of conversion of the excitation energy into the visible light is the most important property of a phosphor.

The most general measure of the phosphor performance is the *energy efficiency*. This quantity is defined as the ratio of the energy of emitted light quanta and the required excitation energy. For cathodoluminescence, the average energy of an

emitted photon is divided by the energy needed for generation of a thermalized electron-hole pair in the phosphor (taking backscattering into account),[5] which is equivalent to the ratio of the total emitted radiant power and the total energy of the electrons impinging on the surface of the phosphor within unit time. In the case of photoluminescence, the energy efficiency is represented by the ratio of energies of the emitted and absorbed photons multiplied by the *quantum efficiency* (QE) of the phosphor. Quantum efficiency (also called *quantum yield*) is the number ratio of the emitted and absorbed photons, i.e., it is another indicator of the performance of photoluminescent phosphors. For cathodoluminescence, QE is obtained by dividing the number of emitted photons by the number of generated electron-hole pairs. Typical figures of QE for the phosphors applied in the fluorescent lamps and plasma display panels (PDPs) are quite close to 100 % and, sometimes, may even exceed it (i.e., *multiphoton emission* takes place).[3,5] The performance of cathode ray phosphors is not much different in this aspect and also approaches a QE of unity.[5] A comparison of energy efficiency, however, reveals a difference between these types of luminescence. The energy efficiency of common photoluminescent phosphors is on the order of 50 %. For the cathodoluminescent phosphors, the values of energy efficiency are usually below 25 %.[5]

The complete performance analysis of luminescent devices must include the efficiency of the excitation sources (e.g., generation of the cathode rays in the cathode ray tubes (CRTs) or ignition of gas discharges in the fluorescent lamps and PDPs) and other inherent energy losses. The overall energy efficiency of luminescent displays is usually in the range of several percent. For applications in lighting, such values would not suffice. Fluorescent lamps have an energy efficiency of 15-25 %.[5] Semiconductor light emitting devices (LEDs) which are based on electroluminescence can achieve higher energy efficiency. It is expected that they will replace fluorescent lamps in the future. The high energy efficiency, however, is not the only requirement imposed on general light sources.

Some of the factors determining the perceived brightness of luminescence do not belong to the physics of luminescence. For example, human eyes have unequal sensitivity to different wavelengths of light. Spectral luminous efficiency function of the eye under conditions of *photopic vision* (i.e., in bright environments, which allow for perception of colors) has a maximum at a wavelength of 555 nm and gradually decreases towards both ends of the visible range (380-760 nm).[1] As a consequence, for the equal radiant intensities, blue or red light sources will appear noticeably fainter than green ones.

The color of light emitted by doped phosphors is to a large extent determined by the nature of activator. In many cases, it is possible to obtain luminescence of different colors for the same host material doped with various impurity ions. Furthermore, particular activator ions quite often produce luminescence of the same color in

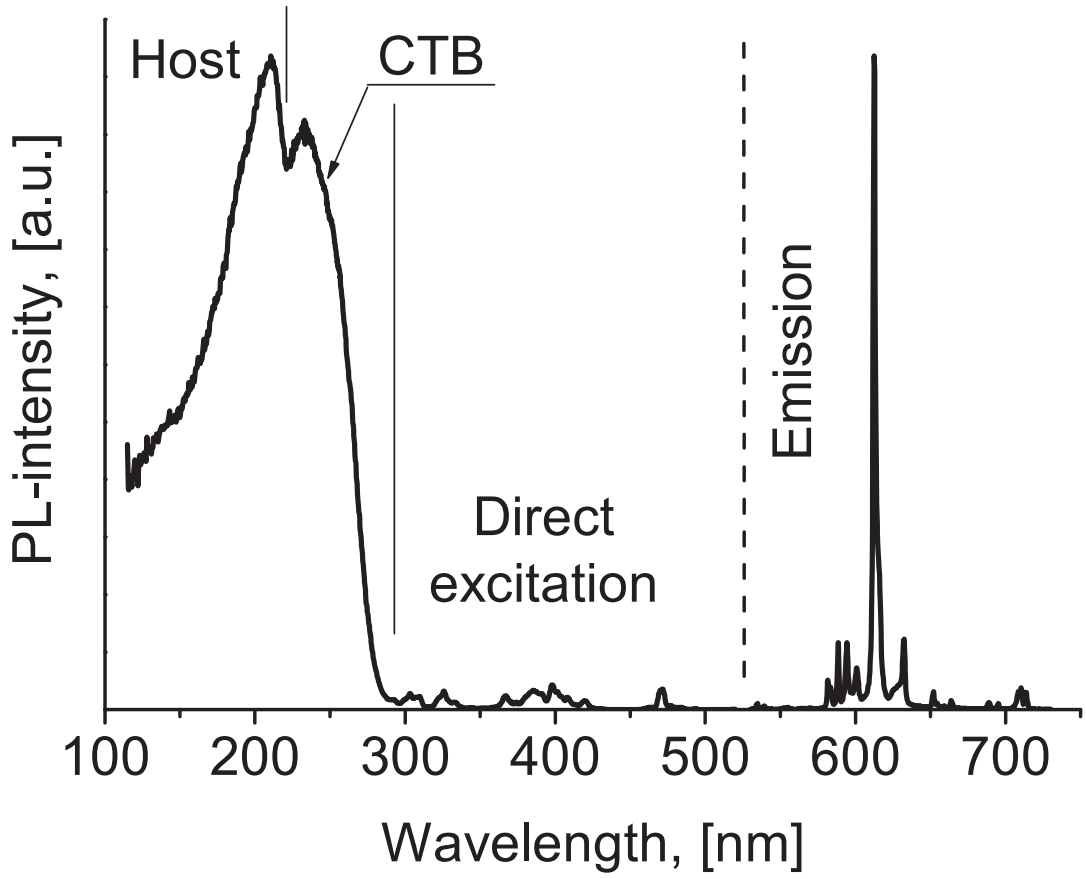

Figure 2.1 – Example of the emission and excitation spectra (for a commercial Y_2O_3:Eu phosphor).

different hosts. However, in general, the exact spectral distribution of emission (usually presented in an *emission spectrum* of the phosphor, see Figure 2.1) depends on the chemical environment of the luminescence centers.

Reproduction of different colors in the information displays and lighting is facilitated by simultaneous emission at several wavelengths. Usually in such cases, two or more different phosphors are blended together based on the concept of human *color vision*.[1,3,6,7] Photometric quantities such as luminous intensity, luminous flux, illuminance, and luminance are obtained by integrating the energy of the optical radiation at different wavelengths over the standard spectral efficiency function for photopic vision.[1] It is convenient to characterize the performance of a light source by its *luminous efficacy* defined as a ratio of the total luminous flux to the consumed electric power (i.e., measured in units of *lm/W*). Another important characteristic derived from the spectral distribution of emission is the *color rendering index*, which measures the ability of a light source to reproduce colors of various illuminated objects.[5]

2.1.2. Photoluminescence performance of doped phosphors

The optimization of excitation conditions allows for increasing the intensity of emission and/or decreasing the amounts of the consumed phosphors. The photoluminescent performance of any phosphor can be characterized with an *excitation spectrum* (Figure 2.1), which shows the dependence of the intensity of emission upon the excitation at different wavelengths.

In general, excitation spectra of doped phosphors include three wavelength ranges corresponding to different mechanisms of excitation of the optically active ions. In the range of *direct excitation*, which is the closest to the emission bands, luminescence takes place if the energy of incident photons equals the energy of transition from the ground state of the ions to some of the excited states (i.e., they directly absorb exciting light). For shorter wavelengths, the energy of exciting light quanta increases and at some point, excitation of the luminescent ion by charge transfer from the top of the valence band of the host material becomes possible. The corresponding wavelength range is referred to as the *charge transfer band* (CTB). For even shorter wavelengths, in the *range of host absorption*, the energy of absorbed photons becomes sufficient for band-to-band transitions between the valence band and conduction band. The free charge carriers generated in this process can recombine at the activator ions resulting in intensive emission of light.

Low efficiency of the direct excitation is mostly due to a weak absorption of photons in the corresponding wavelength range. A substantial part of the exciting radiation is either reflected by the phosphor or transmitted through it. An increase in the concentration of the activator ions leads to more efficient absorption and thus can improve the performance of the phosphor. As it can be seen from the curves in Figure 2.2,[8] the dependence of the intensity of emission on the dopant concentration is pronounced for all three mechanisms of excitation. In each case, there is a limit on the PL-brightness that can be achieved by increasing the amount of luminescent centers. If their concentration exceeds the limit, the light output decreases. This phenomenon is referred to as the *concentration quenching* of the phosphor. For increasing concentration of the optically active ions, the average distance between the neighboring ions decreases and they start to interact with each other. The rate of energy transfer between the ions increases so that the excitation energy can migrate from one ion to another until it is lost non-radiatively at a quenching site (a *killer*), e.g., at non-luminescent impurity ions or some other defects, which are inevitably present in the crystalline structure. The values of the optimum activator concentration corresponding to the maxima of the *concentration dependence (CD)*-curves can be quite different. For example, the concentration of luminescence centers in the ZnS-based phosphors, which have been used in the cathode ray tubes, never exceeds 1 %. The dopant concentration in the rare earth based phosphors is typically

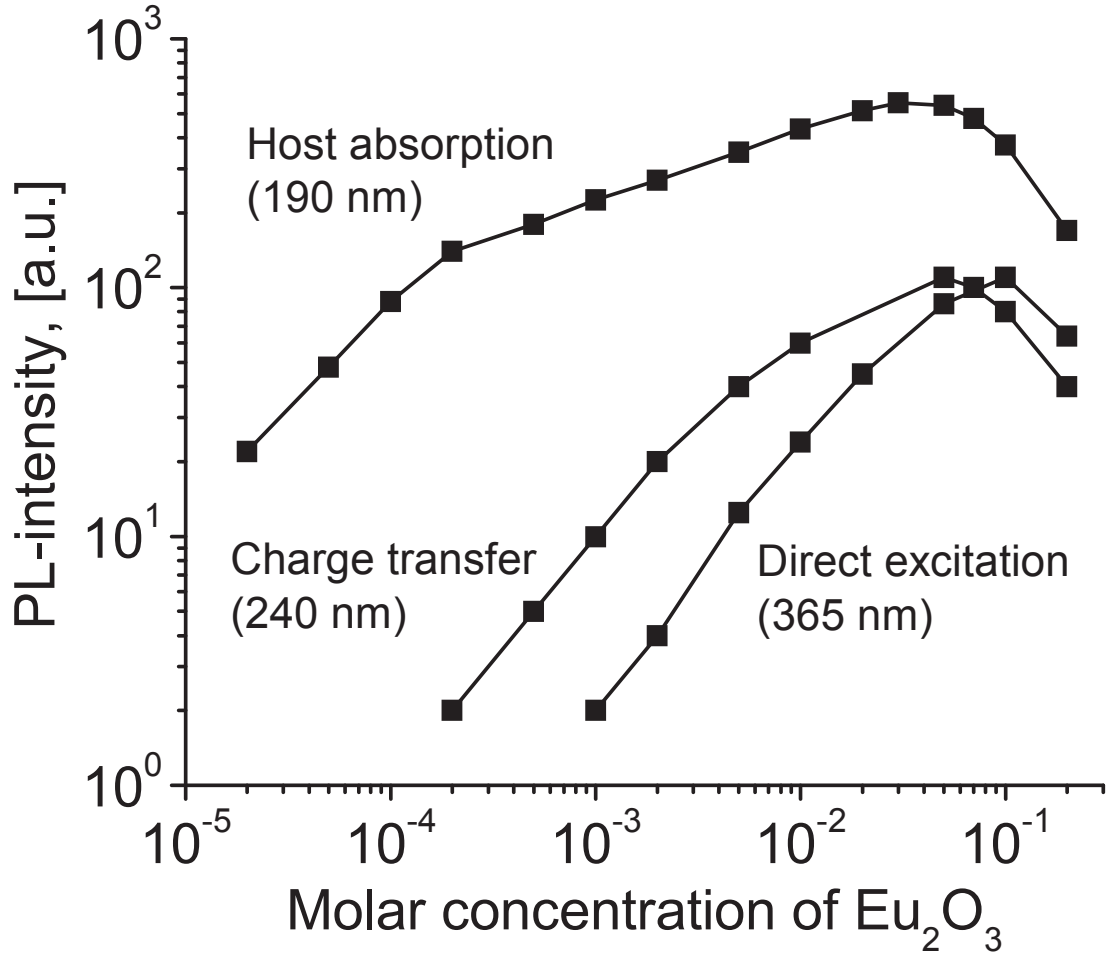

Figure 2.2 – Concentration dependence of photoluminescence intensity for the different mechanisms of excitation of the Y_2O_3:Eu phosphor (after Ozawa[8]).

noticeably higher and totals to a few percent of the cations in the compound. There are several phosphors (e.g., the $CaWO_4$ phosphor used in X-ray intensifying screens) which have no concentration quenching.[3]

In general, the presence of unintended impurities (contaminants) in the phosphor is detrimental at any concentration of the activator ions because they can act as additional absorption centers and increase the probability of non-radiative relaxation of the exciting energy. The first contribution (additional absorption) may be figured out by comparing the excitation spectra with the spectra of optical absorption (or reflection). The increased rate of non-radiative transitions can be confirmed by a decrease of the decay time constant of photoluminescence. In the simplest case, when both the radiative and non-radiative contributions can be represented by a first-order exponential decay, the emission decay time constant τ would change according to

$$\frac{1}{\tau} = \frac{1}{\tau_R} + \frac{1}{\tau_{NR}}, \qquad (2.1)$$

where τ_R is the radiative decay time constant (without non-radiative processes) and τ_{NR} is the non-radiative decay time constant.[5]

If the radiative decay time is known, one can assess the degradation of the efficiency of the phosphor from the measured value of τ

$$q = \frac{\tau}{\tau_R}, \qquad (2.2)$$

where q is the quantum efficiency of the phosphor.[5]

It should be noticed that quenchers can be generated in the phosphor during its use. For example, the decrease of brightness of the fluorescent lamps in the first minutes of lamp burning is attributed to *color centers* (structural defects which absorb light) generally formed in phosphors upon exposure to Hg radiation at 185 nm.[1] Generation of color centers is reversible. The long-term degradation of the inorganic phosphors is usually attributed to the ion or electron bombardment. The efficiency loss over the operational lifetime for the fluorescent lamps is relatively small (~10 %).[1,5] In the case of CRTs, the maintenance is usually much worse (30-50 %).[5]

The probability of non-radiative recombination is not exclusively determined by the structural perfection of the phosphor material and concentration of activator. Changes of temperature also affect the quantum efficiency of a phosphor. In general, QE degrades at elevated temperatures. This process is called *thermal quenching*.

2.1.3. Configurational coordinate diagram

A *configurational coordinate model* can be used to explain the dynamics of the luminescence process (Figure 2.3). This model represents the potential energy curves of an absorbing center as a function of a *configurational coordinate* which describes the symmetrical stretching vibrational mode of the center.[1–3,5] This mode is assumed to be harmonic and curves corresponding to different electronic states all have parabolic shapes. Nuclei surrounding the ion very slowly accommodate to a change of the electronic state (as compared to durations of electronic transitions) and therefore electronic and vibronic transitions can be treated separately (*Born-Oppenheimer approximation)*.[9] In the terms of the model, it means that the configurational coordinate does not immediately change upon an electronic transition between different states. As a result, electronic transitions always have vertical direction in the diagram (*Franck-Condon principle*).[1] Generally, each transition is accompanied by emission of phonons (process of *thermalization*). The average amount of phonons involved in the absorption and emission processes (expressed by *Huang-*

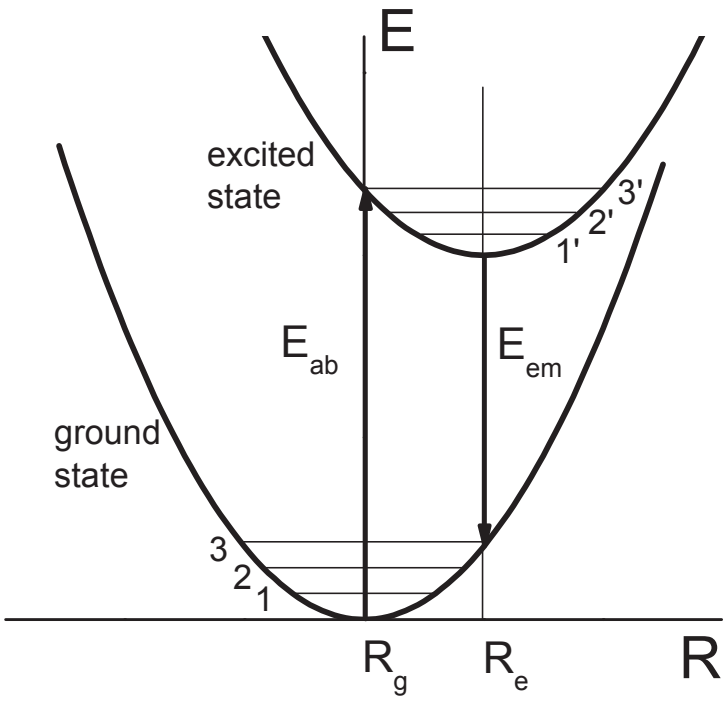

Figure 2.3 – Configurational coordinate diagram (schematically).

Rhys factors) corresponds to the difference between the energies of electronic transitions E_{ab} and E_{em} in Figure 2.3, which is termed the *Stokes shift*.[3,5]

The diagram sketched in Figure 2.3 shows why the wavelength of light emitted by a phosphor is usually longer than that of the light, which excites luminescence (*Stokes law*). It can also be seen that the Stokes shift increases with increasing offset of parabolae along configurational coordinate axis (represented by the distance between R_g and R_e). Based on this offset, emission from luminescence centers in different materials can be classified into cases of *weak, intermediate,* and *strong coupling*, which determines the shape of the peaks in the emission spectra.[3] The probability of thermal quenching is also determined by the mutual arrangement of the two parabolas.

The configurational coordinate model can include charge transfer states and multiple excited states of the dopant inside the band-gap of the host material. However, it delivers a somewhat oversimplified description of optical processes because more than one vibrational mode actually exists (i.e., several configurational coordinates may be needed) and thermal expansion of the host lattice is not taken into account.[1,3,5] Furthermore, behavior of real systems often significantly deviates from harmonic approximation.[3] Nevertheless, the model is very helpful for interpretation of dynamic effects and is commonly used in addition to the theory dealing with static interaction of luminescence centers with their surroundings.

2.1.4. Quantum mechanics

A detailed description of radiative transitions of an optically active ion in a solid is based on quantum mechanics and involves group theory. The application of the theory of groups in the field of optical spectroscopy has started its way to a wide acceptance about one century ago. In the 1930s, the nature of the optical transitions was unknown and even the number of energy levels participating in light emission, in many cases, was puzzling for spectroscopists.[10] Group theory provided a strategy for analysis of the symmetry properties of the luminescence center and its local environment and helped solving many spectroscopic problems such as:[11]

- Determining the number of energy levels of particular center.
- Labeling these electronic energy levels in a proper way (according to irreducible representations) and determining their degeneracy.
- Predicting the energy level splitting induced by a reduction of symmetry (e.g., due to application of pressure).
- Establishing selection rules for optical transitions and determining their polarization character.
- Determining the symmetry properties of the active center eigenfunctions.
- Analyzing the vibrations of the center's environment.

The energy levels E_i of a luminescent ion in a solid are determined by the Schrödinger equation

$$H\psi_i = E_i\psi_i, \tag{2.3}$$

where *H* is a *Hamiltonian* (the operator of the total energy) of the ion and ψ_i are its eigenfunctions.[11] The multi-electron Schrödinger equation cannot be solved analytically and even for the simplest case of a *free ion* (i.e., an isolated ion not embedded in any lattice), approximate methods must be applied. Usually the *Hartree-Fock approach* is used.[9,12] First, within the framework of the *central field approximation*, the Hamiltonian of the *free ion* H_{FI} is split in the following terms:

$$H_{FI} = H_0 + H_C + H_{SO}, \tag{2.4}$$

where H_0 is the *central field Hamiltonian* (reflecting the spherically averaged interaction of the valence electrons of the ion with the electric field created by the nucleus and all other electrons), H_C is the Hamiltonian that accounts for Coulomb repulsion between the valence electrons, and H_{SO} is due to the spin-orbit interaction (a magnetic interaction between the spin and angular moment of these electrons). Second, some initially assumed value of the *central field potential* (a part of the central field Hamiltonian representing potential energy which constitutes the greatest calculation complexity) is used for calculating one-electron wavefunctions that satisfy the Pauli

exclusion principle and the orthonormality condition. These wavefunctions produce new values of the central field potential. The calculation is iterated until the difference between successively obtained values falls below a predefined threshold (i.e., the *self-consistent field* is found). The effect of non-central field interactions is considered by diagonalizing the Hamiltonian with additional effective parameters derived from the experimental data.[9,12] As the standard Hartree-Fock method neglects relativistic effects and configuration interactions, numerous extensions of this approach relying on the availability of ever increasing computational resources were recently proposed.[13,14]

The problem of calculating the energy states of an ion embedded in a crystalline host is most commonly handled by the *crystal field theory,* which assumes that the effect of the lattice on the optically active ion can be represented by the electrostatic field created by surrounding ions and the Hamiltonian can be rewritten as

$$H = H_{FI} + H_{CF}\,, \tag{2.5}$$

where H_{CF} is the *crystal field Hamiltonian*.[9,11]

The Hamiltonian of the ion in the crystal is then

$$H = H_0 + H_C + H_{SO} + H_{CF}\,. \tag{2.6}$$

Each term of the Hamiltonian introduces the splitting of the levels of electron configuration of the ion (Figure 2.4). The relative magnitudes of the different terms have an essential influence on the properties of the luminescence center and the choice of the proper analytical methods. First, depending on the ratio of H_C and H_{SO}, an appropriate coupling scheme for the construction of the wave function of a free multi-electron ion can be chosen. For lighter atoms, the spin-orbit interaction is usually weaker than the Coulomb interaction between the electrons. In such cases, the *Russel-Saunders*, or *LS coupling*, is preferable because *L* (the total orbital angular momentum) and *S* (the total spin momentum) are good quantum numbers.[12,15] In this coupling scheme, orbital momentum *l* and spin momentum *s* of individual electrons are summed separately

$$L = \sum l_i\,, \qquad S = \sum s_i\,. \tag{2.7}$$

Russel-Saunders terminology is generally used for labeling the electronic energy levels of the ions. Each energy state is denoted by a term symbol

$$^{2S+1}L_J\,, \tag{2.8}$$

where *J* is the total angular momentum of the electronic configuration

$$(J = L + S)\,. \tag{2.9}$$

L is traditionally specified by letters S, P, D, F, G, H, … corresponding to L = 0, 1, 2, 3, 4, 5, etc.[12,15]

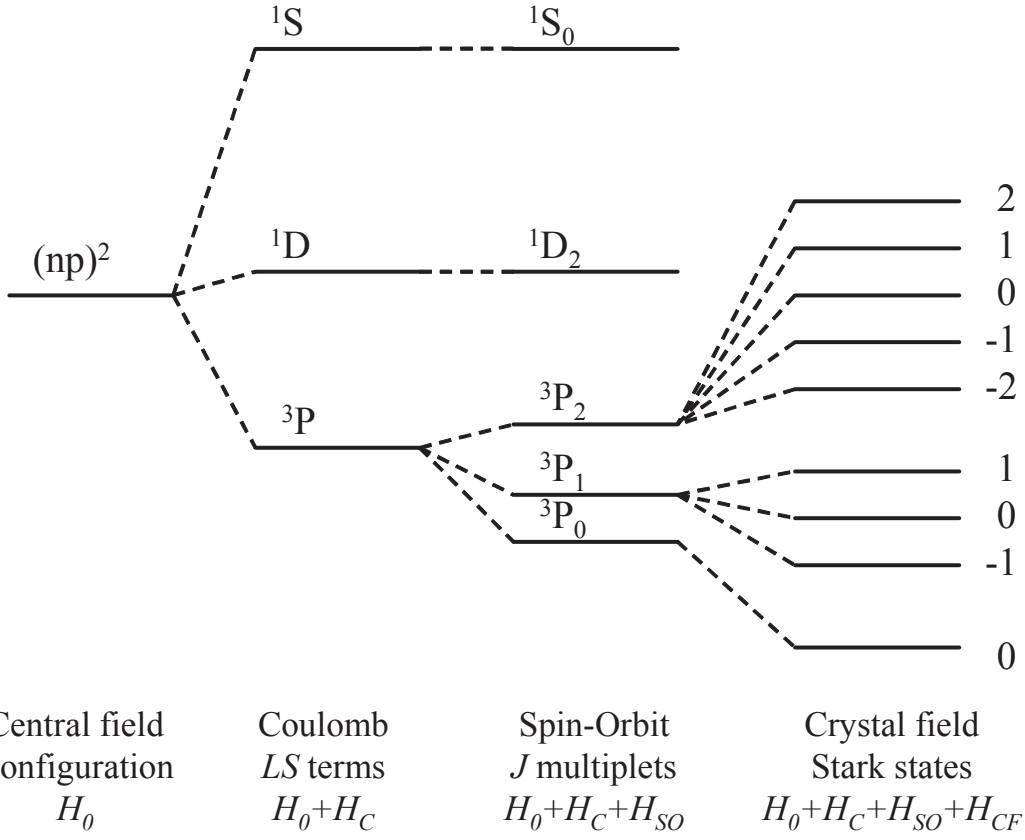

Figure 2.4 – Splitting of electronic energy levels (schematically, after Henderson and Imbusch[9] and Ropp[15]).

For the heavier atoms, H_C is small in comparison with H_{SO}, and *LS-terms* become "mixed" (i.e., they are no more pure "spin-orbit" coupling states).[15] Thus, *L* and *S* are not appropriate quantum numbers and the *j-j coupling scheme*, in which the total angular momentum *j* is calculated for every electron and the summation over individual *j*-values is performed, should be preferred.[12,15] For the lanthanides, the magnitudes of H_C and H_{SO} are comparable and the *intermediate coupling scheme* (developed from the *LS-coupling*) has to be applied.[12]

The crystal field is able to lift the degeneracy of *J* multiplets and produces up to $(2J+1)$ or $(J+1/2)$ split components for integer or half-integer *J*, respectively (see Figure 2.4).[11] Depending on the relative contribution of the crystal field to the Hamiltonian, again different cases are considered:[9]

Strong crystal field: $H_{CF} > H_C > H_{SO}$.

Intermediate crystal field: $H_C > H_{CF} > H_{SO}$.

Weak crystal field: H_{CF} is much smaller than the other terms.

The strong or intermediate crystal field usually applies for transition metal ions in different crystalline environments.[11] Crystal field levels are denoted with

$$^{2S+1}X_J\,, \tag{2.10}$$

where *X* is determined by degeneracy of the level; *A* stands for no degeneracy, E stands for twofold degeneracy, and T stands for threefold degeneracy.[2] Special diagrams, known as *Tanabe-Sugano diagrams*, are used for representing the influence of the crystal field of a particular symmetry on the splitting of the energy levels of such ions.[2,9,11]

The weak crystal field is characteristic for the trivalent lanthanide ions. Their valence electrons are situated in the 4f-shell, which is shielded from the crystal field by 5s and 5p electrons and therefore only a slight shift of the energy states and relatively insignificant additional splitting is introduced. As a consequence, optical spectra of rare earth ions usually consist of sharp peaks and their energy level structure in different crystalline solids is quite similar (and also similar to that of the free ions). This greatly simplifies the calculations of the energy-level parameters of the RE^{3+}-ions in any crystalline host (they can be obtained by least-squares fitting the parameters of the free-ions into the corresponding experimental data[12]) and makes such materials to a very convenient investigation object.

The energy states of trivalent rare earth ions are conveniently represented in the *Dieke diagram* shown in Figure 2.5.[16] The magnitude of the crystal field splitting is shown by the width of each state. Light-emitting states are denoted by semicircles below them. All other states are depopulated by non-radiative processes. The Dieke diagram can be used for predicting the positions of the peaks in the spectra of luminescence and optical absorption of rare-earth-doped crystals. Furthermore, the diagram helps to properly assign the observed peaks to the transitions between *J*-multiplets.

Based on *selection rules*, all these transitions are classified into *electric dipole transitions*, *magnetic dipole transitions*, *electric quadrupole transitions,* and further higher order transitions.[9,11,12,15] For the intraconfigurational f-f transitions of lanthanide ions, only the *induced* (or *forced*) electric dipole transitions, magnetic dipole transitions, and electric *pseudo-quadrupole* transitions (i.e., *hypersensitive* induced electric dipole transitions) are of practical relevance.[17] Actually, the electric dipole transitions are forbidden by *Laporte (parity) selection rule* but for ions in *noncentrosymmetric* environment, this rule is not strict and therefore transitions of this kind can be *induced*.

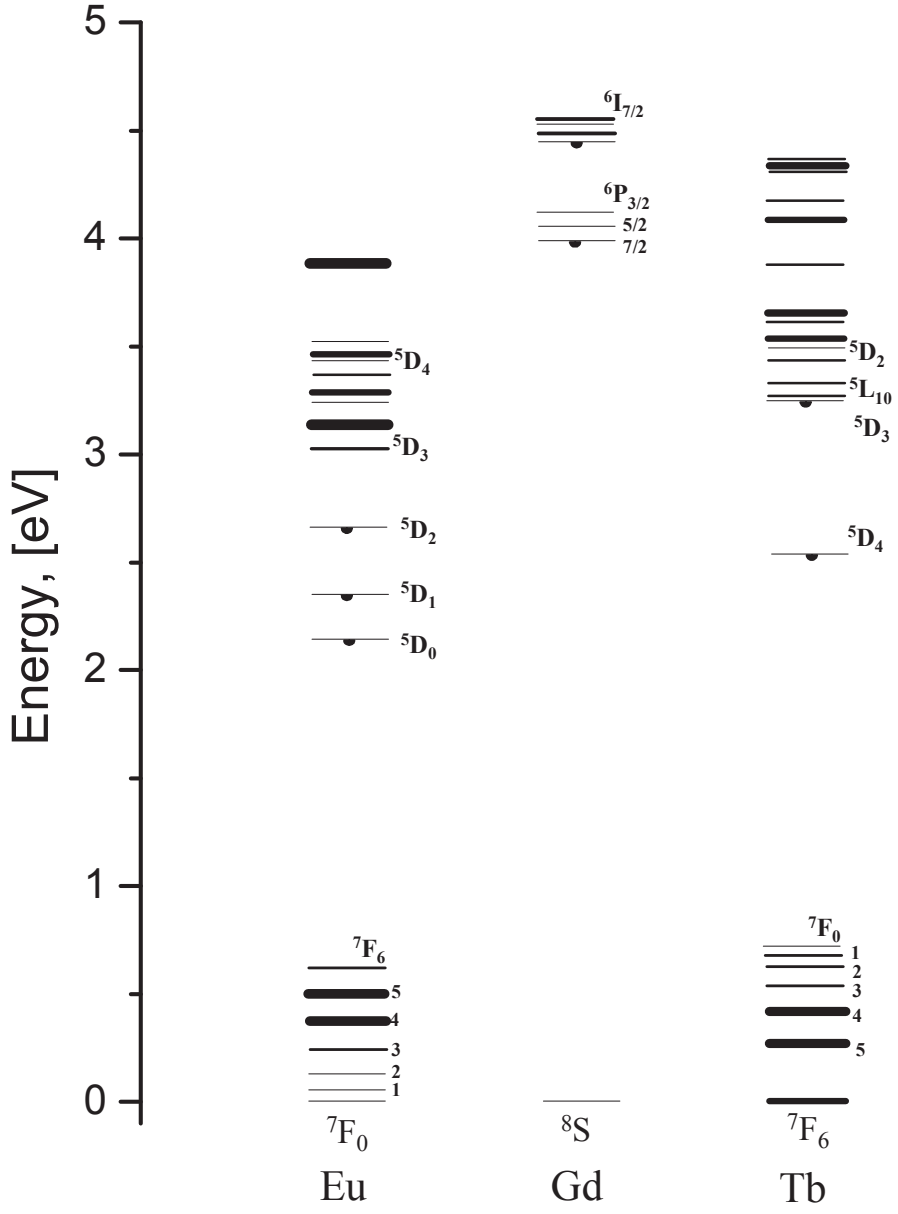

Figure 2.5 – Energy-level diagram for trivalent ions of Eu, Gd, and Tb in $LaCl_3$ (after Dieke *et al.*[16]). Semi-circles denote light-emitting levels.

2.1.5. Judd-Ofelt theory

As most of the emission peaks in the spectra of lanthanides are due to the induced electric dipole transitions, the *Judd-Ofelt theory*, which allows to predict intensities (i.e., *oscillator strengths*) and decay rates of such transitions, constituted a crucial development in the field of luminescence.[11,18,19] The theory assumes static interaction of an ion with its environments and treats the influence of the host as a perturbation of the free ion Hamiltonian. Interactions between different electron configurations are neglected and all Stark states are assumed to be equally populated. The

oscillator strength *f* can be defined as follows[11]

$$f = \frac{2m\overline{\omega}_0}{3\hbar e^2(2J+1)} \times |\mu|^2, \qquad (2.11)$$

where *m* and *e* are the electronic mass and elementary charge, respectively; $\overline{\omega}$ is the average frequency corresponding to the transition $J \to J'$; $\hbar$ is the reduced Planck constant; the factor $(2J+1)$ accounts for the degeneracy of the initial state; and μ is the *matrix element of the electric dipole moment*.

In the Judd-Ofelt theory, the matrix element is determined by the so-called *Judd-Ofelt intensity parameters* Ω_t:

$$|\mu|^2 = e^2 \sum_{t=2,4,6} \Omega_t \times \left| \left\langle \alpha J \left\| U^{(t)} \right\| \alpha' J' \right\rangle \right|^2, \qquad (2.12)$$

where $\left\langle \alpha J \left\| U^{(t)} \right\| \alpha' J' \right\rangle$ are the reduced matrix elements of tensor operators of rank *t*; α and α' represent all quantum numbers defining *J* and *J'* states. The reduced matrix elements are generally independent of the host and can be found in the literature.[20–23] The Judd-Ofelt intensity parameters are material-specific and have been tabulated for many hosts.[17] Usually these are obtained from absorption spectroscopy of the rare-earth-doped materials (if the doping concentration and refractive index of the crystal are known) by a least squares fit of the calculated oscillator strengths to the values extracted from experimental data. An example of such calculation can be found, e.g., in the work by Ivankov *et al.*[24] The so-called *Smakula's formula* relates the oscillator strength to the concentration of absorbing ions and the intensity of the corresponding peak in the absorption spectrum. Once the oscillator strength is known, the spontaneous emission probability (i.e., the radiative lifetime) can also be determined.[11,12] Typically, relatively long luminescence decay times on the order of 1 ms are observed for rare-earth-doped phosphors because the induced electric dipole transitions are parity-forbidden.

In spite of the remarkable success of the Judd-Ofelt theory in spectroscopic analysis of lanthanide ions, it excludes the magnetic dipole transitions. Intensities of the latter ones almost do not depend of the host matrix and can be calculated from the free ion wavefunctions.[12,17] Some transitions include contributions from both electric and magnetic dipole interactions.

Unlike other induced electric dipole transitions, the hypersensitive transitions are strongly affected by the chemical environment of lanthanide ions and often require some special treatment as well.[12,17] The Judd-Ofelt formalism does not provide a theoretical explanation of the phenomenon of hypersensitivity. Several possible mechanisms have been proposed (e.g., the dynamic interaction of the ion with the environment) and it is assumed that different causes can contribute to the observed effect simultaneously.[10,17,18]

2.2. Basics of phosphor screens

The general function of any phosphor is to convert some particular kind of energy into visible light. This conversion process can serve different purposes and, from this point of view, all practical applications of phosphors can be classified into several main groups:

- Light sources (fluorescent lamps, backlights of liquid crystal displays (LCDs), phosphor-converted light-emitting diodes (pc-LEDs), lasers, etc.).
- Information displays (plasma display panels (PDPs), field emission displays (FEDs), cathode-ray tubes (CRTs), etc.).
- Radiation converters (X-ray intensifying screens, UV-to-visible converters for excimer laser beam profilers, viewing screens for transmission electron microscopy (TEM), various image intensifiers, etc.).
- Fluorescent pigments and tracers (nondestructive testing, non-invasive medical imaging, biolabeling, security labeling, leisure goods, etc.).

With very few exceptions, luminescent substances are utilized in the form of a coating, i.e., a film of relatively small thickness extended in the other two dimensions. Such a coating deposited on a substrate is usually referred to as a *screen*, if it is used for representation of any visual information. Each application imposes a corresponding set of requirements on the properties of the phosphor coating, e.g., its chemical composition, homogeneous or patterned structure, and its thickness. Usually, a trade-off between the maximum light output for the given excitation conditions, desired transient characteristics, quality of image reproduction, environmental stability, and costs (of the phosphors and their processing) has to be found.

For the given excitation conditions, if the phosphor material is fixed, the brightness of the screen is determined by the geometrical configuration of the screen, the excitation source, and the observer. Generally, one distinguishes two different modes of the screen observation. In the *transmission (T-)mode*, the screen is placed between the excitation source and the observer (Figure 2.6, Observer A). In the *reflection (R-)mode*, the observer and the source of excitation are situated on the same side from the screen (Figure 2.6, Observer B). The intensity of light exiting the screen in both modes depends on the screen thickness.

2.2.1. Perfect non-scattering screens

Let us consider the simplest model of the phosphor screen - an infinite continuous self-supporting plate with perfectly smooth boundaries. If we assume a uniform excitation by unpolarized light (from one side of the screen), the time-averaged spatial distribution of intensity of luminescence from any volume element inside of the

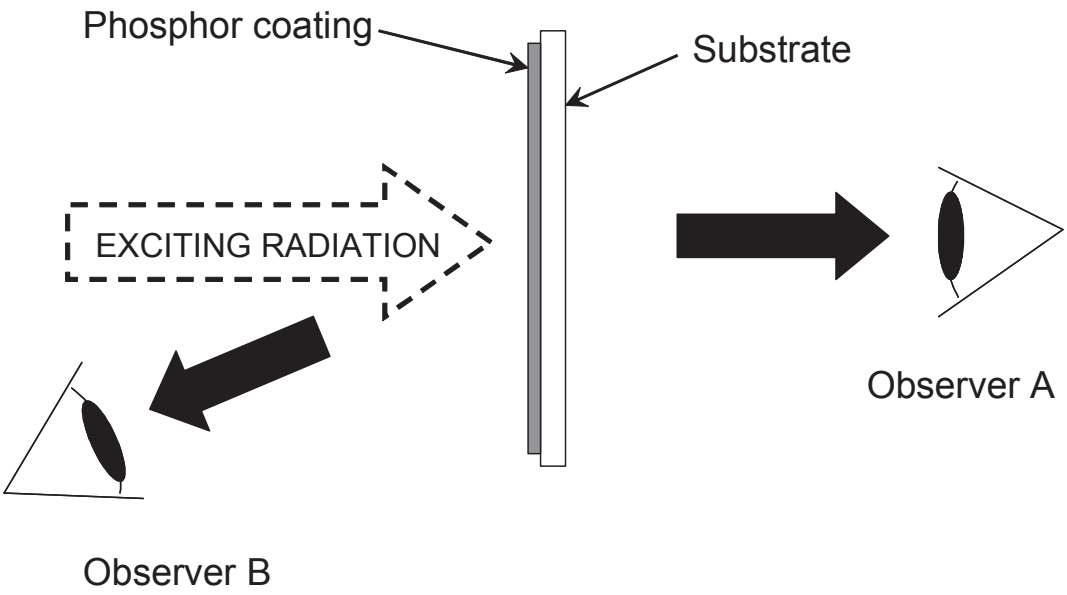

Figure 2.6 – Transmission and reflection modes of screen observation.

phosphor plate should be fully isotropic (i.e., spherically symmetric). We also assume a perfect match between the refractive indices of the phosphor and the surrounding medium, so that the light reflection at the boundaries of the phosphor layer can be neglected. Any light scattering and self-absorption of emitted light are neglected. In such case, intensities of light emitted forward (T-mode) and backward (R-mode) should be equal and constant everywhere outside of the screen

$$I_T = I_R , \tag{2.13}$$

where I_T and I_R stand for the transmission-mode and reflection-mode intensities, respectively, expressed as the number of photons emitted in unit time. Their sum equals the total intensity of luminescence and it can be related to the intensity of exciting radiation absorbed in the phosphor coating I'_A multiplied by the quantum efficiency q of the phosphor (from now on, symbols with a prime will be used for exciting radiation)

$$I_T = I_R = q\frac{I'_A}{2} . \tag{2.14}$$

Exciting radiation incident on the phosphor screen either gets absorbed or is transmitted through the screen. The sum of the corresponding contributions equals the initial intensity of excitation

$$I'_0 = I'_A + I'_T . \tag{2.15}$$

The part of exciting radiation transmitted through the phosphor is given by the *Beer-Lambert law*

$$I'_T = I'_0 \exp(-\alpha' d)\,, \tag{2.16}$$

where α' is the coefficient of absorption measured in the units of inverse length, e.g., cm^{-1}, (it is related to the molar absorption coefficient used for calculation of oscillator strengths of electronic transitions) and *d* is the thickness of the screen. We obtain the following final expression

$$I_T = I_R = q\frac{I'_0\,(1-\exp(-\alpha' d))}{2}\,. \tag{2.17}$$

Obviously, both R- and T-mode brightness increase for thicker phosphor screens and asymptotically approach the values corresponding to complete absorption of exciting radiation. When considering brightness of a perfect non-scattering screen, there is no finite optimum value of the screen thickness; the phosphor layer theoretically should be as thick as possible.

In most practical cases, the refractive index of the luminescent material is substantially higher than that of the surrounding medium and resulting light intensities should be corrected for the *Fresnel reflection* at the interface between the media. Equation 2.16, which describes transmission of the exciting radiation (for the normal incidence on the screen), should now become[1]

$$I'_T = \frac{(1-R_0)^2(1+\kappa^2/n^2)\exp(-\alpha' d)}{1-R_0^2\exp(-2\alpha' d)} \approx \frac{(1-R_0)^2\exp(-\alpha' d)}{1-R_0^2\exp(-2\alpha' d)}\,, \tag{2.18}$$

where *n* and κ are the real and imaginary part of the refractive index, respectively; and R_0 is the normal surface reflectivity

$$R_0 = \frac{(n-1)^2+\kappa^2}{(n+1)^2+\kappa^2}\,. \tag{2.19}$$

Equation 2.15 should now include the part of radiation I'_R reflected from the surface of the phosphor plate

$$I'_0 = I'_A + I'_T + I'_R\,, \tag{2.20}$$

which equals

$$I'_R = R_0(1+I'_T\exp(-\alpha' d))\,. \tag{2.21}$$

The emitted light undergoes reflection from the layer boundaries and a significant fraction of all light quanta cannot escape the phosphor plate due to the *total internal reflection* because their angle of incidence exceeds the *critical angle*

$$\theta_C = \arcsin(n_A/n_P)\,, \tag{2.22}$$

where n_A and n_P are the refractive indices of the ambient medium and phosphor material, respectively. Such photons experience multiple reflections inside of the phosphor plate while propagating towards the lateral edges of the structure (this phenomenon is often referred to as *waveguiding*) until they finally get absorbed and transformed into heat. Equation 2.14 does not hold anymore and we obtain

$$I_T = I_R < q\frac{I'_A}{2}. \qquad (2.23)$$

Trapping of light inside of the luminescent layer (or in an adjacent transparent substrate) can have a dramatic effect on device performance. For example, the *light extraction efficiency* of semiconductor light-emitting diodes (LEDs) (i.e., the ratio between the intensity of light emitted into the ambience and the total intensity of light generated by the device) would only total 2-4 %, if no special design measures were taken.[25,26] Such inefficient light outcoupling results from high refractive indices of semiconductors (e.g., *n*[GaN] = 2.5). However, even for organic LEDs (OLEDs) which employ materials with moderate values of refractive index ($n \sim 1.5$) only about 20-30 % of light would escape into air.[27] Refractive indices of dielectrics used as phosphor hosts fall into the range between 1.5 and 2.5 and therefore, brightness of any single-crystalline phosphor screen should also be strongly affected by the internal reflection. Enhancement of the light extraction can be achieved by optimization of device structure (e.g., "flip-chip" LEDs[28] or truncated cone patterns in single-crystalline phosphor screens[29]) and/or intentional roughening of the emitting surfaces, which is introduced in order to disrupt waveguiding by means of light scattering. LEDs with extraction efficiencies of 80 % have been demonstrated.[28] Elimination of the effect of the total internal reflection led to a remarkable improvement in performance so that power efficiencies of semiconductor LEDs and OLEDs could approach that of conventional fluorescent lamps (60-70 lm/W).[28,30] This can be considered as a great success because the light extraction efficiency of the fluorescent tubes is close to unity.

2.2.2. Single scattering model

Fluorescent lamps and many other devices in which phosphors are used in a powder form are relatively unaffected by waveguiding due to the absence of sufficiently smooth layer boundaries. Intensive scattering at the surface of phosphor particles, pores, and other inhomogeneities has a drastic influence on the propagation of both the exciting radiation and emitted light. The equations describing the relation between the thickness of a screen and its brightness have to be changed accordingly.

Mathematically, the simplest case of the scattering phosphor screen is when the entire intensity of scattered light is immediately lost without any further effect on resulting screen brightness. The Beer-Lambert law for the exciting light (Equation 2.16) should now include the scattering coefficient β':

$$I'_T = I'_0 \exp(-(\alpha'+\beta')d). \qquad (2.24)$$

The scattering coefficient is not a material-specific constant; it is determined by processing-dependent properties of the phosphor powder. The absorption coefficient α' in Equation 2.24 also depends on the condition of the phosphor powder and therefore it should be distinguished from α' for the bulk phosphor material in Equation 2.16.

The assumption of equality of the T- and R-mode intensities of the emitted light (Equation 2.13) does not hold anymore, especially for thick screens (i.e., when intensity of excitation substantially changes with the screen depth) due to the effects of scattering. The T-mode intensity changes with the increasing thickness of the phosphor layer as follows

$$dI_T = aq\alpha' I'_T\, dx - \beta I_T dx\,, \tag{2.25}$$

where *a* is a fraction of light emitted in the forward direction, *q* is the quantum efficiency of the phosphor, β is the scattering coefficient for the light at the wavelength of emission. When combined with Equation 2.24, this results in a differential equation

$$\dot{I}_T + \beta I_T = aq\alpha' I'_0 \exp(-(\alpha'+\beta')d)\,. \tag{2.26}$$

The solution of Equation 2.26 is

$$I_T = \frac{aq\alpha' I_0}{\alpha'+\beta'-\beta}[\exp(-\beta d) - \exp(-(\alpha'+\beta')d)]\,. \tag{2.27}$$

For the R-mode,

$$dI_R = dI_{Rx} \exp(-\beta x)\,, \tag{2.28}$$

where I_R is the intensity of light coming out from the phosphor plate in the backward direction and I_{Rx} is the intensity of light emitted in the backward direction at a depth *x* in the screen. Equation 2.28 results in a differential equation

$$\dot{I}_R = aq\alpha' I'_0 \exp(-(\alpha'+\beta'+\beta)x)\,, \tag{2.29}$$

which is solved using

$$I_R = \frac{aq\alpha' I'_0}{\alpha'+\beta'+\beta}[1 - \exp(-(\alpha'+\beta'+\beta)d)]\,. \tag{2.30}$$

Figure 2.7 shows the curves of the R- and T-mode brightness, which were obtained by fitting published experimental data.[8,31] This is rather a special case of the *thickness dependence* (TD)-curves, which could only be obtained in the conditions when the scattered photons cannot reach the detector. The T-mode data in Figure 2.7 could be fitted with a pulse function of the general form

$$y = A[1 - \exp(-\frac{x}{t_1})]\exp(-\frac{x}{t_2})\,, \tag{2.31}$$

which can be easily reformulated to match with Equation 2.27 by setting

$$A = \frac{aq\alpha' I'_0}{\alpha'+\beta'+\beta}\,, \qquad t_1 = \frac{1}{\beta}\,, \qquad t_2 = \frac{1}{\alpha'+\beta'-\beta}\,. \tag{2.32}$$

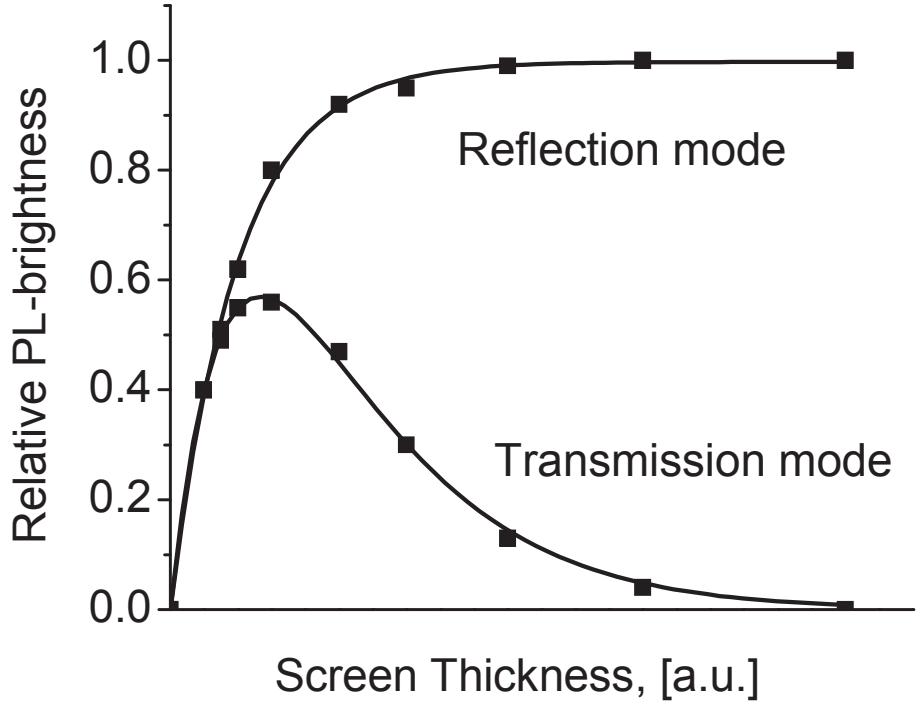

Figure 2.7 – Special example of the transmission- and reflection-mode brightness curves of powder phosphor screens (after Fran and Tseng[31] and Ozawa[8]).

The R-mode curve is a single exponential decay curve which also agrees with the corresponding formula derived above (Equation 2.30). The obtained formula should also be applicable to other types of luminescence, e.g. cathodoluminescence. In such cases, the values of the absorption coefficients α' and the scattering coefficient β' have to be changed accordingly.

Even though the single scattering scenario is an oversimplification in most of the practical cases, it allows us to draw a conclusion which is generally valid. For any scattering phosphor screen observed in the T-mode, there always exists an optimum screen thickness corresponding to the maximum brightness at given conditions of excitation. When the exciting radiation is almost completely absorbed inside of the phosphor plaque, each additional infinitesimal phosphor layer introduces a net decrease in the T-mode intensity because the losses due to scattering exceed the intensity of light generated in this layer.

2.2.3. Models for multiple scattering of light in the powder screens

Even though the shape of the T- and R-mode curves in Figure 2.7 could be predicted by simple mathematical derivations, the obtained equations (Equations 2.27 and 2.30) do not describe the general case of light generation in a powder

phosphor screen because usually photons are not immediately lost upon the first scattering event and can still contribute to the light output of the screen after being scattered several times. Even for relatively low concentration of scatterers (e.g., atmospheric aerosols), this causes significant deviations from the Beer-Lambert law.[32,33] In the case of densely packed particles, propagation of light practically does not obey the Beer-Lambert law.[34]

Figure 2.8 shows an example of the typical dependence of intensity of cathodoluminescence on thickness of the screen. As opposed to the single scattering model, the R-mode intensity neither obeys the exponential law nor reaches saturation when the exciting radiation is fully absorbed in the screen. Both the T- and R-mode curves have approximately linear character in the range of large screen thickness, while the sum of the corresponding intensities stays approximately constant. The comprehensive mathematical description of the process of light generation in the layers of packed phosphor particles is rather complicated. The most often implemented theoretical approaches to this problem are based on the *Kubelka-Munk's theory, Johnson's theory,* and *Monte Carlo method*, which will be discussed below.[1] In some cases, simple practical techniques for optimization of the screen weight could be developed. For example, for strongly absorbed exciting radiation, the maximum of the T-mode intensity corresponds to the minimum thickness of the powder screen fully covering the substrate (i.e., there should be no direct transmission of exciting radiation via the voids between the particles).[35]

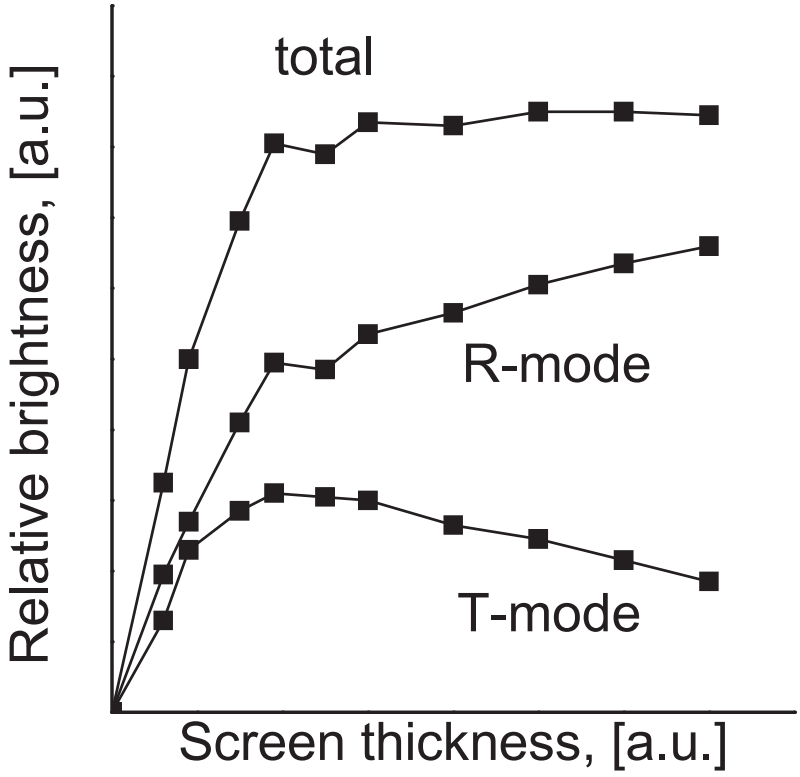

Figure 2.8 – Relative brightness of cathodoluminescent screens (after Ozawa[8,50]).

2.2.3a. Kubelka-Munk theory

The theoretical framework of Kubelka-Munk's two-flux approach can be used in many various fields of application of phosphor screens. Along with modeling of fluorescent tube performance,[1,36] it was successfully adopted for electroluminescent devices,[37] X-ray and vacuum UV (VUV)-excitation,[38–40] and cathodoluminescence.[1]

In the approximation of the infinite screen uniformly excited from one side, scattered light produces a diffuse light flux opposite to the initial direction of propagation of the exciting radiation or emitted light. In the standard Kubelka-Munk theory, optical properties of a particle layer (e.g., a pigment coating[41]), which is assumed to be a continuous optical medium, are completely determined by two optical constants: the absorption coefficient *K* and the scattering coefficient *S*. These coefficients correspond to the previously introduced coefficients α and β generalized to three dimensions, i.e., when incident light is diffuse and scattering takes place in all directions.[1] In the one-dimensional case, light incident on the layer of non-luminescent particles is scattered in the forward and backward directions with intensities, which are denoted by $I'(x)$ and $J'(x)$ instead of I'_T and I'_R, respectively. For the forward direction, the light absorbed in an infinitesimal layer of thickness *dx* is $\alpha' I'(x)dx$, and the scattered light is $\beta' I'(x)dx$. A part of $J'(x)$ is scattered back and has to be added to $I'(x)$. One obtains

$$\frac{dI'(x)}{dx} = -(\alpha'+\beta')I'(x) + \beta' J'(x). \tag{2.33}$$

For the backward direction, a similar equation can be written

$$\frac{dJ'(x)}{dx} = (\alpha'+\beta')J'(x) - \beta' I'(x). \tag{2.34}$$

The general solutions to this set of differential equations, known as *Schuster-Kubelka-Munk* equations, are

$$I'(x) = A'(1-\beta'_0)\exp(\alpha'_0 x) + B'(1+\beta'_0)\exp(-\alpha'_0 x), \tag{2.35}$$

$$J'(x) = A'(1+\beta'_0)\exp(\alpha'_0 x) + B'(1-\beta'_0)\exp(-\alpha'_0 x), \tag{2.36}$$

where constants *A'* and *B'* are determined by boundary conditions, and α'_0 and β'_0 are defined as

$$\alpha'_0 = \sqrt{\alpha'(\alpha'+2\beta')}, \tag{2.37}$$

$$\beta'_0 = \sqrt{\alpha'/(\alpha'+2\beta')}. \tag{2.38}$$

Kubelka showed that for diffuse light and scattering in all directions the same equations can be derived. As light does not always have normal incidence on the phosphor layer, the mean light path $d\xi$ is longer than *dx*. It was shown that

$$d\xi = 2dx. \tag{2.39}$$

If one defines the new coefficients K' and S' by

$$K' = 2\alpha' , \qquad S' = 2\beta' , \tag{2.40}$$

Equations. 2.37 and 2.38 can be replaced with

$$\alpha'_0 = \sqrt{K'(K'+2S')} , \tag{2.41}$$

$$\beta'_0 = \sqrt{K'/(K'+2S')} , \tag{2.42}$$

and then, the general solutions of the Schuster-Kubelka-Munk equations can be expressed by Equations 2.35 and 2.36 again.

In the case of photoluminescence, one has to account for both exciting and emitted light. There are the following contributions to the light emitted in the forward direction (T-mode)

$$dI(x) = -dI_A - dI_S^I + dI_S^J + dI_E , \tag{2.43}$$

where dI_A denotes changes due to absorption of emitted light; dI_S^I and dI_S^J stand for scattering from the forward and backward modes, respectively; dI_E accounts for the process of light generation from the absorbed exciting radiation. For the backward direction, it holds

$$dJ(x) = dJ_A + dJ_S^J - dJ_S^I - dJ_E . \tag{2.44}$$

The intensity of the light emitted by the infinitesimal phosphor layer of thickness *dx* is

$$dI_E(x) + dJ_E(x) = qK'[I'(x) + J'(x)]dx , \tag{2.45}$$

where *q* is the efficiency of luminescence, K' is the absorption coefficient of the exciting radiation, and $I'(x)$ and $J'(x)$ are the intensities of the exciting light in the forward and backward directions, respectively. By combining Equations 2.35 and 2.36, one obtains

$$dI_E(x) + dJ_E(x) = 2qK'[A'\exp(\alpha'_0 x) + B'\exp(-\alpha'_0 x)]dx . \tag{2.46}$$

For infinitesimal phosphor layers:

$$dI(x)_E = dJ_E(x) , \qquad dI_S^I = dJ_S^I , \qquad dI_S^J = dJ_S^J . \tag{2.47}$$

As a result, one obtains a set of differential equations

$$\frac{dI(x)}{dx} = -(K+S)I(x) + SJ(x) + qK'[A'\exp(\alpha'_0 x) + B'\exp(-\alpha'_0 x)] , \tag{2.48}$$

$$\frac{dJ(x)}{dx} = (K+S)J(x) - SI(x) - qK'[A'\exp(\alpha'_0 x) + B'\exp(-\alpha'_0 x)] . \tag{2.49}$$

The general solutions of these equations are

$$I(x) = \frac{qK'A'}{\beta_0} \cdot \frac{\alpha'_0\beta_0 - \alpha_0}{\alpha'^2_0 - \alpha^2_0}\exp(\alpha'_0 x) - \frac{qK'B'}{\beta_0} \cdot \frac{\alpha'_0\beta_0 + \alpha_0}{\alpha'^2_0 - \alpha^2_0}\exp(-\alpha'_0 x) + \\ + A\exp(\alpha_0 x) + B\exp(-\alpha_0 x) , \tag{2.50}$$

$$J(x) = -\frac{qK'A'}{\beta_0}\cdot\frac{\alpha'_0\beta_0+\alpha_0}{\alpha'^2_0-\alpha_0^2}\exp(\alpha'_0 x) + \frac{qK'B'}{\beta_0}\cdot\frac{\alpha'_0\beta_0-\alpha_0}{\alpha'^2_0-\alpha_0^2}\exp(-\alpha'_0 x) + \\ + A\left(\frac{1+\beta_0}{1-\beta_0}\right)\exp(\alpha_0 x) + B\left(\frac{1-\beta_0}{1+\beta_0}\right)\exp(-\alpha_0 x) \quad . \qquad (2.51)$$

The values of *A* and *B* are determined by the boundary conditions. This allows for taking into account the presence of the substrate or reflecting coatings (which are sometimes deposited over one side of the screen in order to increase the light output from the other side).

In order to perform calculations, a value of either the absorption coefficient *K* or the scattering coefficient *S* must be known. The other constant can be determined from the value of the *Kubelka-Munk function* $F(R_\infty)$ (also called *remission*) by the equation

$$F(R_\infty) = \frac{(1-R_\infty)^2}{2R_\infty} = \frac{K}{S}, \qquad (2.52)$$

where R_∞ is reflectance of a semi-infinite powder layer obtained from experiments

$$R_\infty = \frac{1-\beta_0}{1+\beta_0}. \qquad (2.53)$$

Usually, the scattering coefficient is obtained by measuring the reflectance R_0 of a relatively thin layer coated on a black plate (which has negligible reflectance)

$$S = \frac{R_\infty}{d(1-R_\infty^2)}\ln\frac{R_\infty(1-R_0R_\infty)}{R_\infty-R_0}, \qquad (2.54)$$

where *d* is the thickness of the layer.

If absorption is not strong, the scattering coefficient is practically independent of the absorption coefficient. Furthermore, for conventional phosphor particles which are larger than the wavelengths of emitted light, the scattering coefficient is approximately constant over a wide wavelength range.[42,43] However, in the ranges of strong absorption (e.g., for the UV-light), the described method of measuring the scattering constant cannot be used. The Kubelka-Munk theory does not predict the interdependence of *K* and *S* and requires special care when applied to the UV-range.[1]

Another shortcoming of the Kubelka-Munk theory is that it completely disregards the size and shape of phosphor particles, as well as their mutual arrangement inside of the screen. It is known from experiments that *S* is reciprocally proportional to the particle size between 1 and 10 μm.[1,42] In many practically relevant circumstances, the absorption coefficient *K* linearly depends on the volume concentration of particles f_V (volume fraction filled by particles).[41] However, the onset of multiple scattering results in a strong deviation from the linear dependence between the concentration f_V and the scattering coefficient *S*. It was shown that S/f_V is linearly dependent on $f_V^{2/3}$.[41] Several authors attempted to derive the relations between the coeffi-

cients *K* and *S* and the properties of single particles.[44,45] It is left to be mentioned that the assumption of symmetric and semi-isotropic (two-flux) scattering made in the Kubelka-Munk theory is not always valid. In some cases, a many-flux (>2) radiative transfer calculation procedure can produce noticeably more accurate results.[44]

2.2.3b. Johnson's theory (p-layer model)

A reference to the phosphor particle size is made in the Johnson's theory and other comparable approaches where phosphor screen is treated as a stack of particle monolayers.[1,31,43,46] Once the reflection and transmission of such monolayer are defined, one can calculate the optical properties of the phosphor coating of any thickness. In this case, recursion formulas are used instead of differential equations. The size of the phosphor particles may be accounted for in different ways. For example, the surface mean diameter of particles $\bar{\phi}_{SM}$ (also called *Sauter diameter*[47,48]) constituting the phosphor powder can be used[8]

$$\bar{\phi}_{SM} = \frac{\int_0^\infty n\phi^3 d\phi}{\int_0^\infty n\phi^2 d\phi}, \tag{2.55}$$

where *n* is the number of particles and ϕ is the diameter.

The thickness of one monolayer of particles is sometimes merely assumed equal to the mean particle size,[1,49] which hardly corresponds to the actual geometric arrangement of phosphor particles in the screen. It appears difficult to define a monolayer of randomly packed particles having considerable size distribution. Furthermore, thickness of the phosphor screen is most conveniently characterized in screen density, i.e., in weight of phosphor powder per unit of area of the screen. It was suggested that one conventional standard phosphor layer can be represented by N_L closely packed particles per unit area[50]

$$N_L = \frac{2}{\sqrt{3}} \int_0^\infty n\phi^2 d\phi \ . \tag{2.56}$$

The density of particles in the screen N_A (number of particles on the unit area) can be found as follows

$$N_A = \frac{6W}{\pi\rho \int_0^\infty n\phi^3 d\phi}, \tag{2.57}$$

where *W* is the screen density of the phosphor powder and ρ is the bulk density (specific gravity) of the phosphor material. Then, the number of phosphor layers *L* can be calculated from the screen density (Equation 2.55 is used)

$$L = \frac{N_A}{N_L} = \frac{3\sqrt{3}W}{\pi\rho\bar{\phi}_{SM}} = 1.65\frac{W}{\rho\bar{\phi}_{SM}}. \qquad (2.58)$$

It was shown experimentally that for phosphor powders with mean particle sizes of 6, 10, 15, and 25 μm, the optimum value of thickness of cathodoluminescent screens corresponding to the maximum of the T-mode brightness did not change when expressed in phosphor layers according to Equation 2.58.[50,51] This fact provides a physical justification of the proposed definition of the monolayer of phosphor particles. The total surface area of particles in one so-defined layer is independent of phosphor particle size. For conventional commercial phosphors (i.e., those with particles much larger than the wavelength of light), the intensity of light scattering is directly proportional to the area of the interface between the two phases with unequal refractive indices.[50] Thus, the contribution from a single phosphor layer should have approximately the same value for phosphor powders with different size of particles (still provided that the phosphor particles are sufficiently larger than the wavelength of emission).

Some authors successfully applied this definition of the phosphor layer in their calculations.[31] However, it should be noticed that there are no strict reasons for the unit particle layer to be related to the phosphor particle size when used for the purposes of modeling of optical properties of phosphor screens. Thickness of such an elementary layer may actually be chosen arbitrarily small. For example, a single phosphor layer can be assumed infinitesimally thin, and then the recursive formulas reduce to differential equations equivalent to the Schuster-Kubelka-Munk equations.[52] In other words, Johnson's theory and other "discontinuous" models based on the notion of the particle layer are very similar to the "continuous" theory of Kubelka and Munk, and also do not explicitly account for the size and shape of phosphor particles.

2.2.3c. Monte-Carlo method

There were certain attempts to develop a theory revealing the influence of the size and shape of particles on properties of phosphor powders. For example, in the work of Melamed,[53] the reflectance and transmittance of a phosphor layer were derived for an ordered packing of phosphor particles of uniform size. In most of the practical cases however, phosphor particles have unequal size and are randomly packed. Therefore, the relationship between the properties of single particles of phosphors and resulting optical properties of the screens usually constitutes a mathematical problem that cannot be solved analytically. The simplest bottom-up approach to modeling of the collective properties of packed phosphor particles is based on stochastic computational algorithms, which explicitly use random numbers. There

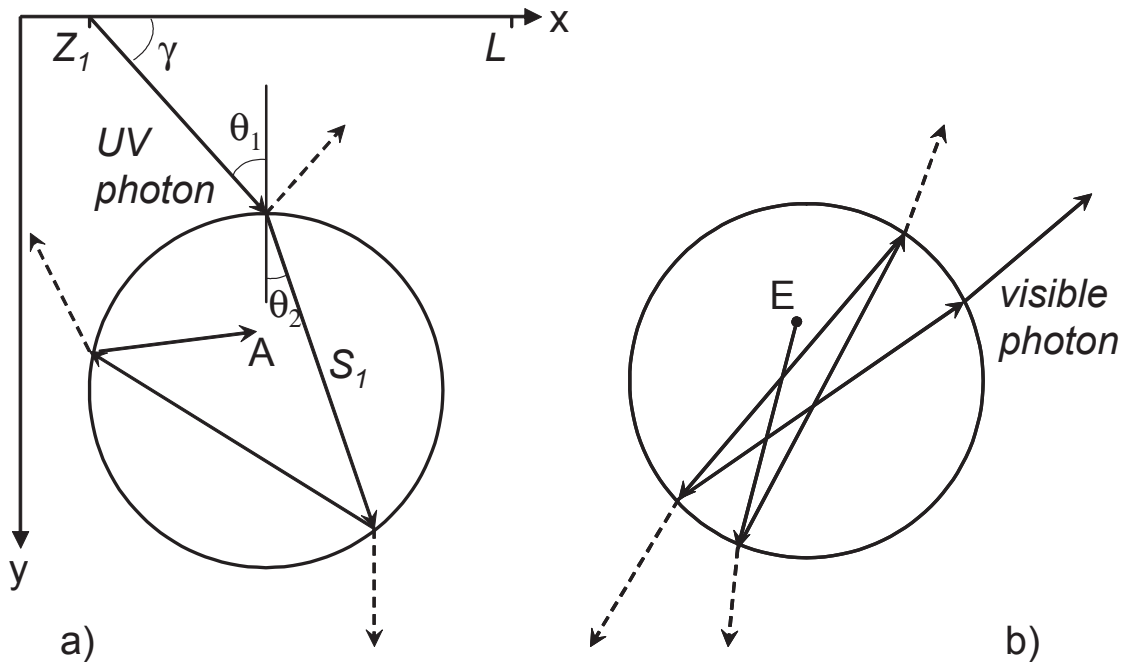

Figure 2.9 – Tracing of exciting and emitted photons. A UV-photon is absorbed in *A* (a), which leads to the emission of a visible photon in *E* (b).

exist numerous different implementations of this technique generally termed as the *Monte-Carlo method*.

In order to demonstrate the basic principle of the method, let us consider its application to a single spherical phosphor particle exposed to the UV radiation (see Figure 2.9). First, a UV-photon is generated. Its direction of propagation (if it is not fixed) and initial location are determined by Monte-Carlo decisions. For example, at the origin of the coordinate system, a virtual UV-lamp is located so that emitted UV-photons can appear between the points (0;0) and (L; 0). In this case, the initial coordinates of the UV-photon should be (Z_1;0), where Z_1 is a random number picked between 0 and L. If the UV-light is diffuse, the direction of the photon can also be chosen randomly between 0 and 180°($\gamma_0 = Z_2$).

The next Monte-Carlo decision is made upon the incidence of the UV-photon on the surface of the particle. At this point, the photon either penetrates the particle volume or is reflected away. The probability of being reflected is determined by the reflectance R_1 obtained from the Fresnel equation (assuming unpolarized light and a perfectly smooth particle surface)[54]

$$R_1 = \frac{1}{2}\left[\left(\frac{\cos(\theta_2) - m\cos(\theta_1)}{\cos(\theta_2) + m\cos(\theta_1)}\right)^2 + \left(\frac{\cos(\theta_1) - m\cos(\theta_2)}{\cos(\theta_1) + m\cos(\theta_2)}\right)^2\right]. \qquad (2.59)$$

In this equation, *m* is the relative refractive index

$$m = \frac{n_P}{n_A}, \qquad (2.60)$$

where n_P and n_A are the refractive indices of the phosphor material and interparticle medium, respectively. θ_1 denotes the angle of incidence and θ_2 is the refraction angle, which can be calculated from the Snell's law

$$\theta_2 = \arcsin\left(\frac{\sin(\theta_1)}{m}\right). \qquad (2.61)$$

If the random number Z_3 is smaller than or equals the value of R_1 obtained from Equation 2.59, the photon gets reflected from the surface of the particle. For $Z_3 > R_1$, the photon propagates inside of the particle in the direction of θ_2. In the latter case, it can get absorbed by the phosphor. The corresponding probability can be assessed by the Beer-Lambert law. Equation 2.16 can be rewritten as

$$T'_1 = \exp(-\alpha' S_1), \qquad (2.62)$$

where T'_1 is the transmission probability; α' is the absorption coefficient, and S_1 is the path length between the intersections of the photon with the surface of the particle. The next random number ($Z_4 \in [0,1]$) is picked and, if it is smaller than T'_1, the photon arrives at the opposite surface of the particle. Here, it would experience internal reflection or escape from the particle depending on the subsequent Monte-Carlo decision. If Z_4 is larger than T'_1, one calculates a location *A* along the path of the photon where the event of absorption takes place[55]

$$A = \frac{1}{\alpha'}\ln\left(\frac{1}{Z_4}\right). \qquad (2.63)$$

If absorption is weak, a significant fraction of incident photons is transmitted by the particle. As a consequence, the exciting photons can be absorbed after several scattering events (both reflection and refraction, see Figure 2.9). Otherwise, they can be *diffusely* reflected from the screen. Such particles are called *semi-transparent*. In the case of *opaque* particles, absorption is strong and UV-photons do not reach the opposite particle surface, so that multiple scattering is suppressed.

Once the UV-photon is absorbed, the next Monte-Carlo decision has to be made. At the location *E* (approximately coinciding with *A*, quantum efficiency of 100 % is assumed), a visible photon with random direction of propagation is generated. This photon can be traced in an analogous manner until it escapes from the simulated volume. Phosphor particles are usually *translucent* in the visible range, i.e., ab-

sorption of emitted photons can be neglected and at the same time, the number of scattering events experienced by photons increases.

After the visible photon has left the simulation volume (e.g., reached a virtual detector or was absorbed elsewhere), another UV-photon is generated. The accuracy of the calculations requires a large number of repetitions. The complexity of the model (number of simulated particles, their shape, size, and mutual arrangement) is usually limited by available calculation resources.

The Monte-Carlo methods can be applied to any problem, which allows for probabilistic formulation. It was used for spherical and polyhedral particles, monosized and those possessing a size distribution, ordered and randomly distributed on the substrate.[55–57] There are numerous reports on the Monte-Carlo modeling of properties of CRTs,[58] X-ray imaging systems,[59,60] and LEDs.[61,62] Along with the possibility to explicitly account for the size, shape, and arrangement of phosphor particles on the substrate, it allows for adding further parameters (e.g., roughness of the particle surface[55]) and can be combined with theoretical methods (e.g., *Mie scattering theory*,[56,59] see Section 2.3.3).

The very important advantages of the Monte-Carlo method over the two-flux methods discussed previously in this section are that it can be used for calculations of angular distribution of light intensity, for assessing the quality of image reproduction by the information displays and radiation converters (this topic will be discussed in the next subsection), and can handle powder screens with a complicated structure.[1] Furthermore, in the two-flux methods, the forward and backward intensities are set equal (see Equations 2.47), which is not always physical.[63] When using the ray (photon) tracing technique, such implications are resolved without any additional efforts. On the other hand, the application of geometric optics sets a limit on the particle sizes that can be simulated to those significantly larger than the wavelengths of light.[55] All reported works treating the optical properties of the phosphor screen by the Monte-Carlo method are dedicated to micrometer-sized phosphor particles. It should to be noted that the Melamed's theory[53] also cannot be applied for submicron phosphor particles.

2.2.4. Resolution of the phosphor screens

Along with high efficiency of conversion of external energy into visible light, phosphor screens used for acquiring or displaying any visual information have to satisfy several additional requirements. The imaging performance of a phosphor screen is determined by the amount of the information it can convey and is usually assessed by the limit of *resolution*, i.e., by size of the finest structural details of an image that a display or an image converter is able to reproduce.

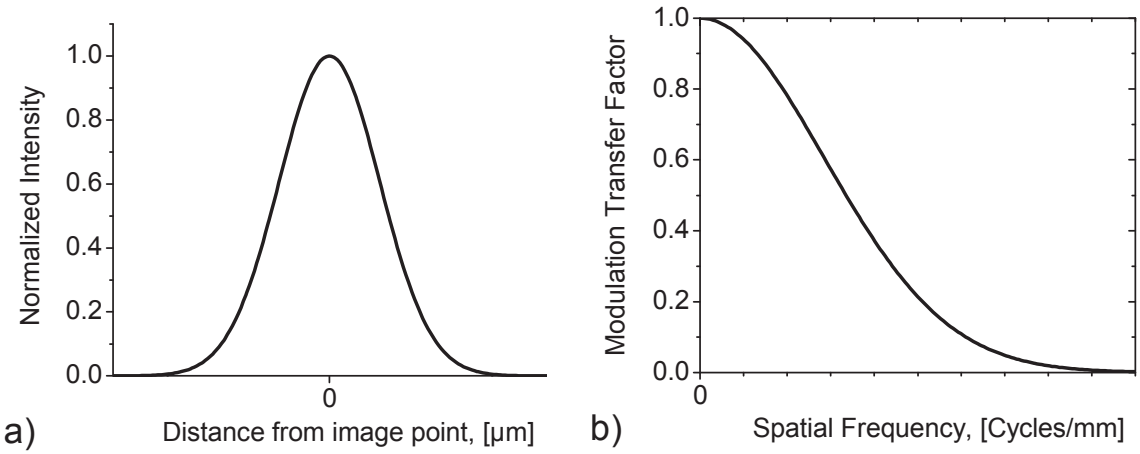

Figure 2.10 – Example of a point spread function (a) and the corresponding modulation transfer function (b).

The smallest element of an image is a single point. In an ideal imaging system, excitation by a radiation beam of infinitesimal diameter would result in a perfect infinitesimal image point. In reality, the smallest point always has some certain finite size. Therefore, the resolution of the screen can be characterized by defining a corresponding *point spread function* (PSF), i.e., measuring the size of the spot produced by the point-like excitation source. The PSF is a unique characteristic of the imaging performance of a phosphor screen. The intensity distribution in the entire image, which should be considered as an aggregate of image points, can be obtained by convolution of the intensity distribution of exciting radiation with the PSF of the phosphor screen. When two image points are spaced by less than the width of the PSF, they cannot be fully resolved. Such blurring of an image leads to losses of visual information.

For *isotropic* imaging systems, the two-dimensional point spread function is rotationally symmetric[64] and can be described by a curve for one spatial dimension (Figure 2.10a). Often a simple Gaussian intensity profile is assumed and the full width of the PSF at half of the maximum intensity (FWHM) is commonly used as the representative value. The shape of the PSF of different screens, however, may significantly vary, so it is advisable to measure it down to at least several percent of the peak intensity[65] and the full width corresponding to 1-5 % of the maximum is sometimes specified as well.[66]

Direct measurement of the PSF is quite cumbersome because it requires a point source of excitation. In many applications, it is difficult to reduce the area of the screen exposed to the exciting radiation to a vanishingly small size and have sufficient intensity at the same time. It can be more convenient to measure the *line spread function* (LSF) – another *transfer characteristic* of phosphor screens. Similarly

to the PSF, which describes the *transfer* of intensity distribution from the point source of excitation to its image, the LSF defines the intensity profile of the image of a line source. The LSF is related to the PSF by the expression[65]

$$LSF(x) = \int_{-\infty}^{+\infty} PSF(x, y)dy\,. \tag{2.64}$$

The LSF is a one-dimensional function but, for the isotropic imaging systems, the two-dimensional PSF can be obtained from the single LSF by the Abel transform.[64,67] If a PSF has a Gaussian shape, the corresponding LSF is a Gaussian function as well.[7] The width of the LSF is also usually measured by its FWHM value and by the full width at some intensity in the range of several percent of the peak response.[58] Sometimes, the full width comprising most of the area of the integrated LSF (e.g., 90 %) is applied.[67]

How much overlap of the spread functions is needed for adjacent points/lines in the image to become irresolvable? There are several resolution criteria used in various fields of applied optics. The most well known is the *Rayleigh criterion*, which states that two equally bright point objects can be resolved if the maximum of the PSF of the first point falls into the first minimum of the PSF of the second one.[68] This definition of the limit of resolution was developed for diffraction-limited optical systems, where the PSF is represented by the *Airy pattern* of concentric rings with multiple minima. For the PSFs without local minima (e.g., those of Gaussian shape) the Rayleigh criterion is ambiguous. Furthermore, it cannot be applied to the resolution of unequally bright point objects. Very often the limit of resolution is simply identified with the FWHM of the PSF. The so-defined *Houston criterion* can be used with spread functions of any shape. However, it is also impractical for resolving the points/lines of different brightness. In many cases, the *Sparrow criterion* is preferred.[68] Sparrow has suggested that the natural definition of resolution is the point separation at which the saddle point between the two maxima first develops, i.e., when the second derivative of the sum of the PSFs in the midpoint between the points vanishes. If the distance between the points is less than or equal to the Sparrow limit, they will be perceived as a single elongated point. The same applies to the LSFs. For example, it is known that a series of equidistant Gaussian profiles separated by 2σ, where σ is the standard deviation of the spatial intensity distribution, should produce a uniform intensity ($2\sigma \approx 0.85FWHM$). This property, referred to as a *merging raster*, is utilized for reproduction of images with *pixelated screens*, i.e., screens composed of an array of pixels (discrete picture elements).[7] If the distance between the lines increases, a variation of intensity with the corresponding *spatial frequency* will be observed as soon as this variation exceeds some perceivable threshold, i.e., the lines will be resolved.

For a general case of an arbitrary LSF, any quantitative treatment would require extensive calculations and it has been long recognized that the problem can be

simplified by solving it in the (spatial) frequency domain. This approach is based on the notion of the *optical transfer function* (OTF), a representation of the frequency response of the optical system. The one-dimensional OTF can be obtained by the Fourier transform of the LSF (or of the PSF for two dimensions).[67,69] It can also be directly measured for sinusoidal excitation patterns. As the emission and excitation of luminescence are incoherent, only the modulus of the OTF, termed *modulation transfer function* (MTF), has importance and its phase component (*phase transfer function*) can be disregarded. *Modulation* is defined as the ratio of the amplitude of the sinusoid to its average value and, therefore, cannot be greater than unity.[64] An example of MTF is shown in Figure 2.10b. The limit of resolution of a phosphor screen is usually associated with spatial frequency (measured in cycles per unit length) at which the MTF decreases to 3-5 %.

The list of transfer characteristics conventionally applied to phosphor screens would be incomplete, if the *contrast transfer function* (CTF) was not mentioned. The CTF quantifies the frequency response of an imaging system for a square-wave input instead of the sine wave, which is more convenient for experiments (e.g., with *bar charts* or rectangular slits).[70] For the same reason of simpler experimental procedure, the line spread function is sometimes obtained by differentiating an *edge trace*, i.e., the intensity distribution on a boundary between “black” and “white” half-planes in the image of the knife edge.[69] A CTF equal to one designates perfect transfer of contrast. The limit of resolution of the imaging system is specified in lines per unit length. Such units are very convenient for pixelated displays and radiation converters, where the smallest resolvable details of an image are inherently limited by the size of single pixels. However, when two neighboring lines of pixels have the same intensity, they cannot be resolved. “Black” lines should be interlaced with “white” lines, i.e. at least two lines of pixels are needed for reproduction of each line in the image. In the sampling theory, this is justified by the *Nyquist-Shannon theorem*. In order to avoid confusion in specification of resolution, the units of line pairs per unit length (e.g., lp/mm) are widely accepted. Generally, the cutoff spatial frequency for pixelated screens is, in the best case, approximately equal to half the density of lines in the raster (or pixels in the line). Strictly, it is often somewhat worse if the PSFs of the neighboring pixels significantly overlap.

The resolution of unstructured (*unpixelated*) screens is determined by a number of parameters. The following primitive example, adopted from Ozawa,[8] reveals the major factors of influence. Let us consider a double layer of phosphor particles deposited on the transparent substrate (Figure 2.11). The coated side is exposed to an electron beam and the screen is observed in the T-mode. It is assumed that the incident electrons are completely absorbed in the top layer of phosphor particles and particles in the deeper layer(s) merely scatter emitted light without contributing to the output of luminescence. It can be concluded from the discussion in Section 2.2.3c

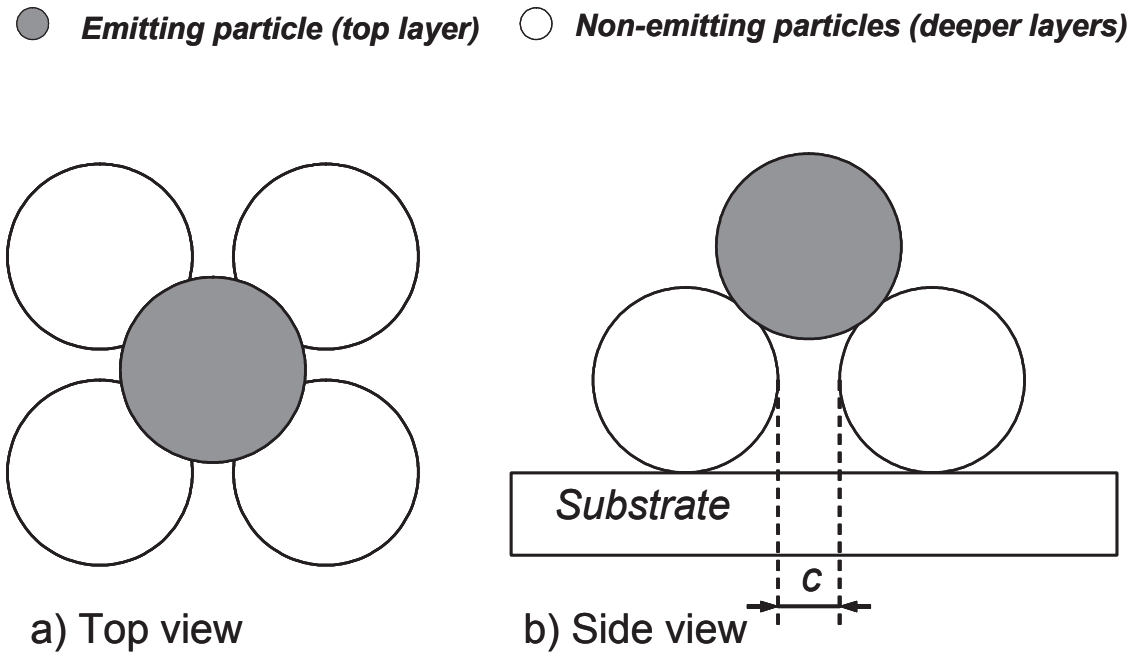

Figure 2.11 – Schematic illustration of expansion of the light spot in the deeper layers of phosphor particles (after Ozawa,[8] see text for explanation).

that light emitted inside of the phosphor particle usually experiences multiple internal reflections and can escape the volume of the particle in any direction at an arbitrary point of its surface (especially if the particle surface is rough and randomly scatters incident photons). Therefore, even for a single layer of phosphor particles, the smallest light emission spot would be approximately equal to the phosphor particle size. For the sake of simplicity, optical interaction between particles in the top layer is neglected. If we assume spherically symmetric intensity distribution of emission from a single particle, nearly 50 % of the light is emitted towards the substrate. Some of these photons impinge upon the particles in the second layer and get either reflected or refracted on their surface. The rest reaches the substrate and either goes through it or is partially reflected back. For the situation depicted in Figure 2.11 where each particle in the top layer has four nearest neighbors underneath, this means that the size of the light spot D_{LS} produced by one emitting particle increases to approximately

$$D_{LS} = 2\phi + c\,, \tag{2.65}$$

where ϕ is the phosphor particle size and *c* is the inter-particle clearance (i.e., the width of the gap between the particles) for neighboring particles situated in the same

layer. When there are N_L particle layers below the top layer, the spot increases further and totals to at least

$$D_{LS} = N_L(\phi + c) + \phi . \qquad (2.66)$$

Although this expression is strongly oversimplified, it clearly demonstrates that the resolution of unpixelated screens can be improved by decreasing the thickness of the phosphor screen, increasing the packing density of phosphor particles and, finally, by reducing the phosphor particle size. This conclusion is generally valid for any cathodo- or photoluminescent powder screens as well as for those excited by X-rays. However, each parameter affecting the screen resolution can be varied only within some certain limited range determined by other application-specific requirements or available technology. For example, X-rays are weakly absorbed by phosphors and a considerable thickness of the screen may be required for sufficient efficiency of conversion into visible light. Usually, in such cases, a trade-off between better resolution and fainter emission intensity is found. On the other hand, penetration depth of an electron beam into the phosphor is often much smaller than the size of a single phosphor particle. It was experimentally proven that the optimum thickness of the cathodoluminescent screens optimized for the highest brightness is less than two complete layers of particles ($L_{opt} = 1.4$ conventional layers defined by Equation 2.58 in Section 2.2.3b).[50,51] However, from the point of view of manufacturing CRTs, it is difficult to deposit such thin phosphor coatings free of voids and irregularities. The thickness of phosphor screens in conventional CRTs often has to be increased in order to assure uniformity and thus, the obtained resolution is compromised due to technological constraints.

A general relation for the optimum screen density W_{opt} of CRTs, which accounts for the non-close packing of phosphor particles, was obtained in[58]:

$$W_{opt} = 2\bar{\phi}_{V50}\rho f_V^{2/3}, \qquad (2.67)$$

where $\bar{\phi}_{V50}$ is the volume median diameter (measured by sedimentation), ρ is the phosphor density, and f_V is the packing density of the phosphor screen. The highest packing density of monodisperse spherical particles (as assumed in Section 2.2.3b) is equal to 0.74. Typical values of f_V for conventional phosphor screens are in the range of 0.3-0.6.[58,71] For $f_V = 0.3$ and $\bar{\phi}_{V50} \approx \bar{\phi}_{SM}$, W_{opt} obtained from Equation 2.67 closely matches previously mentioned optimum screen density of 1.4 layers of phosphor particles. For the log-normal *particle size distribution* (PSD) which is approximately valid for most of phosphor powders produced by standard methods, the averages of the PSD are related by the *Hatch-Choate equations* and it holds[47,48,72]

$$\bar{\phi}_{V50} / \bar{\phi}_{SM} = \exp\left(0.5 \ln^2 \sigma_g\right), \tag{2.68}$$

where σ_g is the geometric standard deviation of the PSD. Equations 2.58, 2.67, and 2.68 can be combined to produce

$$L_{opt} = 1.65 \frac{W_{opt}}{\rho \bar{\phi}_{SM}} = 3.3 \frac{\bar{\phi}_{V50} f_V^{2/3}}{\bar{\phi}_{SM}} = 3.3 f_V^{2/3} \exp\left(0.5 \ln^2 \sigma_g\right). \tag{2.69}$$

The values of the geometric standard deviation of phosphors may significantly vary (e.g., $\sigma_g = [1.4..2.5]$ for halophosphates.[73]) For $\ln \sigma_g = [0.35..0.37]$ (i.e., $\sigma_g = [1.42..1.45]$ as reported by Ozawa[50]), Equation 2.69 may be rewritten in the simple form

$$L_{opt} \approx 3.5 f_V^{2/3}. \tag{2.70}$$

The values of L_{opt} corresponding to $f_V = [0.3..0.6]$ span the range from 1.6 to 2.5 layers of phosphor particles, which does not include the primary assumption of $L_{opt} = 1.4$. This discrepancy should be attributed to the rather approximate value of the constant factor in Equation 2.67 and the inherent inaccuracies of measurements of the phosphor particle size and screen weights. The main conclusion is that, if the packing density f_V is fixed, L_{opt} stays constant. However, if we increase the packing density of phosphor powder in the screen, L_{opt} (and W_{opt}) should increase with $f_V^{2/3}$. How would this affect the screen resolution? A simple relation between the width of the LSF at 5 % peak intensity L_{05} and the geometric thickness d of the screen was found for practical CRT phosphors[58]

$$L_{05} = 4.5 d. \tag{2.71}$$

This equation may be rewritten for the optimum screen density W_{opt} and combined with Equation 2.67 to obtain

$$L_{05} = 4.5 \frac{W_{opt}}{\rho f_V} = 9 \frac{\bar{\phi}_{VM}}{f_V^{1/3}}. \tag{2.72}$$

Therefore, an increase in packing density of phosphor particles in the screens of optimized density leads to a “sharpening” of reproduced images. This effect would be even more pronounced if the screen density W would be fixed at some certain value, however this would also cause a noticeable degradation of brightness. It can be considered as a general trend that screens with high packing density of particles have better resolution but decreased brightness.[74]

A combined effect of the size and packing density of phosphor particles can be expressed by the change of the scattering mean free path of the emitted photons.[58] Intensive optical scattering is found to suppress the tails of the spread functions, i.e., to decrease the L_{05} in Equation 2.71. As a result, the MTF of the powder phosphor

screens at low spatial frequencies often surpasses that of non-scattering ones (e.g., single-crystalline or glass plates).[65,75,76]

Scattering of the exciting radiation usually has a minor effect on the quality of image reproduction in most of the applications. For example, in case of CRTs, changes of the MTF introduced by an increase of the energy of electrons from 5 to 40 keV were less than 15 %.[71] For the X-ray excitation, scattering of X-rays can be completely neglected.

It should be emphasized that Equations 2.71 and 2.72 are valid only for the T-mode of screen observation. For powder phosphor screens exposed to the strongly absorbed exciting radiation, the MTF in the R-mode is almost independent of the screen thickness. Scattering of the emitted light in the deep layers of phosphor particles practically does not distort the image observed from the excitation side of the screen. The reflecting CRTs have 3-4 times better resolution as compared to the conventional transmitting ones.[71]

If the exciting radiation is weakly absorbed, the resolution of the screen is still to a large extent determined by its geometric thickness so that the values of the MTF corresponding to the same product of spatial frequency and phosphor thickness stay unchanged.[75] The necessity of large values of thickness for complete absorption of X-rays leads to a relatively low resolution of powder phosphor screens, which usually is limited to the range of 10-20 lp/mm.[60,77] For some given thickness of the X-ray intensifying screen, the resolution may be improved by several methods, e.g., by depositing a reflective or absorbing coating (*backing*) over the rear side of the screen or by the introduction of small amounts of impurities which provide weak self-absorption of luminescence in the phosphor material thus removing long tails of the LSF without strongly impairing the light output.[71,75] Again, the resolution of the screens in the R-mode is somewhat better than that for the T-mode.[71]

Although the R-mode seems to be preferable for high-resolution imaging, it is highly impractical in most of the applications. In order to achieve superior resolution in the T-mode without sacrificing the efficiency of detection of X-rays, special structured screens are sometimes used. Columnar (needle-like) phosphor particles aligned parallel to the incident X-rays allow to eliminate the strong interdependence between the width of the LSF and the screen thickness.[60] Alternatively, a mask with an array of thin holes filled with a phosphor can be used. Screens with resolution on the order of 1 μm were realized based on the latter approach.[78] Nonetheless, the screens with spatial resolution close to the optical diffraction limit could be obtained only by decreasing the thickness of the phosphor film to 1 μm.[67,79]

It can be noticed that similar techniques of screen structuring (e.g., a *black matrix* and a *shadow mask*) were also applied in order to boost the performance of CRTs. For the unpixelated CRTs, the size of the observed spot is dominated by the diameter of the electron beam, which was usually on the order of 200 μm,[50] so that

the resolution of the screen could be experimentally assessed upon the increase of the emitting spot size over the beam diameter rather then upon the PSF or D_{LS} derived above (Equation 2.66).[80] An acceptable difference between the beam diameter and the produced light spot should be within 10 %. By decreasing the electron beam size to 10 µm, a CRT screen with an impressing resolution of 307200 pixels/cm^2 could be realized (corresponding to the resolvable spot size of 18 µm, the average phosphor particle size was 2 µm).[8]

As a closing remark on imaging performance of the phosphor screens, it has to be mentioned that there are several further screen characteristics which are left outside the scope of this section but may be important in some specific cases as, for example, a *detective quantum efficiency* describing the signal-to-noise ratio of the imaging system.[81]

2.3. Luminescent screens with submicrometer phosphor particle size

2.3.1. Limits of performance of the luminescent screens

Let us consider a powder phosphor screen which is excited by UV-light (the wavelength and intensity are fixed). What can be its highest brightness and resolution?

For a semi-infinite unstructured phosphor plaque, the R-mode brightness is at most (see Section 2.2.3a)

$$J_{MAX} = qI'(0)\,, \tag{2.73}$$

where q is the quantum efficiency of the phosphor and $I'(0)$ is the intensity of the incident exciting radiation. For the T-mode, the maximum intensity (for some optimum screen thickness) would be

$$I_{MAX} \le \tfrac{1}{2} J_{MAX}\,. \tag{2.74}$$

Thus, the maximum brightness of the phosphor screen is ultimately limited by the quantum efficiency of the phosphor. The quantum efficiency of phosphors used in fluorescent lamps, PDPs, and LEDs is about 100 %.[5] In this aspect, the performance of the state-of-the-art inorganic phosphors is very close to the physical limits.

The resolution of the unpixelated phosphor screens is mainly determined by their geometric thickness (see Section 2.2.4). In principle, any desired resolution could be obtained with an appropriately thin phosphor coating, provided that it absorbs sufficient amount of exciting radiation for a detectable light output. However, the ultimate limit of resolution is set by diffraction of the light and not by the screen thickness. If no special super-resolution techniques are utilized, the resolution of an optical system cannot be better than

$$k \approx \frac{2n}{\lambda}\,, \tag{2.75}$$

where *k* is the *Abbe limit of detection* (measured in spatial frequency), *n* is the refractive index of the surrounding medium, and λ is the wavelength of emitted light.[82] The highest spatial frequency that can be optically resolved (for $\lambda = 400$ nm) is therefore about 5000 cycles/mm. For longer wavelengths and a finite aperture of the detector, the limit of detection can significantly decrease. If we assume for simplicity that the FWHM of the LSF exactly equals the thickness of the phosphor coating,[67] the corresponding thickness threshold of the diffraction-limited phosphor screen would be on the order of 200 nm. For the pixelated screens, this is also the value of the smallest pixel pitch that could ever be needed for the optical imaging.

It is difficult to obtain high brightness and resolution of the screen at the same time. The thickness of phosphor coatings usually has to be optimized for only one of

these characteristics while meeting some minimum requirements for the other one. For the screens designed for observation with unarmed human eyes, a resolution of 20 lp/mm is usually sufficient.[83] However, there are several imaging applications like excimer laser beam profiling, inspection of photolithographic masks, tunneling electron microscopy, and X-ray microtomography, where phosphor screens with resolution on the order of 1000 lp/mm would provide a definitive advantage. Although a few works on phosphor screens with sub-micrometer resolution have been reported,[67,79,84] still a lot can be done in this direction.

2.3.2. Benefits of the decreased phosphor particle size

A decrease in either thickness or the pixel size of a powder phosphor screen to less than 1 micrometer can obviously be possible only with even smaller phosphor particles. Conventional phosphor powders consist of particles with a size in the range of several micrometers and therefore are not suitable for this purpose. Manufacturing of diffraction-limited phosphor screens would require application of nanophosphors, i.e., *ultrafine* phosphor powders with particle size < 100 nm.

The maximum brightness of such a screen made of any known phosphor with any thinkable powder characteristics (i.e., particle size, width of the PSD, morphology and packing density of particles) most likely will not exceed than of the best commercial samples (see Section 2.3.1). However, this does not mean yet that phosphor coatings utilized in non-imaging application (e.g., lighting) cannot benefit from the decrease in the phosphor particle size.

Inorganic phosphors (especially those doped with rare-earth elements) are very expensive raw materials which substantially contribute to the final price of various luminescent displays and light sources. Phosphor powders scrapped in the process of manufacturing of displays are routinely recovered.[50] In Europe, phosphor powders in the fluorescent lamps are recycled as well as elemental mercury (see *WEEE Regulation* of the European Community). Minimization of consumed amounts of phosphor powders can have a significant impact on the economical attractiveness of the corresponding commercial products. In some cases, this could be achieved by decreasing the phosphor particle size.

The optimum screen weight of phosphor screens excited by strongly absorbed radiation decreases for finer phosphor particles. When the penetration depth of exciting radiation is smaller than the size of phosphor particles, the maximum light output in the T-mode corresponds to the thinnest phosphor coating fully covering the surface of the substrate (see Sections 2.2.3b and 2.2.4). The ability of phosphor powders to cover the surface (i.e., to “cast a shadow”) increases for the smaller particle sizes, as demonstrated in Figure 2.12. Theoretically, the screening density can be reduced without a significant loss of intensity of luminescence unless the phosphor particle

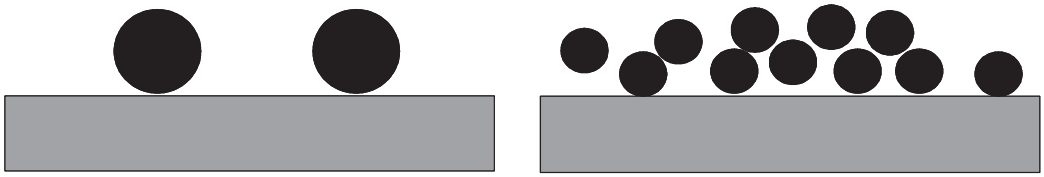

Figure 2.12 – Illustration of the improvement of surface coverage by using smaller phosphor particles. The total volume (weight) of phosphor is the same in both cases.

size falls short of the penetration depth of exciting radiation or there is a degradation of the quantum efficiency of the phosphor (e.g., due to particle size effects discussed in the next section). This conclusion equally applies to most of the fluorescent lamps, CRTs, and PDPs and could provide a possibility to decrease the costs of manufacturing of such devices.

2.3.3. Physical implications of reduction of the phosphor particle size

Although the advantages of finer phosphor powders described in Section 2.3.2 are widely known, the practical downscaling of particle size of conventional phosphors is limited. Y_2O_3:Eu phosphor and some aluminates produced by conventional methods maintain high efficiency only down to a mean particle diameter of 3 μm, whereas for halophosphates, predominantly used in fluorescent lamps, a large diameter of 8 μm is necessary.[1] For finer phosphor particles, luminescence efficiency tends to decrease.

The influence of the phosphor particle size on quantum efficiency and other properties of commercial micrometer-sized phosphors can often be attributed to technological issues. For example, if the synthesis route of the phosphor powder includes firing at high temperatures, the sintered powder cake usually has to be crushed and milled later on, in order to break the agglomerates of particles. Excessive milling results in smaller particles but also introduces structural defects on their surface, which cause a decrease of the phosphor efficiency.[1] In general, any variation of the processing route required for producing phosphor powders with different particle sizes can affect the crystallinity and chemical composition of the phosphor (i.e., concentrations of intentional dopants and impurities) and therefore obscure the purely physical *particle size effects*. The technology-related phenomena are not the subject of this section unless they are based on the “true” particle size effects.

2.3.3a. Scattering and absorption of light by small particles

The technology-independent influence of phosphor particle size upon the performance of powder screens is dominated by changes of characteristics of optical scattering. It is, therefore, desirable to derive a mathematical relation between the particle size and the scattering coefficient β (as used in Sections 2.2.2 and 2.3.2a).

It is convenient to introduce a quantity specifying the ability of a single phosphor particle to scatter light. As discussed in Section 2.2.3b, the total amount of light scattered by a powder coating is directly proportional to the specific surface area of phosphor particles provided that they are large in comparison with the wavelength of light. The amount of light removed from the incident light by each single phosphor particle should be then proportional to its geometric projected area A_P

$$C_{SCA} = Q_{SCA} A_P \,, \tag{2.76}$$

where C_{SCA} is the scattering cross-section of the particle (measured in units of area), the proportionality factor Q_{SCA} is termed *scattering efficiency*. In the general case of particles that are both absorbing and scattering, the *attenuation cross-section* (also called *extinction cross-section*) should be used instead of C_{SCA}

$$C_{ATT} = Q_{ATT} A_P = C_{ABS} + C_{SCA} = (Q_{ABS} + Q_{SCA}) A_P \,, \tag{2.77}$$

where Q_{ATT} and Q_{ABS} are the attenuation and absorption efficiencies, respectively; and C_{ATT} and C_{ABS} are the corresponding cross-sections.

Calculation of the scattering and absorption efficiency factors is the central problem of the *Mie theory* (also called *Lorenz-Mie theory*). The theory provides the exact solution of the *Maxwell equations* describing propagation of electromagnetic radiation for a plane wave incident on spherically symmetric particles. The intensity of scattered light at any angle can be calculated for a particle with the given relative refractive index n_R and size parameter x, defined by expressions

$$n_R = \frac{n_P}{n_A} \,, \tag{2.78}$$

where n_P and n_A are the refractive indices of the phosphor material and ambient medium, respectively; and

$$x = \frac{\pi \phi}{\lambda} \,, \tag{2.79}$$

where ϕ is the particle diameter and λ is the wavelength of light incident on the particle. The desired attenuation/scattering efficiency factors are obtained in the form of a series of Legendre polynomials

$$Q_{ATT} = \frac{2}{x^2} \sum_{n=1}^{\infty} (2n_R + 1) \,\mathrm{Re}(a_n + b_n) \,, \tag{2.80}$$

$$Q_{SCA} = \frac{2}{x^2}\sum_{n=1}^{\infty}(2n_R+1)\left\{|a_n|^2 + |b_n|^2\right\}, \tag{2.81}$$

where the scattering coefficients a_n and b_n are given in terms of Ricatti-Bessel functions ψ_n and ζ_n of increasing orders

$$a_n = \frac{\psi_n'(n_R x)\psi_n(x) - n_R\psi_n(n_R x)\psi_n'(x)}{\psi_n'(n_R x)\zeta_n(x) - n_R\psi_n(n_R x)\zeta_n'(x)}, \tag{2.82}$$

and

$$b_n = \frac{n_R\psi_n'(n_R x)\psi_n(x) - \psi_n(n_R x)\psi_n'(x)}{n_R\psi_n'(n_R x)\zeta_n(x) - \psi_n(n_R x)\zeta_n'(x)}. \tag{2.83}$$

The comprehensive description of the procedure may be found in numerous textbooks on scattering of light by small particles, e.g., by Bohren and Huffman,[54] Mishchenko *et al.*,[85] or van de Hulst.[86] If no additional simplifying assumptions can be made, the required calculations are quite computationally intensive and the results are best represented in a graph such as shown in Figure 2.13 (taken from the book by Mishchenko *et al.*[85]). The lowest curve in both cases corresponds to non-absorbing monodisperse particles with a relative refractive index of 1.4. In Figure 2.13a, changes of the attenuation efficiency due to absorption of light inside of the particles are presented. The imaginary part of the refractive index *k* (often referred to as the *extinction coefficient*) can be transformed into the absorption coefficient α of the bulk solid material by the expression[54]

$$\alpha = \frac{4\pi k}{\lambda_0}, \tag{2.84}$$

where λ_0 is the wavelength of light in vacuum.

Figure 2.13b demonstrates the effect of averaging over a distribution of particle sizes. The width of the PSD (the gamma distribution was used in Figure 2.13b[85]) is stated by the effective variance

$$Var = \frac{1}{\bar{\phi}_{SM}}\frac{\int_{\phi_{MIN}}^{\phi_{MAX}} d\phi\, n(\phi)(\phi - \bar{\phi}_{SM})^2\phi^2}{\int_{\phi_{MIN}}^{\phi_{MAX}} d\phi\, n(\phi)\phi^2}. \tag{2.85}$$

The Sauter diameter $\bar{\phi}_{SM}$ (surface mean) is used as a representative average particle size for the calculations of the effective variance as well as for the effective size parameter x_{EFF} according to Equation 2.79. It should be noticed that both the presence of absorption and unequal size of scattering particles lead to a “washing-out” of the ripple structure. An important outcome for non-absorbing particles is that the scattering efficiency factor asymptotically tends to a value of 2 as the size parameter increases (i.e., for particles much larger than the wavelength of light). In the range of small values of the size parameter, a steep decrease of the scattering efficiency is

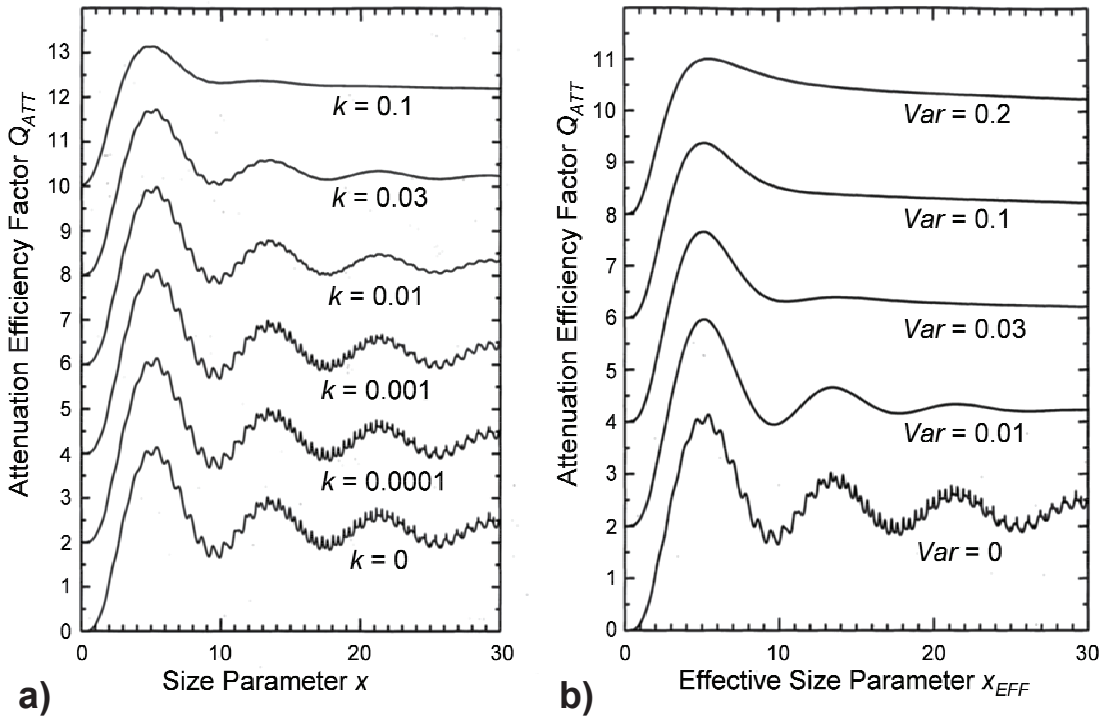

Figure 2.13 – Influence of absorption (a) and distribution of particle sizes (b) on the attenuation efficiency factor obtained from the Mie theory for the relative refractive index n_R = 1.4.[85] See text for details.

observed in all cases. This is the only feature surviving in the graphs, when the width of the PSD substantially increases.[85]

For particles which are much smaller than the wavelength of light ($\phi < 50\ nm$) the intensity and pattern of scattering can be obtained by the much simpler *Rayleigh scattering theory*. For such particles, the incident electromagnetic field behaves almost as an electrostatic field and is homogeneous inside the particle. This results in the following equations for the scattering and absorption efficiencies[85]

$$Q_{SCA} = \frac{8}{3} x^4 \left| \frac{n_R^2 - 1}{n_R^2 + 2} \right|^2, \tag{2.86}$$

$$Q_{ABS} = 4x \,\mathrm{Im}\left(\frac{n_R^2 - 1}{n_R^2 + 2} \right). \tag{2.87}$$

The use of suitable approximations as in the case of the Rayleigh scattering theory facilitates a dramatic reduction of computational effort. In the recent years however, ever increasing computational capacities become available for scientists. This trend manifests itself in the development of new theoretical methods which can overcome the limitations of the Mie theory at the cost of higher complexity of calcula-

tions. For example, the *T-matrix method* becomes popular because it can be applied for particles lacking spherical symmetry. Details on further popular methods as, e.g., the separation of variables method (SVM) or the discrete dipole approximation (DDA) can be found in Mishchenko *et al.*[85]

2.3.3b. Independent scattering and absorption in particulate media

If the effective attenuation cross-section of phosphor particles is known, it can be used for assessing the collective optical properties of an ensemble of particles. For the idealized scenario of single scattering by N particles per unit of volume (particles are assumed to be sparsely spaced), the Beer-Lambert law (see Equation 2.24) can be rewritten to yield[47]

$$I_T = I_0 \exp(-(\alpha+\beta)d) = I_0 \exp(-NQ_{ATT}A_P d)\,. \tag{2.88}$$

Alternatively, it could be reformulated for the particle volume fraction f_V by assuming particles of spherical shape and diameter ϕ

$$f_V = \frac{\pi N \phi^3}{6}\,, \tag{2.89}$$

$$A_P = \frac{\pi\phi^2}{4}\,, \tag{2.90}$$

$$I_T = I_0 \exp(-\frac{3f_V Q_{ATT}}{2\phi}d)\,. \tag{2.91}$$

For non-absorbing particles substantially larger than the wavelength of light,

$$Q_{ATT} = Q_{SCA} = 2\,. \tag{2.92}$$

One obtains a simple relation between β and ϕ

$$\beta = \frac{3f_V Q_{SCA}}{2\phi} = \frac{3f_V}{\phi}\,. \tag{2.93}$$

If volume concentration of particles (i.e., f_V) does not change, the scattering constant in the Beer-Lambert law is inversely proportional to the phosphor particle size.

Similar expressions of the general form

$$S = \frac{const.}{\bar{\phi}_{SM}} \tag{2.94}$$

relating the scattering coefficient *S* with the size of phosphor particles can also applied in the framework of the Kubelka-Munk theory.[73] Again, the Sauter diameter is used in order to account for the distribution of particle sizes.

When particles are separated from each other by sufficiently large distances so that the scattering from each single particle is not affected by the proximity of its neighbors, it is possible to directly relate the parameters of the Kubelka-Munk theory with those of the Mie theory by introducing additional parameters[45]

$$K = N\bar{\xi}C_{ABS} = \frac{3f_V}{2\phi}\bar{\xi}Q_{ABS}, \tag{2.95}$$

$$S = N\bar{\xi}(1-\bar{\sigma}_d)C_{SCA} = \frac{3f_V}{2\phi}\bar{\xi}(1-\bar{\sigma}_d)Q_{SCA}, \tag{2.96}$$

where $\bar{\xi}$ is the average path-length parameter (assumed equal to 2 in the original Kubelka-Munk theory) and $\bar{\sigma}_d$ is the forward-scattering ratio for diffuse radiation (i.e., a fraction of the energy that each particle scatters in the forward direction; it can also be determined by the Mie theory).

2.3.3c. Dependent scattering and absorption in densely packed powders

For powder screens, which primarily consist of packed phosphor particles with very small amounts of binders, the condition of large separation of particles is, strictly, never fulfilled. If the thickness of a coating equals at least one complete layer of particles, the average interparticle clearance (as shown in Figure 2.11) in the first layer does not exceed the average particle size. Every particle in further layers directly contacts at least two other phosphor particles (one in the previous and one in the next particle layer) unless it is situated in the surface layer. With increase of the packing density, the distances between neighboring particles decrease and more particles get into contact with each other. The mean free path of the photons between two successive scattering events is determined by the average interparticle spacing and thus it should decrease as well. If it becomes comparable to the particle size, the wavefront of the scattered light incident on the next particle along its path can be appreciably different from the plane wave. As a consequence, the accuracy of calculations based on the efficiency factors obtained from the Mie theory can be impaired. Furthermore, in such a case the phosphor particles cannot be treated as point-like scatterers. The absorption and scattering coefficients (see Equation 2.93) should be corrected for *volume scattering*[87]

$$\alpha = \frac{3f_V Q_{ABS}}{(1-f_V)2\phi}, \quad \beta = \frac{3f_V Q_{SCA}}{(1-f_V)2\phi}. \tag{2.97}$$

These expressions differ from those derived for the point scattering by the factor $(1-f_V)$ in denominator, which is introduced in order to account for *shadowing* of particles by each other for $f_V > 0.1$.

Significant qualitative changes in the interaction of light with particulate mater occur when the interparticle distances enter the size range of the wavelength of the incident light. At this scale, the scattered fields of the neighboring particles can become spatially coherent even for an incoherent radiation source. Coherent addition of

the scattered light strongly affects the scattering characteristics of particles in the far field.[88] At the same time, the near-field interactions become pronounced.[89] At a sub-wavelength distance from the particle surface, electromagnetic fields include contributions from non-propagating *evanescent waves*.[90,91] Their influence on the radiation transfer is manifested, for example, by a phenomenon known as *frustrated total internal reflection*. When two media with high refractive indices are separated by a small gap filled with a material of lower refractive index, transmission of light between the two high-index media is observed at the angles of incidence, for which the total internal reflection would occur in the absence of the second high-index medium. The near-field interactions affect both absorption and scattering of light by particulate matter.[88]

In some cases, the collective optical properties of densely packed particles can still be treated as if these particles were attenuating incident light independently from each other. In many cases, however, the influence of the neighboring particles cannot be neglected. For example, effects generally termed as *particle crowding* play a very significant role in the technology of pigments.[92,93] The corresponding regime of radiation transfer is referred to as *dependent scattering* and *absorption*.[94] The onset of the dependent effects is usually determined by a 5 % deviation from the independent Mie theory. It was found that this threshold is usually surpassed when the interparticle clearance decreases below approximately half the wavelength of the incident radiation[95]

$$c_d \leq 0.5\lambda, \tag{2.98}$$

where c_d denotes the clearance, for which the dependent effects are significant, and λ is the wavelength of light in the medium between the particles (not λ_0 for vacuum). Although in general particles are randomly packed and have different sizes and shapes, the ratio of the average interparticle clearance to the wavelength is very often assessed by a formula derived for a periodical rhombohedral arrangement of monosized spheres[88]

$$\frac{c}{\lambda} = \frac{x}{\pi}\left(\frac{0.905}{f_V^{1/3}} - 1\right). \tag{2.99}$$

Figure 2.14 (originally published by Tien and Drolen[95]) shows the range of particle volume fraction f_V, where scattering is dependent, as a function of the particle size parameter x. For nanoparticles, the clearance and the distance between the centers of the particles are practically equal. The position of the boundary between the independent and dependent regimes almost does not change with the particles size parameter and therefore, for Rayleigh particles, the critical particle volume fraction of 0.006 is generally assumed.

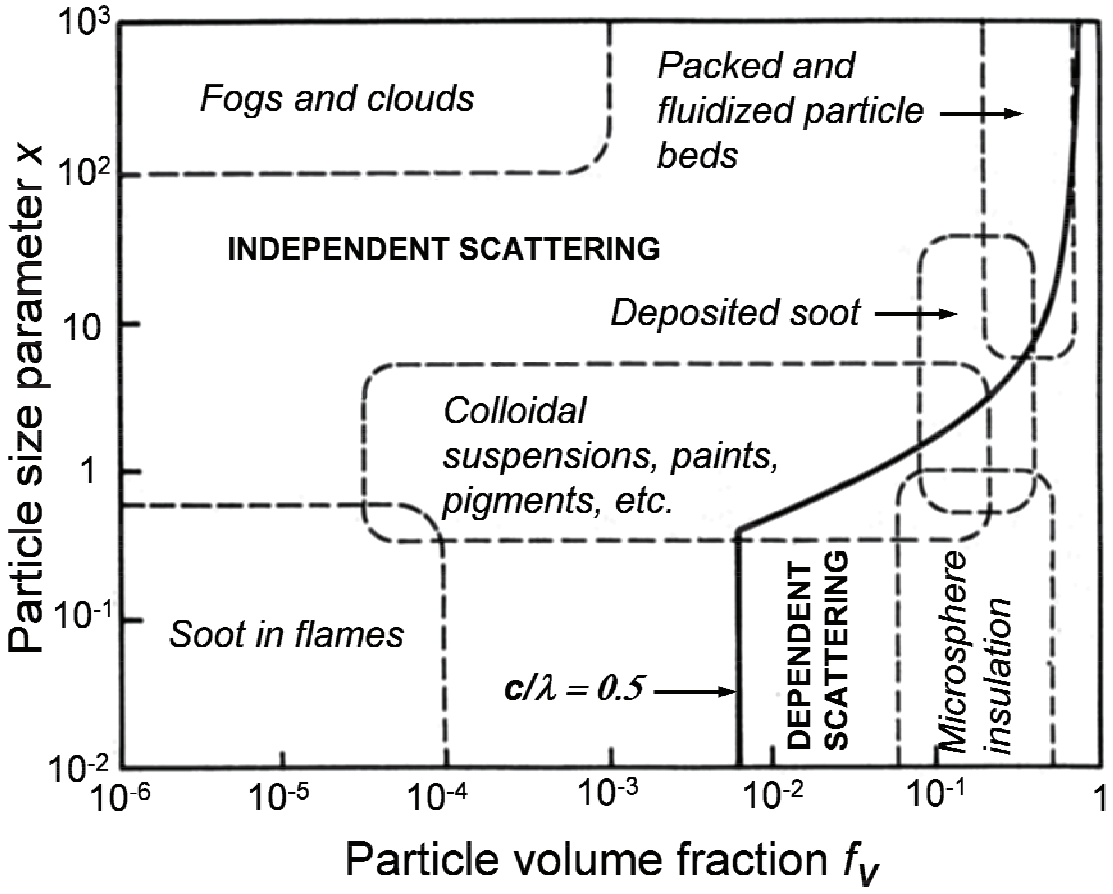

Figure 2.14 – Map of the independent and dependent scattering regimes.[95]

It should be noticed that the near-field effects are not accounted for in the map because they also involve an additional parameter – the refractive index of particles.[88,96] However, it was shown that the criterion given by Equation 2.98 approximately corresponds to the clearance, at which the near-field zones of scattering particles begin to overlap.[97]

The “dependent” effects described above result in a decrease of the effective scattering cross-section of particles. For small absorbing particles, the absorption efficiency factor was found to increase.[98,99] In the range of Rayleigh scattering, the contribution of absorption to the total attenuation dominates over scattering and therefore, the dependent attenuation efficiency of absorbing particles increases as well.[94,98,99]

Quantitatively, the problems of radiation transfer in the regime of dependent multiple scattering are usually solved by numerical simulations.[95] In several cases, analytical relations between the dependent scattering efficiency factor Q_{SCA}^{D} and independent (i.e., Mie) scattering efficiency Q_{SCA}^{M} could be obtained. For example, the

pioneering work by Hottel *et al.*[100] resulted in the following empirical expression for $c/\lambda > 0.092$

$$\log\log\left(\frac{Q_{SCA}^{M}}{Q_{SCA}^{D}}\right) = 0.25 - 3.8\frac{c}{\lambda}, \tag{2.100}$$

which was verified for $x < 1$.[95] For the size parameter $x \to 0$, an analytical relation between Q_{SCA}^{D} and Q_{SCA}^{M} could be derived for the Percus-Yevick hard-sphere model[95]

$$\frac{Q_{SCA}^{D}}{Q_{SCA}^{M}} = \frac{(1-f_V)^4}{(1+2f_V)^2}. \tag{2.101}$$

An approximate expression for the dependent absorption efficiencies Q_{ABS}^{D} in the limit of Rayleigh particles (i.e., $x \to 0$) was identical for several different models[98]

$$Q_{ABS}^{D} = 4x\,\mathrm{Im}\left(\delta\frac{n_R^2-1}{n_R^2+2}\right), \tag{2.102}$$

where

$$\delta = \left[1 - \frac{n_R^2-1}{n_R^2+2}f_V\right]. \tag{2.103}$$

Recently, it was shown that changes of the effective refractive index of a nanoparticulate medium should be taken into account when modeling the radiation transfer with dependent absorption and scattering.[99] A turbid medium filled with particles much smaller than the wavelength of light acts upon photons which traverse it, as an optically homogeneous medium with a refractive index determined by the refractive indices of the constituting media and the particle volume fraction. From this point of view, the influence of the volume concentration of nanoparticles on the effective refractive index can be considered as a further effect of dependent scattering and absorption.

Assuming a substantial number concentration *N* of nanoparticles in the vacuum (there should be many nanoparticles in a sphere with a radius equal to the wavelength of light), it can be related the effective refractive index n_{EFF} by the *Lorentz-Lorenz equation*[86] also known as the *Clausius-Mossotti relation*[101]

$$\frac{4\pi\alpha}{3}N = \frac{n_{EFF}^2-1}{n_{EFF}^2+2}, \tag{2.104}$$

where *N* is the number concentration of particles and α is the polarizabilty of the nanoparticles. The polarizability defines a dipole moment of the Rayleigh particles induced by an external electric field and can be used to describe their scattering. Alternatively, the effective refractive index can be derived from the volume concentration of particles f_V and their refractive index n_P

$$\frac{n_{EFF}^2 - 1}{n_{EFF}^2 + 2} = f_V \frac{n_P^2 - 1}{n_P^2 + 2} \ . \qquad (2.105)$$

For particles dispersed in a medium with refractive index n_A it becomes[102]

$$\frac{n_{EFF}^2 - 1}{n_{EFF}^2 + 2} = f_V \frac{n_P^2 - 1}{n_P^2 + 2} + (1 - f_V)\frac{n_A^2 - 1}{n_A^2 + 2} . \qquad (2.106)$$

In many cases however, a simplified expression below is applied[101,103]

$$n_{EFF} = f_V n_P + (1 - f_V) n_A . \qquad (2.107)$$

2.3.3d. Influence of particle size on emission of luminescence

As we have seen in the previous sections, both absorption and scattering of light by phosphor particles are strongly affected by the ratios of the particle size and interparticle distance to the wavelength of the incident light (the same applies to any particles or droplets). How do the particle size and packing density influence the process of light emission by the particles of doped dielectrics? According to Equations 2.1 and 2.2, the quantum efficiency of a phosphor is determined by the relation between the radiative and non-radiative contributions to the decay times of the excited states. There are several ways in which these parameters may be affected by the size of phosphor particles, and the mechanisms involved for particles with a size exceeding the wavelengths of emitted light (*superwavelength range*) and for nanoparticles (*subwavelength range*) are quite different.

In the superwavelength size regime, the *radiative decay rate* of luminescence (i.e., the inverse of the decay time) can be modified by the Mie resonances. For idealized spherical particles, the spontaneous emission rate of the emitters oscillates due to coupling to the whispering gallery modes and interference in the radial modes.[104] When averaged over all positions of emitting ions in the sphere, it results in an extension of the decay time of luminescence for phosphor particles of decreasing size. A similar trend is expected for particles of other regular shapes.[105] For irregularly shaped particles, particles with rough (i.e., diffusely reflecting) surface, or for phosphors with non-negligible self-absorption of luminescence, this effect can be much less pronounced (if observed at all).

The non-radiative decay time in the superwavelength regime is determined almost exclusively by the technology-related issues as, e.g., chemical purity and crystallinity of the phosphor. This means that, if the non-radiative decay rate does not change or increases, the quantum efficiency of the phosphor can decrease. On the other hand, if the technology is advanced so as to minimize the probability of non-radiative decay of the excited states, thin phosphor screens made of sub-micrometer-sized phosphor powders, in general, can have the brightness of conventional phosphor screens. In order to achieve the maximum efficiency of phosphors with substan-

tially reduced particle sizes, a method of synthesis avoiding the milling step should be chosen. It was reported that the brightness of PDPs manufactured from the phosphor powder with the particle size decreased to below 1 μm could even slightly exceed that of the screens produced from a conventional phosphor powder.[106] At the same time, approximately 5 times less phosphor powder was needed.

Changes of the quantum efficiency and the luminescence decay time of doped phosphors are not pronounced much until they enter the size range of nanoparticles (i.e., < 100 nm). A further reduction of the size of phosphor particles usually has a profound effect on the performance of doped phosphors.

In the subwavelength size regime, the oscillations caused by the Mie resonances disappear and the radiative decay time becomes independent of the particle shape and the position of the emitter inside of the particle.[104] The decrease of the emission rate with decreasing phosphor particle size is mainly attributed to the changes of the effective refractive index of the particulate medium.[107] The radiative decay time of an excited ion embedded in a medium with a refractive index n can be expressed as follows[9,101]

$$\tau_R = \frac{1}{f(ED)} \frac{\lambda_0^2}{\left[\frac{1}{3}\left(n^2+2\right)\right]^2 n}, \qquad (2.108)$$

where $f(ED)$ is the oscillator strength of the electric dipole transition. In the case of nanoparticles, the effective refractive index n_{EFF} defined in the previous section (see Equations 2.104-2.107) should be used. Thus, it can be expected that for vanishingly small phosphor particles separated by large distances ($c > \lambda$, i.e., $f_V \to 0$) the radiative lifetime of electronic transitions can be increased from its bulk value by a factor of

$$\frac{n_P}{9}\left(n_P^2+2\right)^2. \qquad (2.109)$$

For the magnetic dipole transitions, Equation 2.108 should be replaced by [108]

$$\tau_R = \frac{1}{f(MD)} \frac{\lambda_0^2}{n^3}, \qquad (2.110)$$

i.e., the radiative lifetime of the nanoparticles could differ from that of the bulk phosphor by a factor of n_P^3.

Some authors have suggested that in the case of hypersensitive transitions of the lanthanide ions the increase of radiative decay time could also be caused by the changes of the crystal field, e.g., by a decrease of the odd parity crystal field component due to an increase of the lattice constant of the phosphor host material.[109] The increase of the lattice constant was also thought to affect the non-radiative contribution to the decay of the excited states through a decrease of the phonon density.[110]

However, it has been recognized that the phonon density of states in nanoparticles is primarily reduced due to confinement effects.[107]

At room temperature, the decay time of luminescence of conventional phosphors is dominated by the nonradiative relaxation (except for some special cases as that of the $^5D_0$ level of the europium ion). If the energies of involved phonons are assumed to be equal, the temperature-dependent multiphonon relaxation rate can be expressed by[107]

$$\frac{1}{\tau_{NR}} = C \exp\left(\frac{-\alpha \Delta E}{\hbar \omega_m}\right)\left[\frac{\exp(\hbar\omega_m / kT)}{\exp(\hbar\omega_m / kT) - 1}\right]^{\Delta E / \hbar\omega_m}, \qquad (2.111)$$

where $\hbar\omega_m$ is the maximum phonon energy of the lattice vibrations, ΔE is the energy gap between the populated state and the next low-lying state, k is the Boltzmann constant, T is the temperature, and C and α are empirical parameters characteristic for the particular crystals. In most practical cases however, the ion-ion interaction should also be taken into account. The inter-ionic energy transfer could substantially shorten the nonradiative decay time (by the effect of concentration quenching, see Section 2.1.2) and lead to non-exponential characteristics of the luminescence decay time.

In insulating hosts, the excited state can migrate between the activator ions due to resonant energy transfer or phonon-assisted energy transfer processes.[107] Lattice stresses and defects cause slight variation in the energy levels of the embedded ions, thereby decreasing the probability of the resonant energy transfer. The phonon-assisted energy transfer is a predominant mechanism of migration of electronic excitation.

In nanocrystals, the phonon density of states becomes discrete and the low-energy acoustic phonons are gradually eliminated with decreasing particle size.[107] The efficiency of the phonon-assisted energy transfer is reduced. As a result, concentration quenching, sensitization of luminescence, cross relaxation, upconversion (*anti-Stokes luminescence*), and other processes in nanophosphors, which rely on participation of phonons, can significantly differ from those of the bulk phosphors.[107,110,111] The resonant energy transfer is also inhibited for particles which are smaller than 40 nm.[111]

The increase of the nonradiative lifetime of luminescence due to restricted energy transfer should favorably influence the overall quantum efficiency of conventional downconverting phosphors by postponing the onset of the concentration quenching. However, nanophosphors are usually significantly less efficient than their micrometer-sized counterparts.[5,107] The main obstacle for achieving the performance of bulk materials is constituted by the increased specific surface area of nanoparticles (i.e., by large values of surface-to-volume ratio).

In the presence of migration of excitation, the non-radiative relaxation rate is determined not only by the efficiency of the inter-ionic energy transfer but also by the concentration of lattice defects acting as emission quenchers. The particle surface itself should be considered as a distortion of the crystalline structure. Atoms within several lattice constants from the surface are displaced due to the *surface reconstruction*, and *dangling bonds* are often terminated by chemical species with high phonon frequencies (e.g., OH-, CO_3- or NH-groups) adsorbed from the ambient atmosphere.[5,107,112,113] The phonon spectra of nanoparticles are further modified by the introduction of *surface phonon modes*, which are localized at the interface with the surrounding medium and can provide new channels for non-radiative relaxations.[114] For nanoparticles dispersed in solvents, polymers, or glasses, the effect of size confinement leading to the inhibition of energy transfer does not play any significant role and the nonradiative decay time of luminescence is usually shorter than that of the same particles not embedded in any medium.[107] All these effects generally referred to as *surface quenching effects* become more pronounced with decreasing phosphor particle size and may dramatically change the dynamics of the luminescence emission of ultrafine phosphor powders.

Obviously, it is desirable to have a means to suppress the surface quenching. A simple strategy was proposed, which allows an improvement in the quantum efficiency of nanophosphors. A thin shell of undoped host material or some other dielectric with possibly low maximum phonon frequency and similar lattice constant has to be grown around each nanoparticle. The external layer efficiently reduces the energy transfer to the quenching centers at the surface.[5,107,115] The same method has been successfully applied for semiconductor quantum dots with high quantum yield.[107] It should be noticed that “finishing” of the surface of phosphor particles is sometimes also used for conventional micrometer-sized phosphors in order to improve their maintenance or stability in suspensions.[116]

The most important difference between the luminescent properties of dielectric nanoparticles doped with lanthanides and those of semiconductor quantum dots is the absence of the effects of quantum confinement in the former case. Characteristic luminescence results from electron transitions inside single impurity ions, which are strongly localized (this is especially true for transitions between 4f-levels of rare earth ions). As a result, the positions of the energy levels participating in radiative transitions hardly change even for nanophosphors with particle sizes well below 10 nm.[5,107] This is also the reason why the terms *nanophosphors* and *quantum dots* should not be used interchangeably. The first one is appropriate for ultrafine powders of insulating materials, which emit light due to the characteristic luminescence of the dopants, whereas the second one implies bandgap luminescence.

2.3.3e. Non-optical effects of reduced particle size

Not only the optical properties of phosphors are modified by the downscaling of phosphor particle size. There are several further particle size effects, which can either have implications for the technology of manufacturing or indirectly influence the performance of the powder screens. For example, the decrease of the particle size can lead to the lattice softening (i.e., increase of the lattice constant), which is thought to be one of the possible reasons for the reduced emission rates of luminescence in nanoparticles.[109,110,112]

The increase of the surface-to-volume ratio affects the thermodynamics of the phase transformation. The *Gibbs-Thomson effect* favors crystallization of nanoparticles in high-pressure polymorphs due to additional hydrostatic pressure P [117,118]

$$P = \frac{4\gamma}{\phi}, \qquad (2.112)$$

where γ is the surface energy (value of 1.5 J/m^2 is typical for many ceramic materials) and ϕ is the size of nanoparticle. More generally, it can be stated that reduction of the particle size decreases the temperature of phase transformation.[103] Melting points of nanoparticles are lower than those of the bulk substances.[103,119] In addition, it can result in a particle size limit for crystallization of some ceramic hosts (e.g., 8 nm for Al_2O_3).[103]

The contact mechanics of solid particles undergoes major changes when their size decreases. For sub-micrometer-sized particles, the adhesive forces can exceed other common forces by orders of magnitude. As a result, fine and ultrafine particles firmly stick to any surface they contact.[47] Furthermore, such particles become *cohesive*, i.e., they tend to agglomerate with each other. In many cases, this is an unwanted effect. For example, clustering of nanoparticles dispersed in transparent matrices can cause a dramatic increase in light scattering.[103] Agglomeration and large interparticle frictional forces are also responsible for the extremely low filling fraction of a *random loose packing* of fine and ultrafine powders[120] as well as for low density of compacted nanopowders (< 45 % of the theoretical values).[121]

The size of phosphor particles directly influences their stability in colloidal suspensions. A particle in a liquid of lower density settles down with a velocity that is proportional to the square of its size (*Stokes law*).[47] For nanoparticles, this velocity becomes extremely small. This has a strong impact on the technology of phosphor screens.

3. Manufacturing of advanced phosphor screens

3.1. Challenges of deposition of phosphors with decreased particle size

Commercial phosphors are usually manufactured by the *solid-state reaction* method[1] First, the high-purity materials of the host crystal, activator, and flux are blended, mixed, and then fired in a container. As the product obtained by firing tends to agglomerate, it is crushed, milled, and then sorted to remove coarse and excessively crushed particles. The particles prepared by this method usually have unintentionally irregular shapes and sizes in the range of several micrometers. In some cases, the product needs surface treatment.

Many research groups all over the world are currently investigating alternative methods for phosphor powder synthesis in the sub-micrometer and nano-range, *e.g.*, various realizations of *chemical precipitation*,[1,122–124] *combustion synthesis*,[125,126] *sol-gel methods*,[127–129] *pulsed laser deposition*,[130] *laser-assisted gas condensation*,[131] *ultrasonic spray pyrolysis*,[132–134] and *flame spray pyrolysis.*[118,135–137] As a next step towards practical application of phosphors with decreased particle size, optical performance of screens and coatings made of the new materials should be investigated. The choice of the screening technique can be crucial because it affects both the optical and mechanical properties of phosphor coatings.

The most widely used method for depositing flat monochrome screens is *gravitational settling* of a suspension of phosphor particles in a solution containing a binder[1,6,74,138] Solutions of potassium silicate buffered by barium nitrate or barium acetate have been predominantly used over the last decades. However, for particles between 1 μm and 5 μm, a centrifugal force should be applied in order to reduce the settling time and to increase the packing density. In addition to the long duration of the procedure, the unevenness in the screen thickness, due to the subsequent steps of decantation and drying of the phosphor coating, is also a drawback of this method.[74] Excessive amounts of silicates (acting as a binder) should be avoided as they deteriorate the ruggedness of the phosphor.[6] In the case of electron beam excitation (CRTs, FEDs), the silicate can act as an insulator and thereby accelerate the ageing effects (so-called Coulomb degradation or burning). For that reason, the settling solutions for the monochrome CRT production usually contain only about 0.2 wt% of the binder.[139]

The use of organic polymers instead of “liquid glass” has been proposed recently[70,140] Several acrylic compounds doped with commercial lamp phosphors were tested for application in UV-enhanced CCD image sensors. Authors claimed 350 % improvement of the quantum efficiency of the CCDs at 265 nm, but there are two considerations regarding this method. First, the chosen acrylic resins were transpar-

ent only down to 255 - 225 nm and they cannot be applied at shorter wavelengths in the UV-range, which can be necessary in certain applications (the same applies to gelatin used as a binder in preparation of SEM and TEM viewing screens[141,142]). Second, the deposited coatings demonstrated 50 % degradation of the conversion efficiency within the first 3 hours of their exposure to UV-light, which is most probably related to the problem of "yellowing" often encountered with the epoxy encapsulants of phosphor-converted white LEDs.[143,144]

Electrophoretic deposition (EPD) is often used with fine particle size phosphors[74,138,145,146] and nanophosphors.[147,148] In this method, the phosphor in liquid suspension is attracted to an immersed electrode. Phosphor particles can be electrically charged by introduction of charging ions (*e.g.*, Mg^{2+}) to the suspension liquid (*e.g.*, isopropyl alcohol); the particles will then deposit onto the electrode of the opposite charge. Postdeposition samples are then dried and baked. Smooth, dense phosphor layers with exceptional resolution and low noise can be deposited by EPD, although some authors admit that brightness of settled screens is higher[145] The adhesive strength of EPD-coatings is much weaker than that of the ones deposited by sedimentation.[146] A further disadvantage of electrophoresis is the necessity for a conductive substrate (*e.g.*, ITO glasses).

Thick layers of nanophosphors could be deposited with the *Doctor Blade method*.[149] *Dip-coating* combined with sol-gel chemistry can be successfully implemented.[129] Application of *spin-coating* was also reported.[150]

All abovementioned techniques have common disadvantages: they require several processing steps and include immersion of phosphor particles into liquids, which can introduce contamination (from charging species, dispersants, surfactants, etc.). The same applies to novel methods of deposition of nanoparticles developed recently: *layer-by-layer assembly*,[151,152] *Langmuir-Blodgett technique*,[153] and *ink-jet printing*.[154]

There exist methods which do not involve the use of binders and do not require wet processing of powders. For example, in *electrostatic deposition*[138] the dry phosphor and the substrate are oppositely charged and phosphor particles deposit on the glass, giving up their charge. The method is useful for applying smooth, fine particle coatings to the inner surface of spherical bulbs and cylindrical or spiral tubings. The dry procedure reduces the problem of coagulation of particles, however, since no binder is used, the adhesion and cohesion of conventional (micrometer-sized) phosphor particles are relatively poor.[138] The situation would change if nanophosphors were used. As discussed in Section 2.3.3e, cohesive properties of solid particles undergo drastic changes when the particle size decreases below 1 μm. Nanoparticles are extremely cohesive and tend to build agglomerates. On the one hand, they would not require any binder for a strong adhesion to the substrate. On the other hand, it is difficult to avoid agglomeration of dry powders prior to the deposi-

tion of phosphor screens so that the advantages of decreased particle size cannot be fully utilized.

Excessive premature agglomeration of fine and ultrafine powders may be precluded by combining processes of synthesis and film deposition in a single technology step. By this method, all intermediate steps are excluded (i.e., dispersion in liquids is not required) and the deposition of phosphor coatings can be performed very rapidly. This approach is exploited in laser-assisted nanoparticle synthesis (e.g., electrostatic-directed deposition[155]), plasma-based coating methods (microwave plasma synthesis[156] and hypersonic plasma particle deposition[157]), and in various spray-based deposition techniques.

3.2. Deposition of phosphor coatings by spray-based methods

Spraying was first applied for deposition of phosphor powders prepared by other methods. Two related methods, dry and wet spraying, were reported in 1949.[138] In *dry spraying*, a binder is spread over the substrate (e.g., potassium silicate solution) and dried to tackiness. A fine spray of dry phosphor powder is then blown from a gun onto the tacky surface. The screen is dried and air baked. In *wet spraying*, the phosphor should be suspended in a volatile medium (e.g., acetone).[138] Obviously, these methods would not solve the problem of premature agglomeration of cohesive phosphor powders.

In 1966, a novel method of *spray deposition* of inorganic films was reported[158]: inorganic films were deposited by spraying aqueous solutions of appropriate reagents over a heated substrate. The chemical transformation occurs directly on the surface of the substrate. Numerous modifications of this method have been widely used over the past years, e.g., for fabrication of solar cells and optoelectronic devices. Phosphors can also be deposited in this way, e.g., ZnS:Mn,[159] Y_2O_3:Eu,Tb,Tm,[160] $ZnWO_4$ and $CdWO_4$.[161] However, this method produces continuous films rather than powder coatings.

Chemical transformation (most often these are reactions of thermal decomposition or *pyrolysis* of chemicals dissolved in a *precursor solution*) does not necessarily have to occur at the surface of the hot substrate. An electrical furnace or a flame can be used as a source of heat for decomposition of precursors. In the former case, i.e., when droplets of a precursor solution are pyrolysed while passing with a gas stream through an oven, the process of synthesis of phosphor particles is generally referred to as *spray roasting* or *aerosol decomposition*.[162] *Ultrasonic nebulizers* are very often used as droplet generators in setups for production of submicrometer-sized phosphor powders; the corresponding process is conventionally termed *ultrasonic spray pyrolysis* (USP). Many phosphor hosts were successfully obtained with this method, e.g., YAG,[163] Y_2SiO_5,[164] Gd_2O_3,[165] $BaMgAl_{10}O_{17}$,[166] Zn_2SiO_4,[167] ZnS and CdS.[168] USP is

not applied for deposition of coatings. Produced particles are usually collected with bag filters or electrostatic precipitators.

Flame spray pyrolysis (FSP) is a general term used for any spray process, where the high-temperature environment for chemical reactions is provided by heat released by a flame. More specifically, one distinguishes between FSP of flammable precursors (i.e., when a pilot flame is used to ignite a spray flame) and FSP of precursors that are not combustible themselves (e.g., aqueous), where heat is generated exclusively by a flame from external flame source. The latter process is sometimes termed *flame-assisted spray pyrolysis* (FASP). Different methods of synthesis of inorganic powders based on FSP can be further classified into processes of direct *droplet-to-particle conversion* (DPC) and *chemical vapor condensation* (CVC) processes. The droplet-to-particle conversion occurs when the precursor solute is not volatile. In such a case, the final weight of each particle corresponds to the initial size of the droplet it was obtained from and the concentration of the precursor solution. The CVC involves combustion of volatile precursors which evaporize, react in the gas-phase, and condensate to produce nanoparticles of the desired compounds. FSP (including FASP) is widely used for synthesis of various aerosols in commercial quantities, such as fumed silica, pigmentary titania, and superconducting ceramics. Solid particles with a size in the range of 1 nm to about 1 μm can be obtained by these methods.[135,169] Latest reviews on FSP can be found in articles by Strobel and Pratsinis,[170] Teoh *et al.*,[171] and Pratsinis.[172] Numerous phosphors were prepared by FSP in research laboratories, e.g., $SrTiO_3$:Pr, Al,[173] $Sr_5(PO_4)_3Cl$:Eu,[174] $BaMgAl_{10}O_{17}$:Eu,[175] Y_2O_3:Eu,[176,177] Gd_2O_3:Eu,[178,179] Y_2SiO_5:Eu,[136] $Y_3Al_5O_{12}$:Ce.[180] Usually, powders are collected by filtering, electrostatic precipitation or thermophoresis.[135,181]

For the purposes of deposition of particulate coatings, a substrate can be placed directly into the flame. If volatile precursors are used, this could result in heterogeneous condensation of pyrolyzed compounds from the vapor-phase on the surface of the substrate. This film deposition technique, first published in 1993,[182] is called *combustion chemical vapor deposition* (CCVD). The environment required for CVD to occur is provided by the flame. No furnace, auxiliary heating or reaction chamber is necessary. The flame also heats the surface thus providing the conditions for surface reactions, diffusion, crystallite nucleation and growth. CCVD can be used to deposit a wide spectrum of materials in open atmosphere or low pressure conditions. The deposited coatings are mostly applied for catalysis and functionalization of surfaces as well as in fuel cells, lasers, and electronics. CCVD could also be used for deposition of phosphors (e.g., Zn_2SiO_4:Mn[183]) but it is not suitable for the investigation of the effects of phosphor particle size because this method usually produces solid films. For the same reason, well-known methods of thermal spraying (flame

spray, high-velocity oxy-fuel gas spraying, plasma spraying[184–186]) are not considered here.

Spatial separation of the reaction zone and the substrate to be coated can be advantageous for both DPC and CVC processes. High temperature of the flame is often required in order to obtain particles with improved crystallinity without any thermal post-treatment. If the deposition of a coating takes place outside of the flame, the substrate temperature can be decreased by allowing a larger distance to the flame. Such FSP-based coating techniques can be generally referred to as *flame aerosol deposition* (FAD), although several other terms can be found in literature, such as *direct nanoparticle deposition* (DND) used in fabrication of optical fiber preforms.[187,188]

The *in-situ* film deposition was reported in early works on FSP.[169,184,189,190] Currently, the main field of application of FAD is in the technology of optical fibers for telecommunication.[170] FAD-methods could also be applied for manufacturing of advanced gas sensors,[191–193] porous catalysts,[194,195] and battery electrodes,[196] as well as for deposition of anti-fogging films[197] and optical coatings.[198] However, the deposition of phosphor powder coatings by FAD has never been studied. This thesis is focused on application and further development of this method for deposition of advanced phosphor screens.

4. Experimental methods

4.1. FAD setup

As discussed in Section 3.2, flame aerosol deposition can be performed in several different ways. Particularly important is the difference between the processes based on droplet-to-particle conversion (DPC) and chemical vapor condensation (CVC). DPC-synthesis usually results in submicrometer-sized powders (100 nm < ϕ < 1 µm). In order to decrease the particle size, the concentration of the precursor solution can be decreased. The production rate measured as total weight of powder produced in unit time would proportionally decrease. As a result, synthesis of nanopowders (ϕ < 100 nm) with DPC becomes highly impractical. Although decreasing the size of the droplets of the precursor solution could also be attempted, it appears much simpler to switch to CVC when nanoparticles are to be deposited by FAD. In this thesis, deposition of sub-micromer and nano-sized phosphor powder coatings was performed in two different FAD-setups (i.e., DPC- and CVC-based setups, respectively).

4.1.1. Droplet-to-particle conversion

The schematic view of the setup used for DPC-based FAD is presented in Figure 4.1. It includes an ultrasonic nebulizer (U-3002-S, 1.68 MHz, Schulte-Elektronik GmbH) and a premixed air/propane burner. Droplets of precursor solution produced by the nebulizer were carried into the flame with an air current (1-3 l/min) through a flexible hose. Usually, an electrically heated metal hose was used. The flow rate of propane varied between 3-5 l/min. During the deposition, fused silica slides (with a diameter of 30 mm and a thickness of 1 mm, Suprasil, Aachener Quarz-Glas Technologie Heinrich) were fixed on a water-cooled radiator directly above the nozzle of the burner at the distance of approximately 7 cm.

The adiabatic temperature of the stoichiometric propane/air flame is about 2000℃. [199,200] The actual temperature of the flame was measured with a type-B (Pt/Rh) thermocouple.

4.1.2. Chemical vapor condensation

Phosphor nanoparticles were prepared as follows. First, nitrates of rare earths were dissolved in ethanol. Afterwards, 2-ethylhexanoic acid was added so that a 0.5 M solution of the nitrates was obtained. The process parameters for obtaining yttria nanoparticles were adopted from the work on FSP-synthesis of Y_2O_3:Eu

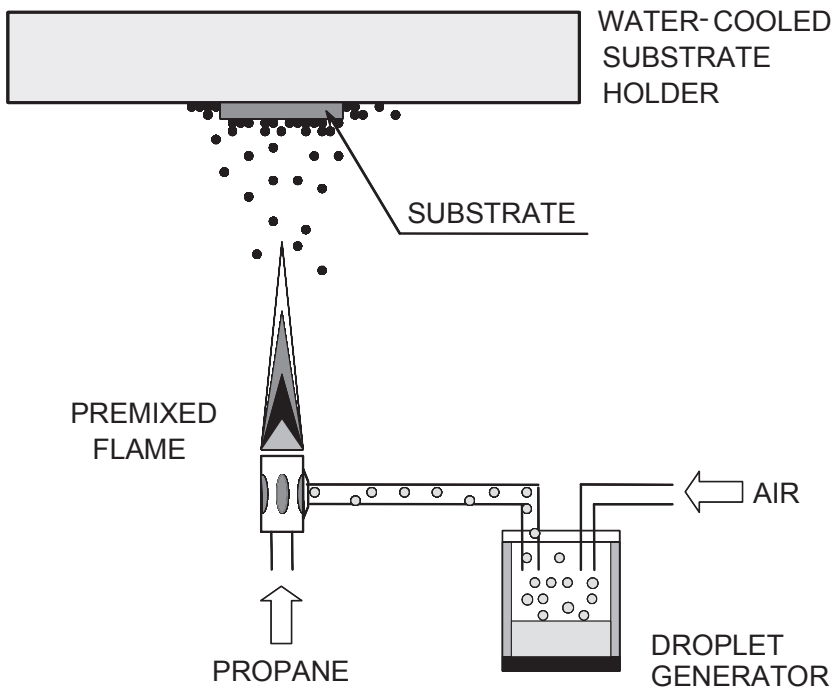

Figure 4.1 – Schematic view of the FAD-setup based on DPC.

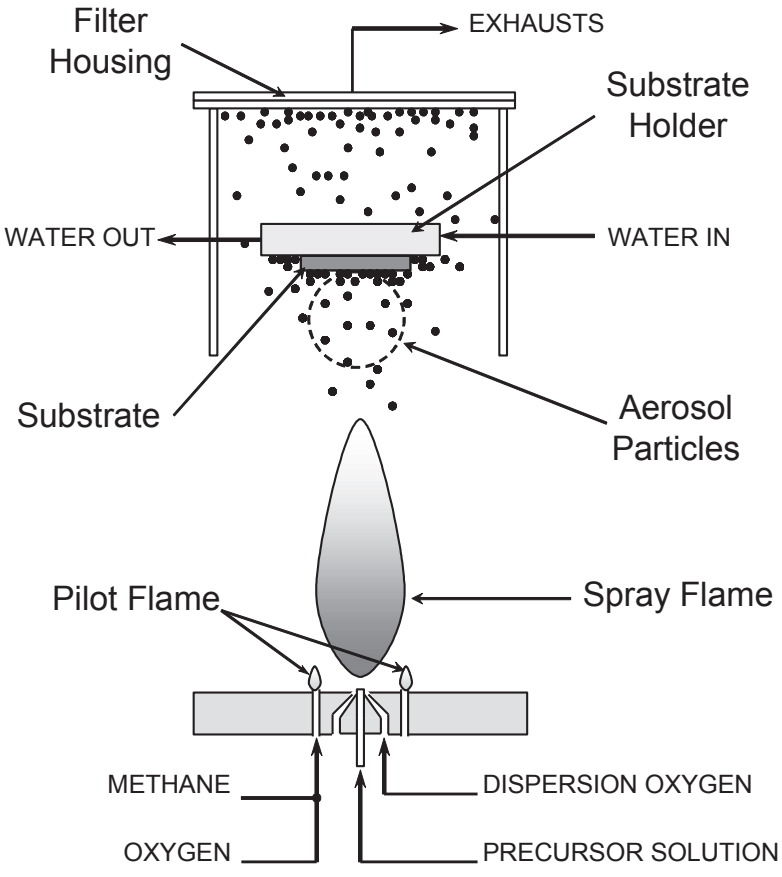

Figure 4.2 – Schematic view of the CVC-based FAD-setup.

phosphor.[137] The flammable liquid precursor was fed into a CVC FSP-unit (Figure 4.2) with a syringe pump at the rate of 11.7 ml/min (if not mentioned otherwise) through a capillary of an outside-mixing two-phase nozzle. The precursor was dispersed with oxygen (at the rate of 3 l/min, with a constant pressure drop of 1.5 bar over the nozzle). The liquid spray was ignited with a methane/oxygen pilot flame (1.4 and 2.8 l/min, respectively).

For screen deposition, the FSP-unit was combined with a water-cooled substrate holder[191] placed 25 cm above the nozzle (directly above the flame tip; Figure 4.2). The temperature at the location of the substrate was measured with a type-K thermocouple. Powder samples were collected downstream of the substrate holder (50 cm above the burner) with a vacuum pump (Vacuumbrand, RE 16) on water-cooled glass-fiber filters (GF/D Whatman, 257 mm diameter).

All experiments with CVC-based FSP/FAD were performed at the Particle Technology Laboratory at the Swiss Federal Institute of Technology (under co-supervision of Prof. S.E. Pratsinis).

4.2. Choice of materials

4.2.1. Phosphors

4.2.1a. Y_2O_3:Eu

Yttrium oxide doped with europium ions (Y_2O_3:Eu) was selected as a standard test material in this thesis due to its superior luminescent properties and simple chemical composition. This phosphor is one of the best studied and extensive literature is available on the properties of Y_2O_3:Eu for any size of particles from bulk single-crystalline samples to nanopowders.

Yttrium oxide host usually crystallizes in cubic bixbyite structure (space group $Ia\bar{3}$) with a lattice constant of 1.0604 nm,[201,202] which corresponds to a gravimetric density of 5.03 g/cm^3. Cubic modification of yttria has a refractive index of 1.9 in the visible range and is highly transparent in the spectral region from 250 nm (the fundamental absorption edge is at 5.6 eV) to 9.6 μm.[203] Yttria powders produced at high temperatures can have monoclinic structure (space group $C2/m$). For Y_2O_3:Eu produced by conventional solid-state reaction, the monoclinic phase is obtained above 1700℃. [176] Bulk yttria melts at a temperature of 2430℃ [201] and therefore belongs to the refractory oxides.

Europium ions doped into the Y_2O_3 crystal substitute yttrium ions and introduce electronic states in its bandgap. The unit cell of the host contains 16 formula units, i.e., 32 Y-sites. There are two distinct sixfold oxygen-coordinated cation sites in the Y_2O_3 lattice, one is noncentrosymmetric (Y1, point group C_2) and another one is

centrosymmetric (Y2, point group C_{3i}). In the unit cell there are 24 Y1-sites and 8 Y2-sites, which could be occupied by Eu-ions with the same probability.[204,205] At room temperature, radiation from Eu(C_2) dominates in the spectra of luminescence not only because of the larger number of C_2-sites but rather due to the fact that the noncentrosymmetric environment relaxes the Laporte selection rule (see Section 2.1.4) and as a result of energy transfer between the two sites.[3]

The emission and excitation spectra of photoluminescence of a standard commercial Y_2O_3:Eu phosphor are shown in Figure 2.1. From the charge transfer states the excitation energy relaxes to the ^5D_j excited states of the $4f^6$ configuration of Eu^{3+}. Theoretically, line emission could be observed from the $^5D_2$ (blue-green), $^5D_1$ (green-orange), and $^5D_0$ (red) levels to the ^7F_i ground term levels (see Figure 2.5). However, normally less than 1 % of the emitted photons originate from the $^5D_1$ excited state, and even less from $^5D_2$. The dominant emission is from the lowest excited state $^5D_0$, particularly in the $^5D_0$-$^7F_2$ hypersensitive transition at 611 nm.[3] The emission due to the magnetic dipole transition $^5D_0$-$^7F_1$ is insensitive to the site symmetry, whereas the emission peaks due to the electric dipole transition of $^5D_0$-$^7F_2$, induced by the lack of inversion symmetry at the Eu^{3+} site, is much stronger. The exponential decay time constant of emission due to the $^5D_0$-$^7F_2$ transition is on the order of 1–1.4 ms.[206,207]

The color of the luminescence of Y_2O_3:Eu shifts from yellow to red with an increase in activator concentration and/or in the phosphor temperature. The color shift is a function of activator concentration due to the difference in the concentration dependence (CD-)curves of the $^5D_2$, $^5D_1$, and $^5D_0$ luminescence in the Eu^{3+} spectrum. The luminescence lines quenched in the order $^5D_2$, $^5D_1$, and $^5D_0$ as the activator concentration increased.[50] Typical CD-curves for $^5D_0$-^7F transitions can be found in Figure 2.2.

The quantum efficiency of Y_2O_3:Eu is near unity for $\lambda \approx 200$ nm (and could approach the value of 2 for wavelengths shorter than 100 nm).[208] When excited at $\lambda = 254$ nm (in the charge transfer band), it approaches 95 %.[3] At longer wavelengths, the efficiency decreases. In some cases, it is possible to improve the performance of the phosphor in a wavelength range where its efficiency is insufficient, by introduction of sensitizers. For example, co-doping with bismuth ions increases the light output of the Y_2O_3:Eu phosphor for excitation at 350 nm.[123] Its quantum efficiency at 254 nm can also be improved by co-doping with gadolinium.[50]

4.2.1b. $Y_3Al_5O_{12}$:Tb

If light emission with spectral or transient characteristics other than those of the Y_2O_3:Eu phosphor is desired, other material systems should be considered. In the simplest case, this could be achieved by doping the same host with a different

activator. However, usually the choice of dopants which have substantial quantum efficiency in any particular host is very limited. For example, although practically all rare-earth ions in Y_2O_3 emit light in the visible, UV- or IR- range,[1,50] doping with Eu-ions produces by far the most efficient phosphor.[209] Therefore, generally the host material also has to be changed and synthetic route should be adjusted accordingly. Certain hosts may require substantially more sophisticated processing.

Yttrium aluminum garnet (YAG) $Y_3Al_5O_{12}$ was used as a secondary host material in DPC FAD experiments. YAG can be doped with various rare earths and transition metals and is widely applied as a host compound due to its superior mechanical properties, low thermal expansion, high threshold for optical/cathode ray damage, and general chemical stability.[1,210,211] Its main application fields are in solid-state lasers (e.g., YAG:Nd), phosphor-converted white LEDs and scintillators (YAG:Ce), lamps and various display devices (e.g., YAG:Tb).

The most important concern about YAG-based phosphors is the difficulty of obtaining the pure phase material.[1,212] Along with YAG, there are two further stable compounds in the Y_2O_3-Al_2O_3 phase diagram: monoclinic $Y_4Al_2O_9$ (YAM) and $YAlO_3$ with the perovskite or hexagonal structure (YAP or YAH, respectively).[180,213] YAM is the easiest to form, whereas other phases are somewhat more difficult to obtain. In the solid-state synthesis, YAM appears first, YAP second, and YAG last, as the firing temperature increases. Accordingly, local deviations from stoichiometric ratios are very probable, so that YAM and YAP are often present in YAG-powders as by-products. Single-phase YAG can be obtained by firing at temperatures as high as 1500℃, even if BaF_2-flux is used.[1] It is possible to obtain phase pure YAG at much lower temperatures (e.g., 800-900℃) by choosing alternative synthesis methods.[211,212]

The crystalline structure of YAG has a body-centered cubic lattice (space group $Ia3d$) with a lattice constant of 1.200 nm.[210] Its theoretical density is 4.55 g/cm^3.[214] YAG has an average refractive index of 1.83 in the visible range[215] and its transparency range spans from 200 nm (the fundamental absorption edge is at 6.73 eV) to at least 4.1 μm.[216] The melting temperature of YAG is 1940℃.[217] At the same time, it is one of the most creep-resistant refractory ceramic materials,[214] which is attributed to its complicated crystalline structure. The unit cell of the YAG crystal lattice contains 160 atoms.[210] The Y ions occupy 24 sites which are dodecahedrally coordinated to eight O atoms (D_2). There are two different sites for Al: 16 sites with octahedral point symmetry (C_{3i}) and 24 sites with tetrahedral point symmetry (S_4). Rare earth dopant ions usually substitute Y-ions.[218,219]

FAD-produced yttrium aluminate powders were activated by terbium ions because characterization of the photoluminescent properties of YAG:Tb could be performed with the same equipment as used for Y_2O_3:Eu phosphor. First, as opposed to

YAG:Nd, YAG:Tb emits in the visible range. Second, as opposed to YAG:Ce, YAG:Tb can be excited with UV-radiation at 254 nm.

Spectra of luminescence of Tb^{3+} also consist of many lines due to ^5D_j-^7F_i transitions (see Figure 2.5). Spectral distribution of emission significantly changes with an increase of Tb-concentration due to cross-relaxation, which quenches emission from the $^5D_3$ level.[1] In nearly all hosts containing a few mol.% of Tb, the most prominent line is due to the $^5D_4$-$^7F_5$ transition at approximately 550 nm. This transition has the largest probability for both induced electric-dipole and magnetic-dipole transitions. Excitation spectra of Tb^{3+}-emission usually feature a broad band in the wavelength range 220-300 nm, which originates from the $4f^8 - 4f^7 5d^1$ transition. Spectra of emission and excitation of Tb^{3+} in YAG and other yttrium aluminate hosts can be found in literature.[1] Typical luminescence decay times for YAG:Tb are on the order of 4 ms.[211,220]

4.2.2. Raw materials and commercial reference samples

Stock solutions for DPC-FAD were prepared by dissolving chlorides or nitrates of yttrium, europium, gadolinium, aluminum, and terbium (99.9 %, purchased from MaTecK GmbH and Alfa Aesar) in deionised water. The overall concentration of the rare-earth ions in the precursor solution was varied between 0.01 and 0.5 M. The standard concentration was 0.2 M. Citric acid monohydrate (puriss., p.a., Sigma-Aldrich), ethylene glycol (p.a., Merck) and polyethylene glycols (ultra grade purity, Fluka) were used as additives in experiments on synthesis of phosphor particles with improved morphology.

Stock solutions for CVC-FAD were prepared as follows. First, nitrates of yttrium (99.9 %, ChemPur) and europium (99.9 %, Alfa Aesar) were dissolved in ethanol (EtOH, p.a.). Afterwards, 2-ethylhexanoic acid (EHA, 99 %, Riedel-de Haën) was added so that 0.5 M solution of yttrium and europium nitrates in a solvent composed of 50 vol.% EtOH and 50 vol.% EHA was obtained.

In order to compare the brightness of FSP-deposited coatings with commercial phosphor coatings, a series of samples was prepared by settling a purchased Y_2O_3:Eu phosphor powder (MaTecK GmbH, 4.5 % Eu, $\overline{\phi}_{SEM}$ = 4 µm) overnight in a solution containing 0.2 wt% potassium silicate and sodium bicarbonate (1 wt%). Brightness of luminescence of Y_2O_3:Eu nanophosphor powders produced by CVC-FSP was normalized to that of another commercial Y_2O_3:Eu phosphor (L 581, Osram GmbH, ϕ_{V50} = 4.8-6.2 µm).

4.3. Characterization methods

4.3.1. Morphology and phosphor particle size

Morphology of the FAD-deposits was investigated by scanning electron microscopy (SEM: LEO 1530 Gemini). The coating density was determined by weighing the substrates before and after the deposition. The porosity of the coatings was calculated from their apparent thickness (obtained from optical microscopy of cleaved samples) and coating density.

In order to calculate the average particle size of powders obtained by DPC-FAD, diameters of 250 particles were measured in each case; confidence intervals were estimated from the Student's t-distribution (on a logarithmic scale) by assuming log-normal PSD and a confidence level of 95 %.

The morphology of phosphor nanoparticles synthesized by CVC-FSP was observed by tunneling electron microscopy (TEM: CM30 microscope, acceleration voltage 300 kV). The elemental composition of the nanophosphor was investigated by energy dispersive X-ray spectroscopy (EDX) with an EDAX Pegasus system (installed into a scanning electron microscope Quanta 200 FEG, FEI). Estimation of the relative concentration of europium was performed by the standardless EDAX ZAF quantification method (implemented in the software available from EDAX) using Y-L and Eu-L lines. The specific surface area (SSA) of powders was measured by the Brunauer-Emmett-Teller (BET)-method (Micromeritics Tristar 3000). The BET equivalent diameter was calculated using the density of 5.3 g/cm^3 (obtained from XRD).

4.3.2. Crystallinity of phosphor powders

X-ray diffraction (XRD)-patterns were obtained by diffractometers Bruker AXS D8 Advance and Philips PW 1710 (40 kV, 40 mA, Cu Kα). The crystal size and weight fractions of cubic and monoclinic yttria phases in nanopowder samples were determined using the Rietveld fundamental parameter refinement (with the software TOPAS 3.0, Bruker).

Raman spectra were detected with a Jobin Yvon LabRam HR800 spectrometer (at 23℃, excitation by He-Ne laser, λ = 633 nm, 2 mW) and a Renishaw InVia Reflex Raman system equipped with laser sources with λ = 633 nm (He-Ne, 17 mW) and λ = 785 nm (laser diode, 300 mW).

4.3.3. Photoluminescence and attenuance

The photoluminescence of the phosphor coatings deposited on fused silica substrates was excited by a low-pressure mercury lamp (NU-8 KL, Konrad Benda) at the wavelength of 254 nm and measured (in the transmission mode) by a photospectrometer (Tristan 4, MUT GmbH). Screen brightness was determined by the amplitude of the main emission peak and then normalized to the highest brightness of the phosphor coatings deposited by sedimentation of the commercial Y_2O_3:Eu phosphor powder (coating density 2.0 mg/cm^2, see Section 4.3). During the first seconds of exposure to the UV-light, the intensity of emission from the FAD-deposited Y_2O_3:Eu coatings decreased by up to 5 % (most probably due to the formation of color centers, see Section 2.1.2) and then stayed constant. When not exposed, the brightness recovered approximately to its initial level. All values of PL-intensity in this thesis refer to the ones obtained after continuous excitation for several minutes. The PL excitation (PLE) spectra were measured with a fluorescence spectrometer (Jobin Yvon Fluorolog). Measurements of luminescence excitation spectra in the VUV-range were performed using the facilities of the SUPERLUMI station at HASYLAB (DESY, Hamburg) - room temperature, reflection mode, resolution of 0.32 nm by the primary 2 m monochromator in 15° McPherson mounting.[221] A correction for the incident photon flux was performed. Time-resolved fluorescence spectroscopy measurements were carried out at the Institute for Laser-Physics at the Hamburg University, Germany. A Nd:YAG laser with a frequency-doubled OPO (OPO-BBO LP 603, SOLAR LS) was used to investigate the decay time of the luminescence (excitation at a wavelength of approximately 260 nm, pulse duration 10 ns, repetition rate 10 Hz).

Photoluminescence of the nanophosphor powders (collected on the filter during CVC-FAD experiments) was examined with a Varian Cary Eclipse fluorescence spectrometer. The brightness of the luminescence was expressed by the intensity of the main emission peak (at λ = 612 nm) and normalized to that of the commercial Y_2O_3:Eu phosphor (see Section 4.3). Measurements of the PL-emission spectra were performed by exciting the phosphor with a Xe flash lamp at a wavelength of 254 nm. Each time, a sample of 100±10 mg of the phosphor powder was loaded into a powder cell and then pressed towards a quartz glass plate which served as the front window. The compaction of phosphor to a volumetric porosity of 0.87±0.02 created a powder tablet, which could withstand further handling. Before performing measurements, the front window of the cell was removed in order to eliminate the influence of the Fresnel reflection of light emitted by phosphor on the interface with the glass. Photoluminescent decay curves were registered and fitted by the “Cary Eclipse” software supplied by Varian in order to extract exponential decay time constants.

Attenuance spectra of the deposited coatings were taken with a Perkin-Elmer UV-Vis-NIR spectrometer Lambda 19 and a Varian Cary 500 UV-Vis-NIR spectrometer. Each coating activated with either Eu- or Tb-ions was measured twice, once with and once without a longpass optical filter (GG-455) installed between the sample and the detector. Any significant signal in the UV-range observed in the spectra taken with the filter was due solely to the photoluminescence, and this contribution was subtracted from the original attenuance spectra (i.e., those taken without the filter). In this way, the attenuance spectra could be corrected for the emission of photoluminescence. At the same time, the spectra taken with the filter could be considered as T-mode photoluminescence excitation spectra in the range where the primary beam from the lamp is blocked.

5. FAD based on droplet-to-particle conversion

5.1. Deposition of Y_2O_3:Eu coatings from aqueous solutions without additives

5.1.1. General quality of the deposited screens

The first experiments showed that DPC-FAD does yield phosphor coatings on quartz plates. Figure 5.1a represents a microscopic view of one of the deposited samples. For comparison, a screen consisting of settled commercial phosphor particles is shown in Figure 5.1b. The thickness of the phosphor coatings is expressed as a coating density of phosphor. FAD-deposits of pure and Eu-doped yttria with thickness of up to 2.4 mg/cm^2 were successfully obtained. Volumetric porosity derived from the geometric thickness of the coatings deposited from 0.2 M and 0.5 M precursor solutions was found to be 92.1 % ($\pm$ 1.5 %). This value of the total porosity was obtained by comparison with the theoretical density of single-crystalline Y_2O_3:Eu, i.e., it includes both the porosity of the phosphor particles and the space between the particles.

The wiping resistance of the layers was rather poor: the coatings could be destroyed with a light touch on the coated surface. On the other hand, they did not suffer any damage when the samples were held upside down and there was no noticeable change in the specific weight of the coating when the coated plate (0.45 mg/cm^2) was dropped on a solid surface either freely from a height of 20 cm or from a height of 1 m when put in a single substrate carrier.

During experiments with chloride-based precursor solutions, homogeneity of the screens was disturbed by the formation of agglomerates of phosphor particles and large single particles of a non-luminescent substance, which decomposed overnight in the ambient air and flawed the screen with visible defect spots (Figure 5.2). The latter problem could be attributed to chloride-based precursors. The products of decomposition of chlorides could contain YCl_3:Eu, YOCl:Eu or Y_2O_3:Eu and various mixtures of these, depending on the reaction temperature. The maximum measured flame temperature was about 1500-1550℃ (2.5-3 cm above the nozzle, on the central axis of the burner). However, all flame-based deposition methods are generally prone to large temperature fluctuations due to the vast temperature gradients present in the flame.[184] Some of the particles probably did not completely react during the residence time in the flame, so that the YCl_3:Eu could have been deposited onto the substrate. When the propane flow rate was equal to 5 l/min, the temperature on the surface of the substrate (fixed at 7 cm above the burner barrel) reached 1100-1150℃ in the middle (at the central axis of the flame) and decreased towards the edge of the substrate to 900-950℃. When the flow rate of propane was 3 l/min, the

Figure 5.1 – SEM pictures of a) FAD-deposited Y_2O_3:Eu (from the precursor solution with the overall concentration of rare-earth ions of 0.2 M); and b) sedimented commercial Y_2O_3:Eu phosphor.

corresponding temperatures on the surface of the substrate decreased by 250-300℃. It is possible that some non-decomposed prec ursors could remain in the coating. YCl_3 is very hygroscopic and in ambient air turns into the hexahydrate.[222] This was supported by the increased content of chlorine detected by the EDX-analysis of

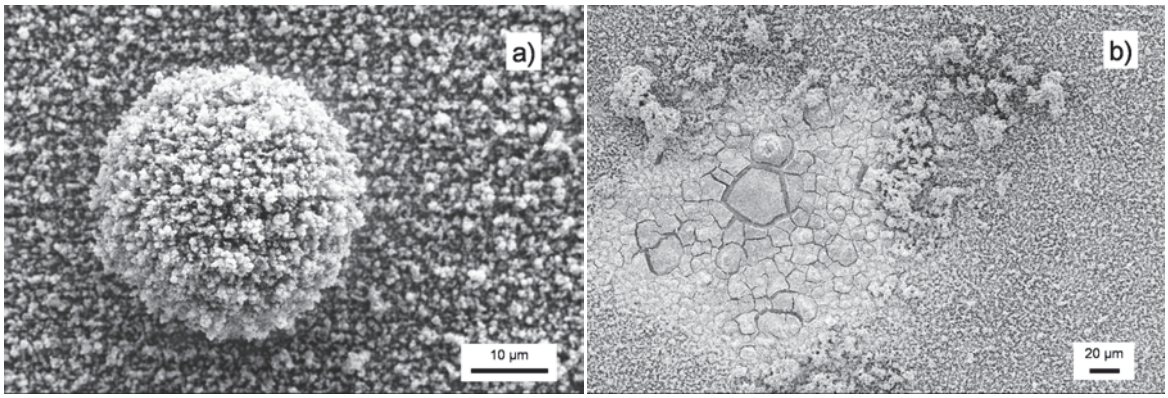

Figure 5.2 – Defects in the FAD screens: a) secondary particles; b) chlorine-rich spots.

the spots such as the one shown in Figure 5.2b. The problem was successfully solved by using nitrate-based precursor solutions instead of chlorides. At the same time, the formation of large agglomerates depicted in Figure 5.2a persisted. The number of agglomerates increased with time after the cleaning of the nozzle. In all experiments, their formation was suppressed by frequent cleaning of the burner.

5.1.2. Influence of the process parameters on the deposition rate

The main disadvantage of the spray deposition methods is significant overspraying. In order to obtain satisfactory uniformity of coatings, the size of the substrate must be a few times smaller than the whole deposition area, which results in considerable losses of produced phosphor powders. The degree of overspraying is also affected by the efficiency of the transport of nebulized droplets into the flame. As a result, only a few percent of the total mass of the phosphor is deposited on the substrate. Calculations show that approximately 3 % of the synthesized Y_2O_3:Eu particles stick to the quartz plates when small concentrations of precursor solution are used, i.e. between 0.01 M and 0.05 M. For higher concentrations of 0.2 M and 0.5 M, this percentage decreases to 2.5 % and 1.5 %, respectively. Such a decrease shows that FAD is not well suited for deposition of larger particles. A dependence of the efficiency of deposition on the air currents inside of the fume hood was also observed. It is for this reason that the deposition of phosphor screens by the original spraying techniques (see Section 3.2) was usually performed in open atmosphere.[138]

The decrease in concentration of the precursor solution in the DPC-FAD process inevitably leads to a decrease of the deposition rate of the phosphor coating. For example, if the concentration of rare earth nitrates was changed from 0.2 M to 0.01 M, the deposition rate expressed in the units of increase of the screen weight per unit time decreases approximately by a factor of 15. This limits the range of ap-

plicability of the DPC-based FAD to particles larger than 100 nm. Obviously, optimization of the process becomes a critical issue.

If scaling-up of the burner and the droplet generator is not considered, the deposition rate can be influenced, e.g., by changing the deposition distance (DD, distance between the nozzle and the substrate). The substrate was usually placed at a distance of 7 cm, i.e., approximately at the tip of the flame. When the DD was decreased to 5 cm, the deposition rate increased by 50 %. The temperature at the surface of the substrate increased as well and at some locations exceeded 1200℃. The substrates made of fused silica could withstand this high temperature. If other substrate materials had to be applied, the temperature would have to be reduced by placing the substrate further away from the flame. In this case, the deposition rate can substantially decrease. When the distance of 10 cm was allowed between the burner and the substrate, the deposition rate was approximately 55 % of that at the standard deposition distance (7 cm).

The major parameter determining the deposition rate at a given concentration of the precursor solution is the amount of droplets entering the flame. The maximum possible concentration of droplets is limited by the power of the droplet generator and the efficiency of the transport to the flame. Figure 5.3 shows the relation between the deposition rate and the flow rate of the carrier gas for the minimum and the maximum nebulization rate. As expected, increase of any or both parameters leads to an increase of the deposition rate. However, it is important to note that the improvement due to the increase in the flow rate of air from 2 to 3 l/min was clearly subproportional and further increase would not be very beneficial. In addition, the entrainment of the air stream with droplets into the flame at the higher flow rates caused a problem with the flame stability. During the further stages of the work, the flow rate of the carrier gas was varied in the range 2-3 l/min.

The increase of the nebulization rate was also attended with difficulties. Most of the ultrasonic energy produced by the nebulizer is dissipated as heat. The temperature of the precursor solution in the ultrasonic cup noticeably increases (T_{prec} > 40℃ after 20 minutes of nebulization). The walls of the hose connecting the nebulizer with the burner were at room temperature and droplets carried by the stream of warm air could impinge on the wall or even be attracted towards colder surfaces due to the thermal force.[47] In order to prevent the losses of aerosol produced by the nebulizer, the flexible plastic hose was replaced by an electrically heated metal hose. Heating the walls of the hose to a temperature of 80-100℃ proved to be efficient for increasing the deposition rate by the described DPC-FAD process. For the standard deposition conditions (DD = 7 cm, flow rate of the carrier gas 3 l/min), this resulted in 40 % increase of the deposition rate. When the flow rate of air was 1 l/min, it was possible to nearly double the deposition rate by heating the hose.

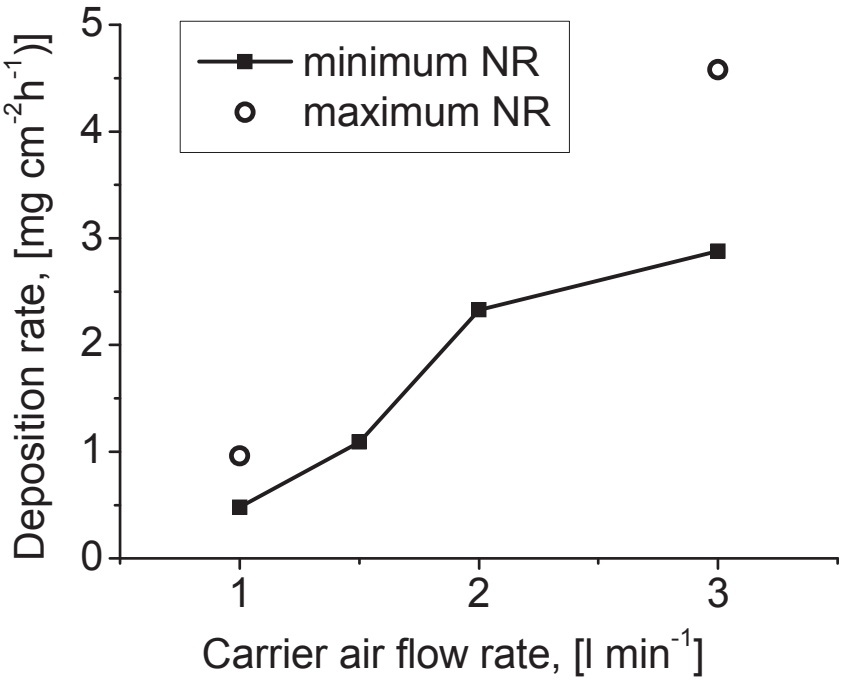

Figure 5.3 – Effect of the carrier gas flow rate on the deposition rate of Y_2O_3:Eu phosphor for different nebulization rates ([RE] = 0.2 M, DD = 7 cm).

The typical value of the deposition rate for the standard parameters ([RE] = 0.2 M; DD = 7 cm; propane feed rate 5 l/min; carrier flow rate 3 l/min; the minimum nebulization rate; heating of the hose ON) was on the order of 4 mg/cm^{2}h.

5.1.3. Crystallinity of the Y_2O_3:Eu phosphor

The necessity of the hose heating was supported by the following observation. In the attenuance spectra of some samples deposited without heating, the fundamental absorption edge was noticeably shifted towards longer wavelengths (Figure 5.4a). The shift was especially pronounced for the samples deposited either at high nebulization rates (i.e., large concentration of droplets in the flame) or at low feed rates of propane (resulting in a smaller flame and lower temperature of the substrate). It can be suggested that the origin of this shift is related to the structural disorder of the crystalline lattice of yttrium oxide, e.g., substantial concentration of vacancies and other defects, presence of an amorphous phase, and/or incomplete decomposition of the nitrates.

In order to prove that the difference in the location of the absorption band is not due to an external contamination, several samples demonstrating such a shift were thermally post-treated. The coated substrates were fixed in the same FAD-

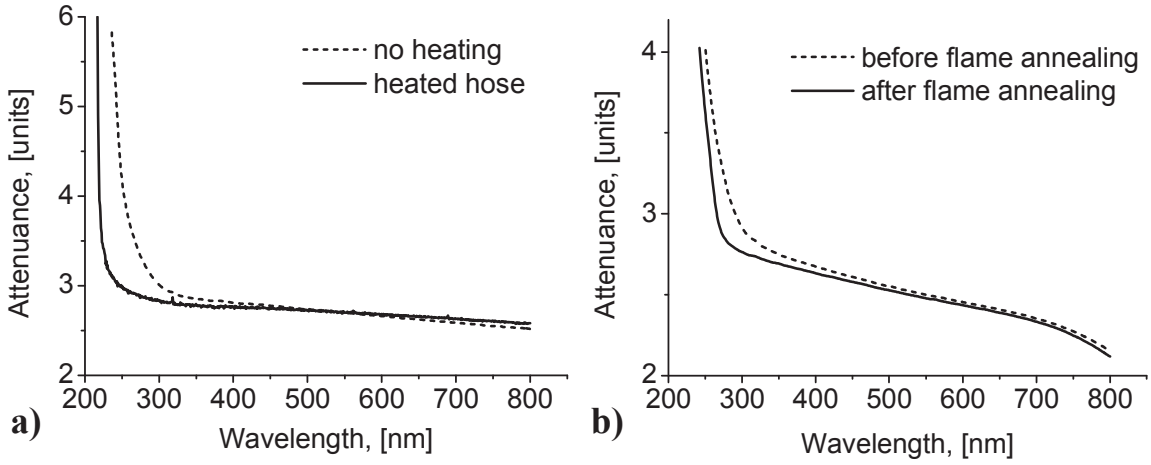

Figure 5.4 – UV-Vis attenuance spectra of FAD-deposited coatings: a) two different Y_2O_3 coatings deposited with and without the heating of the hose (coating density 0.8 mg/cm^2, [RE] = 0.2 M); b) the same Y_2O_3:Eu coating deposited without the heating before and after flame annealing (coating density 0.43 mg/cm^2, [RE] = 0.01 M, [Eu] = 8.5 mol.%).

setup and exposed to the flame without droplets for 5 min. The feed rate of propane was 5 l/min and the temperature on the surface of the substrate was kept higher than 1100℃ (DD = 5 cm). After annealing, the fundamental absorption edge shifted towards shorter wavelengths, to its position in crystalline yttria. For Eu-activated samples, the described procedure resulted in a substantial increase of the intensity of photoluminescence. In some cases, such as the one shown in Figure 5.4b, post-treated samples could gain up to 100 % of their initial brightness. At the same time, the intensity of emission for the coatings deposited at low nebulization rates, high feed rates of propane, and with heating of the hose experienced no definite change upon annealing by the flame impingement. As the droplets pass through the heated hose, their temperature rises and water can be partially evaporated. The effect of such preheating of the droplets can be compared to an extension of their residence time in the flame.

The scope of this thesis does not include any further investigation of the influence of the nebulization rate or thermal history of the droplets on the properties of deposited coatings. In order to assure the complete crystallization of yttria without any post-treatment, FAD of Y_2O_3:Eu coatings was routinely performed at the minimum nebulization rate and with heating of the hose connecting the droplet generator with the flame. This also applies to the comparison between the chloride- and nitrate-based precursors. For very low concentrations of the precursor solution ([RE] = 0.01 M), the maximum nebulization rate was used in order to increase the

deposition rate and the deposited coatings were post-treated by flame annealing as described above.

For the coatings deposited with the heated hose, the conventional annealing in an oven at temperatures in the range 800-1300℃ was attempted. At high temperatures (1100℃ and higher), the performance of t he phosphor coatings significantly degraded due to a devitrification process in the substrate (formation of the crystalline phase in the fused silica) and possibly a reaction between Y_2O_3 and SiO_2. It is known that the phase transformation of silica glass occurs at temperatures in excess of 1000℃ [223] and oxides (*e.g.*, Al_2O_3[224]) may serve as crystal nuclei. The crystallization starts at the surface and the crystalline layer grows into the interior of the substrate.[223] After annealing at low temperatures (10 hours at 800℃), the brightness of the samples increased by up to 10 %. Annealing for longer times did not further increase the brightness, which could be attributed to the high degree of crystallinity of Y_2O_3:Eu particles. Due to the minor increase of the brightness, the conventional annealing was considered impractical and all results reported in this thesis refer to the FAD-coatings which were not treated in the oven.

A representative emission spectrum of synthesized phosphor is shown in Figure 5.5. The main emission peak observed at 611 nm is characteristic for the cubic modification of Y_2O_3:Eu. During the first experiments, the doping level was set to 10 mol% Eu-ions relative to the overall content of (Y + Eu)-ions. This was theoretically predicted to be the optimum activator concentration for this phosphor.[50]

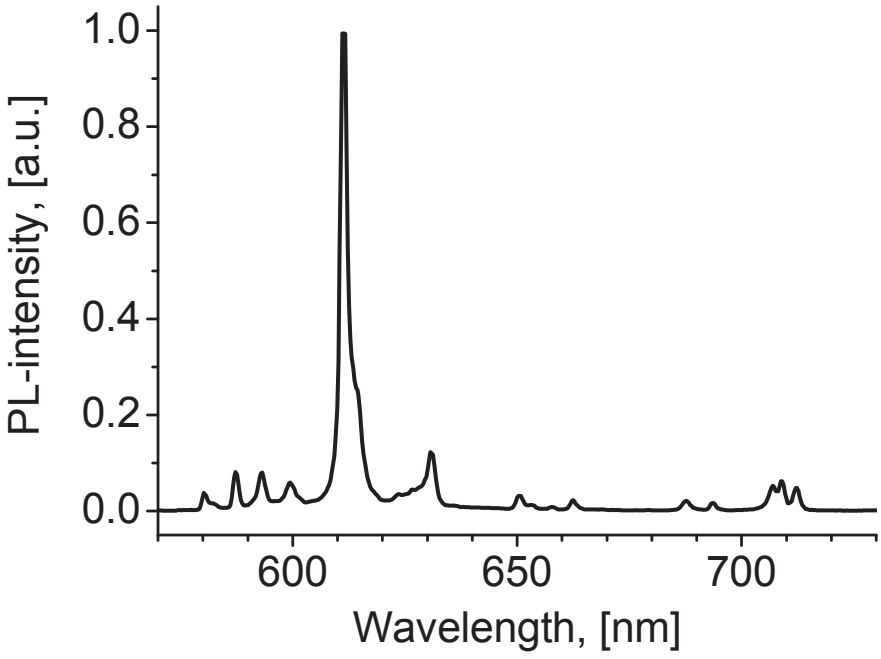

Figure 5.5 - Spectrum of photoluminescence of Y_2O_3:Eu phosphor produced by FAD.

Both XRD (Figure 5.6) and Raman spectroscopy (Figure 5.7) confirmed that the phosphor produced by the FAD-procedure crystallized in the cubic structure with a high degree of crystallinity. The angular positions of the peaks in the XRD spectra agreed with a spectrum of purchased Y_2O_3:Eu phosphor powder, previously published results,[176] and JCPDS card No. 25-1011. The Raman spectra were compared

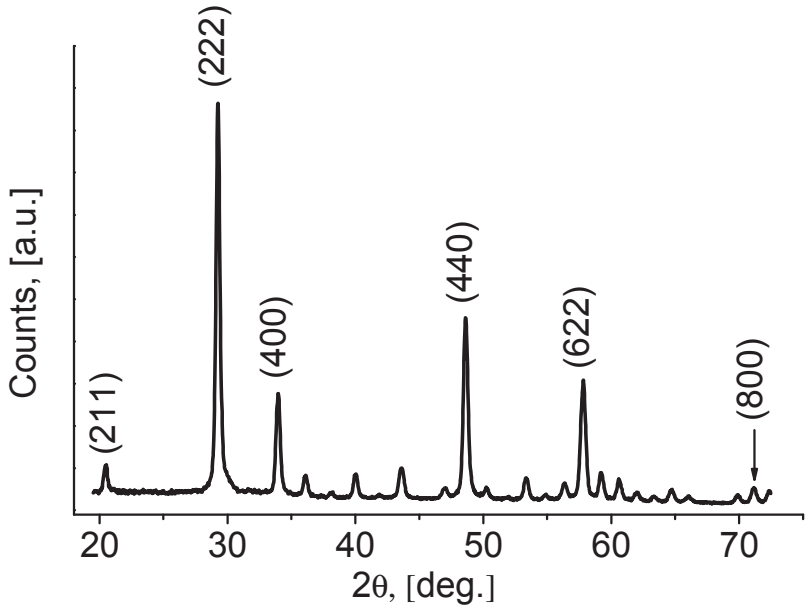

Figure 5.6 – XRD spectrum of FAD-deposited Y_2O_3 coatings ([RE] = 0.2 M).

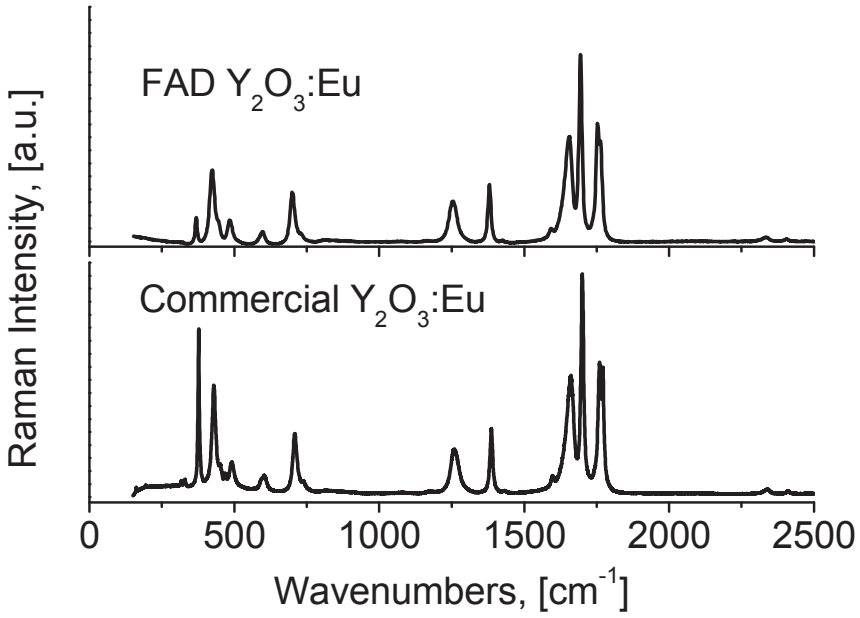

Figure 5.7 – Raman scattering spectra of the FAD-deposited coatings ([RE] = 0.2 M, [Eu] = 10 mol.%) and the commercial phosphor, excited with He-Ne laser.

with that of commercial phosphor and the reported data for Y_2O_3:Eu[225–228] and Y_2O_3.[229,230] The most noticeable difference between FAD samples and commercial phosphor was the decrease in the relative intensity of the peak at 375 cm^{-1}. Usually reported as the most prominent line in the phonon spectrum, it was significantly weaker than the one at 429 cm^{-1} in the spectra of FAD-deposited Y_2O_3:Eu^{3+} powders.

In case of the sprayed phosphor, none of the phonon scattering peaks below 300 cm^{-1} were observed in the spectra. Fitting of the highest phonon frequency line of the purchased phosphor with the Lorentzian shape-function revealed two closely spaced peaks. The peaks at 594 cm^{-1} and 468 cm^{-1} were not present in Y_2O_3:Eu obtained by the FAD procedure. The coatings of both kinds had a peak at 491 cm^{-1} which is not usually found in literature.

There was a very good match between the Raman spectra of the FAD-produced Y_2O_3:Eu phosphor and the work of Zhang *et al.*[225] In the reported spectra, one could observe the peak at about 491 cm^{-1} and the most prominent peak was also situated at 429 cm^{-1}, in full consistency with the present study. It should be noticed that the mean particle size, both in this project and in the cited work, was in the sub-micron range whereas in other cited papers these were, e.g., single crystals and relatively coarse powders obtained by firing. Another common detail is that the spectra in Figure 5.7, as well as in Zhang *et al.*,[225] were taken under exposure to the He-Ne laser radiation at 633 nm. As it can be seen in Figure 5.5, this wavelength appears in the range of emission of Y_2O_3:Eu. The Raman scattering spectra spanning a range up to 2500 cm^{-1} could include the PL-emission peaks in the range 633-750 nm. Indeed, the Raman shift of 1700 cm^{-1} corresponds to the wavelength of about 709 nm, which can explain the presence of the peaks in the Raman spectra observed near this location. The Raman scattering peak at 429 cm^{-1} could be as well attributed to the luminescence peak at 651 nm.

At the later stages of the experiments, the measurements of Raman spectra under excitation by a laser diode at 785 nm could be performed (Figure 5.8). There is a striking difference with the spectra obtained at 633 nm. The peak at 375 cm^{-1} becomes by far the largest in the spectra of both the FAD-deposited Y_2O_3:Eu and commercial phosphor. Locations and intensities of the peaks in the range of $\lambda > 600$ nm have completely changed, as expected.

It was not possible to detect any significant difference in the XRD and Raman scattering spectra of samples produced from the precursor solutions with different concentrations of the rare-earth nitrates. Both the position and the relative intensities of the peaks did not change. This confirms that the lattice constant of the phosphor produced by DPC-FAD does not depend on phosphor particle size.

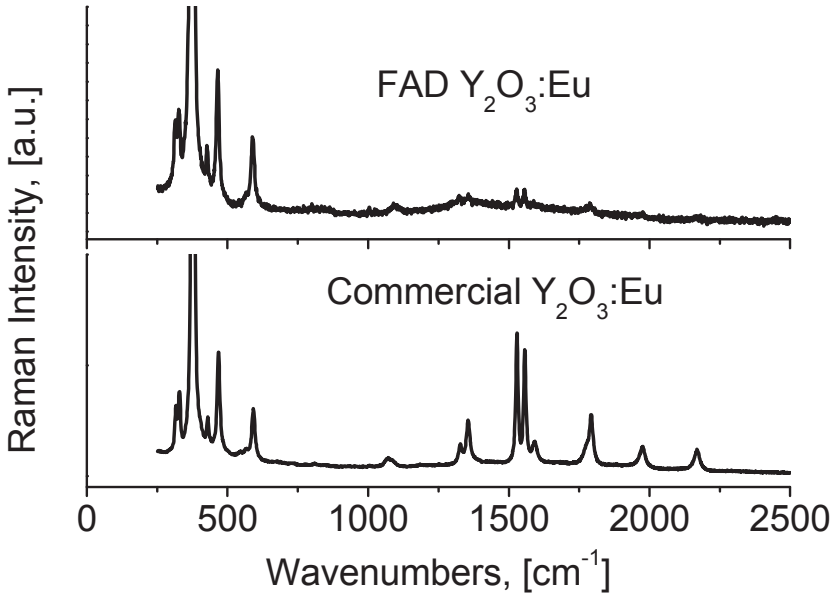

Figure 5.8 – Raman scattering spectra of the FAD-deposited coatings ([RE] = 0.5 M, [Eu] = 8.5 mol.%) and the commercial phosphor, excited at 785 nm.

5.1.4. Control of the phosphor particle size

The direct conversion of droplets of the precursor solution into the solid particles provides an effective means for controlled decrease of the size of the phosphor particles. Equation 5.1 shows a relationship between the sizes of a phosphor particle and the corresponding initial droplet (assuming a dense homogeneous solid particle)

$$\phi = \frac{\phi'}{10}\sqrt[3]{\frac{c\,M}{n\,\rho}}\,, \qquad (5.1)$$

where ϕ and ϕ' are diameters of the particle and the droplet, respectively; *c* is the molarity of the precursor solution in mol/l; *M* is the molar weight of the product in g/mol; ρ is the density of the product in g/cm^3; and *n* is the molar ratio of the precursor and the product. The decomposition of nitrates of trivalent rare earths can be described by the simplified reaction

$$2\,RE(NO_3)_3 \rightarrow RE_2O_3 + 6\,NO_2 + 1.5\,O_2\,. \qquad (5.2)$$

For each mole of the oxide, two moles of the nitrate are consumed. Therefore, *n* in Equation 5.1 equals 2. The molar weight (225.8 g/mol) and density of pure yttria could be adjusted in order to account for the doping. The size of the droplets produced by the ultrasonic nebulizer is determined by the excitation frequency f and can be estimated by an empirical formula[47]

$$\bar{\phi}_{N50} = \left(\frac{\gamma}{\rho' f^2} \right)^{1/3}, \qquad (5.3)$$

where $\bar{\phi}_{N50}$ is the count median diameter (for a lognormal count distribution it is equal to the geometric mean diameter $\bar{\phi}_g$); γ and ρ' are the surface tension and density of the precursor solution, respectively. Ultrasonic nebulizers typically have a narrow droplet size distribution (1.4-1.6 in the terms of geometric standard deviation σ_g).[47] The size of the droplets produced by the droplet generator used in this work, as specified by the manufacturer, was in the range 0.5-5 μm.

Figure 5.9 shows an example of the FAD-sample which was intentionally made very thin for the purposes of collection of the particle size statistics. The results for the deposits obtained from the precursor solutions with different concentrations of rare earths are presented in Figure 5.10 and in Table 5.1. For irregularly shaped particles, Feret's definition of particle diameter was used.[47] The PSD for low concentrations of the nitrates was resembling the lognormal one (although it could not pass the Shapiro-Wilk normality test for logarithms at 5 %-level). For 0.01 M and 0.05 M solutions, a geometric standard deviation of 1.7 was calculated, which was close to the typical width of the droplet size distribution of ultrasonic nebulizers. For higher concentrations of the precursor solution, the PSD of produced powder loses its shape and cannot be described by the lognormal distribution. The mean particle size also

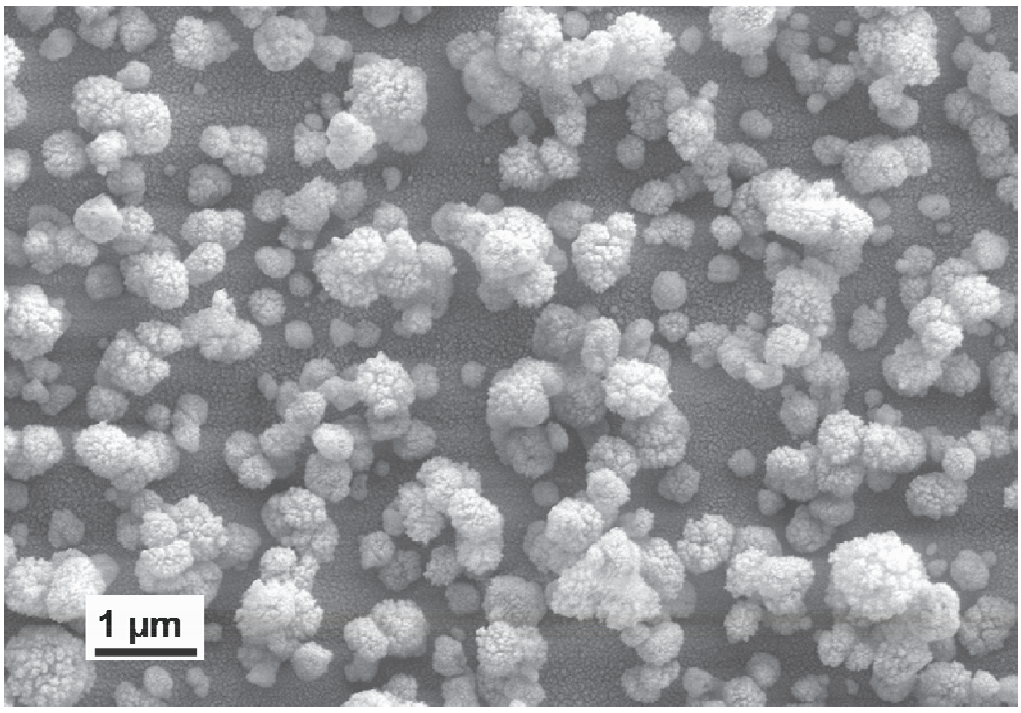

Figure 5.9 – SEM of a thin phosphor layer used for acquiring the statistics of particle sizes ([RE] = 0.05 M).

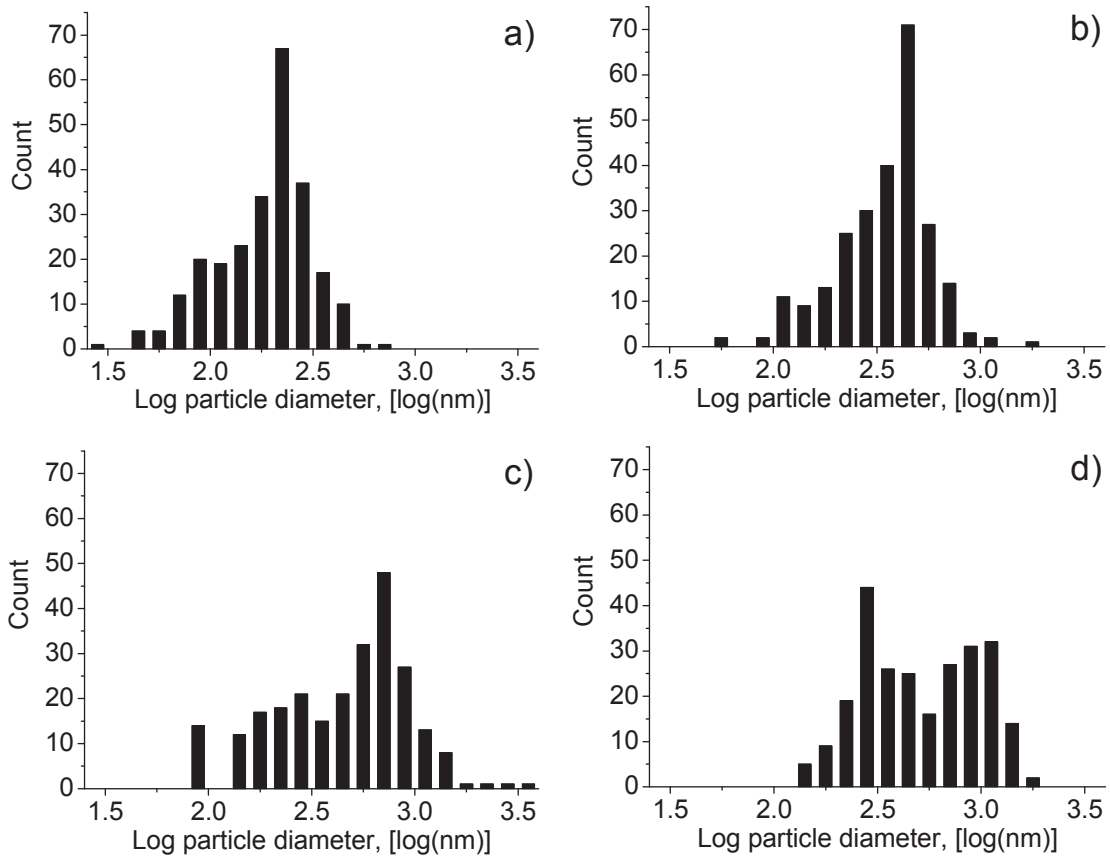

Figure 5.10 – Particle size distribution for the FAD-deposited phosphor powders corresponding to the different concentrations of the precursor solution: a) 0.01 M; b) 0.05 M; c) 0.2 M; d) 0.5 M.

Table 5.1 – Particle size statistics (theoretical values are shown in brackets)

Concentration of the precursor solution	Arithmetic mean particle size, [nm]	Geometric mean particle size, [nm]	Sauter diameter, [nm]
0.01 M	205	180 (120)	300
0.05 M	385	335 (200)	610
0.2 M	570	440 (310)	1400
0.5 M	615	500 (430)	1020
Commercial phosphor	3950	3500	6500

demonstrated a considerable deviation from the cubic root dependence on the solute concentration of precursors set by Equation 5.1.

The strong deviations from lognormal PSD and Equation 5.1 could partly be explained by the insufficient size of the samples (250 particles). It is usually recom-

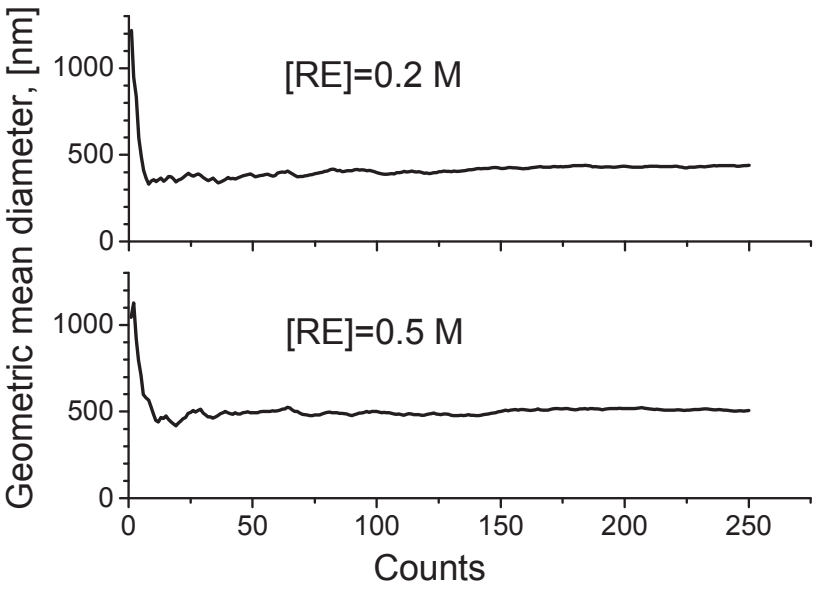

Figure 5.11 – Effect of the sample size on the value of the geometric mean diameter of phosphor particles.

mended to count at least 450 particles in order to determine the average particle size.[15] However, as it can be seen in Figure 5.11, the geometric mean particle size practically does not change for samples larger than 150 counts. It can hardly be expected that counting more particles would significantly change the results. The calculated uncertainty of the mean was less than 10 % in all cases. In addition, some authors state that for samples exceeding 200 particles, good reproducibility (within $\pm 5\,\%$) can be achieved.[50]

The comparison between the values of the geometric mean diameter obtained from SEM-inspection and those obtained from Equation 5.1 (see Table 5.1) shows that the former ones are in all cases greater that the latter. This can be to a large extent attributed to the poor morphology of the phosphor particles. The temperature of the flame was well below the melting point of yttria so that the particles could not approach their theoretical density during the short residence time. This results in considerable hollowness and porosity of the particles and expressed roughness of their surface. The reduced apparent density of the phosphor particles (e.g., to about 70 % of the theoretical density of europium-doped yttria) would explain the underestimated particle sizes calculated from Equation 5.1. Furthermore, it is possible that the presence of rare earth salts in the precursor solution changes its surface tension and causes a shift in the initial droplet size distribution (Equation 5.3), which can also be a reason for the deviation from the cubic root dependence discussed previously.

5.1.5. Optimum screen thickness

As discussed in Section 2.2, the brightness of phosphor coatings strongly depends on their thickness. In the reflection (R-)mode, the intensity of luminescence increases until it reaches saturation (for very thick phosphor layers). On the contrary, the maximum brightness in the transmission (T-)mode corresponds to a certain thickness and gradually decreases for thicker phosphor layers.

A series of samples of different coating densities was prepared for a 0.2 M precursor solution containing 10 mol.% of Eu_2O_3. The changes of the R- and T-mode intensities of photoluminescence excited at 254 nm are presented in Figure 5.12a. Changes of PL-intensity for increasing thickness of phosphor layer were similar to those observed for conventional phosphor screens, e.g., CRTs made of phosphor powder with the particle size of 3.5 μm (see Figure 2.8).[8] However, for FAD coatings deposited from the 0.2 M precursor solution the maximum light output in the T-mode was achieved with coating densities of 0.4-0.5 mg/cm^2, which is significantly lower than the values obtained for conventional micrometer-sized phosphors (e.g., 2-3 mg/cm^2, Figure 2.8). The optimum thickness for the screens deposited by the sedimentation of the commercial phosphor in the present investigation was 2.0 mg/cm^2. The corresponding value of the T-mode emission intensity is used throughout this thesis as a reference.

As it can be seen in Figure 5.12b, the fraction of the exciting radiation reflected by the coatings with densities exceeding 0.3 mg/cm^2 practically did not change, whereas the intensity of the UV-light transmitted through the coatings decreased ex-

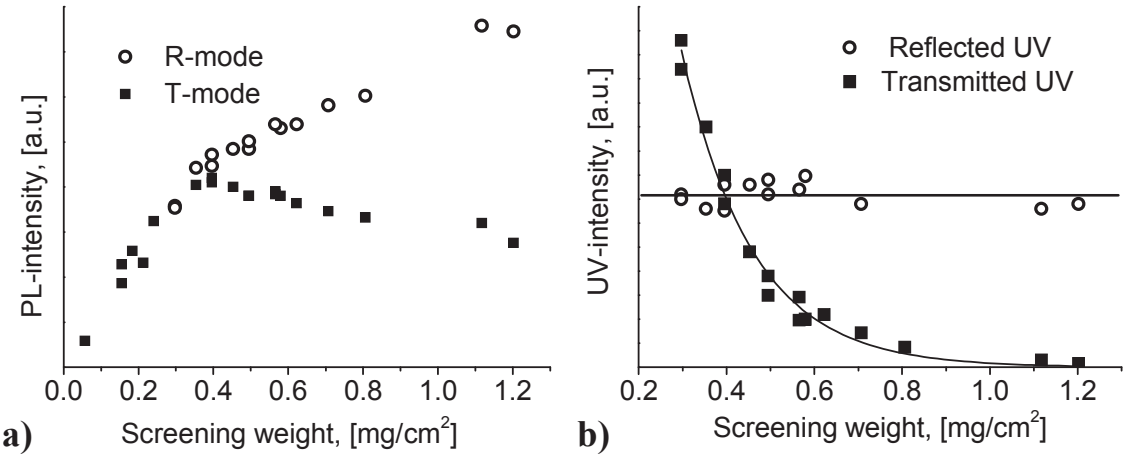

Figure 5.12 – Brightness of the PL-emission at 611 nm (a) and intensity of reflected and transmitted UV-light at 254 nm (b) of the FAD-deposited Y_2O_3:Eu phosphor coatings of different thickness ([RE] = 0.2 M, [Eu] = 10 mol.%).

ponentially with the thickness. The penetration depth of the UV radiation at 254 nm was approximately 0.16 mg/cm^2. For the optimum thickness (~0.4 mg/cm^2), about 97 % of the diffusely incident UV-light was either reflected or absorbed by the phosphor.

It is possible to express the thickness of the phosphor screen in conventional phosphor layers according to Equation 2.58, which is repeated here

$$L = 1.65 \frac{W}{\rho \bar{\phi}_{SM}}, \qquad (5.4)$$

where L is the number of phosphor layers; W is the screening weight; ρ is the density; and $\bar{\phi}_{SM}$ is the Sauter diameter of the phosphor particles.

A Sauter diameter of 1.4 µm was calculated for the chosen concentration of the precursor solution (see Table 5.1). The maximum T-mode brightness of FAD screens was achieved in the range 1.0-1.3 phosphor layers. For comparison, the highest brightness obtained for the settled screens corresponds to approximately 1.0 phosphor layers.

5.1.6. Optimum concentration of europium

The concentration of the activator is one of the major factors influencing the characteristics of deposited phosphor coatings. It affects the brightness of luminescence, the decay time constant of emission, and to a certain extent the crystalline structure of the compound sesquioxide.

The main optimization parameter in this study was the brightness of the phosphor screen. The concentration of europium ions was investigated over the range 0.5 – 25 % relative to the overall concentration of the rare earth ions. Usually, the efficiency of different phosphors is compared in the R-mode for very thick coatings (in the approximation of semi-infinite plaques). This method is, however, hardly applicable for FAD-coatings. In this thesis, the maximum brightness of PL-emission in the T-mode was used for comparison of phosphors with different concentration of the activator. This method is inherently more complex because it demands preparation of phosphor coatings of some certain optimum thickness (see Sections 2.2.2, 2.2.3, and 5.1.5). For phosphor powders produced from the 0.2 M precursor solutions, the optimum values of the screen density were about 0.4 mg/cm^2 (see Figure 5.12). In order to compare FAD-deposited Y_2O_3:Eu phosphor coatings containing different amounts of europium, a series of samples with coating densities spanning the range 0.3 - 0.6 mg/cm^2 was prepared for each particular concentration of the activator. In each series, a sample with the highest T-mode PL-brightness was chosen. Figure 5.13 shows the results of these experiments.

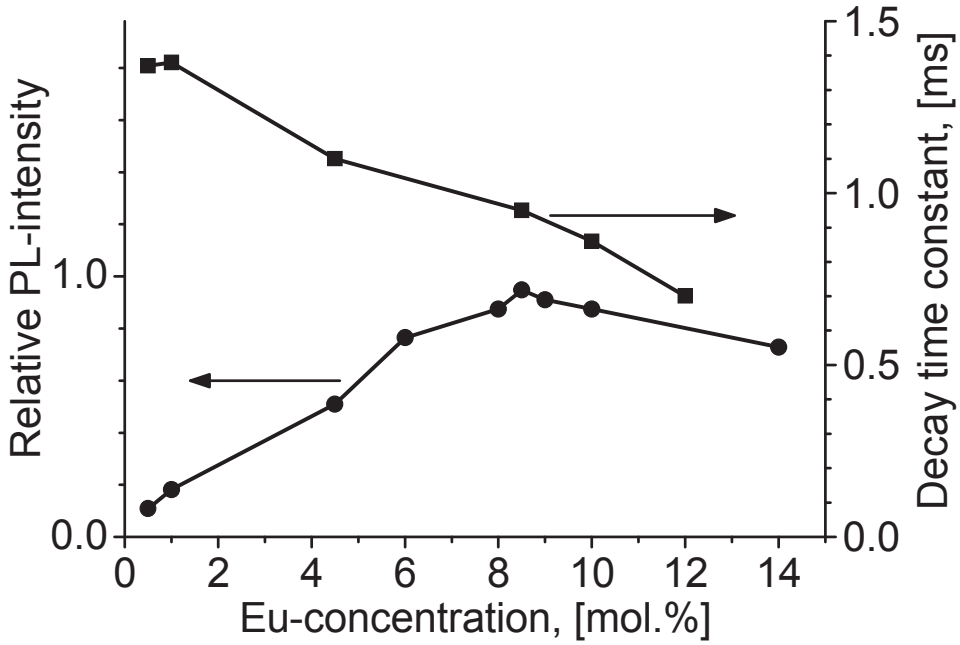

Figure 5.13 - Influence of europium concentration on the PL-intensity and the exponential decay time constant of FAD-produced Y_2O_3:Eu phosphor ([RE] = 0.2 M).

The highest luminescence efficiency was achieved in the range 8-10 mol.% Eu_2O_3. In further experiments, the optimum phosphor composition corresponding to $(Y_{0.915}Eu_{0.085})_2O_3$ was used. This exceeds the concentration of the activator in most of the commercial Y_2O_3:Eu phosphors. The difference is explained by the more uniform distribution of the activator in the matrix as they are mixed at molecular level in the precursor solution as compared to the solid state diffusion of pure oxides during the firing, commonly implemented in industry.[124,135] The lattice constant obtained from the XRD spectrum of the phosphor with the optimized composition was larger than that of the commercial phosphors (1.0619 vs. 1.0608-1.061 nm, respectively), which could be anticipated due to the higher concentration of the activator in the FAD-produced Y_2O_3:Eu. The lattice constant increases with the increasing concentration of the dopant because of the larger radius of Eu^{3+}-ions substituting Y^{3+}.[231]

The most significant outcome was that the brightness of the FAD-coatings of the optimized composition was comparable with the best samples obtained by sedimentation of the commercial phosphor. Intensity of emission of the best as-deposited FAD-screens in the T-mode could reach 97 % of that of the reference sample.

The concentration of the activator influences the rate of radiative transitions due to the effect of concentration quenching (see Section 2.1.2). The decay kinetics of luminescence of the FSP-synthesized Y_2O_3:Eu-phosphor for a few different con-

Table 5.2 – Luminescence decay time of the FAD-produced $(Y_{1-x}Eu_x)_2O_3$ phosphor, [RE] = 0.2 M

Eu concentration	Decay time, ms	
	from 100% to 10%	from 100% to 1%
x = 0.01	3.2	6.8
x = 0.045	2.6	5.4
x = 0.1	1.5	4.0
x = 0.25	0.083	0.46

centrations of the activator was investigated. The results are also presented in Figure 5.13.

In the simplest case of the first order exponential decay, transient behavior of a phosphor could be characterized by a single time constant. For the samples with low europium content (about 1 mol.% and lower), the decay curve could be fitted with the exponent corresponding to the exponential time constant τ of 1.38 ms, which is in good agreement with literature.

As the concentration of the doping increases, the emission is expected to decay faster. For the samples containing 4.5 mol% Eu-ions, τ was measured as of 1.1 ms. When the doping level approached the quenching concentration, the decay curve included higher order exponential terms (see, e.g., Kobler[232]) and could be only roughly approximated by the single exponential time constant. For easier overview and comparison in such cases, phosphors are often characterized by merely measuring a time interval from the interruption of the excitation to the moment when the brightness falls to a defined percentage of the initial value. Table 5.2 summarizes the results of the investigation.

As follows from Table 5.2, the fluorescence decay time from 100 % to 10 % of the brightness lays within the range of approximately 1.5 to 3 ms for all practical Eu-concentrations in the FAD-synthesized Y_2O_3:Eu phosphor. For excessive doping, much shorter lifetimes could be achieved but the brightness of the emission drastically decreased.

The Raman spectra demonstrated the expected shift of the peaks to lower frequencies (e.g., the peak at 375 cm^{-1}, Figure 5.14) due to the increased lattice constant. Their positions differ by at least 3 cm^{-1} between the spectra of the samples containing 6 % to 14 % of europium. For the europium concentration of 25 %, the peaks shifted even further.

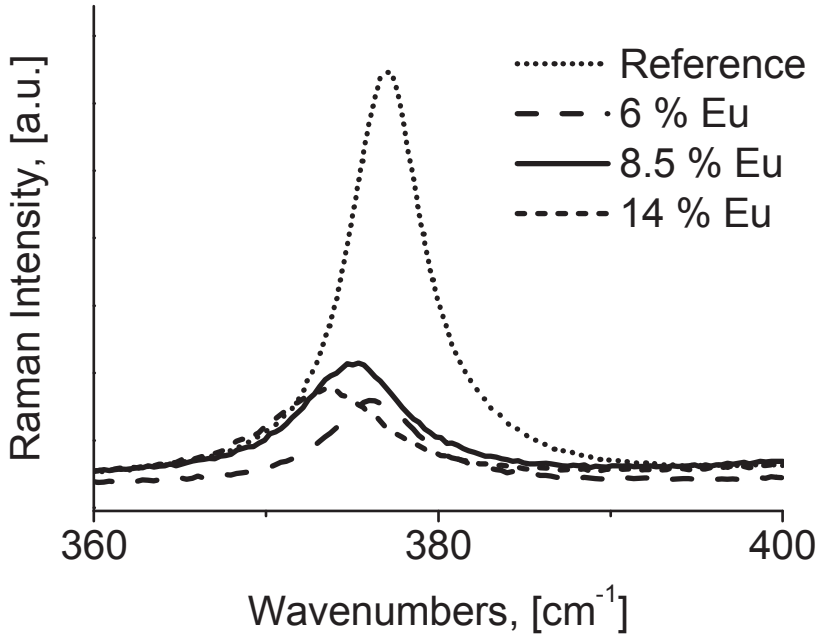

Figure 5.14 – Shift of the Raman scattering peak at 375 cm^{-1} (excited by He-Ne laser) for different concentrations of Eu^{3+} in the Y_2O_3:Eu phosphor.

5.1.7. Effect of decreasing phosphor particle size

Optical properties of powder coatings undergo significant changes when the size of particles decreases below the wavelength of light the coatings are exposed to (see Section 2.3). As discussed in Section 5.1.4, the size of phosphor particles produced by the DPC-FAD technique can be effectively controlled by the concentration of the precursor solution. When the concentration of rare earth nitrates decreased from 0.2 M to 0.01 M, the geometric mean phosphor particle size decreased from 440 nm to 180 nm. The Sauter diameter changed from 1400 nm to 300 nm. The dependence of the T-mode PL-brightness on coating thickness for these two concentrations of precursors is presented in Figure 5.15.

The most important outcome was that the phosphor coatings obtained from the precursor solution with the lowest solute concentration could not reach the brightness of the coatings produced from the solution with the standard concentration of 0.2 M. At the same time, the increase of the precursor solute concentration to 0.5 M did not noticeably change the maximum PL-brightness (i.e., it was approximately equal to the maximum brightness of the phosphor coatings deposited from 0.2 M solution).

The decrease of PL-emission intensity may be attributed to an increased non-radiative decay rate, which shortens the observed decay time of luminescence and leads to a decrease of the quantum yield (see Equations 2.1 and 2.2). The emission

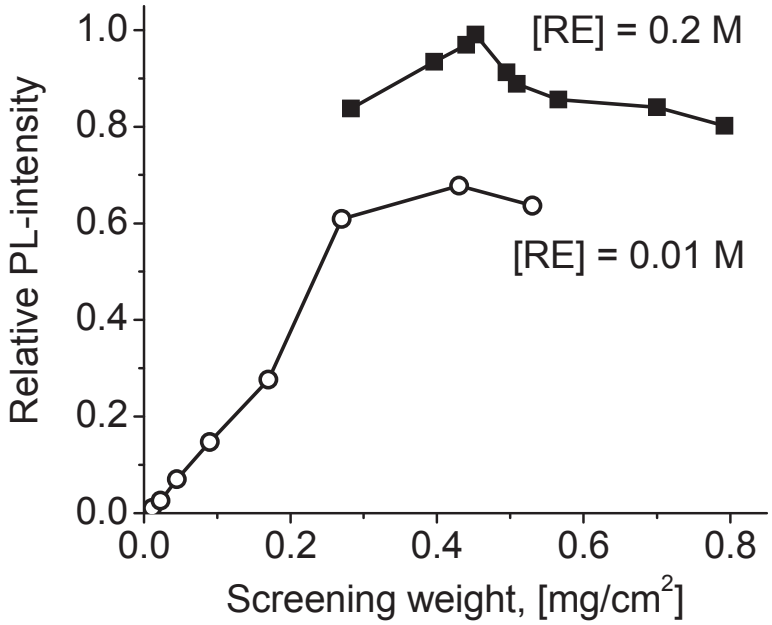

Figure 5.15 – Dependence of the T-mode PL-intensity on the coating thickness for Y_2O_3:Eu coatings deposited from 0.2 M and 0.01 M precursor solutions (full squares and open circles, respectively; [Eu] = 8.5 mol.%).

decay time measured for the coating deposited from 0.01 M precursor solution was approximately 20 % shorter than that of the standard coatings (e.g., 3.2 ms vs. 4.0 ms in terms of a decay from 100 % to 1 % of the brightness; [RE] = 10 mol.%, see Table 5.2). The increased probability of non-radiative decay of the excited states of Eu^{3+}-ions could be explained by an increased concentration of defects in the crystal structure in the powders produced from precursors with low solute concentration. This could to a certain extent be related to the structural defects still remaining after the flame annealing procedure described in Section 5.1.3. However, the fact that the brightness of no single coating produced from 0.01 M or 0.02 M precursor solutions could exceed 70 % of the brightness of the reference sample even after the flame annealing allows a conclusion to be drawn, namely that the defects acting as quenchers cannot be removed by such thermal treatment.

Dosev *et al.*[118] separated the Y_2O_3:Eu powder synthesized by flame spray pyrolysis into fractions of smaller and larger particle sizes. The former also demonstrated shorter decay time. In the cited work, however, the smaller particles had the monoclinic crystalline structure and the larger ones were mostly of the cubic phase, which could cause such a difference. The argumentation by Dosev *et al.*[118] cannot therefore be applied to the results of the current study. No traces of the monoclinic phase could be found in the XRD spectra of the coatings produced by the DPC-FAD technique in the present work.

As discussed in Section 2.3.3d, it can be expected that the increased specific surface area of the smaller phosphor particles provides additional quenching sites at the surface and increases the probability of non-radiative transitions. This quenching mechanism appears especially important, if one considers the extremely rough surface of FAD-synthesized phosphor particles favoring adsorption of contaminants from the ambient atmosphere. The increase of brightness of the coatings could probably be achieved by improving the particle morphology.

Another important conclusion to be drawn from the curves depicted in Figure 5.15 is that the optimum thickness for the coatings consisting of small particles is at least 0.3 mg/cm^2 or larger. For the Sauter diameter of 300 nm, this would correspond to at least 3 phosphor layers as defined by Equation 5.4 (= Equation 2.58), which substantially exceeds the values found for the coatings either deposited from the concentrated precursor solutions or made from commercial phosphor powders (1.0-1.3 phosphor particle layers). Such a deviation can be attributed to the change of the scattering properties of the phosphor particles. When their size enters the subwavelength regime, the scattering efficiency passes through its maximum and then decreases (see Section 2.3.3a). Furthermore, it also becomes noticeably wavelength-dependent. In this case, the concept of the phosphor particle layer described in 2.2.3b cannot be applied anymore because the actual scatterance of one so-defined particle layer starts to decrease and also depends on the wavelength of light.

Figure 5.16 reveals the evolution of the attenuance spectra of the FAD-coatings deposited from 0.2 M and 0.01 M precursor solutions. In both cases as well as for the commercial phosphor, screens with the optimum thickness have very close values of attenuance of about 3 attenuance units at the excitation wavelength (254 nm), which means that the optimum corresponds to a thickness, for which approximately 99.9 % of the normally incident UV-light is either absorbed by the phosphor or scattered away from its initial direction of propagation. A wide peak in the range 500-600 nm can be observed for the standard FAD-coatings. In the spectra of the coatings deposited from diluted precursors, this peak shifted to the short wavelength edge. This shift should be related to the decrease of the phosphor particle size. The location and shape of the peak are determined by the particle size distribution of the phosphor powders and the onset of absorption in the UV-range.

The dependent scattering probably does not play any significant role. FAD deposits have a particle volume filling fraction of less than 8 % (volumetric porosity of 92.1 % was measured for the standard Y_2O_3:Eu coatings). According to Equation 2.99, the dependent effects become important when the value of the particle size parameter falls short of about 1.4. Even for the smallest particles produced by the DPC-FAD technique, i.e., for a Sauter diameter of 300 nm, this would correspond to the wavelengths longer than 670 nm. Even if one assumes the density of the phosphor particles to be 70 % of the theoretical density of the single-crystalline material,

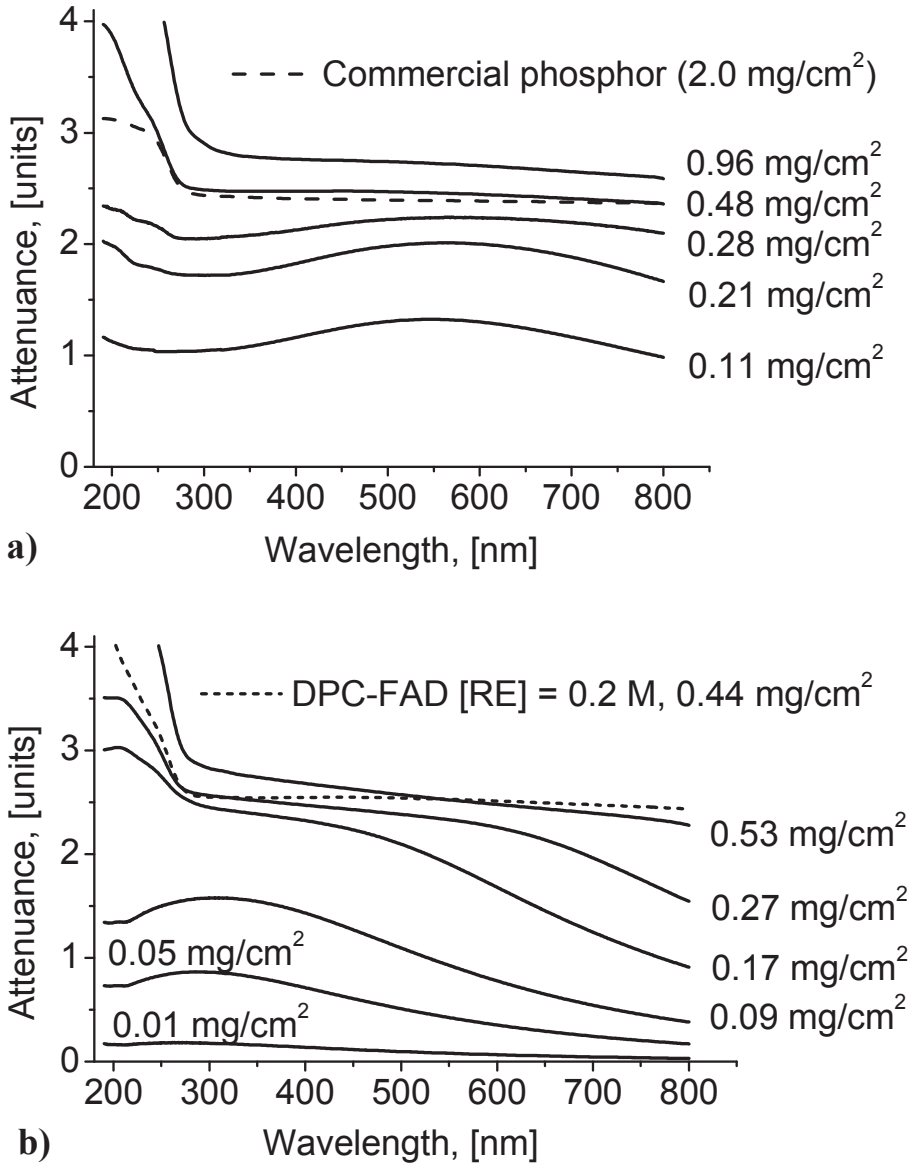

Figure 5.16 – Attenuance spectra of the FAD-deposited Y_2O_3:Eu coatings of different thickness: a) [RE] = 0.2 M, [Eu] = 10 mol.%; b) [RE] = 0.01 M, [Eu] = 8.5 mol.%.

thus increasing the particle filling fraction to approximately 12 %, the dependent effects would be expected for the wavelengths longer than 500 nm in the case of the coatings deposited from the 0.01 M precursor solution. For all FAD-deposits from the solutions of the higher concentrations, the range of the dependent scattering would still be outside the visible range. However, one also has to consider the effect of particle morphology (i.e., internal pores and roughness of the surface) on the scattering properties. Any structural defects with sizes on the order of the wavelengths of light produce additional scattering.

The decrease of the attenuance towards the longer wavelengths observed in Figure 5.15b is probably due to the Rayleigh-like character of light scattering by the particles smaller than the wavelength of the incident light. A change of the steepness of the curves should be ascribed to the lacking linearity of the measurements of attenuance for the values larger than approximately 2 units (i.e., when the difference between the intensities of the beams passing through the sample screen and the reference blank quartz substrate exceeds two orders of magnitude).

5.1.8. Sensitization of photoluminescence of Y_2O_3:Eu by co-doping with gadolinium

Co-doping with gadolinium is often used in order to increase the conversion efficiency of Y_2O_3:Eu for X-rays as the X-ray stopping power critically depends on the atomic numbers of ions constituting the host lattice.[5] Photoluminescence excited in the UV-range can also be influenced by Gd-doping in several ways: i) it changes the width of the bandgap of the host, thereby affecting the efficiency of absorption of UV-photons; ii) there is efficient energy transfer from directly excited Gd^{3+}-ions to Eu^{3+}-ions in the range of the charge transfer band (CTB) of Y_2O_3:Eu[50]; and iii) co-doping increases the refractive index of the medium and thus also increases the rate of radiative transition of Eu^{3+}-ions.[101] These beneficial effects would be more pronounced for higher concentrations of gadolinium. However, with the increase of the molar fraction of Gd_2O_3, the resulting compound tends to crystallize in a monoclinic structure, which has significantly lower light output as compared to the cubic modification.[12]

As described in the previous sections, the brightness of the Y_2O_3:Eu coatings produced by DPC-FAD (expressed by the intensity of the largest emission peak) could reach at most 97 % of the maximum brightness of the Y_2O_3:Eu phosphor coatings made from the commercial micrometer-sized phosphor. Addition of Gd-ions allowed for increasing the transmission-mode PL-intensities to 110 % of the initial value, i.e., up to 108 % of the commercial reference (Figure 5.17). The highest brightness was achieved for the coating containing 20 mol.% of Gd. The single exponential decay time constant decreased from 0.95 ms to 0.85 ms.

For higher Gd-concentrations, the crystalline structure of the host started to change in accordance with the Y_2O_3-Gd_2O_3 phase diagram[233] so that for $(Y_{0.5}Gd_{0.5})_2O_3$:Eu the PL-emission spectrum was already dominated by the contribution from the monoclinic phase. Corresponding changes were also observed in the XRD spectra (Figure 5.18). The luminescence lifetimes of the $(Y_{0.5}Gd_{0.5})_2O_3$:Eu and Gd_2O_3:Eu phosphors were approximately equal (~0.5 ms).

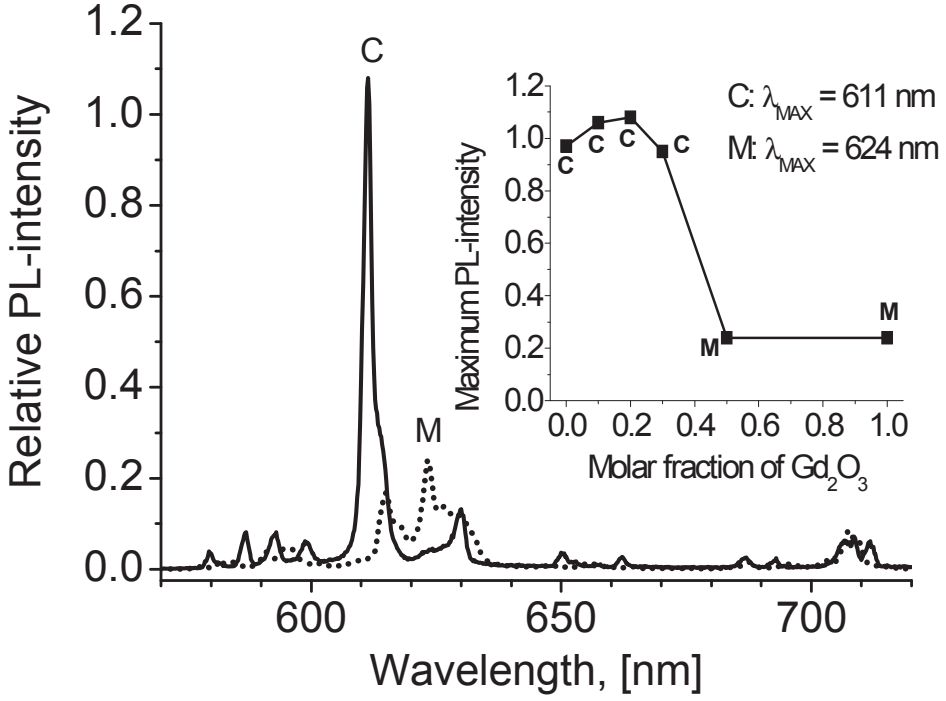

Figure 5.17 – PL-emission spectra of cubic and monoclinic $(YGd)_2O_3$:Eu. Inset: changes of the maximum T-mode intensity with the addition of Gd.

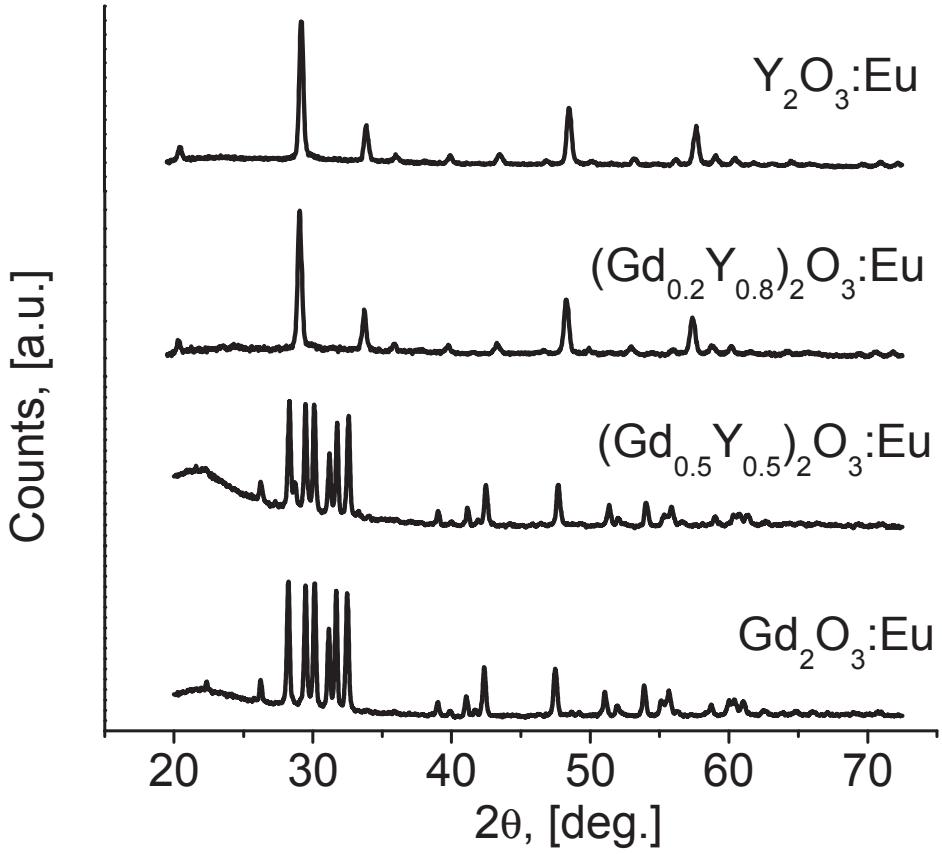

Figure 5.18 - XRD spectra of $(YGd)_2O_3$:Eu coatings deposited by DPC-FAD ([RE] = 0.2 M, [Eu] = 8.5-10 mol.%).

It is known that addition of gadolinium can substantially improve the performance of Y_2O_3:Eu in the VUV-range.[234] There was a noticeable shift of the host absorption peak between the PLE spectra of the FAD-deposited Y_2O_3:Eu and $(Y_{0.8}Gd_{0.2})_2O_3$:Eu coatings (Figure 5.19) leading to more efficient excitation in the CTB (225-280 nm). However, for excitation in the range of $\lambda < 210$ nm, the intensity of emission was equal to that of the Y_2O_3:Eu screens and both were considerably worse than the light output from the commercial phosphor.

The inferior VUV-performance of the phosphor coatings deposited by DPC-

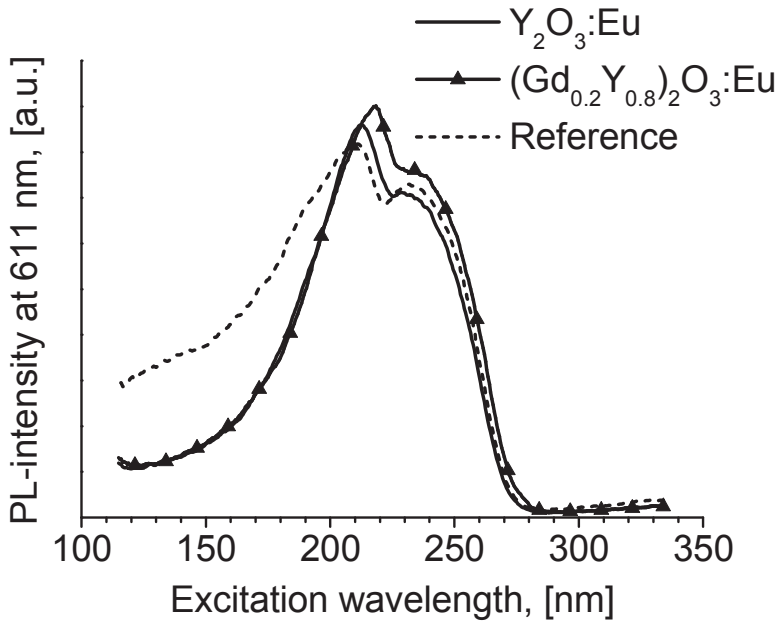

Figure 5.19 - PLE spectra of Y_2O_3:Eu and $(Gd_{0.2}Y_{0.8})_2O_3$:Eu FAD-coatings ([RE] = 0.2 M, [Eu] = 8.5 mol.%).

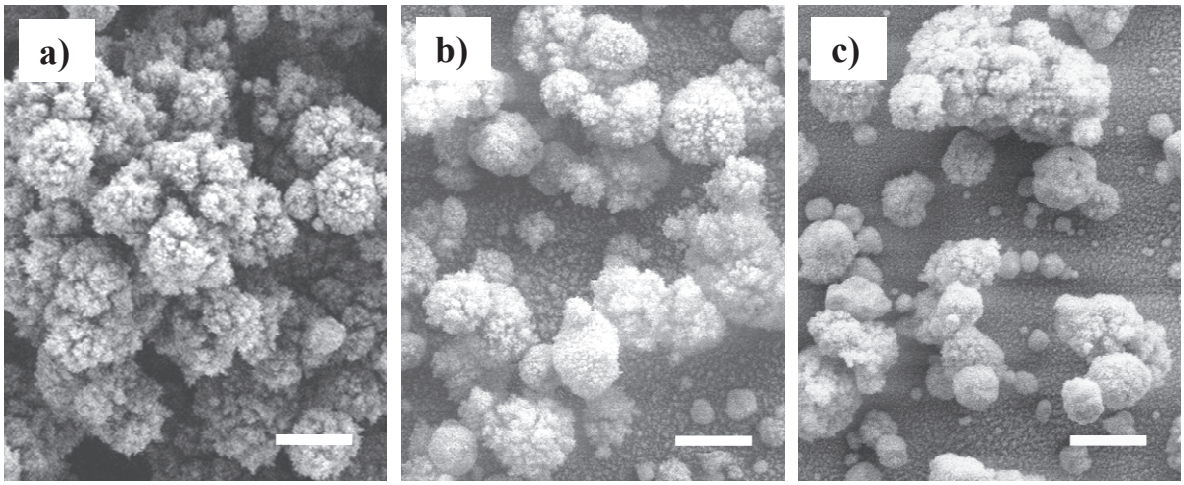

Figure 5.20 – SEM pictures of FAD-synthesized phosphor particles: a) Y_2O_3:Eu; b) $(Gd_{0.2}Y_{0.8})_2O_3$:Eu; and c) Gd_2O_3:Eu. [RE] = 0.2 M, [Eu] = 8.5-10 mol.%, scale bar is 1 μm.

FAD could be attributed to the nanoscopic roughness of the particle surface. The conversion of droplets of the precursor solution into solid phosphor particles is accompanied by the rapid evaporation of water and decomposition of the solute to the corresponding oxides. The surface of $(YGd)_2O_3$:Eu phosphor particles obtained by the standard FAD technique from water-based precursors is affected by phenomena similar to the effflorescence of soluble inorganic salts (Figure 5.20). In order to increase the brightness of the screens in the VUV-range, a means to improve the morphology of the particles had to be found.

5.2. Influence of polymeric additives on morphology and performance of Y_2O_3:Eu phosphor produced by DPC-FAD

The use of air as an oxidizer of propane substantially simplifies the FAD-setup but decreases the flame temperature and causes degradation of the morphology of the particles. The temperature of the flame could be increased beyond the melting point of yttria by enriching the air with oxygen. However, at increased temperatures, yttria tends to crystallize in a monoclinic structure, which significantly decreases the PL-output.[176]

Hollowness and porosity of the produced phosphor particles are the main drawbacks of the ultrasonic spray pyrolysis (USP) in electrically heated furnaces (see Section 3.2). Synthesis of phosphors in low-temperature flames has much in common with the general USP method; thus, the problem of poor morphology of the particles could have a similar solution.

One of the ways to improve the condition of phosphor powders synthesized by USP is by the introduction of polymeric additives to the precursor solution.[235–237] At high temperatures, the esterification reaction between carboxyl and alcohol groups of citric acid (CA) and ethylene glycol (EG), respectively, forms polymeric chains inside the droplets. During spray pyrolysis, a droplet entering into the furnace transforms into viscous gel and decomposes to yield a dense particle of phosphor. In order to improve the morphology of Y_2O_3:Eu^{3+} and boost the performance of the FAD-produced phosphor coatings in the range of deep UV, the feasibility of the introduction of organic additives which polymerize upon heating in the flame (as well as inside the heated hose carrying the droplets of the precursor solution into the flame) was investigated. The amounts of added polymeric components varied up to 0.3 M CA and 0.3 M EG for the overall concentration of rare-earth ions in the precursor solution equal to 0.2 M and 0.5 M. The concentration of the activator was fixed to 8.5 mol.%.

5.2.1. Evolution of particle morphology and PL-output (for excitation at 254 nm)

There was no difference in relative intensities of the peaks in the photoluminescence emission spectra of the phosphors deposited with and without polymeric additives and, therefore, the intensity of the main emission peak at 611 nm (see Figures 5.5 and 5.17) was used as a measure of overall brightness of photoluminescence.

The uniformity of the substrate coverage (Figure 5.21) of coatings deposited by polymer-assisted FASP was similar to that of no-polymer deposition procedure.

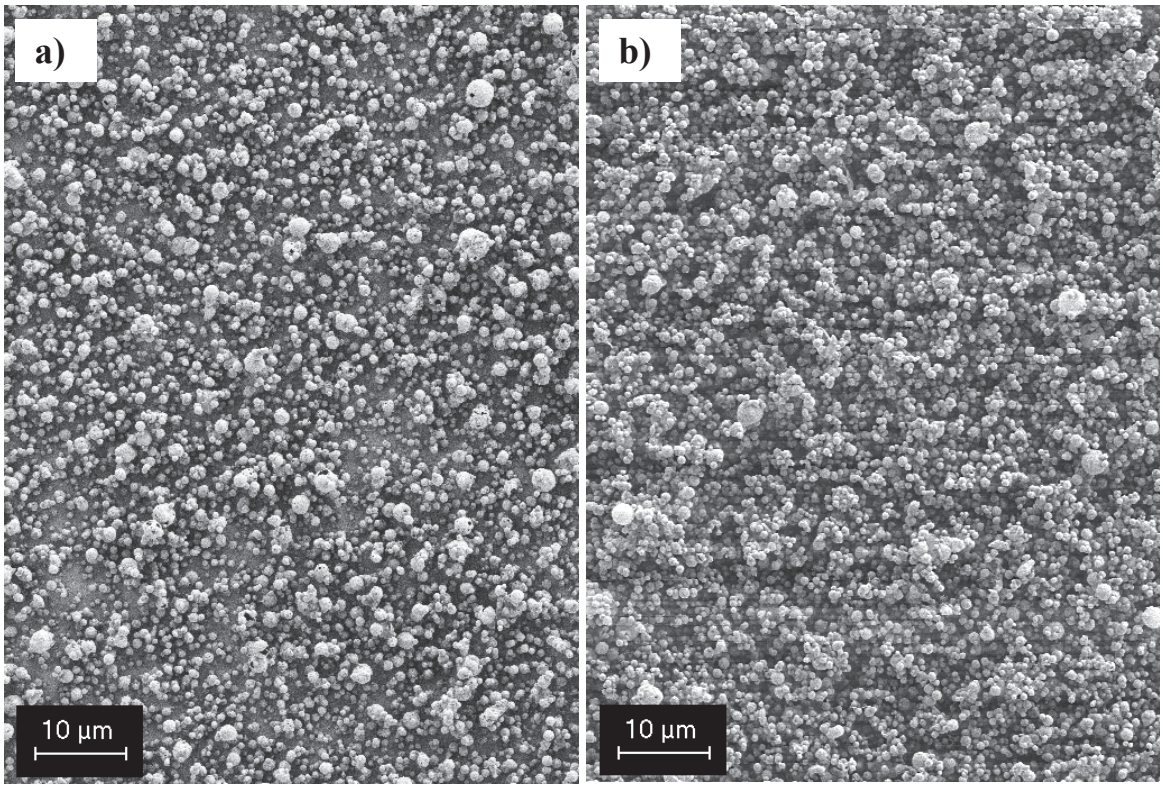

Figure 5.21 - Examples of phosphor coatings deposited from polymeric precursors: a) thin layer (used for calculations of particle size statistics); b) thick layer (used for photoluminescence excitation spectroscopy and attenuance spectroscopy).

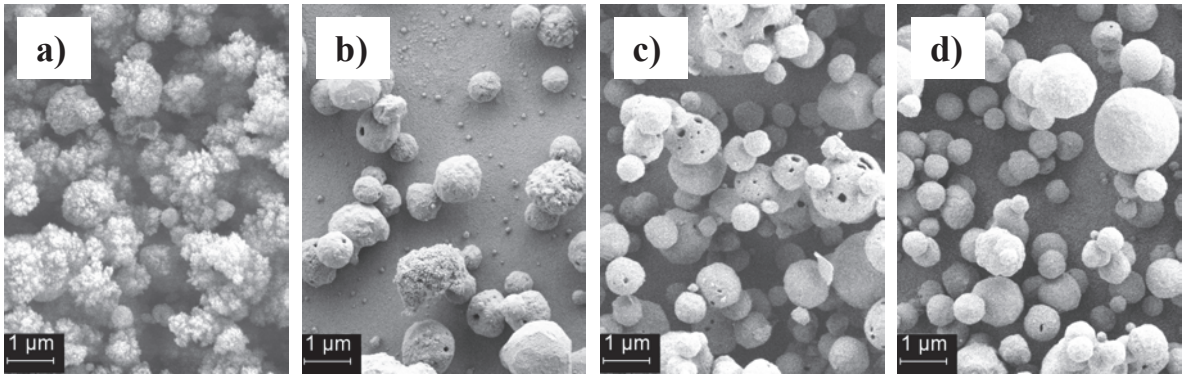

Figure 5.22 - Phosphor particles prepared from the precursor solution with various amounts of polymeric additives: a) no additives; b) 0.02 M CA + 0.02 M EG; c) 0.05 M CA + 0.05 M EG; d) 0.1 M CA + 0.1 M EG; ([RE] = 0.2 M).

Figure 5.22 demonstrates the evolution of morphology of phosphor particles for increasing content of polymeric precursors in 0.2 M solution of rare-earth precursors. In Figure 5.22a, phosphor particles prepared by standard FAD technique are shown. Even small amounts of citric acid and ethylene glycol (0.02 M CA + 0.02 M EG) noticeably improved the surface condition of the particles (Figure 5.22b). As the content

of polymeric components increased, the morphology of the phosphor particles gradually changed, the porosity of the particles decreased (Figure 5.22c) and almost disappeared at concentrations of CA and EG both equal to 0.1 M (Figure 5.22d). However, the PL-intensities measured by excitation at 254 nm were lower than that of no-polymer coatings. The coatings with improved particle morphology approached 90 % of the highest brightness level of the ones deposited without additives, but could not outperform them. The particle size statistics is presented in Figure 5.23 and Table 5.3.

Figure 5.24 demonstrates that excessive and non-stoichiometric amounts of the additives precluded volume precipitation of solid particles and resulted mostly in hollow spheroids with thin walls that easily collapsed and broke apart.

To study the influence of the initial length of the polymeric chain, polyethylene glycol was applied. The resulting morphology of the phosphor particles is presented in Figure 5.25. Due to increased viscosity of the precursor solution prepared with

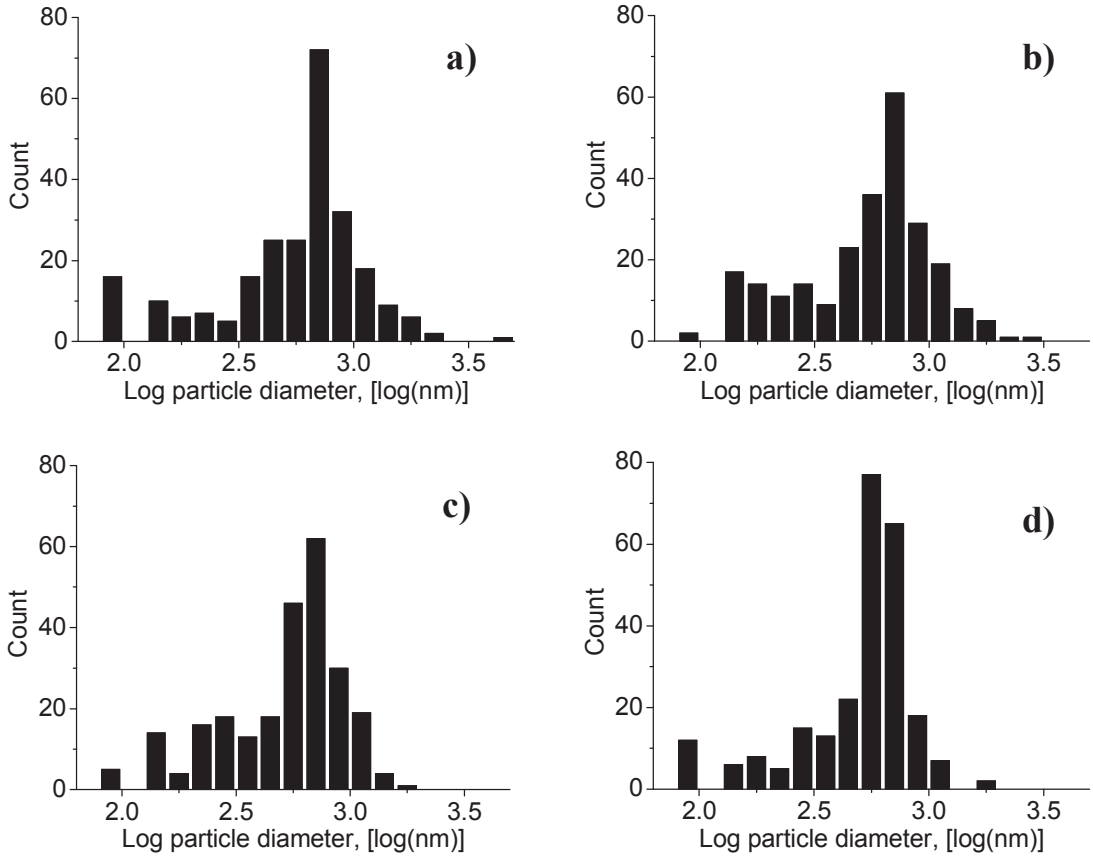

Figure 5.23 - Particle size distribution for the phosphor powders deposited from the precursor solutions with different concentrations of the polymeric additives: a) 0.05 M CA + 0.05 M EG; b) 0.1 M CA + 0.1 M EG; c) 0.1 M CA + 0.1 M PEG (M.W. = 1000); d) 0.1 M CA + 0.1 M PEG (M.W. = 300); [RE] = 0.2 M.

Table 5.3 – Particle size statistics of Y_2O_3:Eu phosphor coatings deposited with addition of polymeric precursors

[RE], M	Amount of CA, M	Amount of EG, M	Arithmetic mean, nm	Geometric mean, nm	GSD	Sauter diameter, nm
0.2	0	0	570	440	2.1	1400
	0.05	0.05	680	550	2.0	1580
	0.1	0.1	640	525	2.0	1100
	0.1	0.1 (PEG 300)	560	490	1.8	760
	0.1	0.1 (PEG 1000)	590	500	1.9	860
0.5	0	0	615	500	1.9	1020
	0.1	0.1	640	470	2.3	1250
	0.2	0.2	740	650	1.8	1100
	0.2	0.2 (PEG 300)	580	480	2.0	860

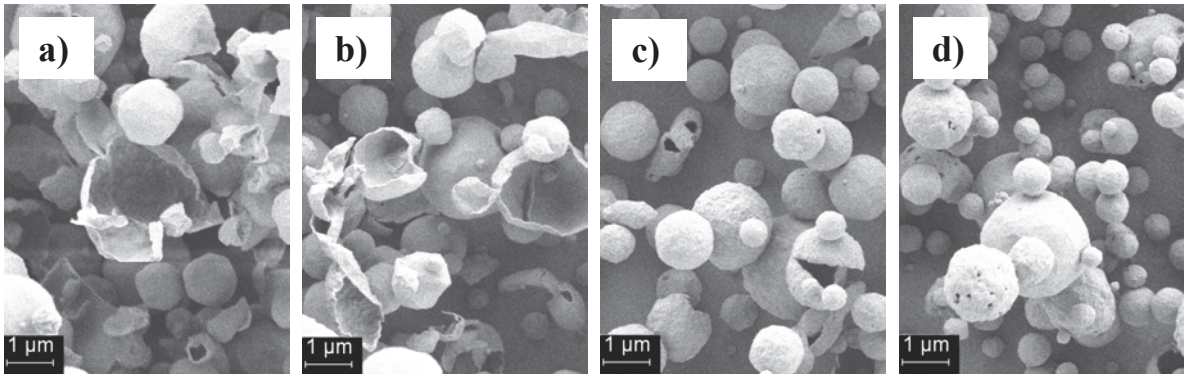

Figure 5.24 - Phosphor particles prepared with excessive and non-stoichiometric amounts of polymeric additives: a) 0.2 M CA + 0.2 M EG; b) 0.2 M CA + 0.1 M EG; c) 0.1 M CA + 0.2 M EG; d) 0.1 M CA + 0.05 M EG; [RE] = 0.2 M.

pure PEG (M.W. = 1000), the efficiency of nebulization significantly decreased and a mixture of EG and PEG with an equivalent molecular weight of 300 was applied (Figure 5.25b). The corresponding geometric mean particle size was 490 nm and GSD decreased to 1.81 (see Figure 5.23 and Table 5.3). However, light output did not improve.

In order to prove the applicability of the technique for higher concentrations of precursors, a series of experiments was performed for a 0.5 M solution of rare-earth ions. Figure 5.26 presents the changes in morphology of the phosphor particles. In

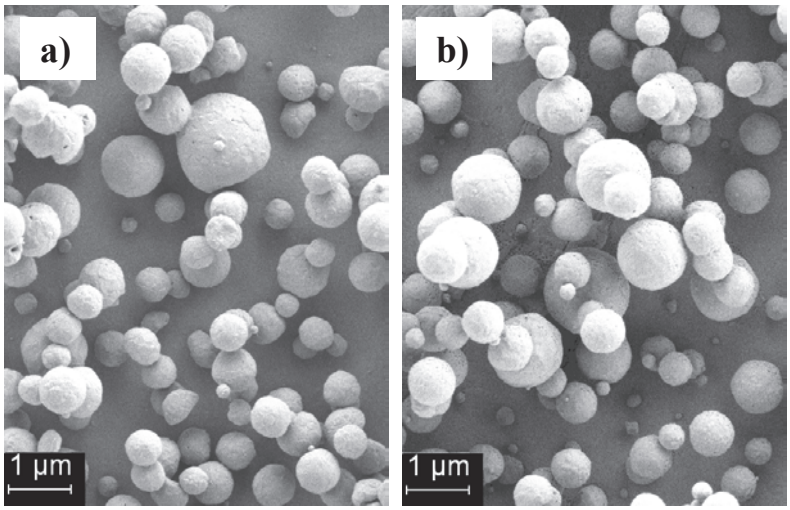

Figure 5.25 - Phosphor particles prepared with polyethylene glycol: a) 0.1 M CA + 0.1 M PEG (M.W. = 1000); b) 0.1 M CA + 0.1 M PEG (M.W. = 300); [RE] = 0.2 M.

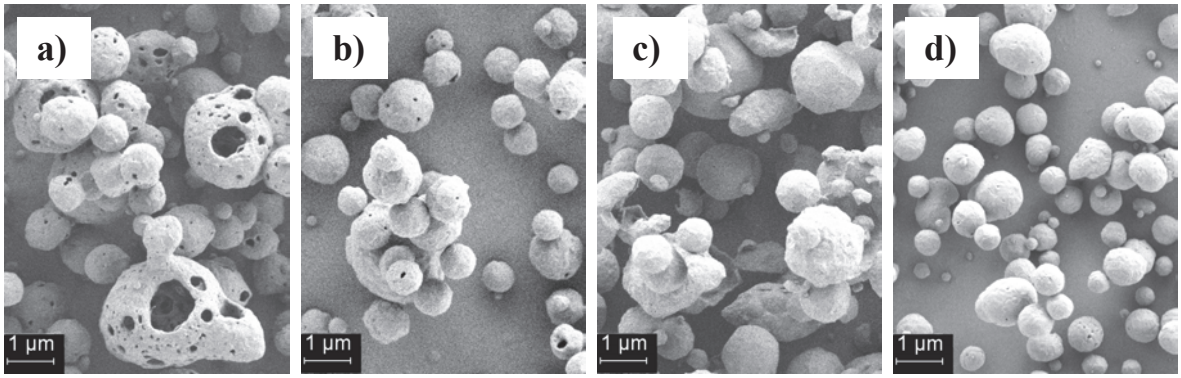

Figure 5.26 - Phosphor particles prepared from the precursor solution with various amounts of polymeric additives: a) 0.1 M CA + 0.1 M EG; b) 0.2 M CA + 0.2 M EG; c) 0.3 M CA + 0.3 M EG; d) 0.2 M CA + 0.2 M PEG (M.W. = 300); [RE] = 0.5 M.

general, it went through the same stages of decreasing porosity to solid spherical particles (Figure 5.26a, b), and further to torn hollow spheres (Figure 5.26c). It should be noted that among all tested concentrations of polymeric components, phosphor particles, with the most filled morphology, were obtained with precursor solutions containing 0.2 M CA and 0.2 M EG, which is considerably higher than the optimum concentration of polymeric components determined for the 0.2 M solution of rare-earth elements. Again, particles of superior spherical morphology were obtained with a stoichiometric mixture of polyethylene glycol and ethylene glycol (Figure 5.26d). Corresponding particle size statistics is shown in Figure 5.27.

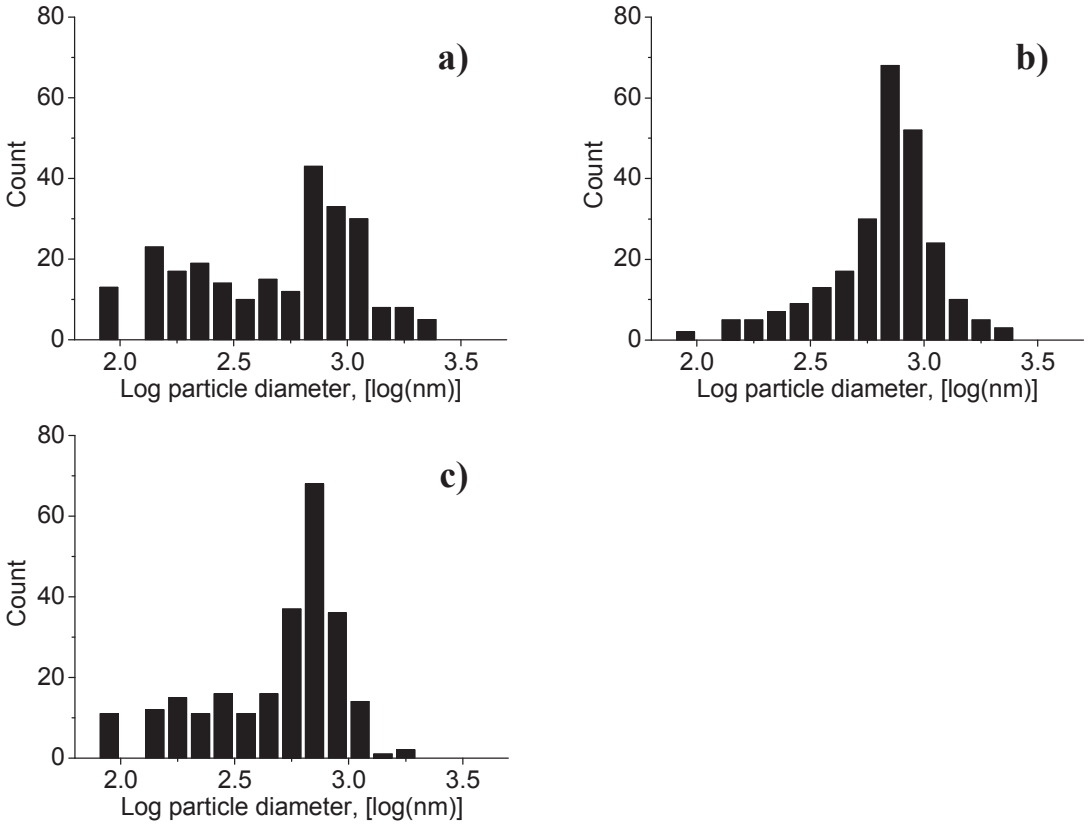

Figure 5.27 - Particle size distribution for the phosphor powders deposited from the precursor solutions with different concentrations of the polymeric additives: a) 0.1 M CA + 0.1 M EG; b) 0.2 M CA + 0.2 M EG; c) 0.2 M CA + 0.2 M PEG (M.W. = 300); [RE] = 0.5 M.

Also for the 0.5 M precursor solution, the highest achieved PL-intensity converged with the brightness of phosphors synthesized without additives; i.e., the brightness of Y_2O_3:Eu phosphor particles produced by the described FAD process, with an excitation of photoluminescence at 254 nm, could not be increased by the introduction of polymeric components to the nebulized solution. This outcome, and the fact that the highest achieved PL-intensities for the screens deposited by flame spray deposition and by sedimentation of commercial phosphor powder were very close to each other mean that the basic FAD-deposition procedure (described in Section 5.1) yields Y_2O_3:Eu phosphor with excellent efficiency for excitation at the wavelength of 254 nm without any further process sophistication.

There could be several possible explanations for the negative effect of improved particle morphology on the brightness of photoluminescence excited at 254 nm. For example, there is an inverse relation between the packing density of phosphor particles in the layer and its brightness. According to Sasaki and Talbot,[74]

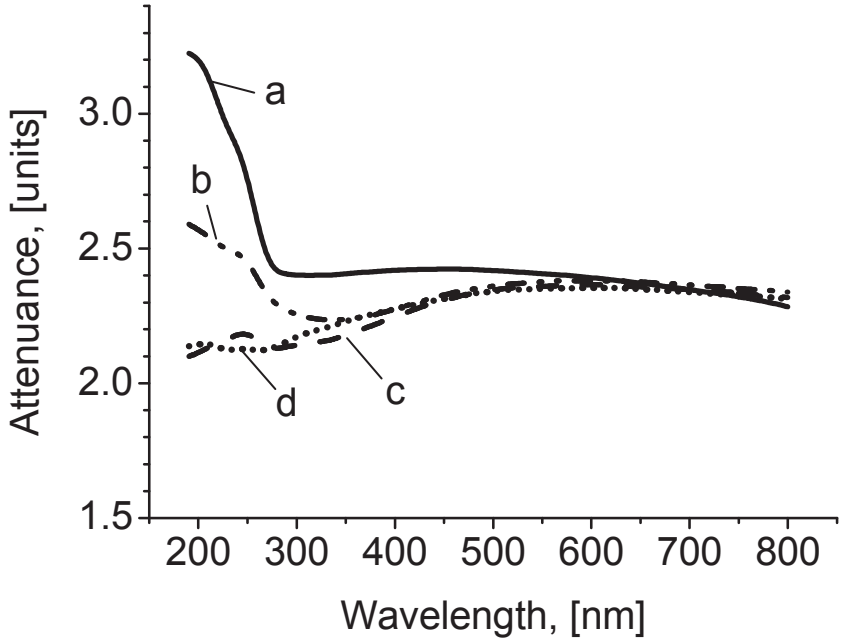

Figure 5.28 - Attenuance spectra of phosphor coatings deposited from precursor solution containing a) no polymer additives; b) 0.05 M CA + 0.05 M EG; c) 0.1 M CA + 0.1 M EG; d) 0.1 M CA + 0.1 M PEG (M.W. = 300); [RE] = 0.2 M, coating densities ~ 0.36 mg/cm^2.

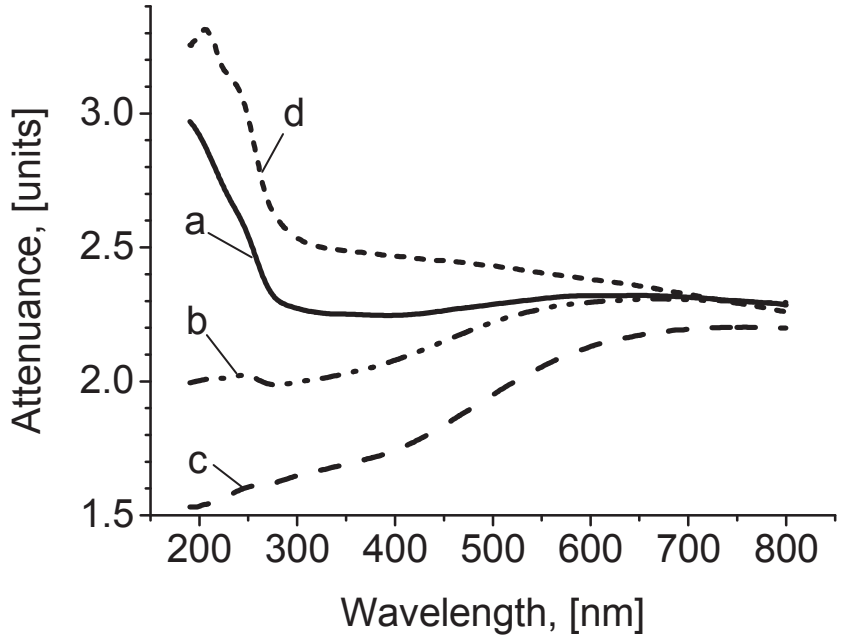

Figure 5.29 - Attenuance spectra of phosphor coatings deposited from precursor solution containing a) no polymer additives; b) 0.1 M CA + 0.1 M EG; c) 0.2 M CA + 0.2 M EG; d) 0.3 M CA + 0.3 M EG; [RE] = 0.5 M, coating densities ~ 0.36 mg/cm^2.

phosphor screens with more densely packed phosphor particles achieve higher resolution but have lower PL-output.

Higher resolution can be related to a reduced scattering of light by the phosphor particles. If one compares screens made from the same phosphor powder by different screen deposition methods, the scattering properties mostly change due to different arrangements of phosphor particles in a screen, which can be characterized by packing density. If phosphor powders in comparison were not synthesized by the same method, one has to account for an influence from different size and shape of phosphor particles on observed scattering as well. In Figures 5.28 and 5.29, the attenuance spectra of the FAD coatings produced with and without polymeric additives are compared. One can observe a substantial decrease of the scattering at shorter wavelengths for the phosphor powders with the improved particle morphology. For excessive amounts of additives, the morphology deteriorates and the corresponding values of attenuance increase again.

It can be expected that, in general, decreased scattering (improved screen resolution) leads to lower brightness of the screen. Unfortunately, the measurements of the attenuance spectra could not be extended to the wavelengths shorter than 190 nm. Furthermore, changes in the light output are not merely determined by scattering; it can also be influenced by minor differences in chemical composition, purity, and crystallinity of the phosphor and should be investigated in the whole wavelength range of destined application.

5.2.2. Analysis of PL-performance throughout the UV-range

In order to test the performance of deposited Y_2O_3:Eu □coatings in VUV, photoluminescence excitation spectra of the three samples with the highest PL-intensity (measured in the T-mode at 254 nm) obtained from 0.2 M solution of rare-earth precursors, were measured in the range from λ = 115 nm to 330 nm using synchrotron radiation: one – deposited without polymers, one – with citric acid and ethylene glycol, one – with citric acid and the mixture of ethylene glycol and polyethylene glycol (M.W. = 300), and the brightest sample deposited by sedimentation of commercial phosphor powder. The results are presented in Figure 5.30.

All photoluminescence excitation spectra in Figure 5.30 feature a peak of efficiency about 210 nm with a noticeable decrease towards shorter wavelengths. This observation agrees with data reported in the literature.[1,208,238–241] The decrease of efficiency is attributed to a strong localization of the conduction band energy levels of Y_2O_3.[240] Some researchers point out that the decrease of the penetration depth of UV light, leading to non-linear energy loss processes, could also be the reason for the minimum of quantum efficiency corresponding to energies of photons equal to ap-

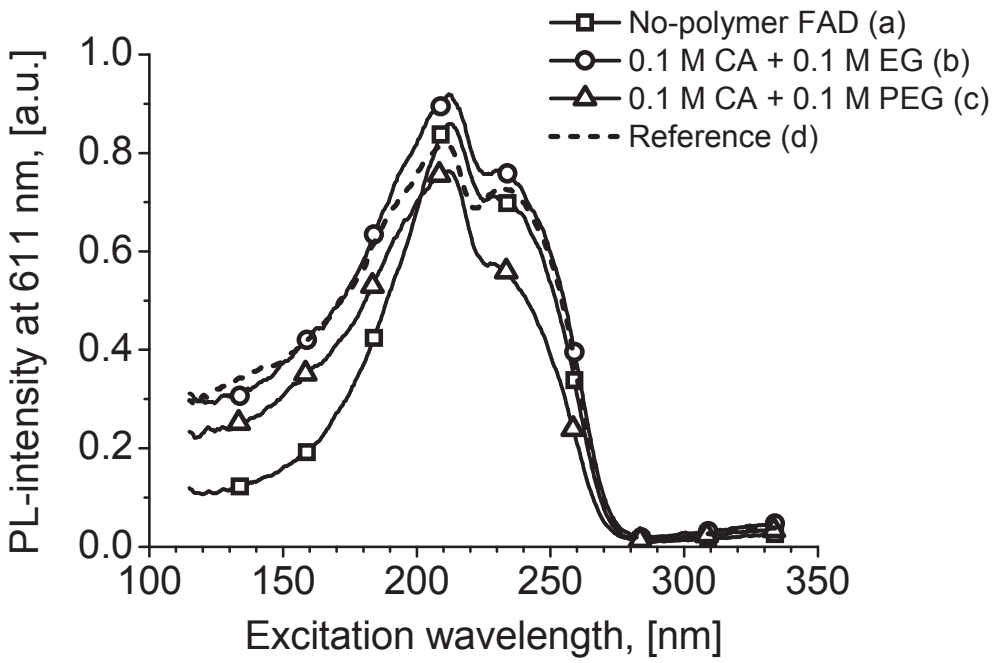

Figure 5.30 – R-mode photoluminescence excitation spectra of phosphor coatings deposited from 0.2 M precursor solution containing: a) no additives, 0.45 mg/cm^2; b) 0.1 M CA + 0.1 M EG, 0.6 mg/cm^2; c) 0.1 M CA + 0.1 M PEG (M.W. = 300), 0.28 mg/cm^2; and d) – reference sample (commercial phosphor), 2.0 mg/cm^2.

proximately 2.5 times the band gap for several different phosphors (14 eV or $\lambda \approx 90$ nm in case of Y_2O_3:Eu phosphor).[242]

For wavelengths shorter than 190 nm, the spectra of the sample deposited with ethylene glycol, and the plate coated by sedimentation of commercial phosphor powder practically overlap. In the range around 157 nm (the wavelength of F_2 excimer laser) - 147 nm (the resonance radiation line of Xe used in most plasma display panels and mercury-free fluorescent lamps) their brightness exceeds that of no-polymer FAD-coating by more than 100 %. This margin further increases towards shorter wavelengths and, at 120 nm, brightness of the sample deposited from the precursor solution containing citric acid and ethylene glycol amounts to 270 % of that of the best sample screened without the additives.

The spectra of PL-excitation in deep UV were measured in the R-mode. Such measurements cannot be done in transmission because, in this regime, intensity strongly depends on the thickness of the phosphor layer. The optimum thickness for the highest brightness in the T-mode is determined by absorption of UV light: the phosphor layer must be thick enough to absorb most of the exciting radiation and emit approximately the same amount of light in both directions (forward and backward). For thinner layers, some of the UV light is not absorbed and therefore overall

brightness is decreased. For thicker coatings, the amount of light emitted backwards gradually increases and output in the transmission mode correspondingly diminishes (see Section 2.2).

In the deep UV range, values of the absorption coefficient steeply increase towards shorter wavelengths,[243,244] and optimum thickness for light output in the T-mode should correspondingly change, i.e., for every wavelength, coatings of different thickness would be needed. As a consequence, it is much more convenient to characterize the efficiency of phosphors by measuring excitation spectra of sufficiently thick layers in the reflection mode.

It should be clarified whether the layer thickness in our case is sufficient and does not influence the measured excitation spectra. If it was not sufficient, the higher brightness of the coating deposited with the addition of polymers (in the reflection mode) could be explained by the fact that its coating density exceeds that of the polymer-free coating. This argument applies well in the case of excitation in the wavelength range about 254 nm, where coating thickness undoubtedly plays an important role: reflection-mode brightness of the coating deposited with citric acid and ethylene glycol (0.6 mg/cm^2) is somewhat higher than the PL-output of the standard polymer-free FAD-coating (0.45 mg/cm^2) and both significantly outperform the coating deposited with citric acid and polyethylene glycol (0.28 mg/cm^2). However, in the range of vacuum UV, the latter coating performs better than the polymer-free one, which cannot be expected from comparison of their thickness.

It is known that the penetration depth of UV-radiation in Y_2O_3:Eu phosphor particles at 254 nm is at least one order of magnitude larger than that, for example, at 173 nm.[243] It should further decrease towards shorter wavelengths because the absorption coefficient is increasing.[244] This means that the dependence of the PL-intensity on the phosphor layer thickness in the reflection mode is not pronounced in this wavelength range and there should be other reasons for the differing performance of FAD coatings.

It can be suggested that the increase of the absorption coefficient towards shorter wavelength could be related to the inferior performance of standard FAD coating in deep UV because the surface condition of phosphor particles becomes extremely important when the penetration depth of UV-radiation into phosphor particles decreases to the several-nm range. It is very likely that the rough surface of the phosphor particles obtained without polymeric precursors has poor light-emitting properties, for example, due to an increased concentration of surface defects which constitute sites of non-radiative recombination of electrons and holes excited by UV radiation.[244] At the same time, spherical phosphor particles produced by polymer-added FAD have a smooth surface and can demonstrate bright PL-output, comparable to that of the commercial phosphor powder throughout the studied wavelength range.

5.3. Deposition of yttrium aluminates doped with terbium

Yttrium aluminum garnet doped by various rare earth ions constitutes an important class of phosphors with numerous applications. The synthesis of YAG:Tb and YAG:Ce powders by conventional ultrasonic spray pyrolysis was reported several times.[245–248] YAG:Ce phosphor has already been obtained by flame-assisted spray pyrolysis.[180,249] Here, for the first time, flame synthesis of YAG:Tb phosphor was studied.

The overall concentration of metal ions in the precursor solution used for deposition of YAG:Tb coatings was 0.2 M. The molar ratio of the rare earths (Y+Tb) and Al-ions was fixed to 3:5. The concentration of Tb was 5 mol.% of the overall concentration of metal ions (i.e., approximately 13 mol.% of the rare earth ions) and was not further optimized. This concentration of the activator is below the concentration quenching threshold, which corresponds to 30 mol.% of the concentration of rare earths in YAG.[250] The standard FAD process parameters were applied (propane flow rate 5 l/min, carrier gas flow rate 3 l/min, minimum nebulization rate, deposition distance 7 cm; see Sections 4.1.1 and 5.1.2).

5.3.1. Morphology and size distribution of synthesized particles

The results of SEM-investigation of the obtained deposits are shown in Figure 5.31a. As opposed to Y_2O_3:Eu FAD-coatings, yttrium aluminate particles had nearly perfect spherical filled morphology with a well defined surface. For comparison, an Al_2O_3 sample was deposited as well (Figure 5.31b). Particles of pure alumina demonstrated a very pronounced hollowness, similar to Y_2O_3:Eu particles produced with excessive amounts of polymeric additives (see Section 5.2).

Particle size statistics for the yttrium aluminate powder is presented in Figure 5.32a. The arithmetic mean particle size was found to be 450 nm (geometric mean 320 nm, Sauter diameter 900 nm). The most remarkable feature of the size distribution is the large number of small particles. The bimodality of the PSD was much more expressed than, e.g., for the yttrium oxide powders obtained from the standard aqueous precursors without additives (see Section 5.1.4). However, a comparable situation was observed when minor amounts of citric acid and ethylene glycol were added to the 0.2 M Y_2O_3:Eu precursor solution (0.02 M CA + 0.02 M EG, see Section 5.2.1). The corresponding PSD is shown in Figure 5.32b.

The bimodal PSD was previously reported for FSP-produced Y_2O_3:Eu.[176] In this pioneering work by Kang *et al.*, the formation of large quantities of nanoparticles was attributed to evaporation and condensation of yttria in the gas phase at flame temperatures close to its melting point. However, in the present work the temperature of the flame was far below the melting points of the synthesized compounds and

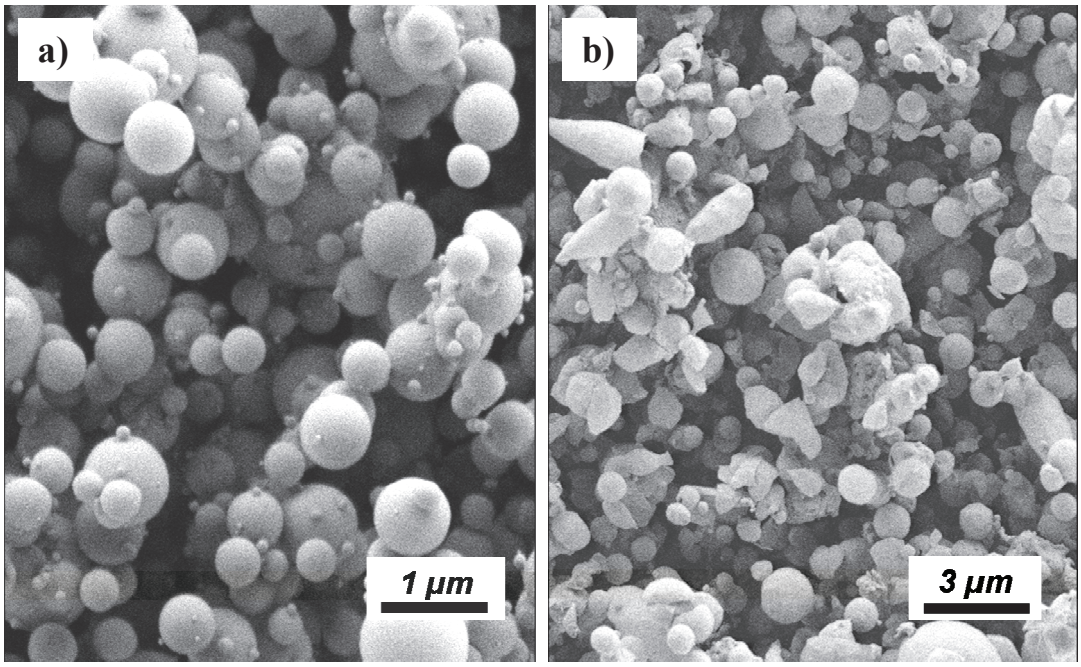

Figure 5.31 – Particles of yttrium aluminate (a) and pure alumina (b) produced by DPC-FAD. The concentration of metal ions in the precursor solution was 0.2 M.

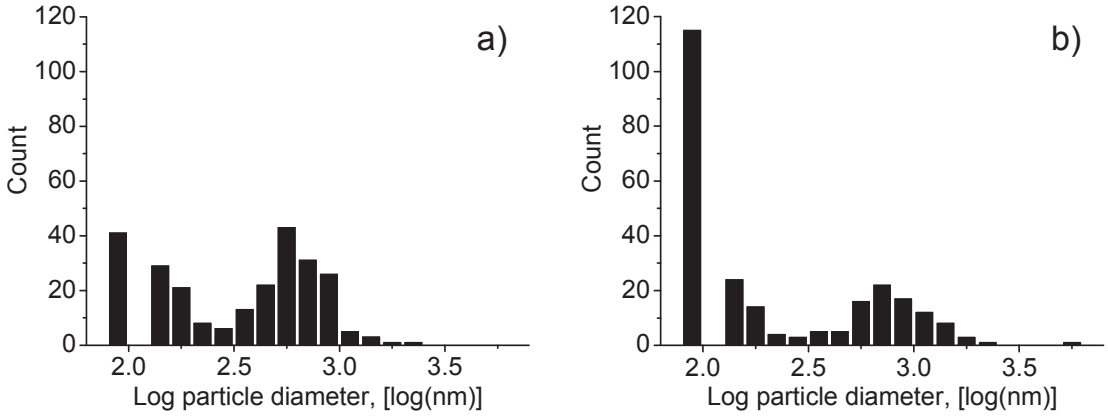

Figure 5.32 – Particle size statistics for yttrium aluminate powder prepared from 0.2 M precursor solution (a) and that for Y_2O_3:Eu powder prepared from the precursor solution containing 0.2 M of rare earth ions and 0.02 M of polymeric additives (b).

therefore, the same argumentation cannot be applied. Furthermore, for both yttrium aluminate and yttria produced with low concentration of polymeric additives in the precursor solution, the deviations from the monomodal PSD become significant for $\log(\phi[nm]) < 2.4$, i.e., for particles with a size just below 250 nm, which is too large for the particles condensed from the gas phase.

In the latest work on FASP-synthesis of YAG:Ce phosphor,[249] formation of nanoparticles was explained by disruption of particles during pyrolysis due to large pressure gradients produced by gaseous products of decomposition of precursors. This effect could be deliberately enhanced by addition of urea to the precursor solution, which leads to a change from the standard DPC mechanism (sometimes abbreviated as ODOP, i.e., “one droplet – one particle”) to a “one droplet - many particles” scheme (ODMP). Powders produced without urea also contained a non-negligible fraction of nanoparticles. Examination of the PSDs of Y_2O_3:Eu powders produced from the concentrated precursors without any additives in the present work (Figure 5.10) confirms that these can also be considered bimodal. Relatively low counts of particles < 100 nm in such coatings could probably be related to the extremely rough surface of particles, which makes nanoparticles difficult to recognize.

Superior particle morphology of FAD-deposited yttrium aluminate coatings is also reflected in higher volume filling fraction (i.e., lower porosity). If the theoretical density of the YAG phase was assumed (4.55 g/cm^3), the volumetric porosity of the deposits would correspond to 86.8 ± 1.5 vol.% (or even less, if one would consider that the density of any amorphous phase is usually somewhat lower than that of the crystalline solids).

5.3.2. Crystallinity of phosphor particles before and after thermal post-treatment

From the point of view of FAD-processing of phosphor screens, there was an important difference between Y_2O_3:Eu and YAG:Tb coatings. Yttria had a cubic crystalline structure immediately after the pyrolysis (see Section 5.1.3) and corresponding coatings could be used without any post-treatment. However, the as-deposited yttrium aluminate powders as well as the alumina coatings (see Figure 5.31) were completely amorphous (Figure 5.33, Curve A) and had to be annealed in order to obtain the desired crystalline phase. This proves again that our implementation of flame spray pyrolysis has much in common with conventional ultrasonic spray pyrolysis, where usually the amorphous yttrium aluminate phase is obtained too.[245] The Ce-doped phosphor powder produced by FSP in a diffusion methane/oxygen flame consisted mostly of the hexagonal (YAH) $YAlO_3$ phase.[180]

The USP-produced powders are usually post-treated at temperatures above 1100℃ in order to obtain a YAG-phase with superior crystallinity. As it can be seen in Figure 5.33 (Curve B), FAD deposits could be converted to YAG (according to JCPDS file # 33-0040) by annealing for 2 h at 900℃. Treatment at higher temperatures resulted in an increase of the size of the YAG crystallites confirmed by reduction of the width of the peaks in the spectra (Curve C). The morphology of phosphor particles did not significantly degrade (Figure 5.34a).

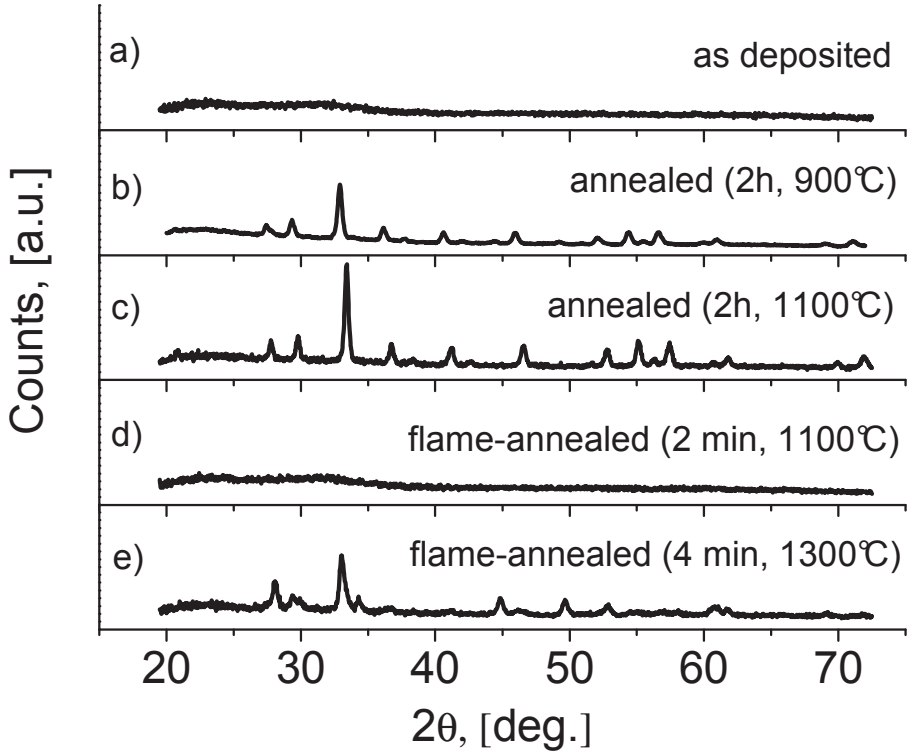

Figure 5.33 – XRD spectra of FAD-deposited yttrium aluminate coatings before and after thermal post-treatment.

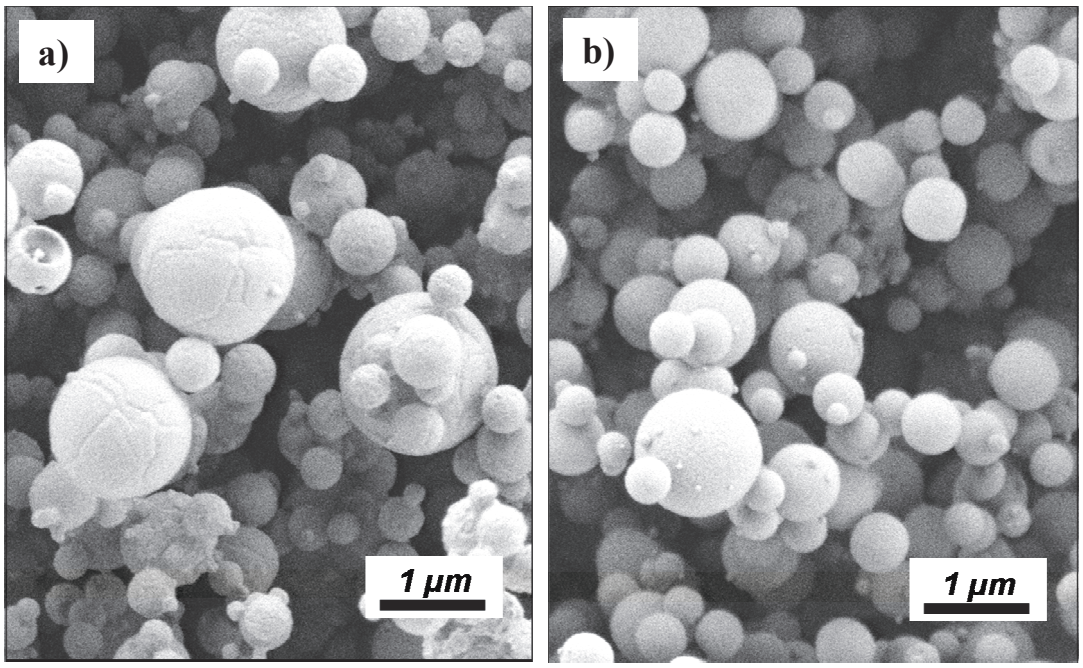

Figure 5.34 – Particles of yttrium aluminate annealed in an oven for 2 h at 1100℃ (a) and flame-annealed for 4 min at 1300℃ (b).

The crystallization of the garnet phase was accompanied by major changes in the efficiency of photoluminescence of the phosphor powder. As-deposited yttrium aluminate coatings produced faint greenish emission when exposed to the UV-light at the wavelength of 254 nm. Its intensity could not even be reliably measured by the standard equipment. After the annealing, the coatings emitted bright green light with the main intensity peak located at 543 nm (Figure 5.35a). A single exponential decay time constant of 2.1 ms was measured. Unfortunately, there were no commercial samples available for the comparison of the photoluminescent performance but it should be noted that the luminescence decay time of the YAG:Tb phosphor obtained by other authors (e.g., Park *et al.*[220]) was 4.2 ms, i.e., twice as long as that measured in the present work. The concentrations of Tb were equal in both cases, which points to the increased probability of non-radiative relaxation of excitation in the FAD-deposited phosphor powder (see Equation 2.1). This issue can be related to the defects of the crystalline structure (e.g., impurities or incomplete crystallization). It was not attempted to further improve on the PL-efficiency of the YAG:Tb phosphor. However, from the results of deposition of Y_2O_3:Eu phosphor screens it can be expected that post-treated YAG:Tb powders synthesized by FAD could also achieve efficiencies very close to the best values for this phosphor produced by other methods.

5.3.3. Flame annealing of amorphous FAD-deposits

The conventional annealing of the initially amorphous $(YTb)_3Al_5O_{12}$ samples in an oven is a relatively time-consuming procedure. The flame annealing, which was previously used for improvement of the luminescent properties of Y_2O_3:Eu (see Section 5.1.3), was also tested. It was found out that the samples treated by the flame for just one minute also started to emit bright green light under UV radiation at 254 nm. Noticeable emission of luminescence was observed even during the flame annealing procedure (it was probably excited by the UV-light originating from the flame). The XRD spectra of the coatings annealed by the flame at the standard conditions (5 cm distance between the burner nozzle and the sample fixed on the water-cooled substrate holder; the temperature on the surface of the substrate was about 1100℃) showed that there was still no crystalline phase (Curve D in Figure 5.33). When excited at 254 nm, the brightness of photoluminescence of such quasi-amorphous samples was about 5 times higher than that of conventionally annealed YAG:Tb samples of the same coating density (Figure 5.35b). The fine structure of the emission peaks disappeared as a result of lacking crystalline ordering. The exponential decay time constant of the luminescence was 1.1 ms, almost twice as short as that of YAG:Tb. Further annealing at the same temperature (for a few minutes) did not change much in the performance of the coatings.

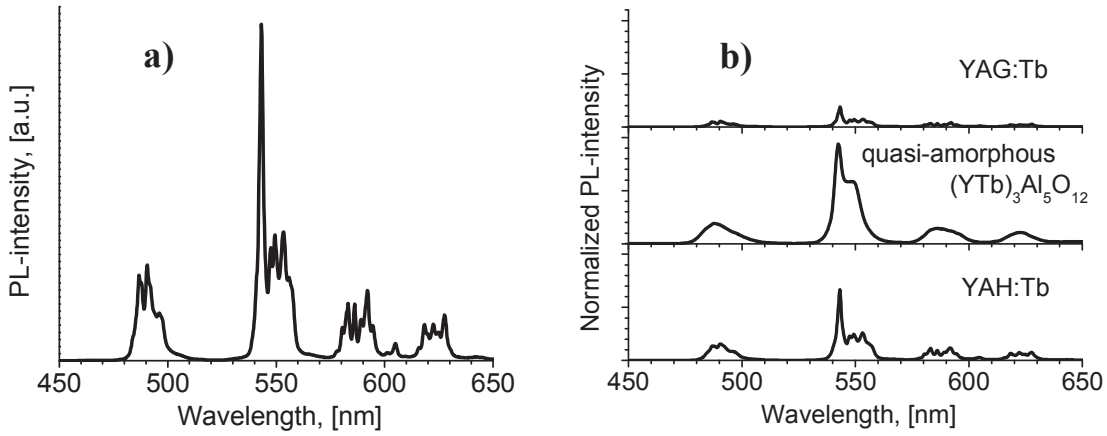

Figure 5.35 – PL-emission spectrum of FAD-deposited YAG:Tb coatings (a) and dependence of brightness of Tb-emission upon crystalline phase of yttrium aluminates for excitation at 254 nm (b).

In order to increase the effective temperature during the flame annealing, several samples were treated without cooling the substrate, i.e., held in the flame with the tweezers at approximately the same distance from the burner as in the standard flame annealing process (5 cm). The temperature measured at the surface of the substrate in this case was approximately 1300℃. Compared to the samples treated at 1100℃, the light output for the excitation at 254 nm decreased by about 50 % (Figure 5.35b). At the same time, a crystalline phase appeared in the XRD spectra (Curve E in Figure 5.33). This phase was identified with the hexagonal modification of $YAlO_3$ (YAH; the JCPDS reference #74-1334). It is important to note that the morphology of the phosphor particles did not change after the repetitive flame annealing (Figure 5.34b). The spectral distribution of the PL-emission of partially crystallized coating was practically identical with that of YAG:Tb. The exponential decay time constants of emission were also quite close (2.3 ms vs. 2.1 ms for YAG:Tb).

The difference in efficiency of luminescence could be clarified by the excitation spectra (Figure 5.36). The YAG:Tb phosphor has a strong excitation band located at about 270 nm and its efficiency substantially decreases towards 254 nm. The efficiency of the quasi-amorphous phosphor gradually increases for wavelengths shorter than 300 nm and at 270 nm it is lower than that of the YAG:Tb. However, they become equal at approximately 260 nm. For even shorter wavelengths of excitation, the quasi-amorphous powder outperforms the fully crystallized phosphor.

The PL-excitation spectra of the partially crystallized coatings (i.e., those containing YAH:Tb) had common features with both the quasi-amorphous and fully crystalline $(YTb)_3Al_5O_{12}$ phosphor. The excitation efficiency had a peak at 270 nm but did not vanish at 250 nm.

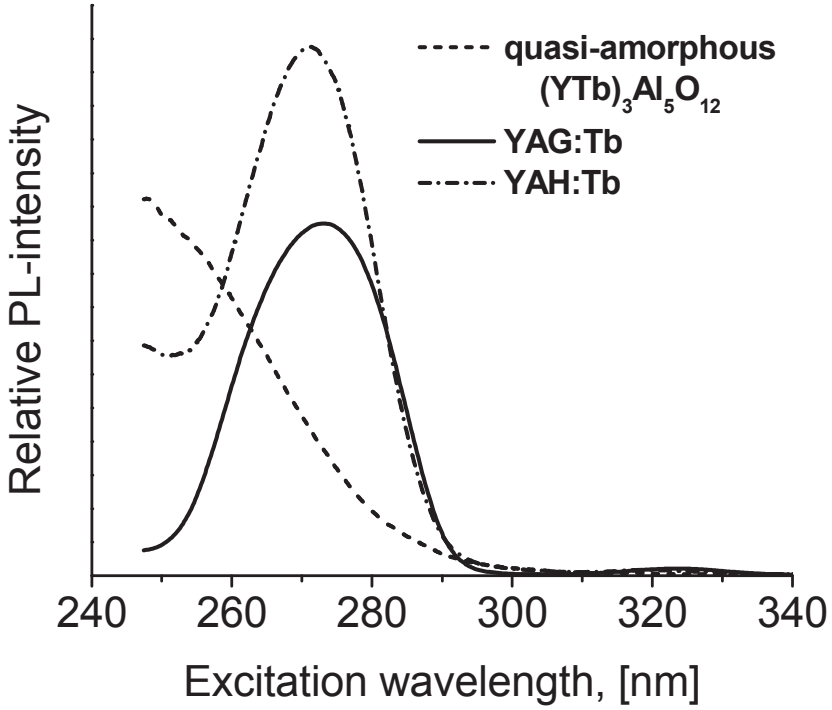

Figure 5.36 – Photoluminescence excitation spectra of post-treated $(YTb)_3Al_5O_{12}$ coatings.

The conventional measurements of the PLE-spectra could not be extended to shorter wavelengths due to the limitations of the available equipment. Fortunately, it was possible to characterize the optical behavior of the coatings for the wavelengths down to 190-200 nm by measuring the spectra of attenuance. The influence of the thermal treatment upon the properties of the $(YTb)_3Al_5O_{12}$ samples is presented in Figure 5.37. One can see that both the oven annealing and the flame annealing noticeably decrease the attenuance in the short wavelength part of the spectra (Figure 5.37a and c). It can also be observed that the shape of the spectrum of the coating treated at 1300℃ becomes similar to the spectrum of the YAG:Tb coating (Figure 5.37b and c, respectively). Finally, the UV-part of the spectra taken with the long-pass filter GG-455 could be converted to the T-mode excitation spectra (Figure 5.37d) by the equation

$$I(\lambda) = 10^{-ATT}, \qquad (5.5),$$

where $I(\lambda)$ is the total PL-intensity at wavelengths longer than 455 nm excited during the measurement at a wavelength λ, ATT denotes the corresponding value of attenuance, which in this case is merely due to the photoluminescence. For non-luminescent samples, the measurements with the filter deliver zero intensity in the UV-range (i.e., $ATT = 6$). The values of attenuance used for derivation of the lumi-

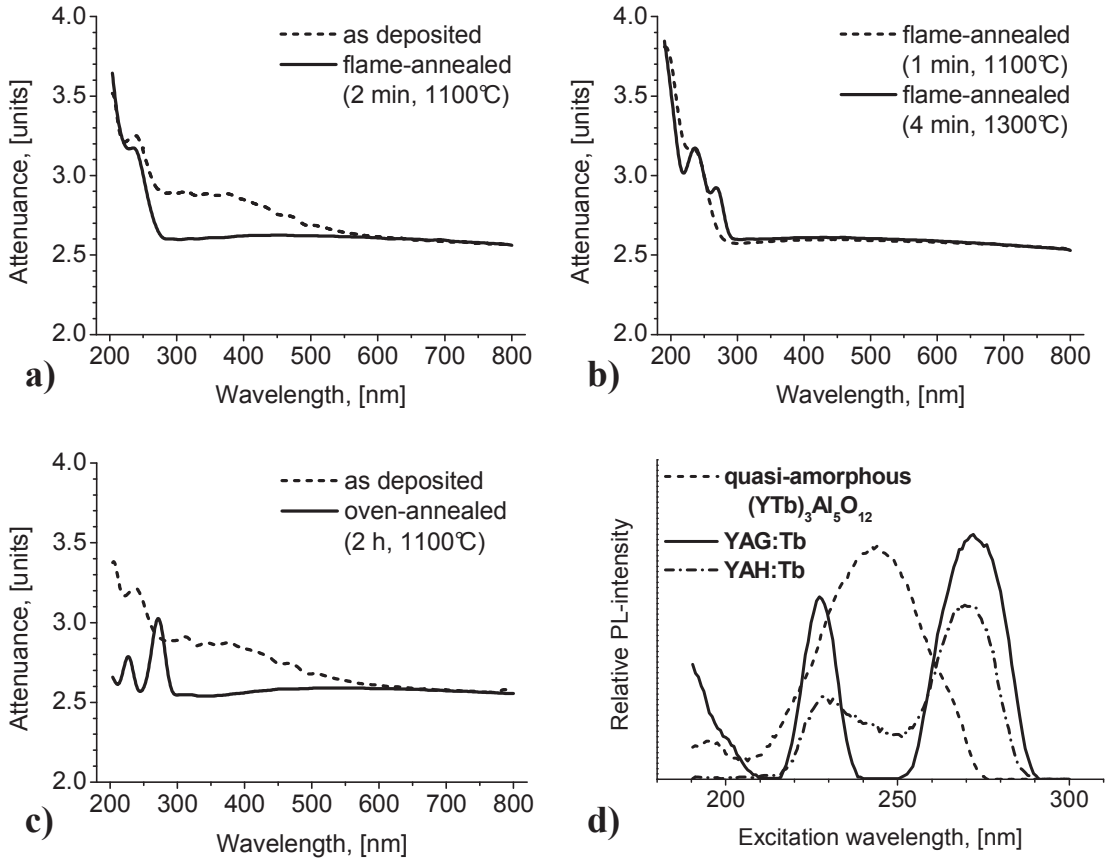

Figure 5.37 – Changes of the attenuance spectra after the thermal post-treatment: a) flame annealing at 1100℃ (resulting in quasi-amorphous $(YTb)_3Al_5O_{12}$); b) flame annealing at 1300℃ (crystallization of YAH:Tb); c) conventional annealing in an oven at 1100℃ (YAG:Tb); and d) PLE spectra derived from corresponding attenuance spectra taken with the filter GG-455.

nescence intensity generally were in the range of large values (> 2) and thus they could not be used for any quantitative analysis. Nevertheless, there is a good agreement with the "classical" excitation spectra in Figure 5.36 so that the spectra obtained from attenuance spectroscopy can be used for a qualitative comparison of the efficiency of luminescence of the coatings outside the span of the conventional PLE-spectra.

One can see in Figure 5.37d that the emission intensity of the quasi-amorphous $(YTb)_3Al_5O_{12}$ coating starts to decrease below 240 nm and reaches the minimum at about 200 nm. The spectrum of the YAG:Tb screen, along with the peak shown in Figure 5.36, features a second peak centered at 225 nm and a part of the third peak below 210 nm. The spectrum of the partially-crystallized YAH:Tb sample also has two peaks at 225 and 270 nm but does not show any increase below

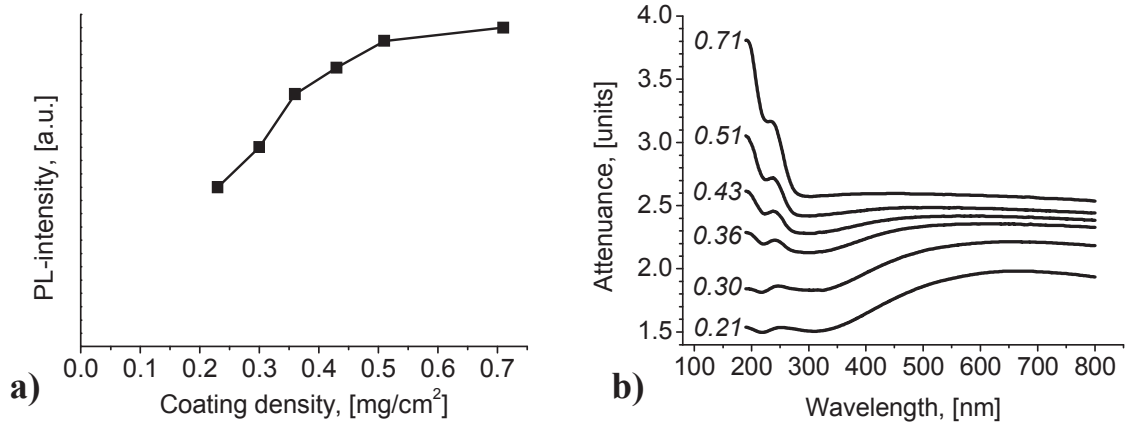

Figure 5.38 – Dependence of the T-mode PL-brightness (a) and attenuance (b) on coating density of the flame-annealed quasi-amorphous $(YTb)_3Al_5O_{12}$ coatings. The values of screen density in (b) on the left from the corresponding curves are in units of mg/cm^2.

210 nm. The spectra of the quasi-amorphous and fully crystalline YAG:Tb coatings completely match those found for the Tb-activated yttrium aluminates produced by the sol-gel technique.[220] There is also a fair agreement with a further recently published investigation on annealing of sol-gel-derived YAG:Tb.[251]

A series of quasi-amorphous $(YTb)_3Al_5O_{12}$ coatings of different densities ranging between 0.21 and 0.71 mg/cm^2 were prepared in order to investigate the dependence of the T-mode PL-brightness on the thickness of the screen. As it can be seen in Figure 5.38a, the highest intensity was measured for the thickest coating. This means that the optimum thickness is greater than 0.51 mg/cm^2. One could apply the conclusion made in Section 5.1.7 that the optimum thickness for a given wavelength of excitation corresponds to the attenuance of about 3 units. The attenuance spectra depicted in Figure 5.38b allows the coating density of approximately 0.7 mg/cm^2 to be considered as the optimum for excitation at 254 nm. It is worth emphasizing that also in the case of yttrium aluminate coatings deposited by DPC-FAD the attenuance decreases towards the shorter wavelengths in the visible range as a consequence of the sub-micrometer size of the phosphor particles.

5.4. Summary on DPC-FAD of phosphor coatings

In this chapter, the deposition of monochrome unpixelated phosphor screens by the FAD-technique based on droplet-to-particle conversion was investigated. As the most important result, the feasibility of coatings with submicron phosphor particle size and brightness comparable to the conventional micrometer-sized phosphors was demonstrated. The optimum thickness of phosphor coatings under excitation at 254 nm was in the range 0.4-0.7 mg/cm^2, which was 3-5 times less than would be required with commercial phosphors. The deposition procedure starting with aqueous solutions of rare earths took less than 15 minutes.

The phosphor particle size could be effectively controlled by changing the concentration of the precursor solution. Practically relevant concentrations of the precursor solution were higher than 0.01 M due to the decrease of the deposition rate, thus limiting the size of the phosphor particles produced by pure DPC-FAD to those substantially larger than 100 nm (in terms of the geometric mean). This can be considered as a general drawback of the DPC-based methods although it could be potentially overcome by addition of chemicals, which stimulate production of many nanoparticles from a single droplet of the precursor solution (e.g., urea[249]). Another disadvantage limiting the deposition rates of FAD is the considerable loss of material (overspraying); only a few percent of the produced powder could be deposited on the substrate.

It was found that the morphology of particles prepared in the low-temperature propane/air premixed flames strongly depends on the chemical nature of the synthesized compound. As-synthesized Y_2O_3:Eu phosphor particles had rough surface and expressed porosity, whereas $(YTb)_3Al_5O_{12}$ particles had nearly perfect filled spherical morphology. At the same time, the as-synthesized Y_2O_3:Eu phosphor powder had the desired cubic crystallographic phase unlike the amorphous yttrium aluminate coatings, which had to be thermally post-treated in order to obtain the YAG phase. Along with the conventional annealing in an oven, the flame annealing procedure was found to be effective for improving the brightness of both the crystalline Y_2O_3:Eu and the quasi-amorphous $(YTb)_3Al_5O_{12}$ phosphors. In the latter case, the changes of the optical properties between the quasi-amorphous, partially crystalline (YAH) and fully crystalline YAG:Tb phases could be studied.

For the first time, it was demonstrated that the morphology of the Y_2O_3:Eu phosphor particles prepared by low-temperature flame spray pyrolysis could be improved by the addition of polymeric compounds to the precursor solution. The optimum content of polymeric additives for a spherical filled morphology of the phosphor particles changed according to the concentration of rare-earth ions in the precursor solution. The light output of the deposited phosphor coatings could not be increased by the application of polymeric additives in the case of excitation of photolumines-

cence in the wavelength range from 330 nm down to 220 nm, where the standard FAD-procedure suffices. However, in UV-light with shorter wavelengths, polymer-added FAD provided significant advantages in performance due to the improved surface condition of the phosphor particles.

The particle filling fraction of FAD-deposited phosphor screens (8-13 vol.%) was at least two times lower than that of the conventional phosphor screens (30-60 %[58,71]). In the worst case, i.e., 8 % vs. 60 % particle fraction, the difference would be much greater. The resolution of a screen is mainly determined by the geometric thickness of the phosphor layer (see Section 2.2.4). Therefore, when comparing the performance of the screens optimized for the highest T-mode brightness, FAD-screens could hardly offer a better resolution. According to Equation 2.71, the LSF (L_{05}) of about 60 µm could be expected for the standard Y_2O_3:Eu FAD phosphors with the optimum thickness. If some application would require the maximum possible brightness, the practical advantages of FAD would be limited merely to the extremely rapid processing. In order to make use of the advantage of reduction of the screening densities achieved for sub-micrometer-sized phosphors, a means to decrease material losses is needed. The consumption of phosphors could be reduced, e.g., if the powders synthesized by flame spray pyrolysis were collected by a filter, dispersed in a liquid, and then deposited on the screens by electrophoresis.

For applications demanding very high screen resolution, the thickness of the phosphor layer can be decreased at the cost of brightness of emission as long as the phosphor particles still fully cover the substrate (i.e., without large gaps between the neighboring particles). From the SEM investigation, FAD screens deposited from the 0.2 M precursor solutions can still be considered “continuous” down to approximately 0.15 mg/cm^2. The corresponding T-mode PL-intensity would total about 40 % of the maximum value. The LSF would be decreased to 15-20 µm (assuming that Equation 2.71 still holds). Only a slightly better resolution would probably be achieved with the screens deposited from the 0.01 M precursor solutions, which could cover the substrate at 0.1 mg/cm^2. The benefit of substantially decreased particle size for the screen resolution cannot be efficiently exploited when the particles are packed very sparsely. In order to realize a diffraction-limited phosphor screen, both the largest phosphor particles and the interparticle spacing should be smaller than a half of the wavelength of light emitted by the phosphor. It is, therefore important to be able to deposit nanoparticle phosphor screens ($\phi < 100$ nm). However, this requires a change of the mechanism of formation of phosphor particles. For example, the “one droplet to one particle” conversion can be modified to the “one droplet to many particles” mechanism.[249] In the present work, the feasibility of FAD based on chemical vapor condensation was investigated for this purpose.

6. FAD based on chemical vapor condensation

6.1. Choice of the process parameters

The FSP synthesis of yttria from precursors obtained by dissolving yttrium nitrate in ethanol and 2-ethylhexanoic acid was suggested by Jossen *et al.*[252] Prior to the experiments described here, this precursor composition had never been applied to luminescent Y_2O_3:Eu nanoparticles. The reader should refer to the article by Strobel and Pratsinis[253] for discussion of the influence of the chemical composition of the precursor solution on the properties of the FSP-produced oxide powders.

Successful preparation of ultrafine Y_2O_3:Eu phosphor powders by CVC-based FSP has already been reported.[137,177] The choice of the FAD process parameters was based on these reports. Particularly, it was found that the size and crystalline phase of the synthesized nanoparticles of the phosphor strongly depend upon the feed rates of the precursor and dispersion gas (oxygen). For example, at 5 ml/min of 0.4 M solution of rare earth ions and 5 l/min of dispersion oxygen (i.e., “5/5 flame”), the synthesized nanophosphor had a mean diameter ϕ_{BET} of 11 nm and phase-pure monoclinic crystalline structure. At higher feed rates of the precursor and lower feed rates of the dispersion oxygen (e.g., 8/3 flame), the size of particles gradually increased and collected powders consisted almost entirely of cubic yttria. As discussed in the previous chapter, cubic modification is desirable for higher brightness of PL-emission.

Changes of the crystalline structure of the Y_2O_3:Eu nanophosphor obtained in the present work are presented in Figure 6.1. The observed trends were in a good agreement with the work on FSP synthesis of the Y_2O_3:Eu phosphor.[137] The maximum precursor feed rate, however, had to be increased from 8 to 11.7 ml/min in order to adjust the total heat release rate and the length of the flame – the heat of combustion of the precursor solution used in this study was lower than the heat of combustion of the previously used 2-ethylhexanoates dissolved in 2-ethylhexanoic acid (EHA) and toluene[137] (25.1 kJ/ml and 33.4 kJ/ml, respectively). The concentration of rare earth metal ions was also increased from 0.4 to 0.5 M so that for the appropriate FAD conditions (precursor feed rate of 11.7 ml/min and 3 l/min of dispersion O_2, denoted by “12/3 flame”), the length of the flame was equal to that used in the previous work (24 cm) and the size of produced phosphor particles was comparable (d_{BET} = 23 nm[137] vs. 24 nm, here). The results of TEM-inspection of the powders produced in 12/3 and 5/5 flames are shown in Figure 6.2.

Relations between the process parameters and properties of the Y_2O_3:Eu phosphor powders are summarized in Table 6.1. As can be seen in Figure 6.3, the increase of the precursor feed rate and/or the decrease of the flow rate of dispersion oxygen led to an increase of both the phosphor particle size and the weight fraction

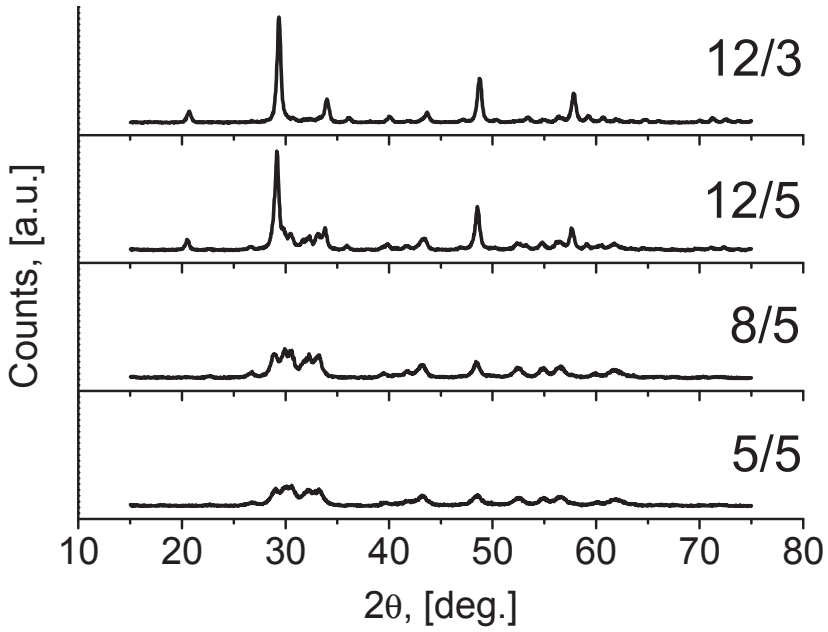

Figure 6.1 – XRD spectra of Y_2O_3:Eu powders synthesized by CVC-based FAD at different feed rates of the precursor (x, ml/min) and dispersion oxygen (y, l/min) denoted by x/y; [RE] = 0.5 M.

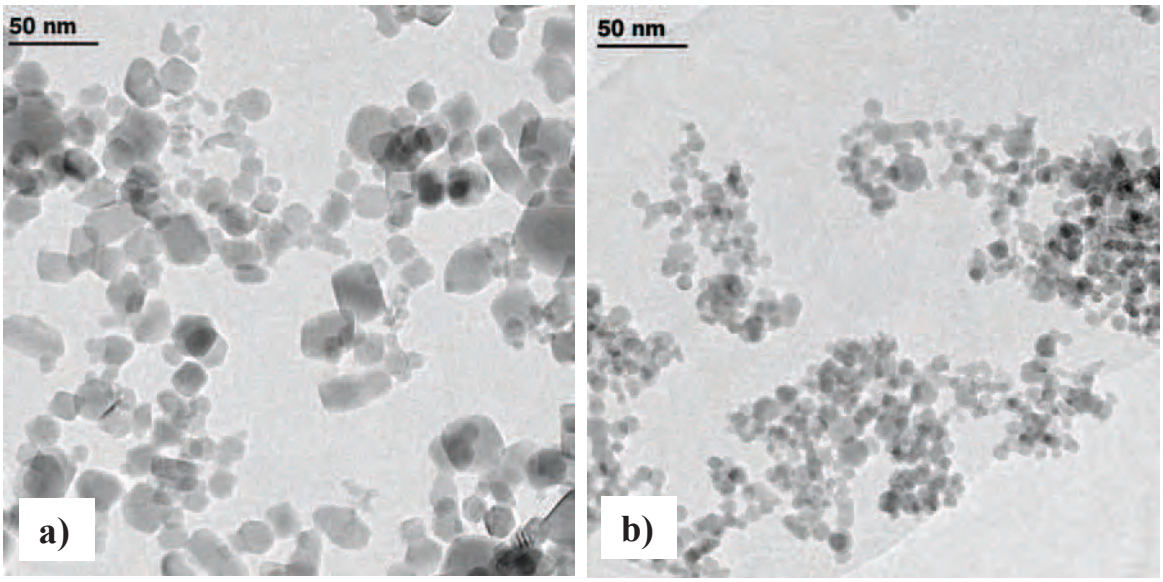

Figure 6.2 – Morphology of Y_2O_3:Eu nanoparticles obtained from 12/3 flame (a) and 5/5 flame (b); [RE] = 0.5 M.

of the cubic phase. The relationship between the crystalline phase and the size of the particles is important for various realizations of flame synthesis because it can substantially complicate production of fine and ultrafine powders in a desired crystallographic modification.

Flame synthesis of cubic and monoclinic yttria and various sesquioxides of rare earths was extensively studied.[118,254–257] It has been proposed that there is a certain critical particle size and particles exceeding this value mostly have the cubic crystal structure, whereas those smaller than the threshold tend to crystallize in the metastable monoclinic phase. Such behavior can be explained by the Gibbs-Thomson effect (see Section 2.3.3e), i.e., by a sufficiently high internal pressure produced by the surface energy of particles with very small radii of curvature.[258] However, the critical particle size is not a material-specific constant: it strongly depends on

Table 6.1 – CVC-FAD parameters and properties of synthesized of Y_2O_3 powders (concentration of precursors: 0.5 M, undoped, except for the sample obtained from 0.1 M precursor solution, which was doped with 5 mol.% of Eu-ions)

Precursor feed rate, [ml/min]	Dispersion oxygen feed rate, [l/min]	Stoichiometric consumption of O_2, [l/min]	Weight fraction of cubic phase	XRD cubic grain size, [nm]	XRD monoclinic grain size, [nm]	BET particle size, [nm]
5.0	5	6.4	2 %	25	12	12
8.4	5	10.6	3 %	24	15	16
11.7	5	14.8	43 %	25	17	18
8.0	3	10.2	53 %	28	20	21
11.7	3	14.8	86 %	29	22	24
11.7 [0.1 M]	3	14.8	84 %	21	16	

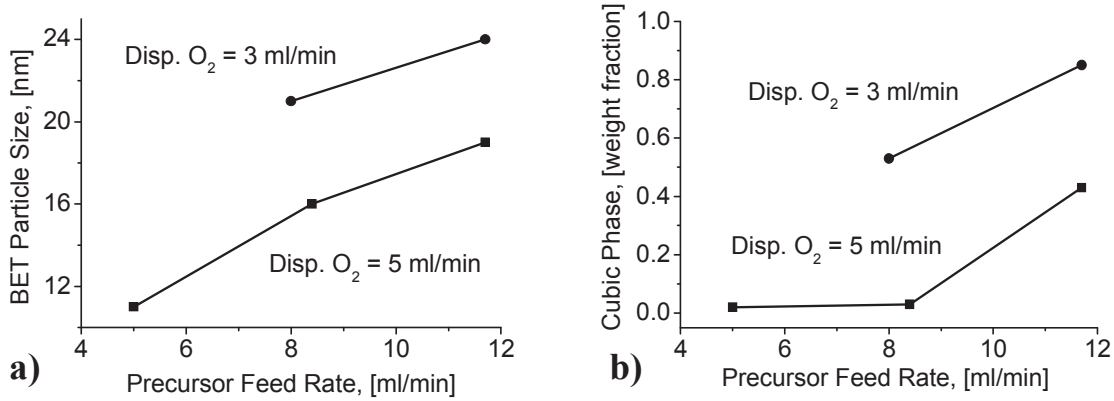

Figure 6.3 – Influence of the process parameters on the particle size (a) and phase composition (b) of the FAD-produced yttria nanoparticles; [RE] = 0.5 M.

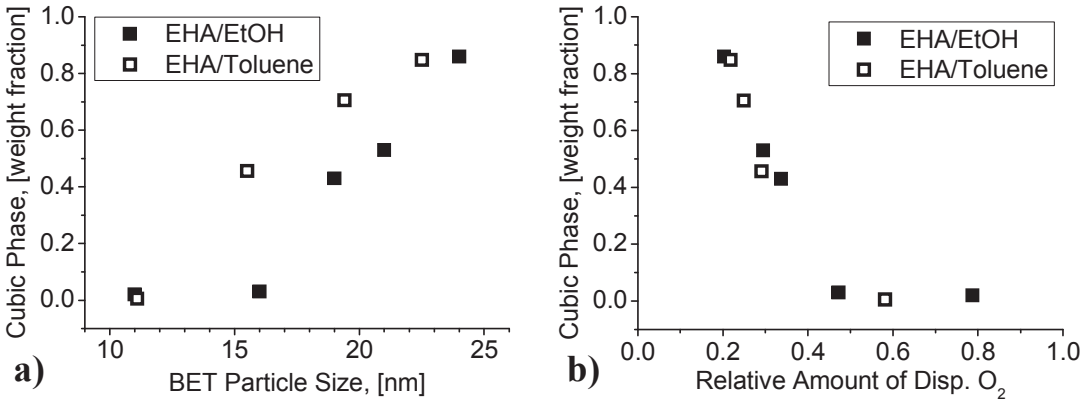

Figure 6.4 – Influence of the particle size (a) and the feed rate of dispersion oxygen normalized to the stoichiometric consumption rate (b) on the fraction of the cubic yttria. Data for the EHA/toluene precursor are taken from Camenzind *et al.*[137]

the temperature of the flame and can be decreased by tuning the conditions of synthesis. Furthermore, in some cases the concept of the critical particle size cannot be reliably applied. A comparison between the FAD-coatings deposited from the 0.5 M and 0.1 M precursor solutions at otherwise equal process conditions revealed no significant difference concerning the phase composition of the powders (see Table 6.1) although the particle size decreased by about 30 %.

Figure 6.4a depicts the interdependence of the BET particle size and the fraction of the cubic phase for the yttria nanoparticles obtained in the present work. Points corresponding to the results of the previous study on CVC-FSP[137] are also shown for comparison. One can see that powders with approximately equal mean size of particles can contain considerably different amounts of the cubic phase depending on the particular process parameters.

An important parameter affecting the temperature of the flame is the composition of the oxidizer. During combustion of the spray, the dispersion oxygen should be consumed. However, if the oxygen flow rate is insufficient for complete combustion of the fuel, the rest is taken from the ambient atmosphere. A stoichiometric combustion of 1 ml of the mixture of EHA and ethanol at normal conditions requires 1.35 l of oxygen. In all studied cases, there was a deficiency of the dispersion oxygen so that considerable amounts of atmospheric oxygen were involved in the reactions. This also means that the temperature of the flame was inevitably decreased by dilution with the atmospheric nitrogen. Each liter of oxygen taken from air brings approximately 3.7 l of nitrogen into the flame zone. Therefore, the fraction of the dispersion gas in the stoichiometric consumption of oxygen can be related to the flame tempera-

ture and as a consequence, to the relative amount of the cubic phase. The corresponding graph is shown in Figure 6.4b. The data points obtained with the precursors based on the EHA/toluene mixture[137] are also shown. In the latter case, the complete combustion of 1 ml of fuel consumed 1.7 l of oxygen. It is not attempted to assess the corresponding values of the temperature of the flame due to the considerable complexity of modeling the air entrainment during the FSP process. The reader can refer, for example, to the study of Heine *et al.*[259] for discussion of the problem. Direct measurements of the flame temperature also could not be performed because the temperature of the spray flames was outside the application range of the thermocouples.

It is possible to compare our results with the prior work on the flame synthesis of nanoparticles by considering the ratio between the minimum flow rate of diluting gases and the stoichiometric oxygen consumption rate. In the work of Guo *et al.*,[254] the oxidizer was deliberately diluted with nitrogen or argon and yttria nanoparticles of purely monoclinic phase were synthesized in the gas phase when the diluent/oxygen ratios were less than 0.25. Cubic yttria could be obtained when this ratio was greater than 1. As can be seen in Figure 6.4b, FAD- and FSP-produced yttria nanoparticles had a nearly pure monoclinic phase when the dispersion oxygen contributed at least 40-50 % of the stoichiometric oxygen consumption rate. A significant fraction of the cubic yttria could be obtained only when more than 60 % of the required oxygen was taken from the atmosphere, which leads to a threshold value of approximately 2 for the ratio of the volumes of nitrogen brought with air to the total consumption of oxygen. The phase-pure cubic yttria would be obtained in the flames corresponding to diluent/oxygen ratios in excess of 3, which would require the use of synthetic air or nitrogen as the dispersion gas or addition of pure nitrogen as a sheath gas. The difference between the threshold values found in the present work and those reported by Guo *et al.*[254] is likely to be due to the unequal temperature of the flame due to the different specific combustion enthalpy of the fuels.

For all further experiments, the Y_2O_3:Eu nanophosphor powders were produced in the 12/3 flames. The influence of the traces of the monoclinic phase still present in these powders is considered to be very small and therefore no further optimization of the FAD-process was undertaken.

6.2. Effects of Eu-doping

A detailed XRD spectrum of the nanophosphor obtained from the 12/3 flame is shown in Figure 6.5. The peaks corresponding to the cubic and monoclinic phases are denoted by “C” and “M”, respectively. In full agreement with literature,[137] the fraction of the monoclinic phase increased with the addition of europium from less than 15 wt.%, for pure yttria, to 23 wt.%, for the powder containing 12 mol.% of the dopant

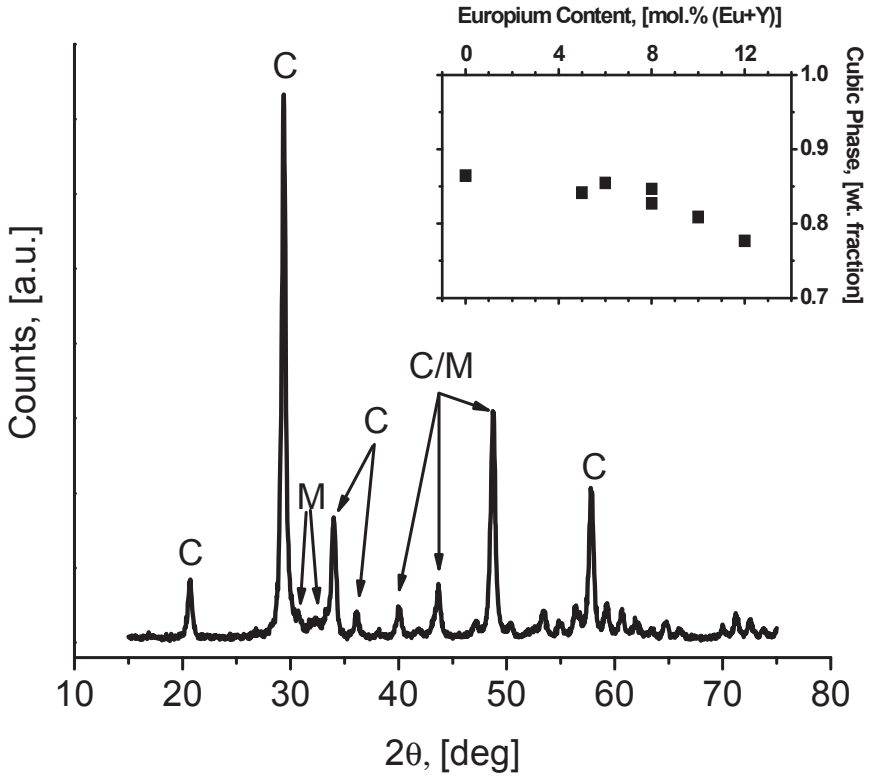

Figure 6.5 – Peaks of the cubic and monoclinic phases in the XRD spectrum of the phosphor nanoparticles obtained from the 12/3 flame. Changes of the amount of the cubic phase due to Eu-doping are shown in the inset. [RE] = 0.5 M.

(see the inset in Figure 6.5). The influence of the Eu-doping can fully explain the small difference between the phase composition of the nanophosphor powders produced from the 0.5 M and 0.1 M precursor solutions (see Table 6.1). It can be concluded that the amount of the cubic phase is not directly affected by the size of phosphor particles.

Figure 6.6 shows a representative EDX-spectrum of the Y_2O_3:Eu nanopowder. The samples did not contain any significant amount of elements other than yttrium, europium, and oxygen. The carbon peak comes from the material of the substrate holder for the EDX-analysis. The relative concentration of europium in the precursor solution and in the obtained powder was equal within the measurement error (8±1 mol.% and 8.8±2.6 mol.%, respectively). The inaccuracy of europium concentration in the precursor arises from the procedure of weighing the rare earth salts before dissolving them in ethanol. Nitrates of yttrium and europium are highly hygroscopic and may contain varying amounts of absorbed water.

The spectra of photoluminescence were identical with those of the commercial Y_2O_3:Eu phosphors and sub-micrometer-sized phosphor produced by DPC-FAD.

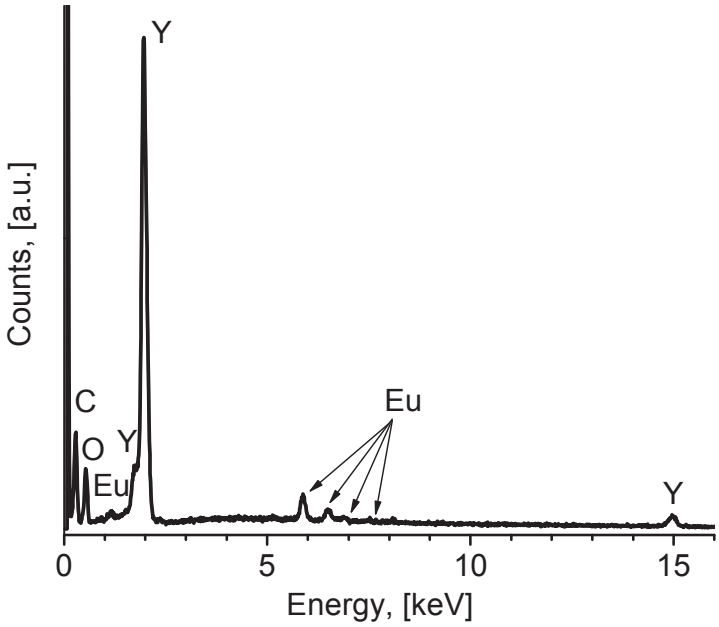

Figure 6.6 - EDX spectrum of Y_2O_3:Eu nanopowder, produced from the precursor solution containing 8 mol.% Eu.

They also did not differ from the PL-spectra of the nanophosphor synthesized from the EHA/toluene precursor mixture.[137] Thus, it can be concluded that the nitrates of rare earth elements dissolved in ethanol and 2-ethylhaxanoic acid can be used instead of the significantly more expensive 2-ethylhexanoates.

The influence of the dopant concentration on the intensity and the exponential decay time constant of photoluminescence is presented in Figure 6.7. The brightness of nanophosphor powders reached 40 % of that of the commercial reference, which is in the range of reported values for Y_2O_3:Eu nanophosphors.[260,261] The single-exponential PL-decay time constant gradually decreased from 3.3 ms to 2.4 ms between 4 and 12 mol.% Eu, respectively. For the optimum concentration of europium (8 mol.%), a value of approximately 2.8 ms was obtained. Such low decay rates (compare with 1.0-1.4 ms for conventional and sub-micrometer-sized phosphors) are characteristic for nanophosphors[5,107,137]

It must be mentioned that even at the lowest tested concentration of the activator the decay curve noticeably deviated from the single exponential decay. The goodness of fit could be substantially improved by using a sum of two exponential terms. One can see in Figure 6.7b that the faster decay component provides the main contribution to the PL-intensity. It also goes through a peak at 8 mol.% Eu, whereas the amplitude of the slower component monotonically decreases throughout the studied concentration range. Both decay time constants get shorter with higher

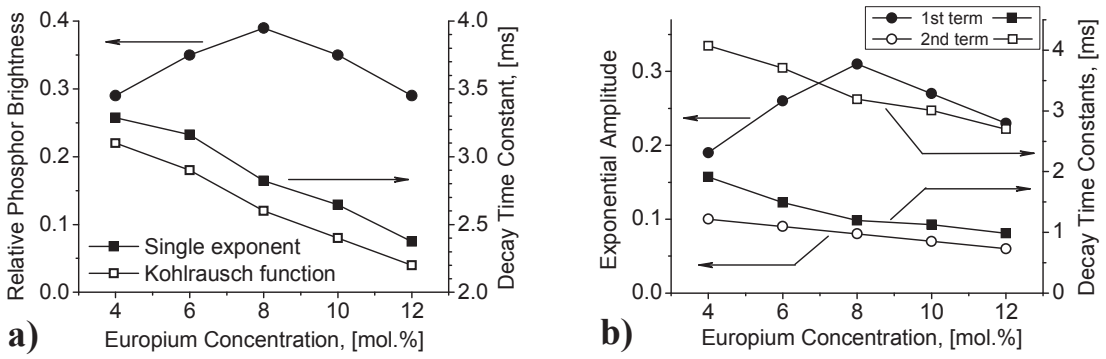

Figure 6.7 - Phosphor brightness and the exponential decay time constants of photoluminescence as a function of Eu-content: a) first-order exponent and Kohlrausch function; b) second-order exponential terms.

europium concentration. However, it is difficult to give a physical interpretation of the observed difference in behavior of the two exponential terms because it is hardly possible to ascribe them to any two distinctive configurations of emitting Eu^{3+}-ions (as it was done, e.g., by Zhang *et al.*[110]). Although such factors as the proximity of the particle surface can cause a modification of the decay rate of the excited activator ions, the change of emission characteristics between the ions located in the middle of the particle and on its surface can take place gradually, i.e., numerous intermediate states may exist between the two extremes. Furthermore, a multi-exponential model (with a sufficient number of terms) can be used to describe a decay curve of practically any complexity and does not necessarily reflect the physics behind it.[262]

In many areas of physics including molecular fluorescence and luminescence of nanoscale semiconductors,[262–265] a *stretched exponential function* also referred to as *Kohlrausch function* is successfully applied to describe relaxation processes

$$I(t) = I_0 \exp\left[-\left(t/\tau\right)^{\beta}\right], \qquad (6.1)$$

where $0 < \beta \leq 1$. The parameter β characterizes the width of the distribution of the lifetimes and can be used as a measure of the "disorder" present in the system under investigation. The goodness of fit obtained with the stretched exponential decay was equal to or better than that of the bi-exponential decay. However, the number of variable parameters could be reduced. The obtained decay time constants are included in Figure 6.7a. The parameter β was equal to 0.90 in all cases and did not depend on the activator concentration within an error of ± 0.01. This emphasizes the difference of the nanophosphors from the conventional phosphor powders. The decay curves corresponding to the commercial samples and DPC-FAD coatings could also be fitted with Equation 6.1. However, the obtained values of β were completely due

to the concentration quenching phenomenon and at low doping concentrations this parameter would approach unity.

In later experiments on the deposition of nanophosphor screens, the europium concentration of 8 mol.% was used. Although this value of the optimum concentration is in agreement with that of submicron-sized Y_2O_3:Eu obtained by DPC-FAD, it is higher than the 5 wt.% value found in the previous study on the CVC-FSP synthesis of Y_2O_3:Eu nanophosphor.[137] Most likely this inconsistency could be attributed to the difference in purity of precursors. Yttrium 2-ethylhexanoate used in the previous study was prepared by conversion of yttrium nitrate to yttrium hydroxide with aqueous ammonia, washing with distilled water, and refluxing in 2-ethylhexanoic acid and acetic anhydride. Such a multi-step route could provide opportunities for the introduction of unintentional contaminants. Relatively low PL-intensities achieved in the previous work and reduced decay time of photoluminescence (compare 2.7 ms for 5 wt.% Eu, i.e., 3.8 mol.%,[137] and 3.3 ms for 4 mol.% Eu, this work) can be considered as evidence of possible contamination.

As it was discussed in Section 2.3.3d, radiation lifetimes are affected by the effective refractive index of the medium so that the decay time of luminescence of Y_2O_3:Eu-nanophosphor should depend on porosity of the powder compacts. Indeed, such dependence was observed: the decay time of loose nanophosphor powder containing 8 mol.% of europium (the sample was deliberately not compacted while loading it into the powder cell; estimated porosity 98 %) was 3.0 ms, as compared to 2.8 ms for phosphor of the same composition compacted by the standard procedure of loading a phosphor sample into the powder cell, which resulted in porosity of approximately 87 %. When the sample was compacted to a porosity of 80 %, the decay time constant decreased even further and reached a value of 2.7 ms. The relationship between porosity and decay time was approximately linear. The decay time constant obtained with the Kohlrausch function, decreased from 2.8 to 2.5 ms between the cases of 98 % and 80 % porosity, respectively. The value of the parameter β did not significantly change.

The theory proposed in Sections 2.3.3c-2.3.3d allows the decay time constant to be predicted from the volume concentration of particles. If the luminescence decay time of the commercial phosphor powder (1.05 ms) is used as a bulk value, assuming a phosphor tablet with a porosity of 87 % (nanoparticles dispersed in air), a decay time constant of 5.6 ms would be obtained. This exceeds the actual value by nearly 100 %. Obviously, some phenomena counteracting the increase of the decay time of luminescence in nanophosphors are also involved into emission dynamics of Eu^{3+}-ions. For example, the difference between predicted and observed values of decay time could be attributed to surface quenching caused by surface-bound species (e.g., OH-groups, see Section 2.3.3d). The increased specific surface area of phosphor

nanoparticles favors the increase in the probability of nonradiative decay of excited states, which also explains the low efficiency of the FAD-produced nanophosphor.

When the photoluminescence excitation spectrum of the nanophosphor with the optimum composition is compared to that of the commercial phosphor powder, one can observe a noticeable *blue*-shift (i.e., a shift towards the shorter wavelengths) in the position of the charge transfer band (Figure 6.8). It is known that the efficiency of excitation in the CTB is affected by the concentration of the activator.[266] The concentration of europium in commercial Y_2O_3:Eu phosphors is usually lower than 8 mol.%. However, the decrease of the doping concentration in the nanophosphor powders causes an even larger blue shift of the CTB (check the curve for 4 mol.% Eu in Figure 6.8). It should be concluded that the shift of the edge of the CTB for the nanophosphor does not result from the difference in the composition of the phosphor. The data in literature is quite contradictory, both blue- and red-shifted CTBs were reported for nanocrystalline Y_2O_3:Eu, which may, at least partly, be explained by the instrumental limitations.[267] One could speculate that the considered shift is in some way related to the altered scattering properties of the phosphor powder because the Y_2O_3:Eu should only weakly absorb light in the relevant spectral range (250-300 nm). A detailed investigation of the generation of light in the plaques of phosphor nanoparticles is required in order to clarify the origin of the observed differences between the PLE spectra of FAD-synthesized nanophosphor and that of the commercial powder.

6.3. Characterization of the deposited nanophosphor screens

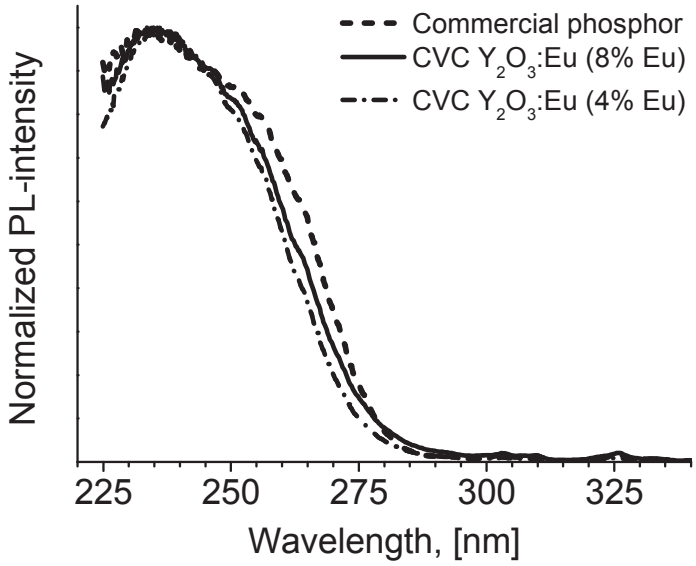

Figure 6.8 – PLE-spectra of the Y_2O_3:Eu nanophosphor produced by CVC-FAD and the commercial phosphor.

The morphology of the FAD-deposits is shown in Figure 6.9. Aerosol particles formed a highly porous foam-like structure on the surface of the substrate, very similar to that of other FAD-deposits (e.g., of tin oxide coatings[191,268]) or the yttria nanoparticles deposited by gas-phase condensation.[269] It is worth noticing that the volumetric porosity of the phosphor coating (0.973±0.004, e.g., coating density 1.06±0.06 mg/cm^2, coating thickness 74±4 μm) was close to that of uncompacted powder, as collected on the filter (0.977±0.006, e.g., 100±1 mg of phosphor powder occupied a volume of 0.83±0.18 cm^3).

Uniform deposits for a wide range of coating densities (0.23 – 3.8 mg/cm^2) were obtained. Deposition of thick coatings was facilitated by several subsequent interruptions of the process in order to refill the syringe with a new portion of the precursor solution. Each time the flame was ignited or extinguished, the substrate had to be covered with a metal sheet in order to prevent unburned spray droplets from impinging on the substrate. When the substrate was placed at the standard distance from the burner nozzle (25 cm), the average deposition rate was 0.22 mg/(cm^2 min). Only about 0.2 % of produced powder was deposited on the substrate. The temperature on the surface of the substrate was in the range 450-550℃. When the deposition distance was decreased to 20 cm, the deposition rate increased by a factor of 2.8 (the temperature at this location could reach 800℃). Increase of the deposition

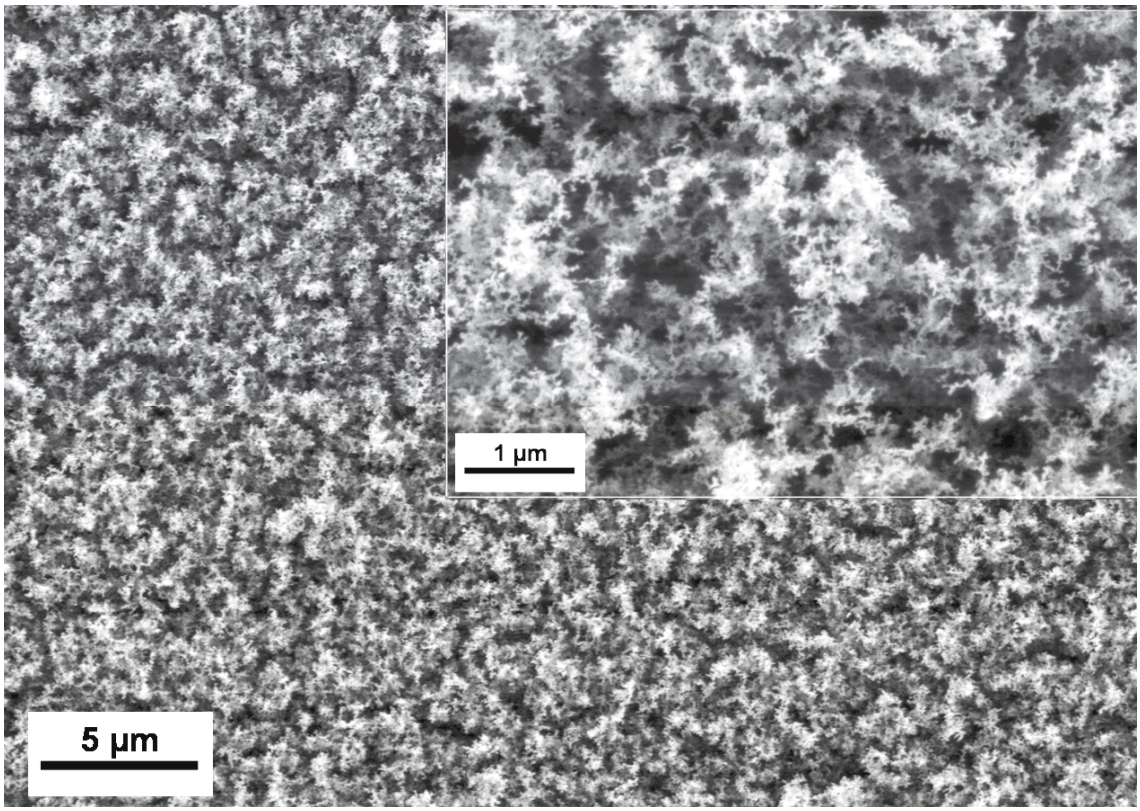

Figure 6.9 - Morphology of FAD-deposited Y_2O_3 nanoparticle coatings.

distance to 35 cm lead to a decrease of the deposition rate to about 50 % of the standard value.

The change in the optical attenuance of the layers of Y_2O_3:Eu phosphor nanoparticles for increasing coating density is presented in Figure 6.10. For comparison, the spectra of the reference samples (deposited by DPC-FAD and by the gravitational sedimentation of the commercial phosphor powder) are also shown. The attenuance of both reference phosphor coatings are approximately equal and constant over the entire wavelength range where the absorption of europium-doped yttria is negligible ($\lambda > 270$ nm), i.e., the scatterance of the reference samples does not depend on the wavelength of incident light. At the same time, the scatterance of light transmitted through the layers of nanophosphor has an expressed dependence on wavelength (similar to Rayleigh scattering) and substantially decreases in the visible range, which agrees with theory (see Section 2.3.3a) and reported data.[270,271] For example, at the wavelength of the main emission peak of Y_2O_3:Eu ($\lambda = 612$ nm), the attenuance of the FAD-deposits is about 2 units of attenuance, corresponding to two orders of magnitude (or 99 %), lower than that of the reference coatings. Such a decrease in the scattering of emitted light should substantially improve the resolution of phosphor screens (i.e., preclude blurring of displayed images).

In addition to the expected improvement of screen resolution, reduced scattering significantly affects the relationship between screen density and its brightness. For excitation at 254 nm, the transmission-mode brightness of the nanophosphor

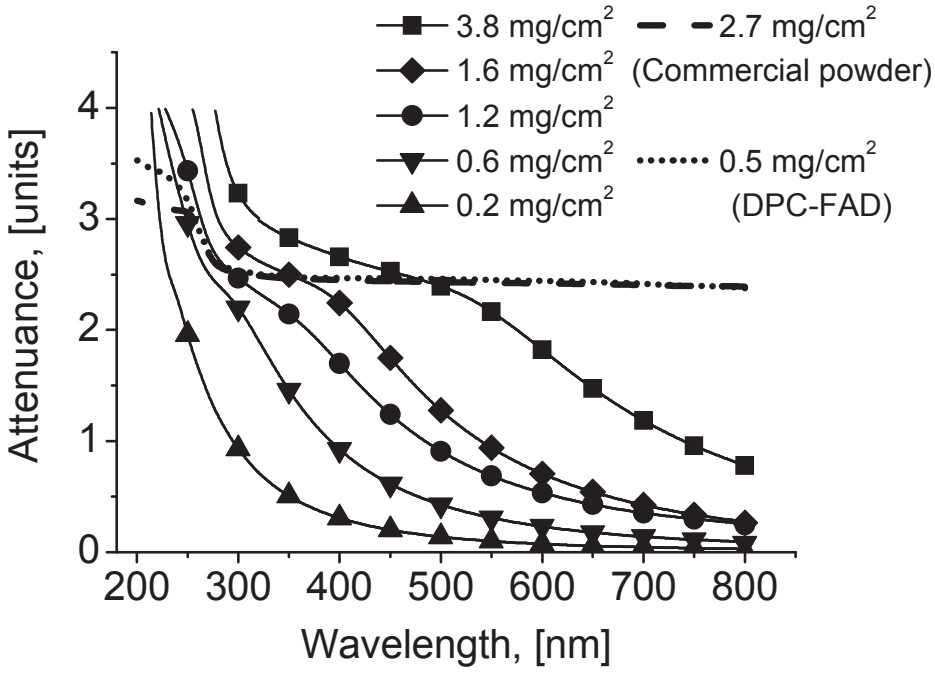

Figure 6.10 - Attenuance spectra of the reference samples and Y_2O_3:Eu nanophosphor coatings (8 mol.% Eu) of the different coating densities.

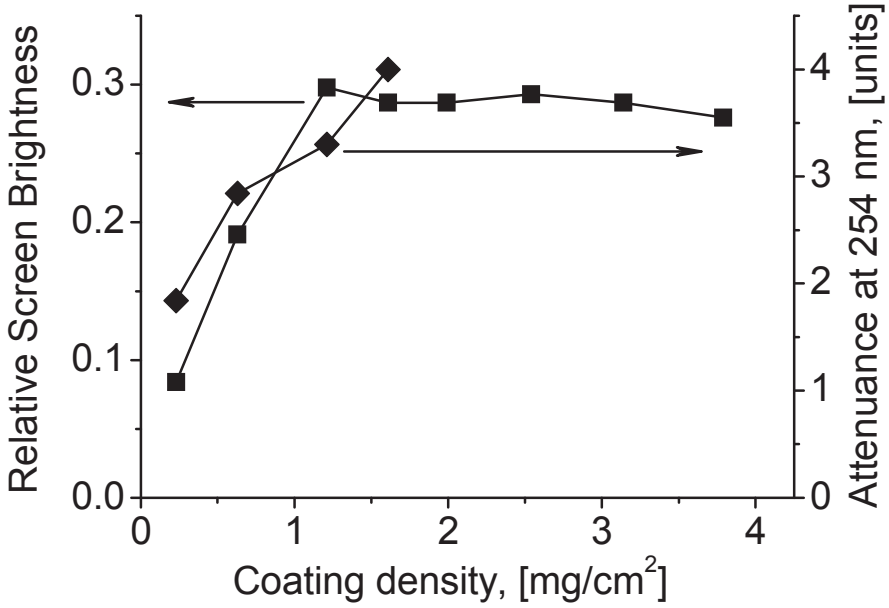

Figure 6.11 - Screen brightness (squares) for excitation at 254 nm and attenuance at 254 nm (diamonds) as a function of the Y_2O_3:Eu nanophosphor coating density (8 mol.% Eu).

screens reached saturation at 1.2 mg/cm^2 (see Figure 6.11). The corresponding value of attenuance shows that for this coating density, about 99.9 % of the incident UV-light is either absorbed in the screen or scattered away. (For weakly absorbing nanoparticles, the scattering coefficient in the UV-range can be relatively large). Thus, thicker coatings cannot have a higher PL-intensity (due to the lack of available UV-photons). At the same time, their brightness barely degrades, which is explained by the extremely weak scattering of light in the visible range.

As discussed in Section 2.2, screen density always has an optimum value corresponding to the highest PL-intensity in the transmission mode. “Thinner” screens do not absorb all available exciting radiation, whereas the light output of “thicker” screens is degraded because some of the phosphor particles are not reached by UV-light (i.e., they do not contribute to light emission) but introduce additional scattering of emitted light. For phosphor coatings deposited by DPC-FAD, a screen with a coating density of three times the optimum value would achieve about 70 % of the maximum transmission-mode PL-intensity (see Section 5.1.5), i.e., it degrades by 30 % due to the additional scattering. For FAD-deposited nanophosphor, a coating with a density of 3.8 mg/cm^2 achieved 92 % of the maximum brightness (obtained with the coating density of 1.2 mg/cm^2). To the best of our knowledge, such an exceptionally weak dependence of brightness on the thickness of the powder phosphor screen is observed for the first time.

The optimum thickness at which the maximum T-mode brightness is achieved changes depending on the efficiency of absorption of the exciting radiation. One can expect a substantial difference between the values corresponding to excitation in the charge transfer band and by the host absorption. Unfortunately, measurements of PLE-spectra of FAD-deposits in the VUV range could not be carried out and their performance below 220 nm could only be studied by subtraction of the spectra of attenuance taken with and without a longpass filter (see Sections 4.3 and 5.3.3). The results are presented in Figure 6.12. The lack of linearity of measurements of attenuance beyond 2 units does not allow for any quantitative treatment. Nevertheless, an important qualitative observation can be made. One can see that within the spectral range of the host absorption, the brightness of the thinnest FAD-deposited coating is at least as high as that of the thicker ones. According to Benitez *et al.*,[244] the absorption coefficient of bulk Y_2O_3 abruptly increases for the shorter wavelength down to at least 120 nm (~10 eV). Therefore, the thickness of the nanophosphor coating required in order to achieve the maximum PL-output should decrease to well below 0.23 mg/cm^2 for the wavelengths shorter than 200 nm. The coating densities of 1.2 and 0.23 mg/cm^2 correspond to a geometric thickness of 83 and 16 μm, respectively. Realization of the diffraction-limited phosphor screen would require either to develop a means to confine the geometric thickness of the coating within 200 nm (see Section 2.3.1) or to assure conditions for which the exciting radiation would be fully absorbed within this thickness. In the latter case, the total thickness of the

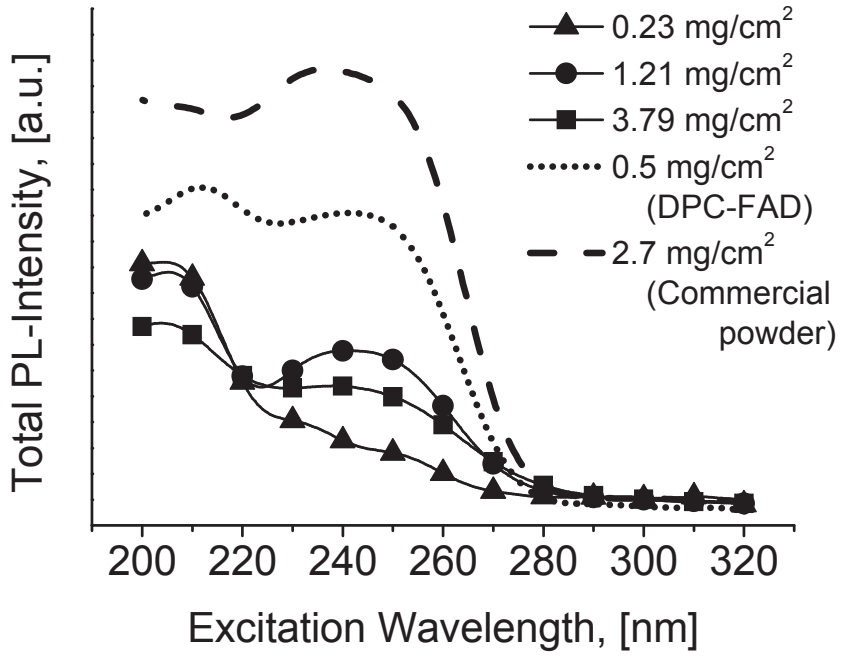

Figure 6.12 – T-mode PLE spectra derived from the measurements of attenuance of the nanophosphor coatings deposited by CVC-FAD.

nanophosphor layer can be kept appreciably thicker than 200 nm because scattering at the wavelength of emitted light is very weak and should have a negligible effect on the resolution of the screen.

As discussed in Section 2.3.3c, the optical constants of nanoparticulate deposits can be calculated from the properties of the bulk and particle volume fraction. If no absorption in the medium between the nanoparticles is assumed, the following simple expression for the absorption coefficient of the phosphor coating can be obtained by combining Equations 2.84 and 2.107

$$\alpha_{EFF} = f_V \alpha, \tag{6.2}$$

where α is the absorption coefficient of the bulk material and f_V is the volume concentration of phosphor nanoparticles. For example, the absorption coefficient of bulk yttria doped with 3.5 mol.% Eu at a wavelength of 173 nm was found to be $(1 \pm 0.1) \times 10^6$ cm.[243] In order to absorb 99 % of the incident UV radiation within 200 nm, the filling fraction of the phosphor should be at least 25 vol.% (i.e., <75 % porosity). Although the Clausius-Mossotti relation (Equation 2.105) should be applied instead of Equation 2.107 for such high concentrations of solid phase, it becomes obvious that having a method to increase the packing density of phosphor nanoparticles would provide a clear advantage for the future applications of FAD and related techniques.

6.4. Influence of light reflection from the substrate

It should be noted that, for excitation at 254 nm, measured values of the relative brightness of nanophosphor coatings did not exceed 30 %, whereas filter-collected nanophosphor powders compacted in the powder cell of the spectrometer achieved 40 % of the relative brightness. This difference may, to some extent, be explained by the fact that commercial phosphors, which were used as references for characterization of filter-collected phosphor powders and for characterization of deposited coatings (purchased from Osram GmbH and from MaTecK GmbH, respectively), were different. The latter phosphor could have a somewhat higher efficiency leading to a reduced relative brightness of nanophosphor samples in comparison to another reference. However, there are two important issues that can substantially affect the measured brightness of nanophosphor coatings regardless of the reference. First, there is an optical interaction with the substrate, e.g., the reflection of emitted light at the interface between the phosphor coating and the substrate. Second, there is the influence of the different packing density (i.e., porosity) of FAD-deposits and of compacted filter-collected phosphor powders (0.973 vs. 0.87, respectively). Several experiments were performed in order to clarify the effect of both contributions.

The influence of the reflection from the substrate was confirmed as follows. Light emitted by a thin phosphor coating undergoes Fresnel reflection at the interface with the substrate causing unequal PL-intensity in the transmission and reflection modes (i.e., of light emitted forwards and backwards). The equality can be fixed by placing a blank substrate on top of the deposited phosphor layer. The transmission mode brightness of the nanophosphor coatings sandwiched between two quartz plates increased by 10-15 %, whereas that of the micrometer-sized reference sample increased only by 3 %. After removing the blank substrate, the PL-intensities decreased to the previous values.

6.5. Compaction of the nanophosphor coatings

In order to investigate the influence of the porosity of the nanophosphor coatings on their PL-performance, a coating sandwiched between its substrate and a blank quartz plate was compacted by pressing from both sides. Upon compaction, the two substrates were glued together by the phosphor layer. The substrates could be separated afterwards by gently pulling them in opposite directions. The phosphor layer remained on its initial substrate and its integrity was, to a large extent, preserved. The micrographs of the compacted sample are shown in Figure 6.13. The volumetric porosity decreased from 0.973±0.004 to 0.903±0.015, i.e., the packing density of nanoparticles increased approximately 4-fold. A 13 % increase in the transmission-mode PL-brightness due to irreversible compaction was observed. It can be suggested that this increase was caused by the increase of the effective refractive index of the phosphor layer as a result of increased particle concentration. In this way, compaction increases the radiative decay rate of excited Eu^{3+}-ions, which leads to an improvement in the quantum efficiency of the nanophosphor (Sections 2.1.2, 2.3.3c, and 2.3.3d). Attenuance spectra of the compacted coating revealed a decrease in light scattering in the visible range (Figure 6.14a). Such a change in performance of the nanophosphor coating can be attributed to the effects of dependent scattering (see Section 2.3.3c). In the range of strong absorption, the attenuance did not significantly change.

The combined effect of the increased efficiency and decreased scattering of the compacted nanophosphor was confirmed by dosing the loose filter-collected Y_2O_3:Eu powder into the powder cell of the Varian Cary Eclipse fluorescence spectrometer and measuring the corresponding T-mode brightness of the so-obtained “thick coating” (excitation by the UV-lamp at 254 nm, detection with the Tristan 4 photospectrometer). One can see in Figure 6.14b that the compacted powder cakes (~87 vol.% porosity) substantially outperform the coatings consisting of “free-standing” uncompacted powder.

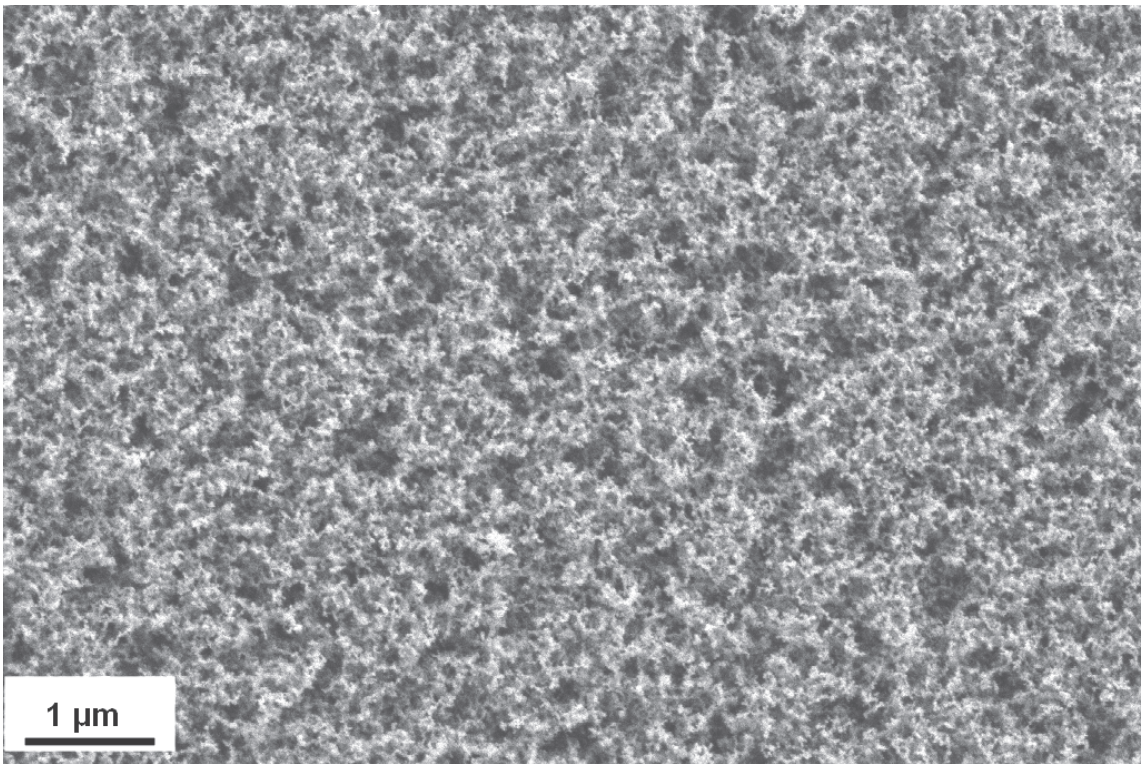

Figure 6.13 – SEM-micrograph of the FAD-deposited Y_2O_3:Eu coating after compaction to a porosity of 90 vol.%, 1.2 mg/cm^2, 8 mol.% Eu.

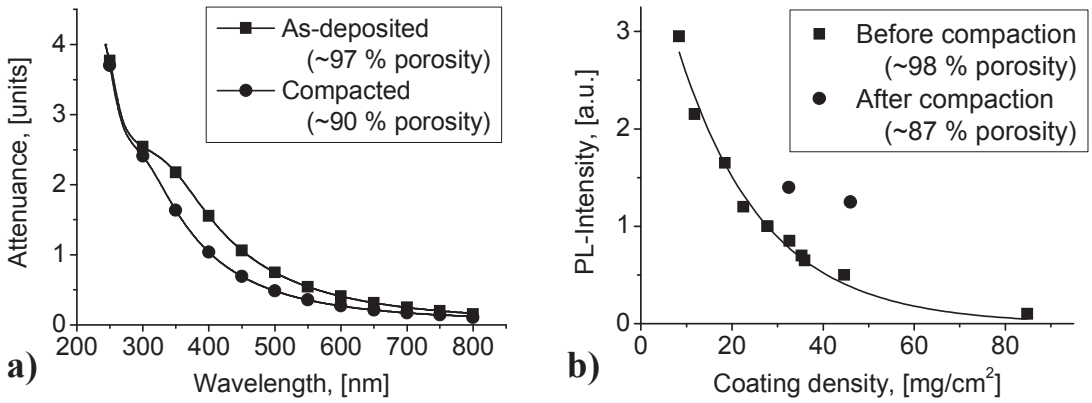

Figure 6.14 – a) Attenuance spectra of a Y_2O_3:Eu nanoparticle coating (1.2 mg/cm^2, 8 mol.% Eu) before and after compaction; b) T-mode brightness of photoluminescence of thick layers of Y_2O_3:Eu nanophosphor (8 mol.% Eu).

The above experiments show that the packing density of phosphor particles (i.e., porosity of the phosphor layer) and light reflection from the supporting substrate significantly influence the PL-performance of the nanophosphor screens. A combina-

tion of both effects may well explain the lower brightness of the FAD-deposited coatings in comparison to the corresponding filter-collected phosphor powders.

6.6. Coating the surface of phosphor nanoparticles with a thin layer of silica

According to Equation 2.2, the quantum efficiency of a phosphor may be estimated by dividing the observed decay time of luminescence with the time constant corresponding to the purely radiative decay of the excited ions. The latter could be assessed from the radiative decay time in the bulk phosphor and the effective refractive index of the nanophosphor layer (see Sections 2.3.3d and 6.2). This leads to values of quantum efficiency on the order of 50 % even for compacted FAD-deposits, i.e., only half of the efficiency of conventional micrometer-sized Y_2O_3:Eu phosphors and sub-micrometer-sized powders produced by DPC-FAD. Such a large difference is attributed to the increased specific area of nanoparticles, which can be directly related to the increased concentration of quenchers of luminescence. One possible way to improve the performance of nanophosphors would be to apply a thin coating on the surface of nanoparticles in order to spatially separate the emitting ions located in vicinity of the surface from the quenchers (see Section 2.3.3d). The “spacer” can be deposited by various methods, e.g., by sol-gel[272] or atomic layer deposition.[273] In the present work, two different approaches for coating Y_2O_3:Eu nanoparticles with a nanoscopic layer of silicon dioxide were tested: 1) the in-situ coating during the flame synthesis of the phosphor nanoparticles; and 2) the conformal infiltration of FAD-deposited phosphor screens by atomic layer deposition (ALD).

The in-situ coating of nanoparticles produced by FSP was already successfully applied for various materials as, e.g., TiO_2 and Fe_2O_3.[274,275] The experiments with Y_2O_3:Eu were arranged as follows.[275] The FSP reactor was enclosed by a 20 cm long quartz glass tube and the spray flame was sheathed by 40 l/min nitrogen flowing through the outermost sinter metal plate at the FSP burner. A stainless steel metal torus pipe ring with 16 radial equispaced openings was positioned at the upper end of that tube, and another 20 cm long quartz tube was placed on top of it. The phosphor nanoparticles were produced by the 5/5 flame in order to obtain a possibly small flame zone, which had to fit inside of the tube. The particles were *in situ* coated with silicon dioxide by introducing a stream of nitrogen carrying hexamethyldisiloxane (HMDSO, Aldrich, purity >98 %) vapor from a bubbler at 10℃ along with an additional 15 l/min of mixing nitrogen gas through the pipe ring. The amount of silica in the product powder was fixed at 25 % and 33 wt.% by setting the N_2 flow rate through the HMDSO bubbler to 0.8 and 1.2 l/min, respectively.

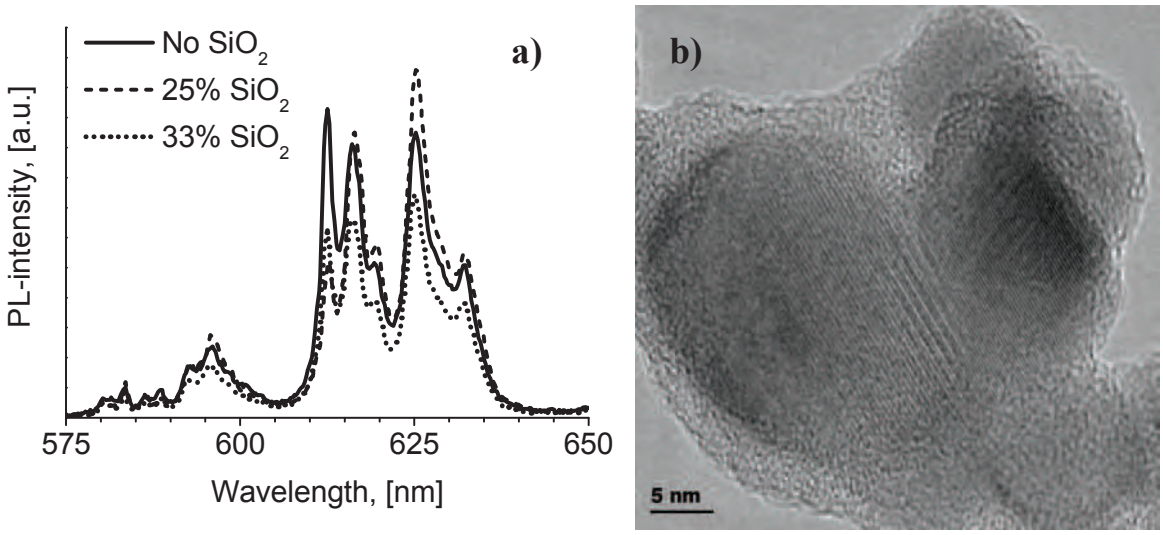

Figure 6.15 – a) PL-spectra of Y_2O_3:Eu nanophosphor powders (8 mol.% Eu) *in-situ* coated with SiO_2; b) TEM of an agglomerate of Y_2O_3:Eu nanoparticles coated by amorphous SiO_2 (33 wt.%).

The resulting changes of the spectra of photoluminescence are presented in Figure 6.15a. One can see that the phosphor powder treated with 25 wt.% of silica has a slightly higher intensity at 625 nm. However, this improvement could merely be explained by a difference in the phase composition of the nanophosphor. Although in the standard FSP setup the 5/5 flame corresponded to the phase-pure monoclinic yttria, inside the quartz tube the flame was strongly diluted with nitrogen and the combustion conditions were fuel-rich rather than stoichiometric. As a consequence, varying amounts of the cubic phase were present in the filter-collected powders. As estimated from the relative intensity of the peak at 612 nm, the phosphor obtained in the modified setup without HDMSO contained 15-20 wt.% of the cubic Y_2O_3:Eu. The corresponding average particle size ϕ_{BET} was 21 nm. For the phosphor produced with 25 wt.% of silica, the fraction of the cubic phase decreased to 5-8 %. The particle size calculated by assuming a homogeneous average density of Y_2O_3:Eu and SiO_2 was increased to 30 nm, thus giving a figure of 4-5 nm for the shell thickness around phosphor particles. The integrated intensity of the PL-emission practically did not change, whereas the decay time of luminescence decreased from 2.6 to 2.1 ms. Such a change could be caused by an increase of either the radiative decay rate due to a modification of the effective refractive index upon introduction of silica or the nonradiative decay, which would mean that silica is not suitable for suppression of surface quenching in the ultrafine Y_2O_3:Eu. It is also possible that both factors play a role because the overall intensity neither improved nor got worse.

Further increase of the amount of added SiO_2 precursor led to a noticeable decrease of the PL-brightness. For 33 wt.% of silica, the particle size derived from the BET-measurements increased to 39 nm, i.e. the shell thickness of 9 nm could be assumed. However, the results of the TEM investigation show that there is a substantial number of agglomerated phosphor nanoparticles sharing their silica shells, which should affect the measured value of the specific surface area (Figure 6.15b). Surprisingly, the weight fraction of the cubic phase increased to 12-16 %. The decay time constant also slightly increased (2.2 ms). Considering the decrease in the integrated PL-intensity, the decrease of the overall decay rate can be attributed to the increase of the radiative decay time constant with no improvement on the probability of nonradiative relaxation of excitation. The decrease of the radiative decay rate could be caused by the presence of the silica shell, which decreases the packing density of phosphor particles (i.e., it acts as a spacer between the neighboring particles of yttria). At the same time, silica itself has relatively low index of refraction, so that the effective refractive index of the phosphor powder compacted in the powder cell of the spectrometer decreases. From this point of view, it would be advantageous to cover the nanoparticles with the protective layer after depositing them onto the screen, thus excluding the effect of the thickness of the silica shell on the particle volume fraction of the phosphor. Furthermore, this would allow for the investigation of the coatings deposited from the standard 12/3 flame, i.e., those mainly consisting of the cubic yttria. Such a possibility is offered by atomic layer deposition.

The ALD experiments were carried out at the Institute of Applied Physics at the University of Hamburg (the research group “Multifunctional nanostructures”). The FAD-coatings deposited in the standard way were cyclically exposed to water vapor (0.5/30/70/RT), ozone (10 % in O_2, 0.2/30/45/RT), and aminoalkyltriethoxysilane ($H_2N(CH_2)_3Si(OEt)_3$, 2/40/80/90℃), where the first three numbers in b rackets in each case stand for the duration of the pulse/exposure/evacuation steps, respectively, and the last position denotes the temperature of the corresponding source with “RT” used for room temperature. The processing was performed at 150℃ and a growth rate of about 0.06 nm/cycle was expected.[276]

The first ALD run consisted of 70 cycles. The weight of the samples was increased by 12-13 % (i.e., the weight fraction of silica was 11-12 %). Assuming a density of silica of 2.0 g/cm^3 and a specific surface area of the phosphor coating equal to that of the corresponding filter-collected powder (in this case, 47 m^2/g), the average thickness of the silica coating totals 1.3 nm. The estimated growth rate is on the order of 0.02 nm/cycle, which is much lower than expected. The difference probably results from the very high surface area of the phosphor. First, consumption of the precursors increases with the increase of the surface available for ALD so that, for example, a deficiency of aminoalkyltriethoxysilane molecules could occur. Second, a uniform ALD-infiltration of thick porous structures requires extended exposures in order to

facilitate the diffusion of precursors, especially for large molecules. As a consequence, the thickness of the coating deposited by ALD can vary at different locations of the sample, particularly at different depths in the phosphor layer. It can be concluded that the density of the phosphor coating should preferably be low.

After 70 ALD cycles, the T-mode brightness of the Y_2O_3:Eu screen with the initial coating density of 0.6 mg/cm^2 decreased by 20 % of the initial value. The luminescence decay time practically did not change: the single-exponential decay time constant was found to be 2.2-2.3 ms both for an “as-deposited” FAD-coating and that treated with ALD.

It should be mentioned that the above decay time constants obtained by laser excitation (at the Institute of Laser-Physics, DESY) were shorter than those measured by the Varian Cary Eclipse spectrometer for the same “as-deposited” FAD coating (3.3 ms). The fitting of the decay curves with the Kohlrausch function (Equation 6.1) not only produces different τ (1.66 vs. 3.0 ms) but also a different value of the parameter β (0.73 vs. 0.90, respectively). There could be several reasons for such a disagreement. High laser fluences at the surface of the phosphor screen could cause a substantial increase of the temperature of the phosphor. For example, in the case of the coatings deposited by DPC-FAD, focusing the laser beam to an energy density of approximately 30 mJ/cm^2 could destroy the phosphor layer. Although the laser fluences used during the measurements of the decay times were always much lower than the destruction threshold, the possibility of heating-up for the nanophosphor coating exposed to the laser radiation could not be completely excluded, especially when its low quantum efficiency is considered. The lower the efficiency of the phosphor, the higher the fraction of the excitation energy which is being converted into the heat. The increase of the temperature can be accompanied by an increase of the decay rate of luminescence.[277,278] It was found that the exponential decay time constant of Y_2O_3:Eu phosphor stays constant up to approximately 500℃ and decreases for higher temperatures so that it falls below 100 ns at the temperatures exceeding 1100℃. [277]

Furthermore, high intensity of excitation can lead to saturation effects (i.e., changes of luminescence dynamics when most of the emitting ions are in the excited state), which also cause shortening of the observed decay time of the emission.[277,278] For Y_2O_3:Eu applied in plasma display panels (excited by ArF excimer laser at 193 nm) a saturation threshold of 0.2 mJ/cm^2 was determined.[279]

The energy density of exciting radiation was not precisely controlled during our measurements. If heating or saturation effects were responsible for the observed difference in the calculated decay time constants, the repeatability of the measurements would be strongly deteriorated. The values obtained for the same samples in the different series of experiments were, on the contrary, in perfect mutual agreement.

It can also be suggested that the peculiarities of the decay of luminescence could result from the temporal excitation conditions. The dependence of the decay time constant on the duration of the excitation pulses was observed, e.g., for sol-gel deposited chromium-doped alumina.[280] The duration of a single flash of Xe lamp installed in the Varian Cary fluorescence spectrometer was approximately 2 µs, whereas the pulse duration for the laser system used for the measurements at the Institute for Laser-Physics at the Hamburg University was only 10 ns. In both cases, duration of the excitation pulses was insufficient for the population of the electronic levels from which the emission takes place to achieve equilibrium. Usually, the intensity of the PL-emission continues to increase immediately after the excitation pulse.[281] The rise time of luminescence in Y_2O_3:Eu, depending on Eu-concentration, can vary between several tens to several hundreds of microseconds.[277] One could speculate that the equilibration processes associated with the time after cessation of excitation proceed in a different (and more complicated) way in the case of nanocrystalline phosphor powders synthesized by FAD. Unfortunately, it is not possible to prove or disprove this hypothesis without additional experiments and therefore the conclusions on the influence of the silica coating on the performance of the nanophosphor screens should be preferably drawn from the change of the PL-intensities.

Although any comparison of the measured decay times should be done extremely carefully, the fact that there was no difference between the FAD-screens after 70 ALD cycles and those not coated by SiO_2 could imply that there was insufficient coverage of the surface of the phosphor particles. In order to clarify how a thicker SiO_2 layer affects the properties of the nanophosphor coating, the samples were treated with a further 300 cycles with the same ALD process parameters. The weight fraction of silica increased to 29 %, which corresponds to an average shell thickness of 4.5 nm. For thick screens (1.5 mg/cm^2), a radial distribution of “whiteness” was observed with the central parts of the samples appearing noticeably fainter than the edge parts. This observation could be related to the lack of uniformity of the silica coating resulting from the deficiency of the precursors discussed above. SEM investigation confirmed that nanoparticles at the edge of the sample appear somewhat larger than those in the middle, although they were too small for any quantitative characterization. Figure 6.16a shows that the morphology of the phosphor coating did not significantly change. For a thin screen, the difference in appearance of the central area and the outer part was less expressed. Nevertheless, the decay times were measured at the edge of the sample in order to assure the maximum possible effect of the surface passivation. An exponential decay time constant of 2.4 ms was obtained. For the Kohlrausch function, the decay time constant also slightly increased and reached 1.75 ms. The value of the parameter β did not significantly change (0.73).

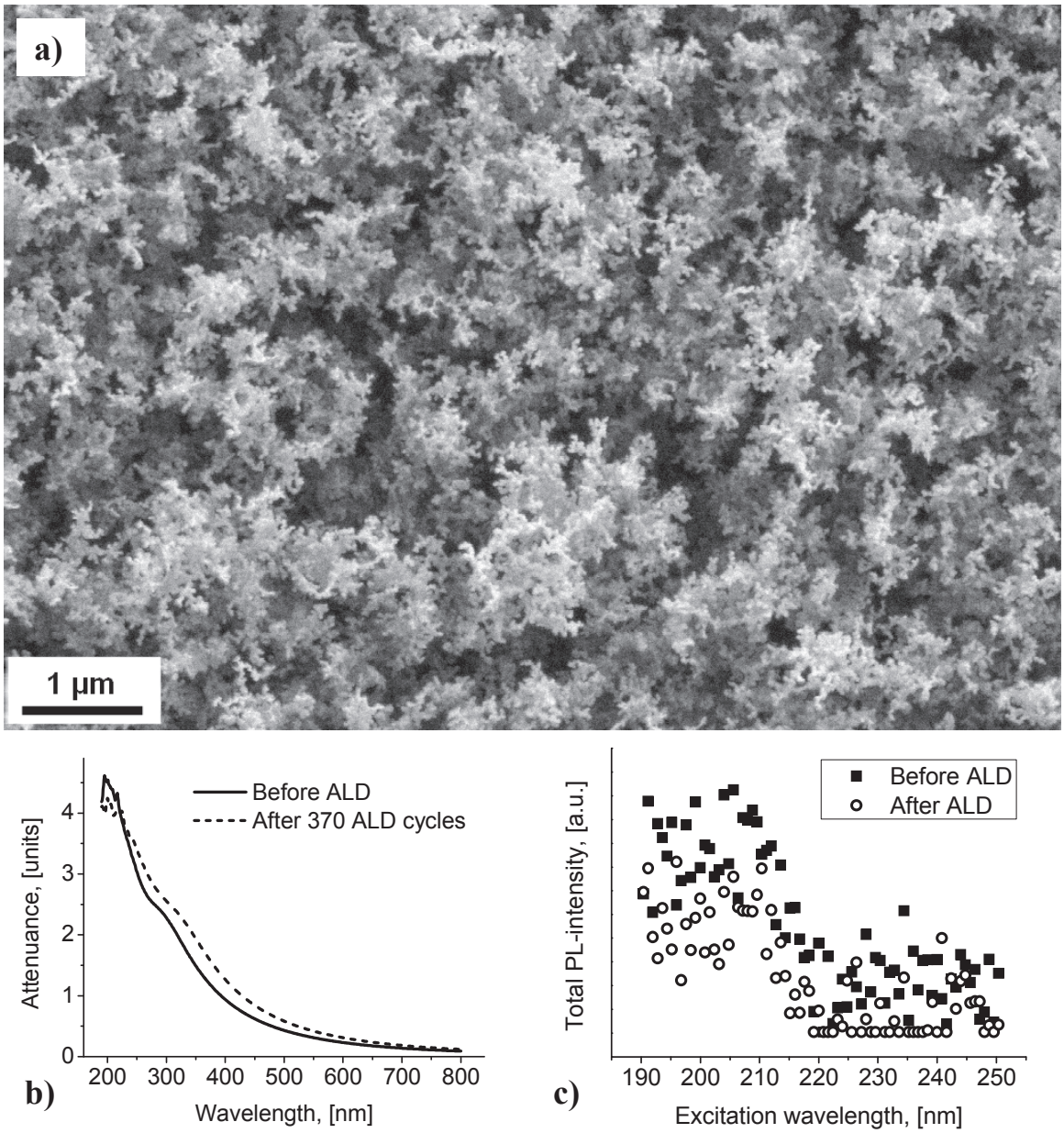

Figure 6.16 – a) SEM of the FAD deposits after ALD treatment with SiO_2 (300 ALD cycles, average SiO_2 coating thickness 6.5 nm), initial Y_2O_3 coating density 1.5 mg/cm^2; b) attenuance spectra and c) T-mode excitation spectra of the FAD screen before and after ALD-deposition of SiO_2, initial Y_2O_3:Eu coating density 0.6 mg/cm^2.

After additional deposition, the T-mode brightness of the Y_2O_3:Eu screen with the initial coating density of 0.6 mg/cm^2 further decreased to 70 % of the initial value. (For the thicker coatings, the degradation of brightness was even stronger). The decrease of brightness can be accompanied by the increase of the decay time constant only when the radiative decay rate decreases. However, partial substitution of

air by silica in the space between the phosphor particles is expected to increase the effective refractive index of the medium and speed up the radiative decay. It can be concluded that the decrease of the brightness is not related to the dynamics of luminescence. The observed changes could be explained by the decrease of the number of UV-photons absorbed by the phosphor. A comparison of the attenuance spectra before and after ALD shows that scatterance in the visible range and near-UV substantially increases (Figure 6.16b). The values of attenuance in the range 220-230 nm seem to be unaffected by the passivation of the surface. However, it is difficult to say whether the incident radiation is absorbed exclusively in the phosphor nanoparticles or if it is just the sum of absorption and scattering both in silica and Y_2O_3:Eu which is equal to the initial attenuation by the phosphor coating. The low signal levels preclude the reliable extraction of the T-mode PL-excitation spectra from the attenuance spectra taken with the long-pass filter (Figure 6.16c). However, even with this strongly scattered data one can arrive at the conclusion that throughout the range 190-250 nm, the brightness of the SiO_2-coated Y_2O_3:Eu nanoparticle coatings does not exceed that of the same phosphor screen before ALD.

To summarize the results of the experiments with encapsulation of phosphor nanoparticles, it should be concluded that thin films of silica do not improve the photoluminescent properties of FAD-synthesized Y_2O_3:Eu for excitation with UV-radiation. It is difficult to make any generalization because the same materials were advantageously combined in a core-shell structure when applied for up-conversion of exciting radiation at 800 nm.[282] Furthermore, silica coating could still be used in order to influence some non-optical properties of nanophosphors such as colloidal stability in slurries or mechanical stability of the deposited coatings. For example, we observed a noticeable improvement in wiping resistance for the ALD-treated screens. When concerning the quantum efficiency of the Y_2O_3:Eu nanophosphor, materials other than silica could be tested, e.g., undoped Y_2O_3 (see Section 2.3.3d).

6.7. Summary on CVC-FAD of phosphor coatings

Rapid (within minutes) manufacturing of nanophosphor screens by FAD was demonstrated for the first time. Coatings of Y_2O_3:Eu phosphor with an average particle size (d_{BET}) of 24 nm were obtained on fused silica substrates with the average deposition rate of 0.22 mg/(cm^2 min). It was shown that the liquid precursors for FSP/FAD can be prepared directly from inorganic salts of corresponding elements, thus substantially decreasing the costs of consumable materials.

Remarkably, the FAD-coatings demonstrated up to two orders of magnitude (or 99 %) weaker light scattering in the visible range than the coatings made of commercial micrometer-sized or submicron-sized phosphor powders. As a result, a con-

stant PL-output (repeatable within ±8 %) was maintained over a wide range of coating densities (from 1.2 to 3.8 mg/cm^2).

The maximum transmission-mode brightness of FAD-deposited phosphor coatings for excitation at 254 nm was 30 % of that of the corresponding reference screen made of the commercial phosphor powder. The PL-performance was found to be substantially affected by reflection of light from the substrate and by the packing density of the phosphor particles. The brightness of the nanophosphor screen could be increased by 13 % upon mechanical compaction of the deposits (volumetric porosity changed from 0.97 to 0.90). At the same time, light scattering in the visible range has further decreased. Therefore, it can be concluded that together with the shortening of decay times of photoluminescence, the brightness and light scattering properties of nanophosphor coatings can be improved by decreasing the porosity of the deposits. It is suggested that diffraction-limited image converters for radiation in the vacuum UV-range can be realized with compacted FAD-deposited screens.

It was attempted to cover the surface of the phosphor nanoparticles with a nanoscale passivating film in order to increase the quantum yield of luminescence by suppressing the surface quenching. The *in situ* encapsulation with SiO_2 during FSP-synthesis and coating the FAD-deposited screens with the same material by atomic layer deposition were tested. In both cases, shortening of the decay time of luminescence was observed but the light output did not increase.

7. Sol-assisted FAD based on droplet-to-particle conversion

The conversion of droplets of precursor solution into solid phosphor particles is accompanied by the rapid evaporation of water and decomposition of solute to the corresponding oxides. The surface of Y_2O_3:Eu phosphor particles obtained by the standard DPC-FAD technique described in Chapter 5 is extremely rough due to the low temperature of the propane/air premixed flame. Improved surface morphology can be obtained in several ways, e.g. by increasing the temperature of the flame over the melting point of the final compounds[176] or by introducing polymeric additives to the precursor solution (see Section 5.2). As an alternative approach, one could arrange the process in such a way so as to avoid any chemical transformation taking place during the residence time of the particles in the flame. If a sol (i.e. a colloidal dispersion of solid nanoparticles in a liquid) was used as a precursor for FAD, the morphology of the phosphor particles produced would change accordingly. Furthermore, this could also help to assure a high degree of crystallinity of the phosphor even for low flame temperatures.

Pyrolysis can be completely excluded when oxide nanoparticles are dispersed in water or other pure solvents. Optionally, a solution of metal salt(s) could be used as a suspending medium for nanoparticles. Then thermal decomposition would occur and nanoparticles in each droplet would act as seeds for the formation of single solid particles. The former scenario resembles spray drying commonly used in the processing of ceramic powders. It could also be compared to the sol spraying technique, a modification of spray pyrolysis in a furnace which does not involve chemical reactions between solid nanoparticles constituting the so obtained larger particles.[283] A modification of the furnace-based spray pyrolysis where nanoparticles dispersed in the precursor liquid serve as particle nuclei during decomposition of the salts has already been studied; it is usually termed colloidal seed-assisted spray pyrolysis.[284,285] The application of colloidal precursors in flame spray pyrolysis has also been reported. In the work by Dosev *et al.*,[179] magnetic (Fe_2O_3:Co,Nd) and at the same time luminescent (Gd_2O_3:Eu) core/shell particles were obtained in this way. Here, the results of a series of experiments on FAD of sols of Y_2O_3:Eu nanoparticles (obtained by CVC-FAD, Chapter 6) are presented. The nanophosphor was suspended either in salt-free solvents or in nitrate-based precursor solutions of different phosphor hosts. Colloidal precursors can be regarded as sols irrespective of the presence of dissolved salts and thus the corresponding realization of the FAD method can be generally referred to as sol-assisted FAD.

7.1. Non-pyrolytic sol-assisted FAD

As a proof of the concept, a series of DPC-FAD experiments with a salt-free sol were carried out. In order to obtain a stable suspension of nanoparticles, filter-collected powders obtained by CVC-FAD were first dispersed in small volumes of ethanol (the concentration was adjusted to 118 mg/ml) and then diluted with deionized water. The final concentration of the sol was set equivalent to the concentration of rare earth ions in the standard precursor solutions. 1 ml of 0.2 M solution of nitrates of yttrium and europium corresponds to 23.6 mg of Y_2O_3:Eu (for 8 mol.% Eu). Thus, the typical concentration of the precursor sol was 23.6 mg/ml and the suspending medium consisted of 80 vol.% water and 20 vol.% ethanol. For safety reasons, the tube connecting the ultrasonic nebulizer with the flame torch was not heated.

Figure 7.1a shows the SEM-picture of the obtained powder. Particle morphology was remarkably different from that of the phosphor particles produced by the standard DPC-FAD technique. Particles formed from droplets of the sol did not have large pores and the roughness of their surface was much less pronounced. On the other hand, they mostly had irregular shapes. The most important outcome was that the suspension of nanoparticles could yield sub-micrometer-sized particles at practically relevant production rates. At a maximum nebulization rate and a carrier gas flow rate of 3 l/min, deposition rates of the phosphor coating of up to 2.2 mg/cm^{2}h were achieved (the substrate was placed at the standard deposition distance of 7 cm). With sufficiently small colloidal particles, deposition rates comparable to that of the standard DPC-FAD would probably be achieved. For larger primary particles, obviously there should be a feasibility limit of FAD. Figure 7.1b shows the results of deposition from a suspension of particles synthesized by the DPC-FAD from the 0.2 M nitrate-based precursor solution. In this case, the deposition rate was rather negligible (deposits in the figure correspond to an FAD-duration of 5 min).

The particle size statistics of the powders deposited from suspensions of nanoparticle and submicrometer-sized particles of the phosphor can be compared in Figure 7.2. The geometric mean diameter for the particles obtained by sintering large numbers of nanoparticles contained in each droplet of the precursor sol was 560 nm and the geometric standard deviation was exceptionally narrow (1.55). The arithmetic mean and the Sauter diameter were equal to 620 nm and 850 nm, respectively. When the primary particles were large, the deposits consisted of relatively small particles because there was rarely more than one particle in a single droplet and particles larger than approximately 500 nm could not be carried into the flame with the droplets produced by the ultrasonic nebulizer. In this case, the geometric mean diameter was 160 nm (GSD = 2.0); the arithmetic mean was 200 nm; and the Sauter diameter was equal to 350 nm. It seems that the efficiency of sol-assisted FAD strongly decreases when the size of the colloidal particles exceeds 200 nm.

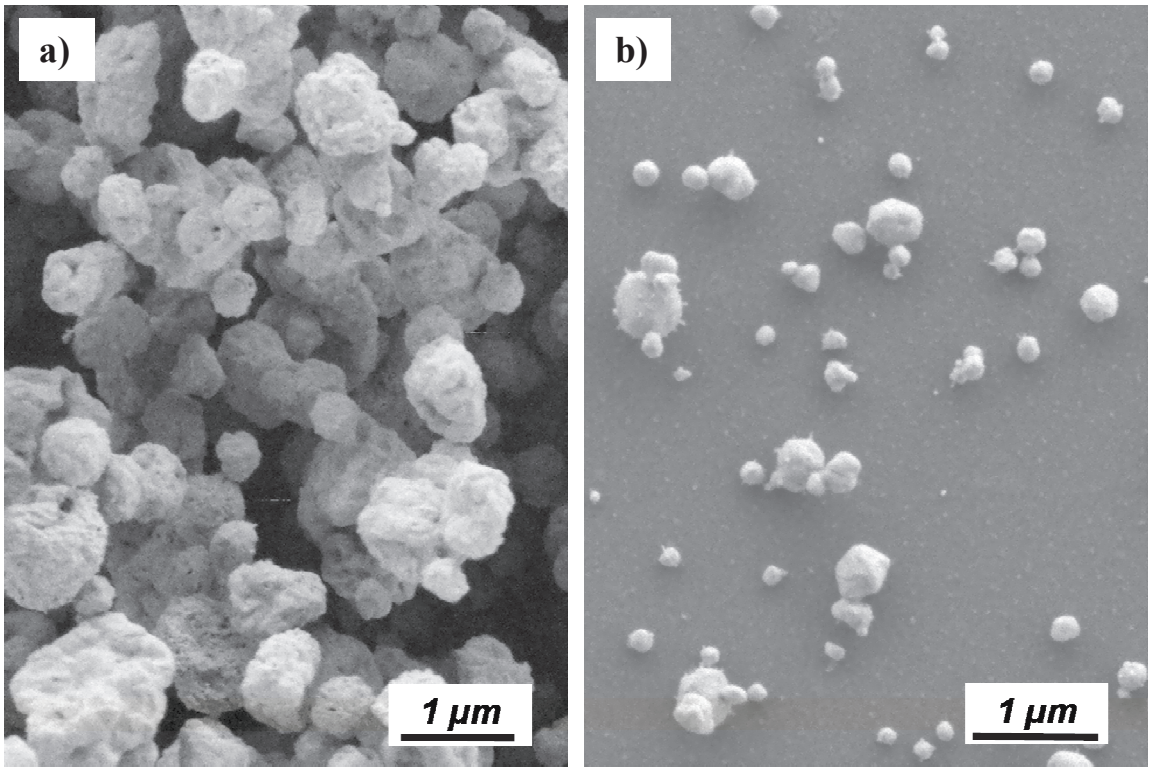

Figure 7.1 – SEM of Y_2O_3:Eu powders deposited by sol-assisted FAD from salt-free suspensions of nanoparticles (CVC-FAD, 23.6 mg/ml) (a) and micrometer-sized particles (DPC-FAD, 15 mg/ml) (b).

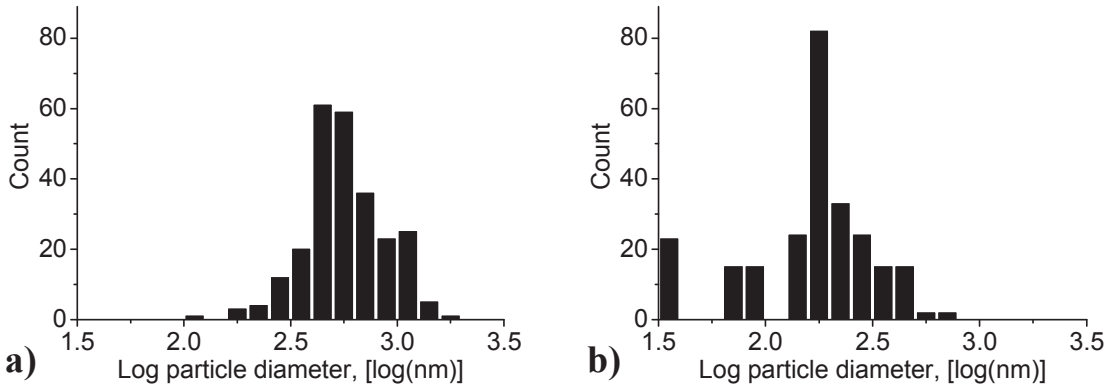

Figure 7.2 – Particle size statistics for Y_2O_3:Eu powders deposited by sol-assisted FAD from salt-free suspensions of nanoparticles (CVC-FAD, 23.6 mg/ml) (a) and micrometer-sized particles (DPC-FAD, 15 mg/ml) (b).

Although the small amount of the nanophosphor powder did not allow the thorough investigation of the relation between the specific weight and brightness of the coatings to be conducted, it is believed that the efficiency of luminescence of the

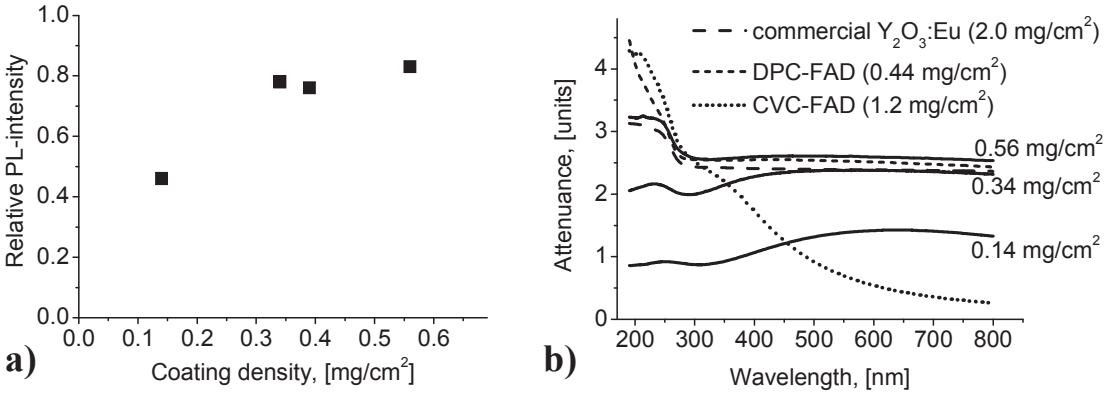

Figure 7.3 – Dependence of the T-mode PL-brightness (for excitation at 254 nm) (a) and attenuance (b) on the coating density of Y_2O_3:Eu phosphor coatings obtained from the sol (23.6 mg/ml of CVC-FAD produced Y_2O_3:Eu nanoparticles dispersed in 4 parts water and 1 part ethanol).

phosphor produced from the sol should be close to that of the powders obtained by the standard DPC-FAD. The highest value of the T-mode PL-intensity for excitation at 254 nm was measured for a coating with a density of 0.56 mg/cm^2; it reached 83 % of the maximum brightness of the reference samples deposited from the commercial phosphor powder (Figure 7.3a). Measurements of attenuance (Figure 7.3b) show that this coating density should approximately correspond to the optimum thickness because the value of attenuance at 254 nm reaches 3 units. Near this wavelength, the curve of the thickest coating deposited from the sol practically coincides with that of the best coating deposited by the standard DPC-FAD. In the visible range, they have a small difference in scatterance, which could be explained by unequal coating densities. In the range of strong absorption, the values of attenuance differ more strongly.

Analysis of the T-mode excitation spectra of photoluminescence (Figure 7.4) which were obtained from the attenuance spectra measured with the long-pass optical filter, shows that in the range of the host absorption the phosphor coating obtained from the sol outperforms the screen deposited from the standard precursor solution based on the nitrates of yttrium and europium. Improving the surface morphology of the phosphor particles was expected to cause changes in the efficiency of photoluminescence at the wavelengths for which the penetration depth of exciting radiation incident on a phosphor particle becomes much smaller than the diameter of the particle. However, it should be clarified whether or not the observed improvement merely results from adding 20 vol.% of ethanol to the precursors.

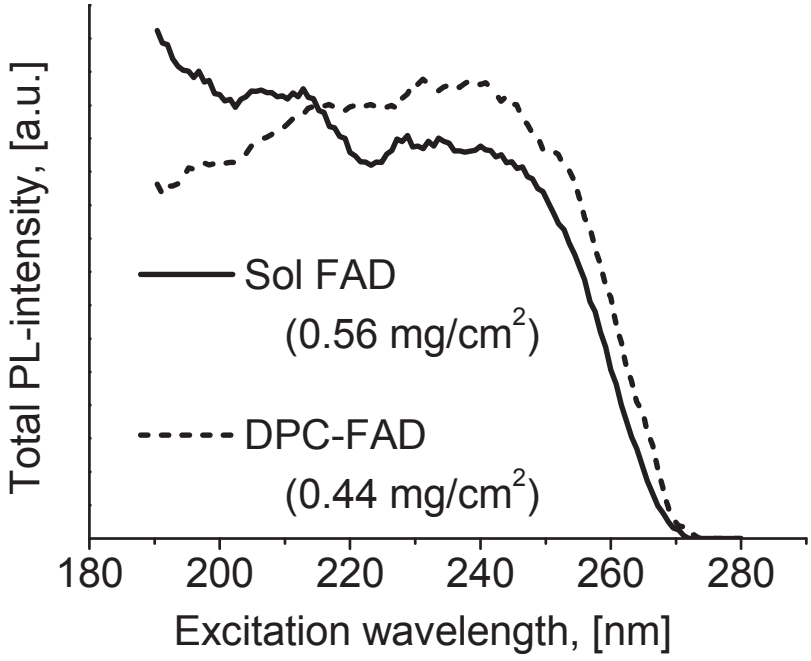

Figure 7.4 - T-mode PLE spectra derived from the measurements of attenuance of the phosphor coatings deposited by the conventional DPC-FAD and non-pyrolytic DPC-FAD.

7.2. Effect of adding ethanol to the standard nitrate precursor solution

A series of samples of europium-doped and pure yttria in a wide range of coating densities were produced from 0.2 M nitrate solutions containing 20 vol.% of ethanol. For a fixed volume concentration of droplets in the flame, the partial substitution of water with ethanol should lead to an increase of the total heat release rate, thus increasing the temperature of the flame and improving the crystallinity and quantum efficiency of the synthesized phosphor powders. On the other hand, the presence of ethanol should also modify the size of the droplets produced by the ultrasonic nebulizer because it is affected by the surface tension of the precursor solution. The efficiency of transport of the droplets into the flame could also change, especially by taking into account that the hose connecting the nebulizer and the burner was not heated during the experiments with ethanol.

Measurements of the flame temperature revealed that the addition of ethanol did not cause any increase in the obtained values. For all other conditions being equal (i.e., without the hose heating), the maximum temperature of the flame without any droplets was about 1500℃. When droplets of pur e water were brought into the flame (the maximum nebulization rate, carrier gas flow rate 3 l/min), the temperature

at the same location decreased to 1460℃ while when spraying water with ethanol, 1450℃ was measured. Additionally it was observed that for extended durations of FAD at high nebulization rates, the deposition rate of the phosphor coating was up to 50-60 % higher when ethanol was added to the precursors. It can be suggested that ethanol influences the nebulization rate of the precursors and the effect becomes more pronounced when the temperature of the liquid in the ultrasonic cup rises. The relationship between the presence of ethanol in the precursor solution and the flame conditions was not further investigated. Nonetheless, the negligible effect on the flame temperature allows for the preliminary conclusion that the crystallinity of the phosphor can not be improved much with moderate amounts of ethanol.

As it can be seen in Figure 7.5, the morphology of the particles obtained with ethanol was not that different from that of the phosphor produced by the standard DPC-FAD technique. The deposited particles were of porous fluffy consistency, which was usually associated with poor photoluminescent performance in the range of strongly absorbed UV-radiation.

The efficiency of luminescence for excitation via the charge transfer band (at 254 nm) was investigated first (Figure 7.6a). The maximum T-mode brightness was achieved with a coating density of 0.43 mg/cm^2, i.e., the value of the optimum screen thickness was not affected by the introduction of ethanol to the precursors (for the standard DPC-FAD without ethanol the optimum value was 0.44 mg/cm^2). The measured PL-intensities were, however, substantially lower than those obtained by the standard implementation of the method (77 % vs. 97 % of the maximum T-mode

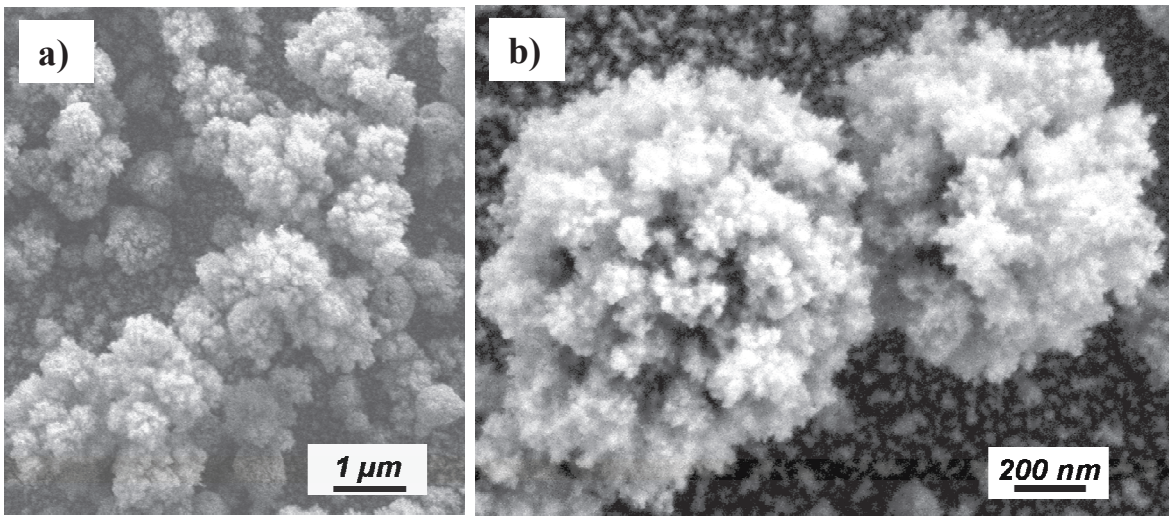

Figure 7.5 – SEM-pictures of yttria particles produced by the standard DPC-FAD with 20 vol.% ethanol added to the precursor solution (final concentration of yttrium ions 0.2 M) at the original magnification of 30,000 (a) and 100,000 (b).

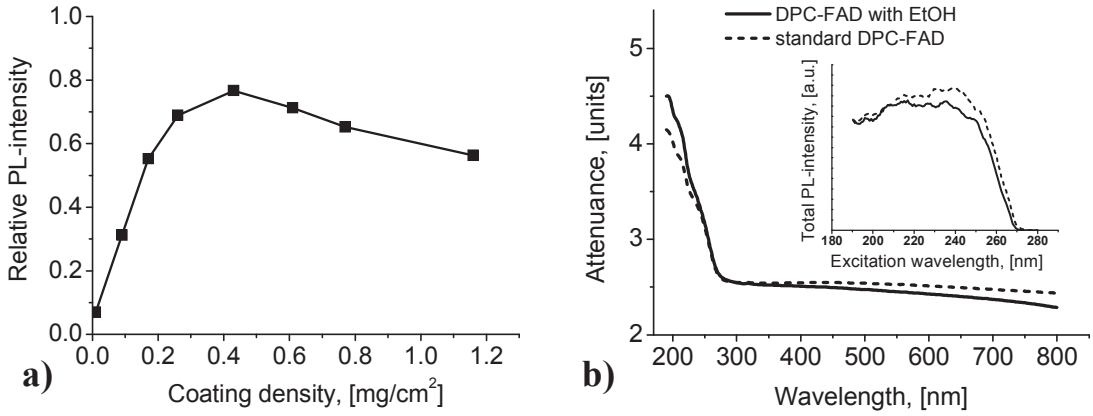

Figure 7.6 - Dependence of the T-mode PL-brightness (for excitation at 254 nm) on the coating density of Y_2O_3:Eu phosphor coatings produced by the DPC-FAD with 20 vol.% ethanol added to the precursor solution ([RE] = 0.2 M, [Eu] = 8.5 mol.%) (a); and attenuance curves of the best samples produced with and without ethanol. The corresponding T-mode PLE spectra derived from the measurements of attenuance are shown in the inset.

brightness of the commercial reference, respectively.) In the attenuance spectra of these two samples, there was a noticeable difference at both ends of the investigated spectral range (Figure 7.6b). Comparison of the derived photoluminescence excitation spectra (see the inset in Figure 7.6b) shows that the brightness of the Y_2O_3:Eu phosphor coating deposited from precursors containing ethanol is lower than that of the coating produced by the standard DPC-FAD in the whole studied wavelength range. The inferior properties of the phosphor could be attributed to the fact that the hose between the nebulizer and the burner was not heated (see Section 5.1.3). Finally, it can be concluded that better performance in the range of the host absorption for the phosphor coatings obtained by non-pyrolytic FAD (i.e., from the sol of Y_2O_3:Eu nanoparticles, Section 7.1) is not due to the presence of ethanol in the precursors.

7.3. Seed-assisted DPC-FAD

Improvement of particle morphology does not necessarily require full substitution of the precursor salts by a sol of nanoparticles with the composition of the desired final compound. It is known from the literature on ultrasonic spray pyrolysis that addition of relatively small amounts of nanocrystalline seeds can also lead to a noticeable decrease in the hollowness of the obtained phosphor particles.[284] Furthermore, by combining solutions of salts with insoluble colloids, one could prepare parti-

cles with deliberately non-uniform composition (e.g. non-uniform distribution of dopants, spatial separation of different activators in the same host, etc.). It could also be expected that seeding may improve the crystallinity of phosphor powders synthesized at low flame temperatures. The influence of the addition of Y_2O_3:Eu nanoparticles to the precursors of Y_2O_3, Gd_2O_3, and YAG hosts was investigated. In each case, two compositions of the sol were tested: 1) 1.18 mg/ml of phosphor nanoparticles produced by CVC-FAD dispersed in 0.19 M solution of the corresponding metal nitrates; and 2) 11.8 mg/ml of the nanoparticles in 0.1 M nitrate solution. For the first composition, the amount of material introduced by the seeds was equal to 5 mol.% of the final product, whereas for the second one the molar ratio of the products of pyrolysis and yttria precursors was approximately 1:1. The amount of ethanol in the precursor sol varied between 1 and 10 vol.% (proportionally to the concentration of the nanoparticles).

7.3.1. Y_2O_3:Eu nanoparticles in Y_2O_3

The morphology of the Y_2O_3:Eu particles produced by seed-assisted flame spray pyrolysis changed according to the amount of nanoparticles added. For high concentration of the seeds, particle shapes and surface roughness were similar to those of the phosphor powder obtained from the sol without any salt (Figure 7.7a). On the other hand, when the precursor solution contained a relatively small fraction of suspended nanoparticles, the surface of the synthesized particles was extremely rough (Figure 7.7b), comparable to that of the particles deposited by the standard DPC-FAD technique based on pyrolysis of rare earth nitrates (see Section 5.1).

Unfortunately, it was not possible to compare the efficiency of photoluminescence of the coatings obtained with and without colloidal seeds because the small number of produced samples did not allow for optimization of the screen thickness for the maximum T-mode brightness. The brightness was undoubtedly observed to increase with the increase in the concentration of phosphor nanoparticles in the precursor solution; however, the improvement could be fully explained by the increase in the total concentration of the activator. Apart from the seeds, the precursor solution did not contain any europium.

Analysis of the decay time of PL-emission showed that the value measured for the powder produced only from the Y_2O_3:Eu nanoparticles (and thus containing 8 mol.% europium) was very close to that of the phosphor prepared by the standard DPC-FAD (without seeds) with 8.5 mol.% Eu-ions (0.92 ms vs. 0.95 ms, respectively). For precursors with 50 % nanoparticles ([Eu] = 4 mol.%), the exponential decay time constant was 1.04 ms, whereas for the standard DPC-FAD phosphor containing 4.5 mol.% Eu it was slightly larger (1.13 ms). The difference was even more pronounced when the concentration of the nanoparticles in the precursors was low. For

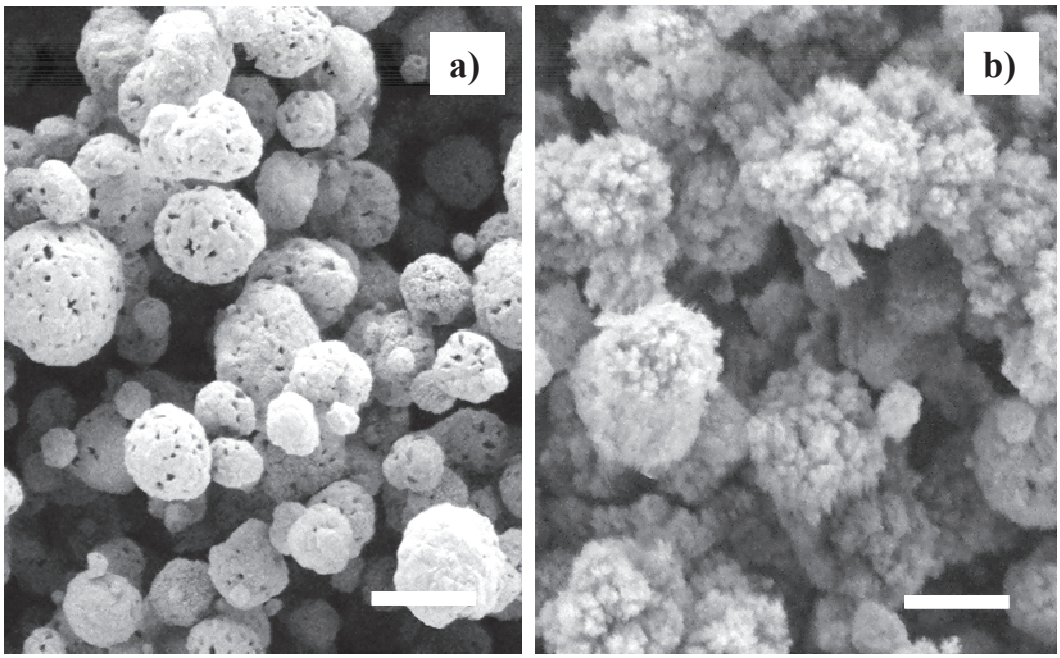

Figure 7.7 – SEM of Y_2O_3:Eu powders obtained by adding 50 % (a) and 5 % (b) of Y_2O_3:Eu nanoparticles to the precursor solution. Scale bar is 1 μm.

5 mol.% nanoparticles in the precursors (0.4 mol.% Eu in the final product), a value of 1.24 ms was found. The standard flame synthesized Y_2O_3:Eu would have a value of 1.37 ms in this range of dopant concentrations (0.5-1 mol.% of the dopant, see Section 5.1.6). The faster decay of the luminescence in the phosphor obtained by the seed-assisted FAD could be explained in several ways. First, this could be the effect of any unintentional impurities introduced during the synthesis of the seeds or in the final processing step. Second, the shortening of the decay time could be caused by the increased number of defects in the crystalline structure. Finally, it is possible that europium ions are not evenly distributed in the interior of the phosphor particles, e.g., a higher concentration in the seeds and a lower concentration in the yttria produced by pyrolysis. In such a case, the energy transfer between the activator ions in the "seed volumes" would have a higher probability than for the material having otherwise the same overall composition but with uniformly distributed doping, which leads to an enhancement of concentration quenching.

The crystallinity of the produced Y_2O_3:Eu phosphor powders, as judged from the XRD-spectra, seems not to be affected by seeding. In all cases, phase-pure cubic modification of yttria was found (Figure 7.8). It should be added that the initial crystalline phase of the seeds had no influence on the purity of the cubic phase in the final product. When a sol of monoclinic yttria nanoparticles was sprayed, there were no peaks of the monoclinic phase in the XRD spectra of the so-obtained powder. The width of the peaks and therefore the grain size did not noticeably change irrespective

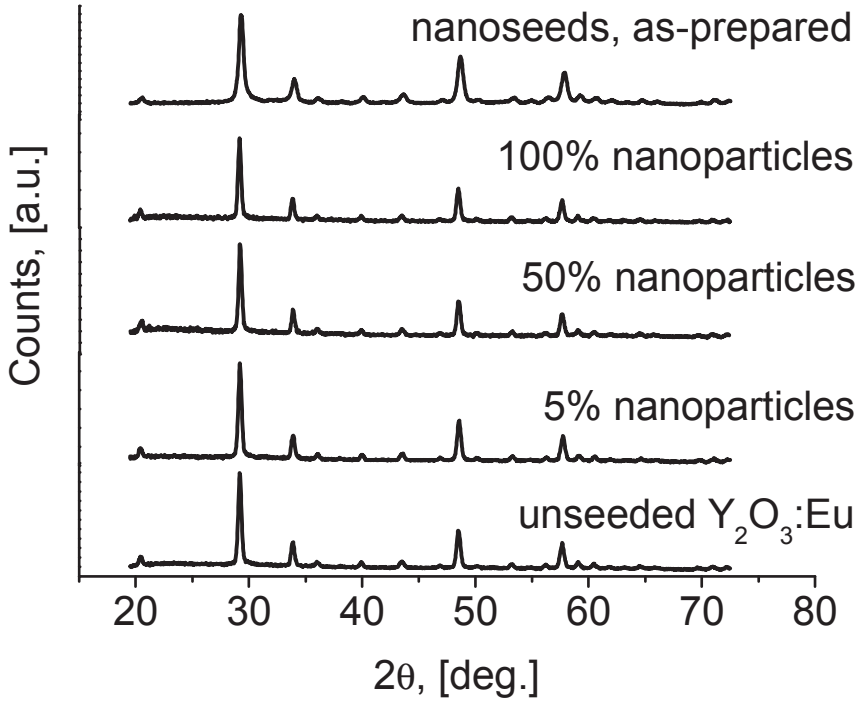

Figure 7.8 – XRD spectra of Y_2O_3:Eu powders obtained by adding different amounts of Y_2O_3:Eu nanoparticles to the precursor solution.

of the ratio between the dissolved nitrates and suspended oxide nanoparticles in the precursors. Crystallites in the synthesized phosphor powders were noticeably larger than the initial size of the seeds (compare the curve corresponding to the as-prepared nanoseeds with the other curves in Figure 7.8).

7.3.2. Y_2O_3:Eu nanoparticles in Gd_2O_3

The changes in morphology of the phosphor particles obtained by seeding Y_2O_3:Eu into gadolinia were similar to those observed for seeded yttria (Figure 7.9). For high amounts of nanoparticles, particles with relatively smooth surface were produced. When the concentration of the seeds was reduced, the surface of the particles became fluffy so that they resembled the $(YGd)_2O_3$:Eu phosphor synthesized by the standard DPC-FAD (see Section 5.1.8).

Again, the phase composition of the products of FAD did not depend on the way in which yttrium ions were added to the precursors. As it can be seen in Figure 7.10, even when the precursor sol contained 50 mol.% of nanoparticles of the cubic yttria, a powder deposited on the substrate consisted completely of the monoclinic phase, in full agreement with the results of the standard seedless DPC-FAD for an

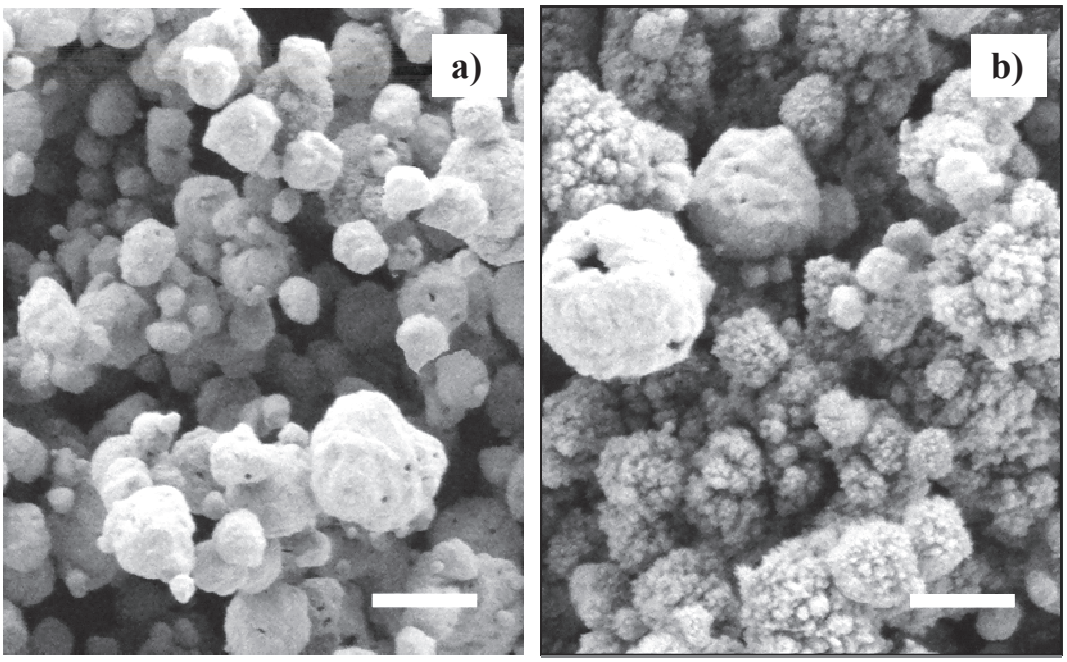

Figure 7.9 – SEM of $(YGd)_2O_3$:Eu powders obtained by adding 50 % (a) and 5 % (b) of Y_2O_3:Eu nanoparticles to the precursor solution of Gd_2O_3. Scale bar is 1 μm.

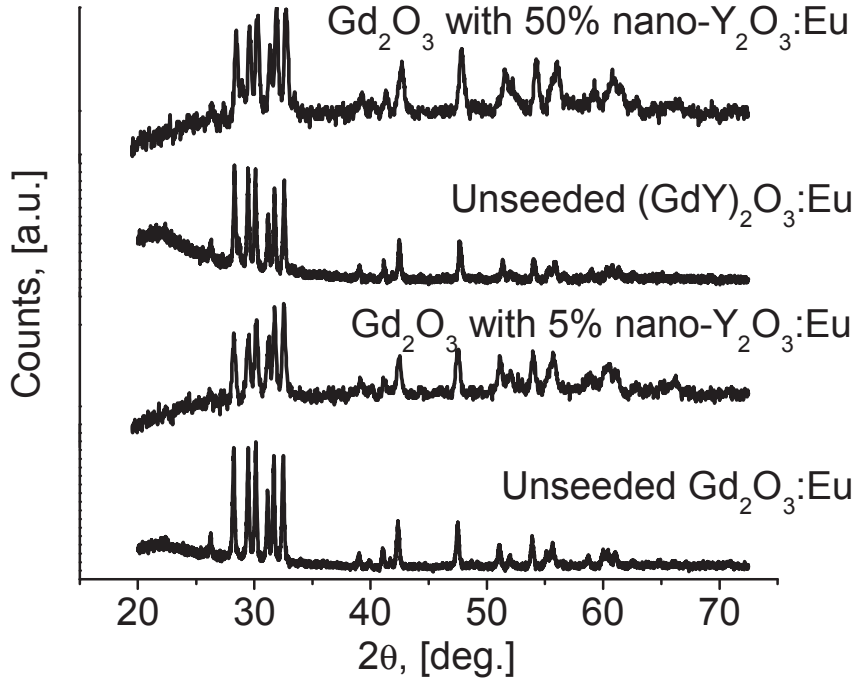

Figure 7.10 – XRD spectra of $(YGd)_2O_3$:Eu powders obtained by adding either Y_2O_3:Eu nanoparticles or nitrates of yttrium and europium to the precursor solution of Gd_2O_3.

equal ratio of yttrium and gadolinium ions (Section 5.1.8). On the other hand, peaks in the XRD spectra of the seeded phosphor powders were generally noticeably wider than those corresponding to the powders, for which all precursors were dissolved and mixed at the atomic level. It can be suggested that the difference between the chemical composition of the seeds (Y_2O_3) and the surrounding medium (Gd_2O_3) inhibits grain growth during the short residence time of the particles in the flame.

Measurements of the decay time of luminescence revealed that the value of the single exponential constant of the $(YGd)_2O_3$:Eu powders containing 50 % nanoparticles (i.e., [Eu] = 4 mol.%) and 5 % nanoparticles ([Eu] = 0.4 mol.%) practically did not change (0.85 ms vs. 0.86 ms, respectively). Usually the decay rate decreases for lower concentrations of the activator. The observed behavior can be attributed to the change of the effective refractive index of the phosphor, which is reflected in the variation of the radiative decay rate (see Section 2.3.3d). Bulk gadolinia has a slightly higher refractive index than that of yttria. If the molar fraction of yttria decreases simultaneously with the concentration of europium, the increase in the refractive index could compensate for the dilution of the emitting ions. Additionally, the effect of a non-uniform distribution of europium ions between the Y_2O_3 seeds and Gd_2O_3 matrix (as proposed in Section 7.3.1) may play a role.

PLE spectra of the $(YGd)_2O_3$:Eu phosphor with a low concentration of seeds featured several additional peaks which are attributed to the charge transfer from Gd-ions to Eu-ions (Figure 7.11). These peaks are not usually observed in the spectra of phosphors produced by spray pyrolysis-based methods because the Gd-sensitization

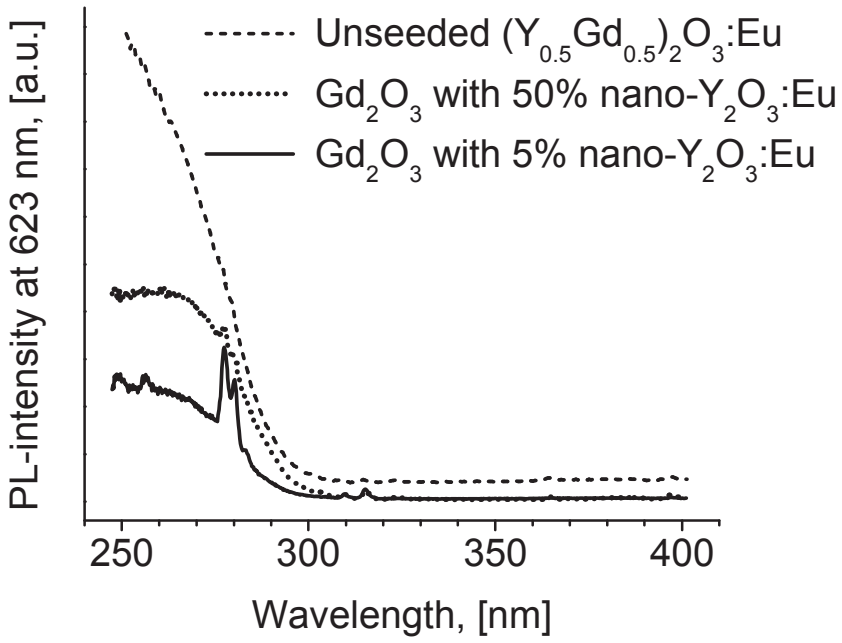

Figure 7.11 – PLE spectra of $(YGd)_2O_3$:Eu phosphor obtained by adding Y_2O_3:Eu nanoparticles to the precursor solution of Gd_2O_3.

effect is not pronounced at high Eu-concentrations.[50] For the $(Y_{0.5}Gd_{0.5})_2O_3$:Eu powder produced by the standard DPC-FAD, the concentration of the activator was 10 mol.% so that there are no such peaks in the corresponding curve in Figure 7.11.

7.3.3. Y_2O_3:Eu nanoparticles in $Y_3Al_5O_{12}$

There is a principal difference between seed-assisted FAD of yttria/gadolinia and that of yttrium aluminate. First, $Y_3Al_5O_{12}$ obtained by the standard DPC-FAD is amorphous (see Section 5.3), whereas $(YGd)_2O_3$ powders are crystalline for any ratio of Y_2O_3 and Gd_2O_3. Second, particles of yttrium aluminate produced by the standard technique have a nearly perfect spherical shape with very smooth surface so that their morphology could change in some different way, as compared to the $(YGd)_2O_3$.

Figures 7.12a and 7.12b show that the surface of the phosphor particles produced with large amounts of yttria nanoparticles is considerably rough, unlike the particles with low seed loads or those synthesized by the standard FAD (see Section 5.3). It is very important to understand why seeding could cause such degradation of the surface morphology. A comparison of the corresponding XRD curves depicted in Figure 7.13 can provide an answer to this question. One can see that the heavily seeded powder is crystalline, whereas those with small amounts of seeds or unseeded are amorphous. Therefore, it could be suggested that roughness of the particle surface correlates with the crystallization of the pyrolyzed compounds. From this

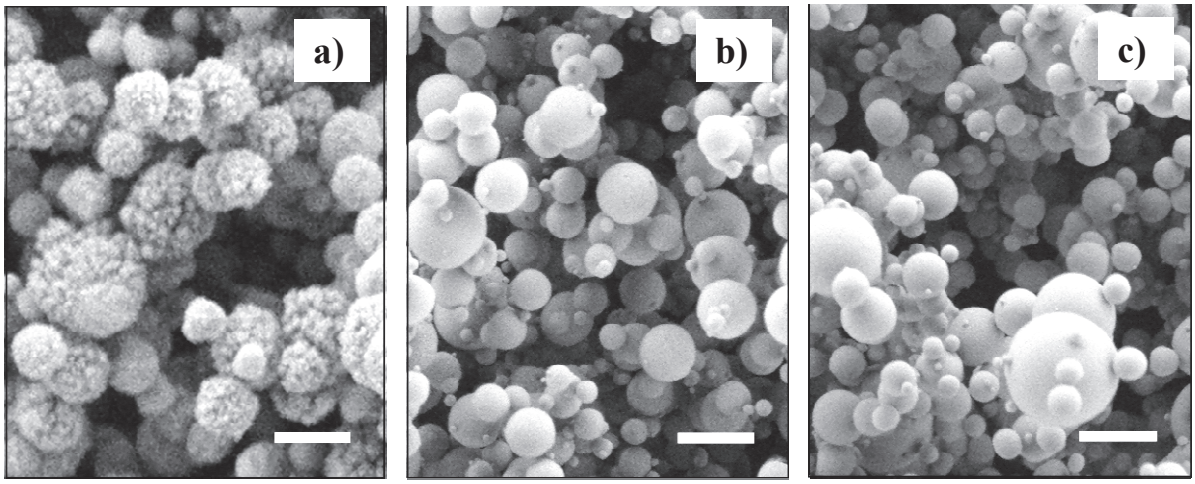

Figure 7.12 – SEM of $(YAl)_2O_3$:Eu powders obtained by adding 50 % (a) and 5 % (b) of Y_2O_3:Eu nanoparticles to the precursor solution of $Y_3Al_5O_{12}$; and $Y_3Al_5O_{12}$ powder obtained by adding 37.5 mol.% of Y_2O_3 nanoparticles to the precursor solution of Al_2O_3 (c). Scale bar is 1 μm.

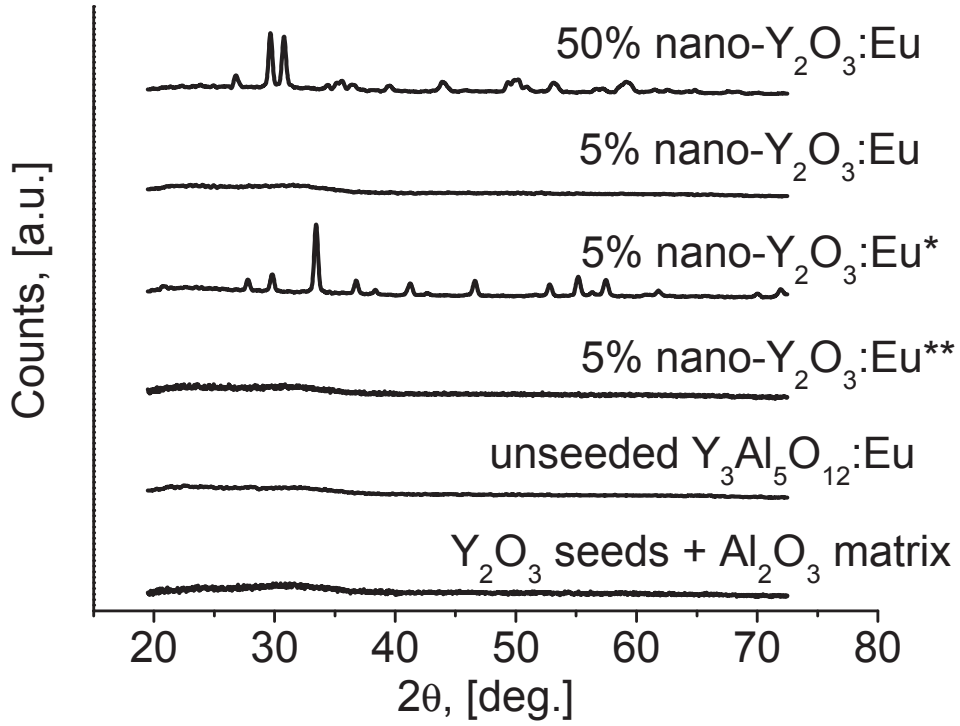

Figure 7.13 – XRD spectra of $(YAl)_2O_3$:Eu powders obtained by adding Eu-doped or pure Y_2O_3 nanoparticles to the precursor solution of either $Y_3Al_5O_{12}$ or Al_2O_3. Samples denoted by * were annealed in an oven, and those with ** were flame-annealed.

point of view, the degradation of the surface morphology of phosphor particles results not from the presence of colloidal particles in the precursors but rather from the change in the overall ratio of yttrium and aluminum ions.

The XRD spectrum of the powder produced from precursors containing 50 % nanoparticles could be identified with the monoclinic modification of the yttrium aluminate.[107] The addition of yttria seeds changed the relative concentrations of yttrium and aluminum ions in the flame synthesized powder from the stoichiometry of YAG (3 parts of Y per 5 parts of Al) to the yttrium-rich (11 parts of Y per 5 parts of Al), which is very close to that of the YAM phase (2:1, respectively, see Section 4.2.1b). It is known that YAM crystallizes more readily than YAG, so that no thermal post-treatment was required. For a low concentration of yttria nanoparticles in the precursor sol, the fraction of yttrium ions is only slightly over-stoichiometric with respect to the composition of YAG. In this case, as-deposited powders stay amorphous and should be post-treated. The phase-pure YAG was obtained after annealing in an oven for 4 h at 1100℃ (see the corresponding curve i n Figure 7.13). The *in situ* flame

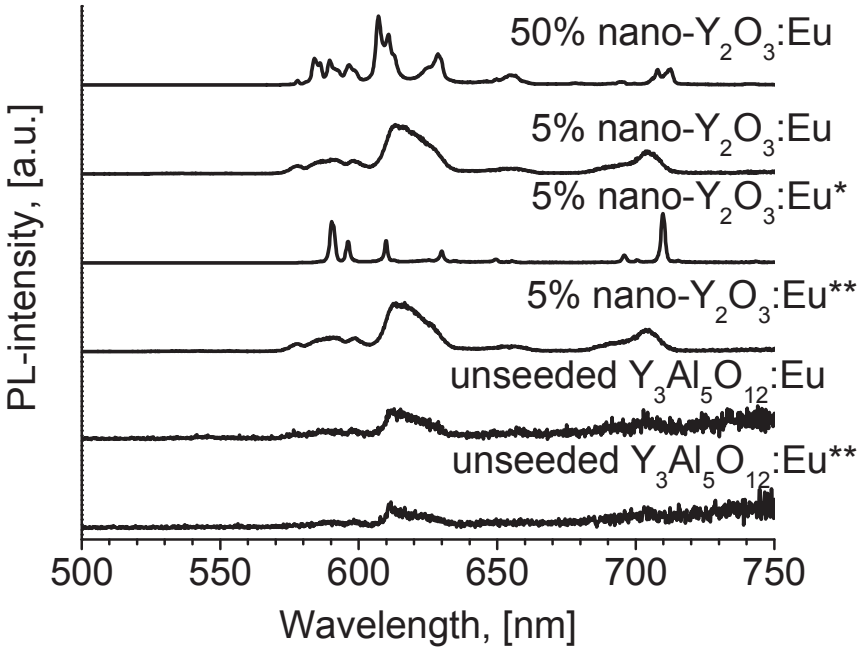

Figure 7.14 – PL-emission spectra of $(YAl)_2O_3$:Eu powders obtained by adding Y_2O_3:Eu nanoparticles to the precursor solution of $Y_3Al_5O_{12}$. Samples denoted by * were annealed in an oven, and those with ** were flame-annealed.

annealing for 5 min (the procedure is discussed in Sections 5.1.3 and 5.3.3) did not noticeably affect the amorphous powder produced with 5 % of yttria nanoparticles.

An additional experiment with precursors possessing the stoichiometry of YAG was made by introducing Y_2O_3 nanoparticles (8.5 mg/ml) to the precursor solution containing only aluminum nitrate (0.125 mol/l). This composition corresponds to the stoichiometric ratio of 3 parts of yttrium per 5 parts of aluminum. As one see in Figures 7.12c and 7.13, there was no significant difference in particle morphology or crystallinity (or, strictly speaking, non-crystallinity) between the powders produced with nanoparticles and those synthesized by the standard FAD without colloidal seeds.

Photoluminescence emission spectra were strongly affected by the crystallographic state of the phosphor powders (Figure 7.14). Amorphous coatings emitted in the range characteristic for Eu-ions in Y_2O_3. The peaks were relatively broad, which is explained by non-crystalline environment of the emitting ions. For the same nominal concentration of the activator (0.4 mol.%), the brightness of the seeded powders was somewhat higher than that of the powders produced in the standard way. A spectrum of luminescence of the powder with the increased yttria fraction was in

good agreement with that of YAM:Eu phosphor[107] although several peaks could be identified with the superimposed spectrum of the crystalline Y_2O_3:Eu. The annealed YAG:Eu sample had the main intensity peak at a wavelength of 710 nm.

The luminescence decay time of as-deposited coatings was measured as well. Amorphous powder seeded with 5 % Y_2O_3:Eu nanoparticles (0.4 mol.% Eu) had an exponential decay time constant of 1.15 ms. PL-emission from the YAM:Eu phosphor (4 mol.% Eu) was observed to cease with a constant of 2.7 ms.

7.4. Summary on sol-assisted DPC-FAD

It was shown that substitution of the salts dissolved in the precursor solution by a sol of nanoparticles with chemical composition corresponding to the desired final product of FAD can be successfully carried out to improve the morphology of phosphor particles. The Y_2O_3:Eu phosphor powder obtained from the colloidal suspension of Y_2O_3:Eu demonstrated the narrow particle size distribution, as well as low porosity and reduced surface roughness of the particles. The T-mode PL-brightness of the coating deposited from the sol was found to exceed that of the best sample produced by the standard DPC-FAD technique when excited in the range of the host absorption (λ < 220 nm). The UV-light with such short wavelengths has a very shallow penetration depth into the particle volume so that the efficiency of conversion into visible light is strongly affected by the surface condition.

It was discovered that the efficiency of FAD from the sol abruptly decreases for particles larger than 200 nm. The deposition rates for the precursor sol of nanoparticles (ϕ_{BET} = 24 nm) with particle concentration equivalent to the 0.2 M precursor solution was comparable to that obtained by the standard DPC-FAD.

Finally, the possibility of the partial substitution of precursor salts by the oxide nanoparticles was investigated. When the relative concentration of the seeds was low (5 mol.%), the morphology of the obtained phosphor particles was very similar to that of the powders synthesized without seeds. Higher loads of nanoparticles substantially changed the particle morphology; the surface roughness was especially affected. For yttria and gadolinia, seeding with 50 mol.% of Y_2O_3:Eu nanoparticles resulted in particles with a smoother surface. At the same time, for the stoichiometric composition of the precursor solution of the YAG-host, addition of colloidal particles of yttria leads to crystallization of the YAM-phase and considerable surface roughness. It was suggested that in general, smoothness of the particle surface correlates with the amorphous structure of the deposited solid particles.

8. Conclusions and outlook

8.1. Conclusions

8.1.1. Pros and cons of FAD

The main purpose of the investigations presented in this thesis was to assess the potential of flame spray pyrolysis for deposition of phosphor powder coatings with reduced particle size. In this section, the general advantages and disadvantages of FAD will be discussed. The following subsections will be devoted to more specific results on FAD techniques based on droplet-to-particle conversion and, separately, on chemical vapor condensation.

FAD is a method combining the advantages of flame spray pyrolysis with cohesive properties of the aerosol particles. In this way, unpixelated phosphor screens on the scale of several square centimeters could be manufactured within minutes, in a single step starting with precursor solutions of inexpensive inorganic salts. Larger areas could be coated, e.g., by slowly moving either the substrate or the burner during the deposition. The possibility of rapid processing should be considered as the general practical advantage of various realizations of FAD.

The second advantage of the direct deposition of aerosols by FAD is that it does not involve application of any binder. Once the particles contact a surface (or each other), they stick on it (or stick together). FAD-deposited coatings demonstrated remarkable mechanical stability: there was no significant weight loss after shaking the sample, dropping it (provided that it did not fall on the coated surface), annealing by the flame impinging on the coating, and exposure to moderate blows from an air blow gun. The absence of binding and tackifying agents assures the maximum possible efficiency of luminescence of the phosphor for excitation with strongly absorbed radiation (e.g. in the vacuum UV range). This is especially important for nanophosphors because their luminescent properties are strongly affected by contamination of the particle surface.

The third advantage of FAD consists in the efficient means of control over the size of the phosphor particles. In most cases, a desired average particle diameter can be obtained by simply adjusting the concentration of the precursor solution. FAD based on droplet-to-particle conversion is better suited for submicrometer-sized particles, although nanoparticles could also be produced by slightly modifying the process.[249] For the chemical vapor condensation of nanoparticles, it can be more complicated to control the particle size as there are more parameters affecting it. Flame synthesis of nanoparticles is an area of intense investigation, and new flexible approaches are being developed even for quite complicated problems (e.g., Rudin *et al.*[286]).

As the fourth important general advantage of FAD, one should mention the possibility of a rapid (also on the scale of several minutes) thermal post-treatment of the deposited coatings in the same setup used for deposition. The *in situ* direct annealing was successfully carried out for stabilization of nanoparticle coatings deposited by CVC-FAD.[197,268] In this thesis, a very similar procedure was utilized for either improving the crystallinity or initiation of crystallization processes in the phosphor powders deposited by DPC-FAD.

The major drawback of FAD is the considerable overspraying. Only a very low fraction of the synthesized powder is actually deposited onto the exposed substrate. In this work, the values of deposition efficiency obtained for DPC-FAD were on the order of a few percent, and less than one percent of the total weight of produced nanophosphor was deposited on the substrate by CVC-FAD. Although the losses of powder could surely be reduced by optimizing the size and location of the substrates, FAD could hardly be compared to some other screening methods (e.g., sedimentation) from this point of view.

The second disadvantage of FAD is that it usually produces extremely porous structures. In the case of phosphor coatings, especially if high resolution of the screen is required, the phosphor particles have to be densely packed in order to reduce light scattering. For DPC-FAD, porosities in excess of 85 vol.% were obtained. Nanoparticle coatings deposited by CVC-FAD had particle volume concentration of less than 3 vol.% (i.e., > 97 % porosity).

The third weakness of FAD is related to the inevitable exposure of substrates to high temperatures. Mounting the substrate in immediate proximity of the flame is essential for deposition. This may bring about certain implications and, for example, limit the applicability of FAD for the substrates which cannot withstand temperatures of at least 500℃.

Finally, as a process based on combustion, FAD is mainly limited to depositing oxides. Although there are exceptions to this rule,[170] some important practical phosphors (such as Y_2O_2S:Eu and Gd_2O_2S:Tb) cannot be processed by FAD unless an appropriate chemical post-treatment of the deposited coatings is developed. The feasibility of the chemical transformation of phosphor nanoparticles produced by flame spray pyrolysis has already been demonstrated.[287]

8.1.2. Conclusions on DPC-FAD and new findings on FASP

The most important outcome of the experiments on deposition of phosphor screens by DPC-FAD is that it can yield coatings with brightness equal to that achieved with conventional micrometer-sized phosphors. Furthermore, it was shown that required screen weights can be simultaneously decreased by 60-80 % due to the increased scattering efficiency and improved substrate coverage by submicrometer-

sized phosphor particles. Potentially, utilization of phosphor powders with particles in this size range could lead to a substantial decrease in the consumption of expensive raw materials. However, the vast overspraying characteristic for FAD-methods outweighs this advantage. The decrease of the coating densities also does not guarantee any improvement of the screen resolution because the degree of blurring of an image is mostly determined by the geometric thickness of the coating and not by its weight. FAD-deposits typically have very high porosities so that for excitation by radiation which is relatively weakly absorbed (e.g., in the charge transfer band), there is only a small difference, if any, between the optimum thickness of the conventional phosphor coatings and that of the FAD-screens. It should be concluded that the practical benefits of DPC-FAD are mainly constricted to its rapidness, which can allow for drastic reduction of the processing times of the phosphor screens.

In addition to the investigation of the relationship between the process parameters of DPC-FAD and resulting properties of the deposited coatings, there were several important contributions to the general research on flame-assisted spray pyrolysis of phosphor powders (i.e., without the purpose of depositing them onto any substrate). It was found out that polycrystalline phosphor particles obtained from the aqueous precursors in the low-temperature flames had extremely rough surface, whereas amorphous powders consisted of particles with very smooth surface and nearly perfect spherical morphology. It was demonstrated that surface roughness causes a remarkable degradation of the photoluminescent performance in the wavelength range of strong absorption of exciting radiation by the phosphor host. Morphology of the phosphor particles was successfully improved by adding the polymeric components to the precursor solution or by substituting the dissolved precursor salts with the sol of phosphor nanoparticles.

8.1.3. On CVC-FAD

The brightness of emission from the nanophosphor coatings deposited by CVC-FAD reached roughly one third of that of the conventional phosphor coatings and screens deposited by DPC-FAD. The scatterance of the nanoparticle films was appreciably wavelength-dependent so that the values of attenuance in the visible range (e.g. at the wavelength of emission of Eu^{3+}-ions in Y_2O_3) were much below those of the screens made of micrometer- or submicrometer-sized phosphor powders. As a consequence, the PL-brightness of the nanophosphor screens practically did not change for the coating densities in excess of the optimum value. It is also expected that the resolution of such screens (for excitation by the strongly absorbed radiation) will be significantly less dependent on their geometric thickness. The screen brightness was found to be affected by the light reflection from the substrate and by the porosity of the nanophosphor coating. Mechanical compaction of the de-

posits facilitated the substantial improvement of efficiency of luminescence and also noticeably decreased the scatterance of the coating in the visible range.

8.2. Outlook

Although the study presented in this thesis answers many questions, the research on FAD of phosphor coatings should be continued further in several directions. For example, there are a few experiments and measurements which could have a relatively high importance but unfortunately could not be included in this work. Additional research would be required in order to prepare FAD for industrial implementation. Finally, both the DPC- and CVC-FAD techniques could be further developed and augmented by other processing methods for the purpose of extending the application field of the deposited phosphor coatings.

First, the photoluminescent performance of the coatings obtained by CVC-FAD in the VUV-range has to be thoroughly investigated (preferably in the T-mode). Changes of the optimum thickness of the nanophosphor screens with the decrease of penetration depth of the exciting radiation into the interior of the particles should be studied and compared to the coatings made of micrometer- and submicrometer-sized phosphors. Systematic experiments on mechanical compaction of the nanoparticle deposits could also produce interesting results concerning the improvement of their PL-brightness and achievable screen resolution. The resolution of both the DPC- and CVC-FAD screens has to be experimentally characterized, especially for excitation in the VUV range. It could also be attempted to passivate the surface of the phosphor particles by a layer of the corresponding undoped host material in order to improve the quantum efficiency of the CVC-produced nanopowders. For the screens obtained by DPC-FAD and excited in the VUV range, it could be advantageous to develop a seed-assisted technique for the synthesis of core/shell particles with a relatively thin luminescent shell and inexpensive non-luminescent core (e.g. undoped host), which will not be reached by the exciting radiation. In this way, the cost efficiency of FAD could be improved because substantially less activator would be consumed.

Industrial application of FAD would undoubtedly require gaining experience on deposition of other luminescent materials and minimization of the typical drawbacks of this method (see Section 8.1.1). For example, it is expected that the increase in the deposition efficiency of phosphor particles (i.e., decrease in the overspraying) could be achieved by introducing an electric field between the flame and the substrate to be coated.[288] Various methods of chemical transformation of the FAD-coatings to desired non-oxides could be investigated. It would also be very useful to develop a strategy for reliable transfer of deposited coatings from one substrate to another, thus avoiding exposure of the latter substrate to high temperatures.

A large field for experimentation is offered by the research on manufacturing of deliberately structured phosphor coatings (e.g. pixelated or multilayer screens) including coatings with added functionality (e.g. electrically conducting phosphor films). The deposits of oxide nanoparticles are usually non-conducting, which leads to a charge build-up under excitation by an electron beam. When current densities exceed some threshold value, detachment of phosphor particles from the substrate can be observed (e.g. during the SEM investigation at high magnifications). It is therefore desirable to have a means for increasing the conductivity of the phosphor layer so that an efficient charge sink could be realized. The aluminizing technique developed for the conventional CRTs[1] could hardly be applied for such porous structures as those obtained by FAD. It could be attempted to coat the phosphor particles with a very thin layer of transparent conductive oxide. Alternatively, the conductive oxide nanoparticles could be co-deposited by FAD.[289]

CVC-FAD coatings consisting of several layers of phosphors emitting at different wavelengths could be tested as beam-penetration screens which change their color upon excitation by photons or electrons of different energies.[1] Similar functionality could also be obtained with DPC-FAD, if core/shell particles composed of several different phosphors were deposited.[290,291]

These suggestions do not exhaust the list of future research activities in the field of flame aerosol deposition of phosphor coatings. As the interest in nanotechnology grows, it can be expected that the number of potential applications of nanophosphors will constantly increase so that FAD will face many new challenges in the coming years. The progress in science and technology of miniaturization will surely introduce even more drastic changes to our way of life in the second half of the first century of the nano-age that mankind entered in 1959. Flame spray pyrolysis and especially its modifications based on chemical vapor condensation can make an appreciable contribution to these changes.

References

1. S. Shionoya & W. M. Yen (eds.). *Phosphor handbook* (CRC Press, Boca Raton, Fla. 1999).

2. Blasse, G. & Grabmaier, B. C. *Luminescent materials* (Springer, Berlin, Heidelberg, New York, London, Paris, Tokyo, Hong Kong, Barcelona, Budapest, 1994).

3. Kitai, A. H. *Solid state luminescence. Theory, materials and devices.* 1st ed. (Chapman & Hall, London, 1993).

4. Lakshmanan, A. *Luminescence and display phosphors. Phenomena and applications* (Nova Science Publ. New York, NY, 2008).

5. Ronda, C. *Luminescence. From theory to applications* (Wiley-VCH, Weinheim, 2008).

6. Widdel, H. *Color in electronic displays* (Plenum Press, New York, 1992).

7. Bosman, D. *Display engineering. Conditioning, technologies, applications* (North-Holland, Amsterdam, 1989).

8. Ozawa, L. *Cathodoluminescence and photoluminescence. Theories and practical applications* (CRC Press, Boca Raton, Fla. 2007).

9. Henderson, B. & Imbusch, G. F. *Optical spectroscopy of inorganic solids* (Clarendon Press, Oxford, 1989).

10. Judd, B. R. in *Handbook on the Physics and Chemistry of Rare Earths,* edited by K. A. Gschneidner & L. Eyring (Elsevier Science Publishers, Amsterdam, 1988), pp. 81–195.

11. Garcia Sole, J. Bausa, L. E. & Jaque, D. *An introduction to the optical spectroscopy of inorganic solids* (Wiley, Chichester, 2005).

12. Liu, G. Jacquier, B. & Liu-Jacquier. *Spectroscopic properties of rare earths in optical materials* (Springer [u.a.], Berlin, 2005).

13. Carnall, W. T. Goodman, G. L. Rajnak, K. & Rana, R. S. A systematic analysis of the spectra of the lanthanides doped into single crystal LaF3, *J. Chem. Phys.* **90,** 3443–3457 (1989).

14. Naleway, C. *et al.* An ab initio study of the ionization potentials and f–f spectroscopy of europium atoms and ions, *J. Chem. Phys.* **116,** 5481–5493 (2002).

15. Ropp, R. C. *Luminescence and the solid state* (Elsevier, Amsterdam, 1991).

16. Dieke, G. H. Crosswhite, H. M. & Crosswhite, H. *Spectra and energy levels of rare earth ions in crystals* (Interscience Publishers, New York, 1968).

17. Görller-Walrand, C. & Binnemans, K. in *Handbook on the Physics and Chemistry of Rare Earths,* edited by K. A. Gschneidner & L. Eyring (Elsevier Science Publishers, Amsterdam, 1998), pp. 101–264.

18. Peacock, R. in *Rare Earths* (Springer, Berlin / Heidelberg, 1975), pp. 83–122.

19. Walsh, B. in *Advances in Spectroscopy for Lasers and Sensing,* edited by B. Di Bartolo & O. Forte (Springer Netherlands, Dordrecht, 2006), pp. 403–433.

20. Carnall, W. T. Fields, P. R. & Rajnak, K. Electronic Energy Levels in the Trivalent Lanthanide Aquo Ions. I. Pr3+, Nd3+, Pm3+, Sm3+, Dy3+], Ho3+, Er3+, and Tm3+, *J. Chem. Phys.* **49,** 4424–4442 (1968).

21. Carnall, W. T. Fields, P. R. & Rajnak, K. Electronic Energy Levels of the Trivalent Lanthanide Aquo Ions. II. Gd3+, *J. Chem. Phys.* **49,** 4443–4446 (1968).

22. Carnall, W. T. Fields, P. R. & Rajnak, K. Electronic Energy Levels of the Trivalent Lanthanide Aquo Ions. IV. Eu3+, *J. Chem. Phys.* **49,** 4450–4455 (1968).

23. Carnall, W. T. Fields, P. R. & Rajnak, K. Electronic Energy Levels of the Trivalent Lanthanide Aquo Ions. III. Tb3+, *J. Chem. Phys.* **49,** 4447–4449 (1968).

24. Ivankov, A. Seekamp, J. & Bauhofer, W. Optical properties of Eu3+-doped zinc borate glasses, *J. Lumin.* **121,** 123–131 (2006).

25. Windisch, R. *et al.* Impact of texture-enhanced transmission on high-efficiency surface-textured light-emitting diodes, *Appl. Phys. Lett.* **79,** 2315–2317 (2001).

26. Fujii, T. *et al.* Increase in the extraction efficiency of GaN-based light-emitting diodes via surface roughening, *Appl. Phys. Lett.* **84,** 855–857 (2004).

27. Wei, M.-K. *et al.* The influence of a microlens array on planar organic light-emitting devices, *J. Micromech. Microeng.* **16,** 368 (2006).

28. Krames, M. R. *et al.* Status and Future of High-Power Light-Emitting Diodes for Solid-State Lighting, *J. Display Technol.* **3,** 160–175 (2007).

29. Jianbo, C. Wenbin, C. & Kaiyu, Y. High luminance YAG single crystal phosphor screen, *Displays* **21,** 195–198 (2000).

30. Reineke, S. *et al.* White organic light-emitting diodes with fluorescent tube efficiency, *Nature* **459,** 234–238 (2009).

31. Fran, Y. S. & Tseng, T. Y. Involvement of scattered UV light in the generation of photoluminescence in powdered phosphor screens, *J. Phys. D* **32,** 513 (1999).

32. Wind, L. & Szymanski, W. W. Quantification of scattering corrections to the Beer-Lambert law for transmittance measurements in turbid media, *Meas. Sci. Technol.* **13,** 270 (2002).

33. Tam, W. G. & Zardecki, A. Multiple scattering corrections to the Beer-Lambert law. 1: Open detector, *Appl. Opt.* **21,** 2405–2412 (1982).

34. Dick, V. P. Applicability Limits of Beer's Law for Dispersion Media with a High Concentration of Particles, *Appl. Opt.* **37,** 4998–5004 (1998).

35. Donofrio, R. L. & Rehkopf, C. H. Screen Weight Optimization, *J. Electrochem. Soc.* **126,** 1563–1567 (1979).

36. Grossman, M. W. Effect of radiation transport on the kinetics of phosphor degradation, *J. Appl. Phys.* **84,** 1251–1262 (1998).

37. Ishida, K. Mitsuishi, I. Hattori, Y. & Nunoue, S. A revised Kubelka--Munk theory for spectral simulation of phosphor-based white light-emitting diodes, *Appl. Phys. Lett.* **93,** 241910–241913 (2008).

38. Jeon, B. S. Hong, K. Y. Yoo, J. S. & Whang, K.-W. Studies on the Phosphor Screen Prepared by Electrophoretic Deposition for Plasma Display Panel Applications, *J. Electrochem. Soc.* **147,** 4356–4362 (2000).

39. Baciero, A. *et al.* Vacuum ultraviolet and x-ray luminescence efficiencies of Y3Al5O12:Ce phosphor screens, *J. Appl. Phys.* **85,** 6790–6796 (1999).

40. Kandarakis I. *et al.* X-ray induced luminescence and spatial resolution of phosphor screens, *Phys. Med. Biol.* **41,** 297–307 (1996).

41. Buxbaum, G. *Industrial inorganic pigments.* 3rd ed. (Wiley-VCH, Weinheim, 2005).

42. Kortüm, G. Braun, W. & Herzog, G. Prinzip und Meßmethodik der diffusen Reflexionsspektroskopie, *Angew. Chem.* **75,** 653–661 (1963).

43. ter Vrugt, J. W. Optical Properties of Thin Powder Layers, *Philips Res. Repts* **20,** 23–33 (1965).

44. Mudgett, P. S. & Richards, L. W. Multiple Scattering Calculations for Technology, *Appl. Opt.* **10,** 1485–1502 (1971).

45. Liu, L. Gong, R. Huang, D. Nie, Y. & Liu, C. Calculation of emittance of a coating layer with the Kubelka-Munk theory and the Mie-scattering model, *J. Opt. Soc. Am. A* **22,** 2424–2429 (2005).

46. Fonger, W. H. Two-constant models of luminescence in particle layers. 1: The p-layer model, *Appl. Opt.* **21,** 1219–1221 (1982).

47. Hinds, W. C. *Aerosol technology. Properties, behavior, and measurement of airborne particles.* 2nd ed. (Wiley, New York, 1999).

48. Reist, P. C. *Aerosol science and technology.* 2nd ed. (McGraw Hill, New York, 1993).

49. Lindstroem, J. & Carlsson G.A. A simple model for estimating the particle size dependence of absolute efficiency of fluorescent screens, *Phys. Med. Biol.* **44,** 1353 (1999).

50. Ozawa, L. *Cathodoluminescence. Theory and applications* (Kodansha [u.a.], Tokyo, 1990).

51. Ozawa, L. & Hersh, H. N. Optimum Arrangement of Phosphor Particles in Cathode-Ray Picture Tube Screens, *J. Electrochem. Soc.* **121,** 894–899 (1974).

52. Fonger, W. H. Two-constant models of luminescence in particle layers. 2: The layer luminescence, *Appl. Opt.* **21,** 1222–1227 (1982).

53. Melamed, N. T. Optical Properties of Powders. Part I. Optical Absorption Coefficients and the Absolute Value of the Diffuse Reflectance. Part II. Properties of Luminescent Powders, *J. Appl. Phys.* **34,** 560–570 (1963).

54. Bohren, C. F. & Huffman, D. R. *Absorption and scattering of light by small particles* (Wiley-VCH, Weinheim, 2004).

55. Konrad, A. *et al.* Modeling the optical properties of fluorescent powders: Y1.91Eu0.09O3, *J. Appl. Phys.* **85,** 1796–1801 (1999).

56. Soules, T. F. & Klatt W.A. Optical Properties of Powder Coatings, *Journal of the Illuminating Engineering Society* **17,** 92 (1988).

57. Urabe, K. Monte Carlo Calculation on Phosphor Screens with Complicated Boundary Conditions, *Jpn. J. Appl. Phys.* **19,** 885 (1980).

58. Busselt, W. & Raue, R. Optimizing the Optical Properties of TV Phosphor Screens, *J. Electrochem. Soc.* **135,** 764–771 (1988).

59. Liaparinos, P. F. Kandarakis, I. S. Cavouras, D. A. Delis, H. B. & Panayiotakis, G. S. Modeling granular phosphor screens by Monte Carlo methods, *Med. Phys.* **33,** 4502–4514 (2006).

60. Badano, A. Optical blur and collection efficiency in columnar phosphors for X-ray imaging, *Nucl. Instr. Meth. Phys. Res. A* **508,** 467–479 (2003).

61. Borbely, A. & Johnson, S. G. Performance of phosphor-coated light-emitting diode optics in ray-trace simulations, *Opt. Eng.* **44,** 111308 (2005).

62. Chang, C. C. *et al.* Monte Carlo Simulation of Optical Properties of Phosphor-Screened Ultraviolet Light in a White Light-Emitting Device, *Jpn. J. Appl. Phys.* **44,** 6056 (2005).

63. Urabe, K. Calculation of Luminescence Intensities for a Spherical Phosphor Particle, *Jpn. J. Appl. Phys.* **20,** L28 (1981).

64. Rossmann, K. Point Spread-Function, Line Spread-Function, and Modulation Transfer Function, *Radiology* **93,** 257–272 (1969).

65. Gruner, S. M. Tate, M. W. & Eikenberry, E. F. Charge-coupled device area x-ray detectors, *Rev. Sci. Instrum.* **73,** 2815–2842 (2002).

66. Pokric, M. & Allinson, N. M. Testing of gadolinium oxy-sulphide phosphors for use in CCD-based X-ray detectors for macromolecular crystallography, *Nucl. Instr. Meth. Phys. Res. A* **477,** 353–359 (2002).

67. Koch, A. Raven, C. Spanne, P. & Snigirev, A. X-ray imaging with submicrometer resolution employing transparent luminescent screens, *J. Opt. Soc. Am. A* **15,** 1940–1951 (1998).

68. Sayanna, K. R. Sagar, D. K. & Goud, S. L. Effects of defocusing on the Sparrow limits for apodized optical systems, *Opt. Commun.* **217,** 59–67 (2003).

69. Williams, C. S. & Becklund, O. A. *Introduction to the optical transfer function* (Wiley, New York, 1989).

70. Franks, W. A. R. Kiik, M. J. & Nathan, A. UV-responsive CCD image sensors with enhanced inorganic phosphor coatings, *IEEE Trans. Electron Dev.* **50,** 352–358 (2003).

71. Zege, E. P. Ivanov, A. P. & Kacev, I. L. *Image transfer through a scattering medium* (Springer, Berlin, 1991).

72. Allen, T. *Particle size measurement.* 4th ed. (Chapman & Hall, London, 1994).

73. Butler, K. H. *Fluorescent Lamp Phosphors. Technology and theory* (Pennsylvania State Univ. Pr. University Park, 1980).

74. Sasaki, K. Y. & Talbot, J. B. Deposition of Powder Phosphors for Information Displays, *Adv. Mater.* **11,** 91–105 (1999).

75. Swank, R. K. Calculation of Modulation Transfer Functions of X-Ray Fluorescent Screens, *Appl. Opt.* **12,** 1865–1870 (1973).

76. Faruqi, A. R. Andrews, H. N. & Henderson, R. A high sensitivity imaging detector for electron microscopy. Proceedings of the 7th International Wire Chamber Conference, *Nucl. Instr. Meth. Phys. Res. A* **367,** 408–412 (1995).

77. Sklensky, A. F. Buchanan, R. A. Maple, T. G. & Bailey, H. N. Resolution of X-Ray Intensifying Screens, *J. Electrochem. Soc.* **122,** 1089–1092 (1975).

78. Flannery, B. P. Deckman, H. W. Roberge, W. G. & D'Amico, K. L. Three-Dimensional X-ray Microtomography, *Science* **237,** 1439–1444 (1987).

79. Martin, T. & Koch, A. Recent developments in X-ray imaging with micrometer spatial resolution, *J. Synchrotron Rad.* **13,** 180–194 (2006).

80. Sluzky, E. & Hesse, K. High-Resolution Phosphor Screens, *J. Electrochem. Soc.* **135,** 2893–2896 (1988).

81. Moy, J.-P. Signal-to-noise ratio and spatial resolution in x-ray electronic imagers: Is the MTF a relevant parameter?, *Med. Phys.* **27,** 86–93 (2000).

82. Evanko, D. Primer: fluorescence imaging under the diffraction limit, *Nat. Meth.* **6,** 19–20 (2009).

83. Pankove, J. I. *Display devices* (Springer, Berlin, 1980).

84. Zeylikovich, I. Tamargo, M. C. & Alfano, R. R. High Resolution Utraviolet to Visible Image Conversion Using Self-Assembled CdSe/ZnCdMgSe Quantum Dots Photoluminescence, *Conference on Lasers and Electro-Optics/Quantum Electronics and Laser Science Conference and Photonic Applications Systems Technologies,* CME4 (2007).

85. Mishchenko, M. I. Travis, L. D. & Lacis, A. A. *Scattering, absorption, and emission of light by small particles* (Cambridge Univ. Press, Cambridge, 2002).

86. van de Hulst, H. C. *Light scattering by small particles* (Dover, New York, NY, 2009).

87. Brewster, Q. Volume Scattering of Radiation in Packed Beds of Large, Opaque Spheres, *J. Heat Transfer* **126,** 1048–1050 (2004).

88. Tien, C. L. Thermal Radiation in Packed and Fluidized Beds, *J. Heat Transfer* **110,** 1230–1242 (1988).

89. McNeil, L. E. Hanuska, A. R. & French, R. H. Orientation dependence in near-field scattering from TiO2 particles, *Appl. Opt.* **40,** 3726–3736 (2001).

90. Li, C. Kattawar, G. Zhai, P.-W. & Yang, P. Electric and magnetic energy density distributions inside and outside dielectric particles illuminated by a plane electromagnetic wave, *Opt. Express* **13,** 4554–4559 (2005).

91. Mendes, M. J. Tobías, I. Martí, A. & Luque, A. Near-field scattering by dielectric spheroidal particles with sizes on the order of the illuminating wavelength, *J. Opt. Soc. Am. B* **27,** 1221–1231 (2010).

92. Auger, J.-C. Martinez, V. & Stout, B. Theoretical study of the scattering efficiency of rutile titanium dioxide pigments as a function of their spatial dispersion, *J. Coat. Technol. Res.* **6,** 89–97 (2009).

93. Koleske, J. V. *Paint and coating testing manual.* 14th ed. (ASTM, Philadelphia, PA, 1995).

94. Siegel, R. & Howell, J. R. *Thermal radiation heat transfer.* 3rd ed. (Hemisphere Publ. Washington, D.C. 1992).

95. Tien, C. L. & Drolen, B. L. in *Annual review of numerical fluid mechanics and heat transfer,* edited by T. C. Chawal (Hemisphere Publishing Corp. Washington, DC, 1987), pp. 1–32.

96. Tien, C.-L. Majumdar, A. & Gerner, F. M. *Microscale energy transport* (Taylor and Francis, Washington, DC, 1998).

97. Kamiuto, K. Near-field scattering by a small spherical particle embedded in a nonabsorbing medium, *J. Opt. Soc. Am. A* **1,** 840–844 (1984).

98. Kumar, S. & Tien, C. L. Dependent Absorption and Extinction of Radiation by Small Particles, *J. Heat Transfer* **112,** 178–185 (1990).

99. Prasher, R. Thermal radiation in dense nano- and microparticulate media, *J. Appl. Phys.* **102,** 74316–74319 (2007).

100. Hottel, H. C. Dalzell, W. H. Sarofim, A. F. & Vasalos, I. A. Optical Properties of Coatings. Effect of Pigment Concentration, *AIAA J.* **9,** 1895–1898 (1971).

101. Meltzer, R. S. Feofilov, S. P. Tissue, B. & Yuan, H. B. Dependence of fluorescence lifetimes of Y2O3:Eu3+ nanoparticles on the surrounding medium, *Phys. Rev. B* **60,** R14012 (1999).

102. Klein, L. C. *Sol-gel technology for thin films, fibers, preforms, electronics and specialty shapes* (Noyes Publ. Park Ridge, N.J. 1988).

103. Vollath, D. *Nanomaterials. An introduction to synthesis, properties and application* (Wiley-VCH, Weinheim, 2008).

104. Schniepp, H. & Sandoghdar, V. Spontaneous Emission of Europium Ions Embedded in Dielectric Nanospheres, *Phys. Rev. Lett.* **89,** 257403 (2002).

105. Rogobete, L. Schniepp, H. Sandoghdar, V. & Henkel, C. Spontaneous emission in nanoscopic dielectric particles, *Opt. Lett.* **28,** 1736–1738 (2003).

106. Pique, A. & Chrisey, D. B. *Direct-write technologies for rapid prototyping applications. Sensors, electronics and integrated power sources* (Acad. Press, San Diego, Calif. 2002).

107. Liu, G. & Chen, X. in *Handbook on the Physics and Chemistry of Rare Earths,* edited by K. A. Gschneidner, J.-C. Bünzli & V. K. Pecharsky (Elsevier, Amsterdam, 2007), Vol. 1, pp. 99–169.

108. Liu, L. & Chen, X. Energy levels, fluorescence lifetime and Judd-Ofelt parameters of Eu3+ in Gd2O3 nanocrystals, *Nanotechnology* **18,** 255704 (2007).

109. Schmechel, R. *et al.* Luminescence properties of nanocrystalline Y2O3:Eu3+ in different host materials, *J. Appl. Phys.* **89,** 1679–1686 (2001).

110. Zhang, W.-W. *et al.* Optical properties of nanocrystalline Y2O3:Eu depending on its odd structure, *J. Colloid Interface Sci.* **262,** 588–593 (2003).

111. Chen, X. Y. Zhuang, H. Z. Liu, G. K. Li, S. & Niedbala, R. S. Confinement on energy transfer between luminescent centers in nanocrystals, *J. Appl. Phys.* **94,** 5559–5565 (2003).

112. Igarashi, T. *et al.* Relationship between optical properties and crystallinity of nanometer Y2O3:Eu phosphor, *Appl. Phys. Lett.* **76,** 1549–1551 (2000).

113. Nayak, A. Sahoo, R. & Debnath, R. Hydration-induced coupling of the excitonic state of Y2O3 with its phonon: Negative effect on the luminescence efficiency of Y2O3:Eu+3 nanophosphor, *J. Mater. Res.* **22,** 35–39 (2007).

114. Prasad, P. N. *Nanophotonics* (Wiley, Hoboken, NJ, 2004).

115. Wang, F. Wang, J. & Liu, X. Direct Evidence of a Surface Quenching Effect on Size-Dependent Luminescence of Upconversion Nanoparticles, *Angew. Chem. Int. Ed.* **49,** 7456–7460 (2010).

116. Jüstel, T. Nikol, H. & Ronda, C. New Developments in the Field of Luminescent Materials for Lighting and Displays, *Angew. Chem. Int. Ed.* **37,** 3084–3103 (1998).

117. Skandan, G. *et al.* Phase characterization and stabilization due to grain size effects of nanostructured Y2O3, *Nanostr. Mater.* **1,** 313–322 (1992).

118. Dosev, D. Guo, B. & Kennedy, I. M. Photoluminescence of Eu3+:Y2O3 as an indication of crystal structure and particle size in nanoparticles synthesized by flame spray pyrolysis, *J. Aerosol Sci.* **37,** 402–412 (2006).

119. Kondepudi, D. *Introduction to modern thermodynamics* (Wiley, Chichester, 2008).

120. Valverde, J. M. & Castellanos, A. Random loose packing of cohesive granular materials, *Europhys. Lett.* **75,** 985 (2006).

121. Gonzalez, E. J. & Piermarini, G. J. in *Handbook of nanostructured materials and nanotechnology,* edited by H. S. Nalwa (Acad. Press, San Diego, Calif. 2000), pp. 215–249.

122. Wang, Z. L. Liu, Y. & Zhang, Z. *Handbook of nanophase and nanostructured materials* (Kluwer Academic/Plenum [u.a.], New York, 2003).

123. Chi, L. S. Liu, R. S. & Lee, B. J. Synthesis of Y2O3:Eu, Bi Red Phosphors by Homogeneous Coprecipitation and Their Photoluminescence Behaviors, *J. Electrochem. Soc.* **152,** J93-J98 (2005).

124. Silver, J. Ireland, T. G. & Withnall, R. Fine Control of the Dopant Level in Cubic Y2O3:Eu3+ Phosphors, *J. Electrochem. Soc.* **151,** H66-H68 (2004).

125. Vu, N. Kim, A. T. Yi, G. C. & Strek, W. Photoluminescence and cathodoluminescence properties of Y2O3:Eu nanophosphors prepared by combustion synthesis - Proceedings of the 2005 International Conference on Luminescence and Optical Spectroscopy of Condensed Matter, *J. Lumin.* **122-123,** 776–779 (2007).

126. Qi, Z. Shi, C. Zhang, W. Zhang, W. & Hu, T. Local structure and luminescence of nanocrystalline Y2O3:Eu, *Appl. Phys. Lett.* **81,** 2857–2859 (2002).

127. Wang, H. Lin, C. K. Liu, X. M. Lin, J. & Yu, M. Monodisperse spherical core-shell-structured phosphors obtained by functionalization of silica spheres with Y2O3:Eu3+ layers for field emission displays, *Appl. Phys. Lett.* **87,** 181907-3 (2005).

128. Zhang, J. *et al.* Synthesis of nanometer Y2O3:Eu phosphor and its luminescence property, *Mater. Sci. Eng. A* **334,** 246–249 (2002).

129. Pang, M. L. *et al.* Patterning and luminescent properties of nanocrystalline Y2O3:Eu3+ phosphor films by sol-gel soft lithography, *Mater. Sci. Eng. B* **100,** 124–131 (2003).

130. Jones, S. L. Kumar, D. Singh, R. K. & Holloway, P. H. Luminescence of pulsed laser deposited Eu doped yttrium oxide films, *Appl. Phys. Lett.* **71,** 404–406 (1997).

131. Bihari, B. Eilers, H. & Tissue, B. M. Spectra and dynamics of monoclinic Eu2O3 and Eu3+:Y2O3 nanocrystals, *J. Lumin.* **75,** 1–10 (1997).

132. Joffin, N. *et al.* Elaboration by spray pyrolysis and characterization in the VUV range of phosphor particles with spherical shape and micronic size, *J. Phys. D* **38,** 3261 (2005).

133. Lee, C. H. Kang, Y. C. Jung, K. Y. & Choi, J. G. Phosphor layer formed from the Zn2SiO4:Mn phosphor particles with spherical shape and fine size, *Mater. Sci. Eng. B* **117,** 210–215 (2005).

134. Hong, G. Y. Yoo, K. Moon, S. J. & Yoo, J. S. Enhancement of Luminous Intensity of Spherical Y2O3:Eu Phosphors Using Flux during Aerosol Pyrolysis, *J. Electrochem. Soc.* **150,** H67-H71 (2003).

135. Chang, H. Lenggoro, I. W. Okuyama, K. & Kim, T.-O. Continuous Single-Step Fabrication of Nonaggregated, Size-Controlled and Cubic Nanocrystalline

Y2O3:Eu+ Phosphors Using Flame Spray Pyrolysis, *Jpn. J. Appl. Phys.* **43,** 3535 (2004).

136. Qin, X. Ju, Y. Bernhard, S. & Yao, N. Europium-doped yttrium silicate nanophosphors prepared by flame synthesis, *Mater. Res. Bull.* **42,** 1440–1449 (2007).

137. Camenzind, A. Strobel, R. Krumeich, F. & Pratsinis, S. E. Luminescence and crystallinity of flame-made Y2O3:Eu3+ nanoparticles, *Adv. Powder Technol.* **18,** 5–22 (2007).

138. Sadowsky, M. The Preparation of Luminescent Screens, *J. Electrochem. Soc.* **95,** 112–128 (1949).

139. Bechtel, H. Czarnojan, W. Haase, M. Mayr, W. & Nikol, H. Phosphor screens for flat cathode ray tubes. New Flat, Thin Display Technology, *Philips J. Res.* **50,** 433–462 (1996).

140. Franks, W. A. R. *et al.* Inorganic phosphor coatings for UV-responsive CCD image sensors, *Proc. SPIE* **3965,** 33–41 (2000).

141. Comins, N. R. Hengstberger, M. M. E. & Thirlwall, J. T. Preparation and evaluation of P-47 scintillators for a scanning electron microscope, *J. Phys. E* **11,** 1041 (1978).

142. King, M. V. A procedure for making phosphor viewing screens for the transmission electron microscope, *J. Elec. Microsc. Tech.* **8,** 389–390 (1988).

143. Narendran, N. Gu, Y. Freyssinier, J. P. Yu, H. & Deng, L. Solid-state lighting: failure analysis of white LEDs, *J. Cryst. Growth* **268,** 449–456 (2004).

144. Edwards, M. Zhou, Y. & Wyrowski, F. Comparative properties of optically clear epoxy encapsulants, *Proc. SPIE* **4436,** 190–197 (2001).

145. Sluzky, E. & Hesse, K. Electrophoretic Preparation of Phosphor Screens, *J. Electrochem. Soc.* **136,** 2724–2727 (1989).

146. Yum, J.-h. Seo, S.-Y. Lee, S. & Sung, Y.-E. Y3Al5O12:Ce0.05 Phosphor Coatings on Gallium Nitride for White Light Emitting Diodes, *J. Electrochem. Soc.* **150,** H47-H52 (2003).

147. Zhang, H. Cui, Y. Men, Y. & Liu, X. Strong ultraviolet emission from zinc oxide thin films prepared by electrophoretic deposition, *J. Lumin.* **121,** 601–605 (2006).

148. Smith, A. Belomoin, G. Nayfeh, M. H. & Nayfeh, T. Spatially selective electrochemical deposition of composite films of metal and luminescent Si nanoparticles, *Chem. Phys. Lett.* **372,** 415–418 (2003).

149. Fujiwara, R. *et al.* Fabrication of Electroluminescent Devices Using Nanocrystalline Oxide Phosphors, *Key Eng. Mater.* **388,** 123–126 (2008).

150. Khan, A. F. *et al.* Controlled surface distribution and luminescence of YVO4:Eu3+ nanophosphor layers, *Appl. Phys. Lett.* **93,** 073103-3 (2008).

151. Jang, W.-S. & Grunlan, J. C. Robotic dipping system for layer-by-layer assembly of multifunctional thin films, *Rev. Sci. Instrum.* **76,** 103904-4 (2005).

152. Varahramyan, K. & Lvov, Y. Nanomanufacturing by layer-by-layer assembly - from nanoscale coating to device applications, *Proc. Inst. Mech. Eng. Part N J. Nanoeng. Nanosyst.* **220,** 29–37 (2006).

153. Lu, Y. Liu, G. L. & Lee, L. P. High-Density Silver Nanoparticle Film with Temperature-Controllable Interparticle Spacing for a Tunable Surface Enhanced Raman Scattering Substrate, *Nano Lett.* **5,** 5–9 (2005).

154. Fuller, S. B. Wilhelm, E. J. & Jacobson, J. M. Ink-jet printed nanoparticle microelectromechanical systems, *IEEE ASME J. Microelectromech. Syst.* **11,** 54–60 (2002).

155. Tsai, D. H. Kim, S. H. Corrigan, T. D. Phaneuf, R. J. & Zachariah, M. R. Electrostatic-directed deposition of nanoparticles on a field generating substrate, *Nanotechnology* **16,** 1856 (2005).

156. Milewski, P. D. *et al.* Selective deposition and luminescence characterization of Eu-doped Y2O3 nanoparticles by microwave plasma synthesis, *J. Soc. Inf. Display* **6,** 143–147 (1998).

157. Hafiz, J. *et al.* Hypersonic plasma particle deposition of Si-Ti-N nanostructured coatings. Proceedings of the 31st International Conference on Metallurgical Coatings and Thin Films, *Surf. Coat. Technol.* **188-189,** 364–370 (2004).

158. Chamberlin, R. R. & Skarman, J. S. Chemical Spray Deposition Process for Inorganic Films, *J. Electrochem. Soc.* **113,** 86–89 (1966).

159. Falcony, C. Garcia, M. Ortiz, A. & Alonso, J. C. Luminescent properties of ZnS:Mn films deposited by spray pyrolysis, *J. Appl. Phys.* **72,** 1525–1527 (1992).

160. Hao, J. Studenikin, S. A. & Cocivera, M. Blue, green and red cathodoluminescence of Y2O3 phosphor films prepared by spray pyrolysis, *J. Lumin.* **93,** 313–319 (2001).

161. Lou, Z. Hao, J. & Cocivera, M. Luminescence of ZnWO4 and CdWO4 thin films prepared by spray pyrolysis, *J. Lumin.* **99,** 349–354 (2002).

162. Bengisu, M. *Engineering ceramics* (Springer, Berlin, 2001).

163. Nyman, M. Caruso, J. Hampden-Smith, M. J. & Kodas, T. T. Comparison of Solid-State and Spray-Pyrolysis Synthesis of Yttrium Aluminate Powders, *J. Amer. Ceram. Soc.* **80,** 1231–1238 (1997).

164. Kang, Y. C. Lenggoro, I. W. Okuyama, K. & Park, S. B. Luminescence Characteristics of Y2SiO5:Tb Phosphor Particles Directly Prepared by the Spray Pyrolysis Method, *J. Electrochem. Soc.* **146,** 1227–1230 (1999).

165. Kang, Y. C. Roh, H. S. & Park, S. B. Morphology of Oxide Phosphor Particles Prepared by Colloidal Seed-Assisted Spray Pyrolysis, *J. Electrochem. Soc.* **147,** 1601–1603 (2000).

166. Jeon, B. S. Hong, G. Y. Yoo, Y. K. & Yoo, J. S. Spherical BaMgAl10O17:Eu2+ Phosphor Prepared by Aerosol Pyrolysis Technique for PDP Applications, *J. Electrochem. Soc.* **148,** H128-H131 (2001).

167. Lenggoro, I. W. *et al.* One-Step Synthesis for Zn2SiO4:Mn Particles 0.3-1.3 um in Size with Spherical Morphology and Non-Aggregation, *Jpn. J. Appl. Phys.* **39,** L1051 (2000).

168. Okuyama, K. Lenggoro, I. W. Tagami, N. Tamaki, S. & Tohge, N. Preparation of ZnS and CdS fine particles with different particle sizes by a spray-pyrolysis method, *J. Mater. Sci.* **32,** 1229–1237 (1997).

169. Karthikeyan, J. *et al.* Nanomaterial powders and deposits prepared by flame spray processing of liquid precursors, *Nanostr. Mater.* **8,** 61–74 (1997).

170. Strobel, R. & Pratsinis, S. E. Flame aerosol synthesis of smart nanostructured materials, *J. Mater. Chem.* **17,** 4743–4756 (2007).

171. Teoh, W. Y. Amal, R. & Madler, L. Flame spray pyrolysis: An enabling technology for nanoparticles design and fabrication, *Nanoscale* **2,** 1324–1347 (2010).

172. Pratsinis, S. E. Aerosol-based technologies in nanoscale manufacturing: from functional materials to devices through core chemical engineering, *AIChE J.* **56,** 3028–3035 (2010).

173. Chang, H. Lenggoro, I. W. Okuyama, K. & Jang, H. D. Flame Spray Pyrolysis for Preparing Red-Light-Emitting, Submicron-Sized Luminescent Strontium Titanate Particles, *Jpn. J. Appl. Phys.* **45,** 967 (2006).

174. Kang, Y. C. Sohn, J. R. Yoon, H. S. Jung, K. Y. & Park, H. D. Improved Photoluminescence of Sr5(PO4)3Cl:Eu2+ Phosphor Particles Prepared by Flame Spray Pyrolysis, *J. Electrochem. Soc.* **150,** H38-H42 (2003).

175. Jung, K. Y. & Kang, Y. C. Preparation of BaMgAl10O17:Eu blue phosphor by flame-assisted spray pyrolysis: photoluminescence properties of powder and film under VUV excitation, *Mater. Lett.* **58,** 2161–2165 (2004).

176. Kang, Y. C. Seo, D. J. Park, S. B. & Park, H. D. Morphological and Optical Characteristics of Y2O3:Eu Phosphor ParticlesPrepared by Flame Spray Pyrolysis, *Jpn. J. Appl. Phys.* **40,** 4083 (2001).

177. Camenzind, A. Strobel, R. & Pratsinis, S. E. Cubic or monoclinic Y2O3:Eu3+ nanoparticles by one step flame spray pyrolysis, *Chem. Phys. Lett.* **415,** 193–197 (2005).

178. Iwako, Y. Akimoto, Y. Omiya, M. Ueda, T. & Yokomori, T. Photoluminescence of cubic and monoclinic Gd2O3:Eu phosphors prepared by flame spray pyrolysis, *J. Lumin.* **130,** 1470–1474 (2010).

179. Dosev, D. *et al.* Magnetic/luminescent core/shell particles synthesized by spray pyrolysis and their application in immunoassays with internal standard, *Nanotechnology* **18,** 55102 (2007).

180. Purwanto, A. Wang, W.-N. Lenggoro, I. W. & Okuyama, K. Formation and Luminescence Enhancement of Agglomerate-Free YAG:Ce3+ Submicrometer Particles by Flame-Assisted Spray Pyrolysis, *J. Electrochem. Soc.* **154,** J91-J96 (2007).

181. Kammler, H. K. Mädler, L. & Pratsinis, S. E. Flame Synthesis of Nanoparticles, *Chem. Eng. Technol.* **24,** 583–596 (2001).

182. Hunt, A. T. Carter, W. B. & Cochran, J. K. JR. Combustion chemical vapor deposition: A novel thin-film deposition technique, *Appl. Phys. Lett.* **63,** 266–268 (1993).

183. Kang, Z. T. *et al.* Luminescence properties of Mn2+ doped Zn2SiO4 phosphor films synthesized by combustion CVD, *J. Lumin.* **121,** 595–600 (2006).

184. Choy, K. L. in *Handbook of nanostructured materials and nanotechnology,* edited by H. S. Nalwa (Acad. Press, San Diego, Calif. 2000), pp. 533–577.

185. Jiang, H. Lau, M. Tellkamp, V. L. & Lavernia, E. J. in *Handbook of nanostructured materials and nanotechnology,* edited by H. S. Nalwa (Acad. Press, San Diego, Calif. 2000), pp. 159–213.

186. Bach, H. & Krause, D. *Thin films on glass.* 2nd ed. (Springer, Berlin, 2003).

187. Tammela, S. *et al.* The potential of direct nanoparticle deposition for the next generation of optical fibers, *Proc. SPIE* **6116,** 61160G-9 (2006).

188. Mendez, A. & Morse, T. F. *Specialty optical fibers handbook* (Elsevier/Academic Press, Amsterdam, 2007).

189. Koguchi, M. Matsuda, Y. Kinoshita, E. & Hirabayashi, K. Preparation of YBa2Cu3Ox Thin Film by Flame Pyrolysis, *Jpn. J. Appl. Phys.* **29,** L33 (1990).

190. Choy, K. L. & Seh, H.-K. Fabrication of Ni-Al2O3-based reforming catalyst using flame-assisted vapour deposition, *Mater. Sci. Eng. A* **281,** 253–258 (2000).

191. Mädler, L. *et al.* Direct formation of highly porous gas-sensing films by in situ thermophoretic deposition of flame-made Pt/SnO2 nanoparticles, *Sens. Actuator. B* **114,** 283–295 (2006).

192. Sahm, T. *et al.* Formation of multilayer films for gas sensing by in situ thermophoretic deposition of nanoparticles from aerosol phase, *J. Mater. Res.* **22,** 850–857 (2007).

193. Kuehne, S. *et al.* Wafer-level flame-spray-pyrolysis deposition of gas-sensitive layers on microsensors, *J. Micromech. Microeng.* **18,** 35040 (2008).

194. Thybo, S. *et al.* Flame spray deposition of porous catalysts on surfaces and in microsystems, *J. Catalysis* **223,** 271–277 (2004).

195. Kavitha, R. Meghani, S. & Jayaram, V. Synthesis of titania films by combustion flame spray pyrolysis technique and its characterization for photocatalysis, *Mater. Sci. Eng. B* **139,** 134–140 (2007).

196. Chew, S. Y. *et al.* Thin nanostructured LiMn2O4 films by flame spray deposition and in situ annealing method, *J. Power Sources* **189,** 449–453 (2009).

197. Tricoli, A. Righettoni, M. & Pratsinis, S. E. Anti-Fogging Nanofibrous SiO2 and Nanostructured SiO2-TiO2 Films Made by Rapid Flame Deposition and In Situ Annealing, *Langmuir* **25,** 12578–12584 (2009).

198. Pimenoff, J. Hovinen, A. & Rajala, M. in *Proc. 6th Int. Conf. on Coatings on Glass and Plastics* (2006), p. 135.

199. Glassman, I. & Yetter, R. A. *Combustion.* 4th ed. (Elsevier/Acad. Press, Amsterdam, 2008).

200. Fristrom, R. M. *Flame structure and processes* (Oxford Univ. Press, New York, 1995).

201. Carlson, O. The O-Y (Oxygen-Yttrium) system, *J. Phase Equil.* **11,** 61–66 (1990).

202. Xu, Y.-N. Gu, Z.-q. & Ching, W. Y. Electronic, structural, and optical properties of crystalline yttria, *Phys. Rev. B* **56,** 14993 (1997).

203. Nigara, Y. Measurement of the Optical Constants of Yttrium Oxide, *Jpn. J. Appl. Phys.* **7,** 404–408 (1968).

204. Tomiki, T. *et al.* Optical Spectra of Y2O3 Single Crystals in VUV, *J. Phys. Soc. Jpn.* **55,** 4543 (1986).

205. Bär, S. Huber, G. Gonzalo, J. Perea, A. & Munz, M. Pulsed laser deposition of Eu:Y2O3 thin films on (0001) a-Al2O3, *Appl. Phys. A* **80,** 209–216 (2005).

206. Weber, M. J. Radiative and Multiphonon Relaxation of Rare-Earth Ions in Y2O3, *Phys. Rev.* **171,** 283 (1968).

207. Pappalardo, R. G. & Hunt, R. B. JR. Dye-Laser Spectroscopy of Commercial Y2O3:Eu3+ Phosphors, *J. Electrochem. Soc.* **132,** 721–730 (1985).

208. Ilmas, E. R. & Savikhina, T. I. Investigation of luminescence excitation processes in some oxygen-dominated compounds by 3 to 21 eV photons, *J. Lumin.* **1-2,** 702–715 (1970).

209. Ropp, R. C. Spectral Properties of Rare Earth Oxide Phosphors, *J. Electrochem. Soc.* **111,** 311–317 (1964).

210. Xu, Y.-N. & Ching, W. Y. Electronic structure of yttrium aluminum garnet (Y3Al5O12), *Phys. Rev. B* **59,** 10530 (1999).

211. Potdevin, A. Chadeyron, G. Boyer, D. Caillier, B. & Mahiou, R. Sol-gel based YAG:Tb3+ or Eu3+ phosphors for application in lighting sources, *J. Phys. D* **38,** 3251 (2005).

212. Ullal, C. K. Balasubramaniam, K. R. Gandhi, A. S. & Jayaram, V. Non-equilibrium phase synthesis in Al2O3-Y2O3 by spray pyrolysis of nitrate precursors, *Acta Mater.* **49,** 2691–2699 (2001).

213. Mah, T.-I. & Petry, M. D. Eutectic Composition in the Pseudobinary of Y4Al2O9 and Y2O3, *J. Amer. Ceram. Soc.* **75,** 2006–2009 (1992).

214. Sellappan, P. Jayaram, V. Chokshi, A. H. & Divakar, C. Synthesis of Bulk, Dense, Nanocrystalline Yttrium Aluminum Garnet from Amorphous Powders, *J. Amer. Ceram. Soc.* **90,** 3638–3641 (2007).

215. Bond, W. L. Measurement of the Refractive Indices of Several Crystals, *J. Appl. Phys.* **36,** 1674–1677 (1965).

216. Slack, G. A. Oliver, D. W. Chrenko, R. M. & Roberts, S. Optical Absorption of Y3Al5O12 from 10- to 55 000 cm-1 Wave Numbers, *Phys. Rev.* **177,** 1308 (1969).

217. Caslavsky, J. L. & Viechnicki, D. J. Melting behaviour and metastability of yttrium aluminium garnet (YAG) and YAlO3 determined by optical differential thermal analysis, *J. Mater. Sci.* **15,** 1709–1718 (1980).

218. Karaseva, L. G. Konstantinov, N. Y. & Gromov, V. V. Nature of radiation colour centres in single crystals of yttrium aluminum garnet, *Rad. Phys. Chem.* **26,** 723–730 (1985).

219. Bayerer, R. Heber, J. & Mateika, D. Crystal-field analysis of Tb3+ doped yttrium aluminium garnet using site-selective polarized spectroscopy, *Z. Phys. B* **64,** 201–210 (1986).

220. Park, C.-H. *et al.* VUV excitation of Y3Al5O12:Tb phosphor prepared by a sol-gel process, *J. Mater. Sci. Lett.* **19,** 335–338 (2000).

221. Zimmerer, G. Status report on luminescence investigations with synchrotron radiation at HASYLAB, *Nucl. Instr. Meth. Phys. Res. A* **308,** 178–186 (1991).

222. Czack, G. Flachsbart, I. Hein, H. & et al. *Gmelin Handbook of Inorganic Chemistry: Sc, Y, La–Lu. Rare Earth Elements. Chlorides. Part C4b.* 8th ed. (Springer-Verlag, Berlin, 1982).

223. Hlavac, J. *The technology of glass and ceramics. An introduction* (Elsevier, Amsterdam, 1983).

224. Iler, R. K. *The chemistry of silica. Solubility, polymerization, colloid and surface properties, and biochemistry* (Wiley, New York, NY, 1979).

225. Zhang, K. *et al.* Enhanced luminescence and size effects of Y2O3:Eu3+ nanoparticles and ceramics revealed by x rays and Raman scattering, *J. Opt. Soc. Am. B* **21,** 1804–1808 (2004).

226. Schaack, G. & Koningstein, J. A. Phonon and Electronic Raman Spectra of Cubic Rare.-Earth Oxides and Isomorphous Yttrium Oxide, *J. Opt. Soc. Am.* **60,** 1110–1115 (1970).

227. Hunt, R. B. & Pappalardo, R. G. Fast excited-state relaxation of Eu-Eu pairs in commercial Y2O3:Eu3+ phosphors, *J. Lumin.* **34,** 133–146 (1985).

228. Ray, S. Pramanik, P. Singha, A. & Roy, A. Optical properties of nanocrystalline Y2O3:Eu3+, *J. Appl. Phys.* **97,** 94312–94316 (2005).

229. White, W. B. & Keramidas, V. G. Vibrational spectra of oxides with the C-type rare earth oxide structure, *Spectrochim. Acta A* **28,** 501–509 (1972).

230. Repelin, Y. Proust, C. Husson, E. & Beny, J. M. Vibrational Spectroscopy of the C-Form of Yttrium Sesquioxide, *J. Solid State Chem.* **118,** 163–169 (1995).

231. Nazarov, M. V. *et al.* Lattice parameter and luminescence properties of europium activated yttrium oxide, *Solid State Commun.* **133,** 183–186 (2005).

232. Köbler, U. Time resolved investigations of energy transfer in Eu3+:Y2O3, *Z. Phys. A* **250,** 217–227 (1972).

233. Fabrichnaya, O. Wang, C. Zinkevich, M. Aldinger, F. & Levi, C. Phase equilibria and thermodynamic properties of the ZrO2-GdO1.5-YO1.5 system, *J. Phase Equilib. Diff.* **26,** 591–604 (2005).

234. Kim, E. J. Kang, Y. C. Park, H. D. & Ryu, S. K. UV and VUV characteristics of (YGd)2O3:Eu phosphor particles prepared by spray pyrolysis from polymeric precursors, *Mater. Res. Bull.* **38,** 515–524 (2003).

235. Sohn, J. R. Kang, Y. C. & Park, H. D. Morphological Control of Y2O3:Eu Phosphor Particles by Adding Polymeric Precursors in Spray Pyrolysis, *Jpn. J. Appl. Phys.* **41,** 3006–3009 (2002).

236. Roh, H. S. Kang, Y. C. Park, H. D. & Park, S. B. Y2O3:Eu phosphor particles prepared by spray pyrolysis from a solution containing citric acid and polyethylene glycol, *Appl. Phys. A* **76,** 241–245 (2003).

237. Jung, K. Y. & Han, K. H. Densification and Photoluminescence Improvement of Y2O3 Phosphor Particles Prepared by Spray Pyrolysis, *Electrochem. Solid-State Lett.* **8,** H17-H20 (2005).

238. Konrad, A. Herr, U. Tidecks, R. Kummer, F. & Samwer, K. Luminescence of bulk and nanocrystalline cubic yttria, *J. Appl. Phys.* **90,** 3516–3523 (2001).

239. Jüstel, T. Krupa, J.-C. & Wiechert, D. U. VUV spectroscopy of luminescent materials for plasma display panels and Xe discharge lamps, *J. Lumin.* **93,** 179–189 (2001).

240. Berkowitz, J. K. & Olsen, J. A. Investigation of luminescent materials under ultraviolet excitation energies from 5 to 25 eV, *J. Lumin.* **50,** 111–121 (1991).

241. Popma, T. J. A. van der Weg, W. F. & Thimm, K. Excitation of luminescent materials by synchrotron radiation, *J. Lumin.* **24-25,** 289–292 (1981).

242. Ronda, C. R. Phosphors for lamps and displays: an applicational view. Proceedings of the 2nd International Conference on f-Elements, *J. Alloy Comp.* **225,** 534–538 (1995).

243. Joffin, N. Dexpert-Ghys, J. Verelst, M. Baret, G. & Garcia, A. The influence of microstructure on luminescent properties of Y2O3:Eu prepared by spray pyrolysis, *J. Lumin.* **113,** 249–257 (2005).

244. Benitez, E. L. Husk, D. E. Schnatterly, S. E. & Tarrio, C. A surface recombination model applied to large features in inorganic phosphor efficiency measurements in the soft x-ray region, *J. Appl. Phys.* **70,** 3256–3260 (1991).

245. Kang, Y. C. Lenggoro, I. W. Park, S. B. & Okuyama, K. Photoluminescence characteristics of YAG:Tb phosphor particles with spherical morphology and non-aggregation, *J. Phys. Chem. Solids* **60,** 1855–1858 (1999).

246. Kang, Y. C. Lenggoro, I. W. Park, S. B. & Okuyama, K. YAG:Ce phosphor particles prepared by ultrasonic spray pyrolysis, *Mater. Res. Bull.* **35,** 789–798 (2000).

247. Lee, H. J. Hong, S. K. Jung, D. S. & Kang, Y. C. Y3Al5O12:Tb phosphor particles prepared by spray pyrolysis from spray solution with polymeric precursors and ammonium fluoride flux, *Mater. Lett.* **59,** 2383–2387 (2005).

248. Lee, S. H. Jung, D. S. Han, J. M. Young Koo, H. & Kang, Y. C. Fine-sized Y3Al5O12:Ce phosphor powders prepared by spray pyrolysis from the spray solution with barium fluoride flux, *J. Alloy Comp.* **477,** 776–779 (2009).

249. Purwanto, A. *et al.* High luminance YAG:Ce nanoparticles fabricated from urea added aqueous precursor by flame process, *J. Alloy Comp.* **463,** 350–357 (2008).

250. van der Ziel, J. P. Kopf, L. & van Uitert, L. G. Quenching of Tb3+ Luminescence by Direct Transfer and Migration in Aluminum Garnets, *Phys. Rev. B* **6,** 615 (1972).

251. Li, X. Yu, Q. Zeng, Z. & Jing, X. Luminescent properties of amorphous phosphor 1.4Y2O3·2.5Al2O3·0.1Tb2O3 prepared by sol-gel method, *J. Rare Earths* **26,** 35–39 (2008).

252. Jossen, R. Mueller, R. Pratsinis, S. E. Watson, M. & Kamal Akhtar, M. Morphology and composition of spray-flame-made yttria-stabilized zirconia nanoparticles, *Nanotechnology* **16,** S609 (2005).

253. Strobel, R. & Pratsinis, S. E. Effect of solvent composition on oxide morphology during flame spray pyrolysis of metal nitrates, *Phys. Chem. Chem. Phys.* **13,** 9246-9252 (2011).

254. Guo, B. Harvey, A. Risbud, S. H. & Kennedy, I. M. The formation of cubic and monoclinic Y2O3 nanoparticles in a gas-phase flame process, *Phil. Mag. Lett.* **86,** 457–467 (2006).

255. Guo, B. *et al.* Atmospheric Pressure Synthesis of Heavy Rare Earth Sesquioxides Nanoparticles of the Uncommon Monoclinic Phase, *J. Amer. Ceram. Soc.* **90,** 3683–3686 (2007).

256. Guo, B. & Luo, Z.-P. Particle Size Effect on the Crystal Structure of Y2O3 Particles Formed in a Flame Aerosol Process, *J. Amer. Ceram. Soc.* **91,** 1653–1658 (2008).

257. Guo, B. Yim, H. Hwang, W. Nowell, M. & Luo, Z. Crystalline phase of Y2O3:Eu particles generated in a substrate-free flame process, *Particuology* **9,** 24–31 (2011).

258. Zhang, P. *et al.* Energetics of Cubic and Monoclinic Yttrium Oxide Polymorphs: Phase Transitions, Surface Enthalpies, and Stability at the Nanoscale, *J. Phys. Chem. C* **112,** 932–938 (2008).

259. Heine, M. C. Mädler, L. Jossen, R. & Pratsinis, S. E. Direct measurement of entrainment during nanoparticle synthesis in spray flames, *Comb. Flame* **144,** 809–820 (2006).

260. Dhanaraj, J. Jagannathan, R. Kutty, T. R. N. & Lu, C.-H. Photoluminescence Characteristics of Y2O3:Eu3+ Nanophosphors Prepared Using Sol-Gel Thermolysis, *J. Phys. Chem. B* **105,** 11098–11105 (2001).

261. Ye, X. *et al.* Preparation, characterization, and optical properties of nano- and submicron-sized Y2O3:Eu3+ phosphors, *J. Appl. Phys.* **105,** 64302–64306 (2009).

262. Lakowicz, J. R. *Principles of fluorescence spectroscopy.* 3rd ed. (Springer, New York, 2006).

263. Chen, R. Apparent stretched-exponential luminescence decay in crystalline solids. Proceedings of the 2002 International Conference on Luminescence and Optical Spectroscopy of Condensed Matter, *J. Lumin.* **102-103,** 510–518 (2003).

264. Berberan-Santos, M. N. Bodunov, E. N. & Valeur, B. Mathematical functions for the analysis of luminescence decays with underlying distributions 1. Kohlrausch decay function (stretched exponential), *Chem. Phys.* **315,** 171–182 (2005).

265. Martin, J. E. & Shea-Rohwer, L. E. Lifetime determination of materials that exhibit a stretched exponential luminescent decay, *J. Lumin.* **121,** 573–587 (2006).

266. Konrad, A. *et al.* Chemical vapor synthesis and luminescence properties of nanocrystalline cubic Y2O3:Eu, *J. Appl. Phys.* **86,** 3129–3133 (1999).

267. Tanner, P. A. Synthesis and Luminescence of Nano-Insulators Doped with Lanthanide Ions, *J. Nanosci. Nanotechnol.* **5,** 1455–1464 (2005).

268. Tricoli, A. *et al.* Micropatterning Layers by Flame Aerosol Deposition-Annealing, *Adv. Mater.* **20,** 3005–3010 (2008).

269. Tissue, B. M. in *Phosphor handbook,* edited by W. M. Yen, S. Shionoya & H. Yamamoto (CRC Press, Boca Raton, Fla. 2007), 2nd ed, pp. 355–380.

270. Kasuya, R. Kawano, A. Isobe, T. Kuma, H. & Katano, J. Characteristic optical properties of transparent color conversion film prepared from YAG:Ce3+ nanoparticles, *Appl. Phys. Lett.* **91,** 111916 (2007).

271. Takeshita, S. Nakayama, K. Isobe, T. Sawayama, T. & Niikura, S. Optical Properties of Transparent Wavelength-Conversion Film Prepared from YVO4:Bi3+,Eu3+ Nanophosphors, *J. Electrochem. Soc.* **156,** J273-J277 (2009).

272. Do, Y. R. Park, D.-H. & Kim, Y.-S. Al2O3 Nanoencasulation of BaMgAl10O17:Eu2+ Phosphors for Improved Aging Properties in Plasma Display Panels, *J. Electrochem. Soc.* **151,** H210-H212 (2004).

273. Kim, H. S. *et al.* Improvement of Luminescent Properties of Phosphor Powders coated with nanoscaled SiO2 by Atomic Layer Deposition, *Solid State Phenom.* **124 - 126,** 375–378 (2007).

274. Teleki, A. Heine, M. C. Krumeich, F. Akhtar, M. K. & Pratsinis, S. E. In Situ Coating of Flame-Made TiO2 Particles with Nanothin SiO2 Films, *Langmuir* **24,** 12553–12558 (2008).

275. Teleki, A. *et al.* Hermetically Coated Superparamagnetic Fe2O3 Particles with SiO2 Nanofilms, *Chem. Mater.* **21,** 2094–2100 (2009).

276. Bachmann, J. *et al.* A Practical, Self-Catalytic, Atomic Layer Deposition of Silicon Dioxide, *Angew. Chem. Int. Ed.* **47,** 6177–6179 (2008).

277. Allison, S. W. & Gillies, G. T. Remote thermometry with thermographic phosphors: Instrumentation and applications, *Rev. Sci. Instrum.* **68,** 2615–2650 (1997).

278. Khalid, A. & Kontis, K. Thermographic Phosphors for High Temperature Measurements: Principles, Current State of the Art and Recent Applications, *Sensors* **8,** 5673–5744 (2008).

279. Okazaki, C. Shiiki, M. Suzuki, T. & Suzuki, K. Luminance saturation properties of PDP phosphors, *J. Lumin.* **87-89,** 1280–1282 (2000).

280. Atakan, B. Eckert, C. & Pflitsch, C. Light emitting diode excitation of Cr3+ :Al2O3 as thermographic phosphor: experiments and measurement strategy, *Meas. Sci. Technol.* **20,** 75304 (2009).

281. Ranson, R. M. Evangelou, E. & Thomas, C. B. Modeling the fluorescent lifetime of Y2O3:Eu, *Appl. Phys. Lett.* **72,** 2663–2664 (1998).

282. Lü, Q. Li, A. H. Guo, F. Y. Sun, L. & Zhao, L. C. The two-photon excitation of SiO2 -coated Y2O3:Eu3+ nanoparticles by a near-infrared femtosecond laser, *Nanotechnology* **19,** 205704 (2008).

283. Lenggoro, I. W. & Okuyama, K. in *Inorganic display materials,* edited by H. S. Nalwa & L. S. Rohwer (American Scientific Publishers, Stevenson Ranch, Calif. 2003), pp. 327–359.

284. Kang, Y. C. Roh, H. S. & Park, S. B. Preparation of Y2O3:Eu Phosphor Particles of Filled Morphology at High Precursor Concentrations by Spray Pyrolysis, *Adv. Mater.* **12,** 451–453 (2000).

285. Roh, H. S. Kang, Y. C. & Park, S. B. Morphology and Luminescence of (GdY)2O3:Eu Particles Prepared by Colloidal Seed-Assisted Spray Pyrolysis, *J. Colloid Interface Sci.* **228,** 195–199 (2000).

286. Rudin, T. Wegner, K. & Pratsinis, S. Uniform nanoparticles by flame-assisted spray pyrolysis (FASP) of low cost precursors, *J. Nanopart. Res.* **13,** 2715-2725 (2011).

287. Liu, G. K. Zhuang, H. Z. & Chen, X. Y. Restricted Phonon Relaxation and Anomalous Thermalization of Rare Earth Ions in Nanocrystals, *Nano Lett.* **2,** 535–539 (2002).

288. Hwang, J. & Daily, J. W. Electric field enhanced deposition in flame-synthesized materials manufacturing, *J. Aerosol Sci.* **26,** 5–18 (1995).

289. Tricoli, A. & Pratsinis, S. E. Dispersed nanoelectrode devices, *Nat. Nanotechnol.* **5,** 54–60 (2010).

290. Clark, T. E. & Burilla, C. T. Preparation, Optimization, and Cathodoluminescent Properties of a Line Emission Penetration Phosphor, *J. Electrochem. Soc.* **129,** 1540–1546 (1982).

291. Chang, M. & Tie, S. Fabrication of novel luminor Y2O3:Eu3+ @ SiO2 @ YVO4:Eu3+ with core/shell heteronanostructure, *Nanotechnology* **19,** 75711 (2008).

List of publications

Peer-reviewed papers:

- R. Kubrin, W. Bauhofer, A. Ivankov, “No-binder screening of fine phosphor powders by flame spray pyrolysis”, *Journal of the Electrochemical Society* **154** (2007) J253.
- R. Kubrin, W. Bauhofer, “Influence of polymeric additives on morphology and performance of Y_2O_3:Eu phosphor synthesized by flame-assisted spray pyrolysis”, *Journal of Luminescence* **129** (2009) 1060.
- R. Kubrin, A. Tricoli, A. Camenzind, S.E. Pratsinis, W. Bauhofer, “Flame aerosol deposition of Y_2O_3:Eu nanophosphor screens and their photoluminescent performance”, *Nanotechnology* **21** (2010) 225603.
- R. Kubrin, J. Huang, F. Moglia, K. Petermann, W. Bauhofer, “Photoluminescence of $(YGd)_2O_3$:Eu phosphors produced by nanoparticle-seeded flame-assisted spray pyrolysis”, *IOP Conference Series: Materials Science and Engineering* **18** (2011) 102018.

Conferences:

- R. Kubrin, W. Bauhofer, A. Ivankov, “The use of polymeric precursors in low-temperature flame spray pyrolysis”, *International Display Workshops' 06* (Otsu, Japan, 6-8 December 2006) / presentation.
- W. Bauhofer, R.Kubrin, “Properties of Luminescent Screens with Reduced Phosphor Particle Size”, *3rd International Symposium on Structure-Property Relationships in Solid State Materials* (Stuttgart, Germany, 27 June – 2 July 2010) / presentation.
- R. Kubrin, J. Huang, F. Moglia, K. Petermann, W. Bauhofer, “Photoluminescence of $(YGd)_2O_3$:Eu phosphors produced by nanoparticle-seeded flame-assisted spray pyrolysis”, *3rd International Congress on Ceramics* (Osaka, Japan, 14-18 November 2010) / poster.

Acknowledgements

The experimental work on this thesis spanned a period from March 2005 to May 2009 and here I would like to thank all people who helped me to accomplish it.

First of all I wish to express my gratitude to my supervisor Prof. Wolfgang Bauhofer for his support and advice through all these years. I am very grateful to the staff of the Institute of Optical and Electronic Materials: to Christine Kunstmann and Gabriele Birjukov, to Iris Bucher and Carola Micheelsen, to Michael Seiler and Stefan Schön. I thank all my collegues for useful hints and friendly atmosphere, especially Josef Lott, Altan Yildirim, and Andrei Ivankov.

I owe special thanks to Prof. Sotiris E. Pratsinis and the PTL-team 2008 for all the support and many inspiring insights that I collected during my stay at the ETH in Zurich. I very much appreciate the contribution and help of Antonio Tricoli, Adrian Camenzind, Reto Strobel, and Alexandra Teleki.

I also would like to thank Prof. Ernst Heumann, Klaus Petermann, Annabelle Colombet, and Francesca Moglia (at the Institute of Laser-Physics, University of Hamburg, DESY), Prof. Georg Zimmerer and Gregory Stryganyuk (at the HASYLAB, DESY), Prof. Gerold A. Schneider, Ralf-Peter Herber, Katrin Zimmermann, and Manfred Geerken (at the Institute of Advanced Ceramics, TUHH), Prof. Kornelius Nielsch, Julien Bachmann, and Robert Zierold (at the Institute of Applied Physics, University of Hamburg), Prof. Stefan Heinrich and Sergiy Antonyuk (at the Institute of Solids Process Engineering and Particle Technology, TUHH). I am grammatically pretty much obliged to Talayeh Noshiravani, Stephanie Lewellen, and Claire Armstrong.

I am indebted to the other members of our local “The Big Bang Theory” squad - Alexander Petrov, Alexander Vanaev, and Andriy Zolotaryov - for fruitful scientific discussions and educating leisure activities that made these years in Hamburg so unforgettable. Finally, I would like to acknowledge the Probability of Good Things to Happen for its generousity and my wife Natalia for her patience.